



CERN-THESIS-2005-098

*Scale Dependence of Mean Transverse
Momentum Fluctuations at Top SPS
Energy measured by the CERES
experiment*

and studies of gas properties for the ALICE experiment

Vom Fachbereich Physik
der Technischen Universität Darmstadt

zur Erlangung des Grades
eines Doktors der Naturwissenschaften
(Dr. rer. nat.)

genehmigte Dissertation von
Georgios Karolos Tsiledakis
aus Bologna

Darmstadt 2005
D17

Referent: Prof. Dr. P. Braun-Munzinger

Koreferent: Prof. Dr. Dr./h.c.(RUS) D.H.H. Hoffmann

Tag der Einreichung: 28.Nov.2005

Tag der Prüfung: 08.Feb.2006

Boredom and impatience are the most immoral emotions there can be. For man sets time as real in them: he wants it to pass without him having to fill it, without it being mere phenomenal form of his inner liberation and extension, mere form in which he must strive to be realised, but rather independent from him, and he dependent on it. Boredom is at the same time the need to annul time from outside, and the longing for the devil's work.

Otto Weininger (1880-1903)

Summary

The principal aim of the study of ultrarelativistic nucleus-nucleus collisions is the search for evidence of a transient state of deconfined quarks and gluons in the early, dense and hot stage of the reaction. Non-statistical event-by-event fluctuations of mean transverse momentum, p_T , have been proposed as a possible signature for the QCD phase transition, in particular for the critical point. However, the magnitude of the measured fluctuations is not as large as anticipated. Since fluctuations were characterized so far by one single (integral) number, it was difficult to estimate the many possible contributions to them.

Taking into account the high available statistics offered by the CERES experiment combined with the full azimuthal acceptance, a differential study of mean p_T fluctuations is performed, which provides the sensitivity to discriminate among various correlation sources. For the first time at SPS energy, the charge-dependent mean p_T fluctuations have been analyzed as a function of the angular pair separation, $\Delta\phi$, and of the separation in pseudorapidity, $\Delta\eta$. Thus, we are able to show that the overall fluctuations are dominated by the short range correlation peak at small opening angles ('near-side'), most probably originating from Bose-Einstein and Coulomb effects between pairs of particles emitted with similar velocities. Another important contribution is a broad maximum at $\Delta\phi=180^\circ$ ('away-side') originating from back-to-back (jet-like) correlations. Since the fluctuations related to the critical point should be present for all opening angles the best strategy is to focus on the fluctuations in the region of $30^\circ < \Delta\phi < 60^\circ$, free of the influence of the two mentioned components, and where the elliptic flow cancels out. Concerning the observed away-side peak, we demonstrate that it comes from high- p_T correlations that cannot be attributed to the elliptic flow.

The second part of the thesis is dedicated to studies of gas properties for the ALICE experiment at the CERN LHC. Drift velocity and gain measurements have been performed for a number of gas mixtures in order to assess the effect of nitrogen which is expected to accumulate in the gas volume over long periods of running. The ALICE Transition Radiation Detector (TRD) is designed to work with a gas of 85 % Xe and 15 % CO₂. Some of the nine isotopes of Xe have very

high neutron capture cross-section leading to multi-gamma deexcitation cascades which produce background for the physical signals. An exhaustive study of this issue based on Monte Carlo simulations is presented, demonstrating that the level of this background is low enough not to cause deterioration in the performance of the detector. In addition, the resulting radioactivity and dose rate of the active gas system of ALICE TRD activated by slow neutrons is investigated and appear to be low and safe.

Zusammenfassung

Für stark wechselwirkende Materie wird bei hoher Temperatur und/oder Dichte die Existenz einer Phase erwartet, in welcher der Einschluss von Quarks und Gluonen in Hadronen (Confinement) aufgehoben ist. Erzeugung und Nachweis dieses Materiezustands soll durch das Studium von Kollisionen schwerer Ionen erbracht werden. Als mögliche Signatur für den Phasenübergang, insbesondere für einen möglichen kritischen Punkt, wurden nicht-statistische event-by-event Fluktuationen des mittleren Transversalimpulses p_T diskutiert. Die Stärke des beobachteten Signals ist allerdings geringer als erwartet. Bisher wurden Fluktuationen nur durch gemittelte Größen charakterisiert, so dass eine systematische Untersuchung unterschiedlicher Beiträge nur schwer durchführbar war.

In dieser Arbeit werden Fluktuationen des mittleren Transversalimpulses anhand von Daten des CERES Experiments untersucht. Die volle azimuthale Akzeptanz des Experiments sowie die hohe Anzahl an erfassten Kollisionsereignissen erlaubt es, im Rahmen einer differentiellen Analyse verschiedene Beiträge zu den gemessenen Korrelationen zu identifizieren. Wir präsentieren, zum ersten Mal für SPS Energien, eine Studie der Transversalimpulsfluktuationen in Abhängigkeit vom Öffnungswinkel $\Delta\phi$, der Separation in Pseudorapidität $\Delta\eta$ und der Ladung der korrelierten Paare. Wie sich herausstellt sind die gemessenen Fluktuationen durch kurzreichweitige Korrelationen bei kleinem Öffnungswinkel dominiert, in denen sich höchstwahrscheinlich Bose-Einstein Korrelationen und Coulomb-Wechselwirkung zwischen Teilchenpaaren ähnlicher Geschwindigkeit manifestieren. Weiterhin finden wir ein breites Maximum für $\Delta\phi=180^\circ$, deren Ursprung in 'back-to-back' (jetartigen) Korrelationen liegt. Da Fluktuationen in Zusammenhang mit dem Phasenübergang für beliebige Öffnungswinkel erwartet werden, schlagen wir als Signatur für den kritischen Punkt Transversalimpulsfluktuationen im Winkelbereich $30^\circ < \Delta\phi < 60^\circ$ vor, da für diese Öffnungswinkel die diskutierten Komponenten nicht beitragen, ebensowenig wie Korrelationen durch kollektive Effekte im Feuerball (elliptischer Fluss). Weiterhin wird demonstriert, dass die Korrelation für $\Delta\phi=180^\circ$ bei hohem Transversalimpuls nicht auf elliptischen Fluss zurückzuführen ist.

Der zweite Teil der vorliegenden Arbeit widmet sich der Untersuchung von Eigenschaften von Gasen, die im ALICE Detektor am CERN LHC eingesetzt werden sollen. Für eine Reihe von Gasmischungen wurden Messungen der Ladungsverstärkung und Driftgeschwindigkeiten von Elektronen durchgeführt, um den Einfluss der Anreicherung von Stickstoff über längere Strahlzeitperioden zu untersuchen.

Der ALICE Transition Radiation Detector (TRD) operiert mit einem Gasgemisch aus Xe(85 %) und CO₂(15 %). Einige der insgesamt neun stabilen Xenon-Isotope haben hohe Wirkungsquerschnitte für Neutroneneinfang, der zu Gamma-Kaskaden beim Übergang der angeregten Tochterkerne in den Grundzustand führt. Solche Gammastrahlung stellt störenden Untergrund für den Detektor dar. Mittels umfangreicher Monte-Carlo Simulationen können wir demonstrieren, dass der Beitrag durch solchen Untergrund gering ist und die Funktion des Detektors nicht beeinträchtigt ist. Darüberhinaus wird die Dosisrate durch langsame Neutronen innerhalb des ALICE TRD Gassystems bestimmt und gezeigt, dass diese als gering und ungefährlich einzustufen ist.

Contents

1	Preface	1
I		3
2	Introduction	5
2.1	Hot and Dense Nuclear Matter	5
2.2	Experimental program and global observables	7
2.2.1	Collision Characteristics	8
2.2.2	Quark-Gluon Plasma Signatures	9
2.3	Searching for the QCD critical point	11
2.4	Transverse momentum fluctuations	13
3	Measures of Mean p_T Fluctuations	15
3.1	Φ_{p_T} and $\sigma_{p_T, dyn}^2$	15
3.2	The average momentum correlator $\langle \overline{\Delta p_{t,1}} \overline{\Delta p_{t,2}} \rangle$	18
3.3	The normalized dynamical fluctuation Σ_{p_T}	19
3.4	$\Delta\sigma_{\langle p_T \rangle}$ and F_{p_T}	21
3.5	Discussion	21
4	Previous Results on Event-by-Event Mean p_T Fluctuations at SPS energies	23
4.1	Introduction	23
4.2	Beam energy dependence	25
4.3	Centrality dependence	26
4.4	Conclusions	27

5	The CERES Experiment and the Data Analysis	29
5.1	The CERES Experiment	29
5.1.1	Target Area, Trigger and the Two Silicon Drift Detectors .	30
5.1.2	The RICH Detectors	32
5.1.3	The Time Projection Chamber	33
5.2	Data Analysis	36
5.2.1	Event Selection	36
5.2.2	Centrality Determination	36
5.2.3	Track Selection	38
6	Scale dependence of Mean Transverse Momentum Fluctuations in $\Delta\eta$-$\Delta\phi$ space	41
6.1	Inclusive results	42
6.2	Differential analysis	44
6.2.1	Mixed event analysis	44
6.2.2	Same event analysis	48
6.2.3	Centrality dependence	53
6.2.4	Elliptic flow contribution	58
6.3	Two-particle correlation analysis using the cumulant p_T variable x	63
6.3.1	Two-particle correlation plots in several $\Delta\phi$ regions	64
6.4	Discussion	73
II		75
7	The ALICE experiment	77
7.1	Introduction	77
7.2	The ALICE detector layout	78
7.3	Studies of gas properties for the ALICE central detectors	80
8	Drift velocity and gain in argon- and xenon-based mixtures	81
8.1	Introduction	81
8.2	Experimental setup	84
8.3	Drift velocity measurements	86
8.4	Gain measurements	90

8.5	Conclusions	94
9	Background in the ALICE TRD based on FLUKA calculations	97
9.1	Radiation transport code (FLUKA)	98
9.1.1	Radiation units used in FLUKA	100
9.2	Implementation of Xenon capture gammas in FLUKA	101
9.2.1	Neutron transport and (n,γ) reactions in FLUKA	102
9.2.2	Basic nuclear data for Xenon	104
9.2.3	Available information on energy levels	106
9.2.4	Implementation in FLUKA	107
9.2.5	Discussion	110
9.3	Background from thermal neutrons	115
9.3.1	Description of the detector geometry and material	115
9.3.2	Primary event generation and scoring	116
9.3.3	Particle fluxes and energy deposition in the TRD, with and without neutron capture in Xenon	119
9.3.4	Evaluation of the steady state background hit rate in the TRD	122
9.3.5	Results and conclusions	124
9.4	Radioactivity in the gas system of ALICE TRD	126
9.4.1	Calculation of activity	126
9.4.2	Scaling ATLAS results to ALICE TRD	128
9.4.3	Conclusions	129
9.5	Estimation of the radiation level in the ALICE TPC electronics .	130
A	Two-particle correlation plots	145
B	Number of gammas in ^{nat}Xe	149
C	Radiation level in the TPC electronics	163
C.1	TPC detector and front-end electronics	164
C.1.1	Detector geometry and scoring	165
C.1.2	Particle fluences based on FLUKA calculations	166
C.1.3	Admixture of CH_4 or N_2 in the TPC gas.	168

Chapter 1

Preface

Quantum Chromodynamics (QCD) predicts that strongly interacting matter can exist in different phases. The expectation is that at high enough temperature and/or density hadrons dissolve into a new form of elementary particle matter, the Quark-Gluon Plasma (QGP), where quarks and gluons are deconfined. At this phase transition it is expected that chiral symmetry is restored, with significant consequences on particle properties. The goal of heavy-ion collision experiments is to shed light on the thermodynamic properties of strongly interacting matter under these conditions and to investigate the QCD phase diagram.

As fluctuations are sensitive to the dynamics of the system, the analysis of event-by-event fluctuations of the mean transverse momentum has been proposed as a tool to search for the phase transition, especially the QCD critical point via their non-monotonic variation with control parameters such as beam energy and centrality.

In fact, significant non-statistical event-by-event fluctuations and a characteristic centrality dependence have been observed over a wide range of beam energies at different experiments. However, the magnitude of the measured fluctuations is not as large as anticipated.

This work extends the previous study [45] of the CERES experiment of event-by-event transverse momentum fluctuations. The main objective is to resolve them as a function of the angular pair separation, $\Delta\phi$, and of the separation in pseudo-rapidity, $\Delta\eta$. This ‘differential’, scale-dependent analysis, which is presented for the first time at SPS energy, will be compared with two-particle

transverse momentum correlations in order to extract complete information that will be studied to shed light on their origin.

The thesis is structured as follows: Chapter 2 introduces the physics topics discussed in this work. In Chapter 3 the statistical tools used in this analysis are introduced and briefly discussed. The previously published results on fluctuations are presented in Chapter 4. The experimental set-up of CERES as well as the data analysis is described in Chapter 5. In Chapter 6 we present and discuss the results of the scale dependence of mean transverse momentum fluctuations.

The second part of the thesis is dedicated to studies of gas properties for the ALICE experiment. A short description of the ALICE experiment is given in Chapter 7. Measurements of drift velocities and gains in gas mixtures based on Ar and Xe, with CO₂, CH₄, and N₂ as quenchers, are presented in Chapter 8. Finally, the radiation background which will be present in the real LHC environment as well as an estimate of the activity levels of the gas system of the ALICE TRD (Transition Radiation Detector) as calculated by detailed Monte Carlo simulations are discussed in Chapter 9.

Part I

Chapter 2

Introduction

Ultra-relativistic heavy ion collisions offer the unique opportunity to probe highly excited (dense) nuclear matter under controlled laboratory conditions. The compelling driving force for such studies is the expectation that at high enough temperature and/or density hadrons dissolve into a new form of elementary particle matter, the **Quark Gluon Plasma** (QGP), where quarks and gluons are deconfined. Besides this deconfinement, chiral symmetry is expected to be restored in a QGP, which means that the quark masses will approach zero. This phase transition is predicted by Quantum Chromodynamics (QCD), the theory of strong interactions. The opposite phase transition, from quarks and gluons to hadronic matter, took place about 10^{-5} s after the Big Bang, the primeval event which is at the origin of our Universe. The study of phase transitions is of crucial importance for our understanding of the early evolution of the Universe. The QCD phase transition can only be accessible to laboratory experiments in high energy heavy ion collisions [1].

2.1 Hot and Dense Nuclear Matter

We know (since at least 40 years) that hadrons, the particles participating in the strong interaction, such as protons, neutrons and pions, are not elementary, but are made of quarks. Quarks are fermions (spin $\frac{1}{2}$) and come in six varieties, or flavors; These are u (up), d (down), c (charm), s (strange), b (bottom) and t (top). According to QCD, quarks carry a strong interaction charge (colour) which comes

in three types (red, green and blue), while antiquarks carry anticolour. Quarks interact among themselves via the exchange of the colour field quanta (gluons). Gluons themselves carry a colour charge, unlike the photon in QED (Quantum Electrodynamics), which carries no electric charge. All known hadron states are colour singlets (white). These white objects can be constructed by either combining three different colours or a colour with its anticolour (baryons: qqq states; mesons $q\bar{q}$ states). In particular, no free quark has ever been detected and quarks seem to be permanently confined within hadrons.

What if we compress/heat the system so much that the individual hadrons start to interpenetrate? **Lattice QCD**, which is used to address the non-perturbative aspects of QCD [2], predicts that if a system of hadrons is brought to sufficiently large density and/or temperature a deconfinement phase transition should occur. In the new phase, called **Quark Gluon Plasma** (QGP), quarks and gluons are not longer confined within individual hadrons, but are free to move around over a larger volume. Confined quarks acquire an additional mass (~ 350 MeV) dynamically through the confining effect of strong interactions. Deconfinement is expected to be accompanied by a restoration of the masses to the ‘bare’ values they have in the Lagrangian.

The transition to free quarks and gluons is accompanied by the sudden increase of the energy density as a function of temperature, shown in Fig. 2.1 for two and three degenerate flavours [3, 4]. For the 2-flavor case, the transition occurs at a critical temperature $T_c \simeq 170$ MeV with critical energy density $\varepsilon_c \simeq 0.7$ GeV, while for the 3-flavor case T_c is smaller by about 20 MeV. A result for the case of two degenerate flavors and a heavier strange quark (physical values) is also included. The values according to the law of Stefan-Boltzmann for an ideal gas of non-interacting quarks and gluons are indicated at the right edge of the figure. As strange quarks have mass $m_s < T_c$ they will not contribute to the thermodynamics close to T_c , but will do so at higher temperatures. Since all heavier quarks do not contribute in the temperature range accessible in present or foreseeable future heavy-ion experiments, the bulk thermodynamic observables of QCD with a realistic quark mass spectrum will essentially be given by massless 2-flavour QCD close to T_c and will rapidly switch over to the thermodynamics of massless 3-flavour QCD in the plasma phase. This is indicated by the crosses of

Fig.2.1. The transition is second order in the chiral limit of 2-flavour QCD and first order for 3-flavour QCD and it is likely to be a rapid crossover in the case of the physically realized quark mass spectrum. The crossover, however, does take place in a narrow temperature interval, which means that the transition between the hadronic and plasma phase is still well localized. This is reflected in a rapid rise of energy density (ε) in the vicinity of the crossover temperature. This leads to large correlation lengths and a rapid rise in susceptibilities. These might be detectable experimentally through the event-by-event analysis of fluctuations in particle yields.

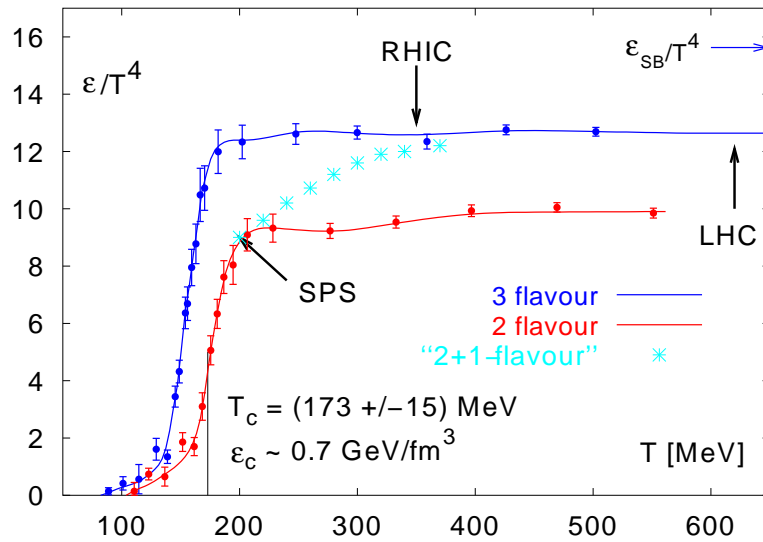


Figure 2.1: Energy density as a function of temperature calculated with lattice QCD (taken from ref.[4])

2.2 Experimental program and global observables

By colliding heavy ions at ultrarelativistic energies, one expects to create matter under conditions that are sufficient for deconfinement [5].

In 1985, the program has started with fixed target experiments at the CERN's Super Proton Synchrotron (SPS) which is just being concluded and at Brookhaven's

Alternating Gradient Synchrotron (AGS) which is essentially completed. The only operational heavy-ion collider is the Relativistic Heavy Ion Collider (RHIC) at Brookhaven National Laboratory (BNL) [6]. The Large Hadron Collider (LHC) will start operating at CERN in 2007 and will provide (in addition to proton beams) heavy ion beams, which will be used in the research program of the dedicated ALICE experiment.

The temporal evolution of a (central) nucleus-nucleus collision at ultrarelativistic energies is understood to proceed through the following stages: i) liberation of quarks and gluons due to the high energy deposited in the overlap region of the two nuclei; ii) equilibration of quarks and gluons; iii) crossing of the phase boundary and hadronization; iv) freeze-out.

Even if QGP is formed, as the system expands and cools down it will hadronize again, as it did at the beginning of the life of Universe: we end up with confined matter again. This is the experimental challenge: to observe in the final state the signatures of the phase transition, physical effects which are consequences of the phase transition or cannot be explained otherwise.

2.2.1 Collision Characteristics

In accordance with the spectator-participant model [7] of a heavy-ion collision, the participating nucleons from overlapping nuclear parts create a volume of high temperature and density, while the spectators move basically undisturbed through the collision. The impact parameter b determines the centrality of the collision. The impact parameter is not directly measurable in the collisions. To determine the collision geometry, measurements of quantities which are strongly correlated to the number of participants are used, such as the transverse and forward energy and the number of produced particles. The transverse energy, E_T , is defined as:

$$E_T = c^2 \sum_{i=1}^N (m_T)_i \quad (2.1)$$

where i runs over all N particles detected in an event and the transverse mass m_T is given by:

$$m_T = \sqrt{m^2 + (p_T/c)^2} \quad (2.2)$$

where p_T is the momentum component perpendicular to the beam direction defined as:

$$p_T = p \sin \theta \quad (2.3)$$

where θ is the polar angle of particle track. In practice, E_T is measured with a segmented calorimeter and calculated as the sum of the energy E_i at polar angle θ_i in each segment (i):

$$E_T = \sum_{i=1}^N E_i \sin \theta_i \quad (2.4)$$

The rapidity y is a very useful variable for description of the longitudinal motion of particles with non zero rest mass. If the particle has an energy E and momentum component along the beam axis p_z , we can define its rapidity as:

$$y = \frac{1}{2} \ln \frac{E + p_z}{E - p_z} \quad (2.5)$$

A frequently used approximation to the rapidity is the pseudorapidity η given by:

$$\eta = -\ln \left(\tan \frac{\theta}{2} \right) \quad (2.6)$$

for which it is enough to measure the polar angle θ of the particle track.

2.2.2 Quark-Gluon Plasma Signatures

Quarks and gluons coexisting in the short-lived QGP state cannot be measured directly and information from the early stages of the collision may get lost when the system hadronizes. Various kinds of measurements have to be combined to get reliable proof of the formation of a QGP. Specific probes of QGP (taken from ref.[3]) have been proposed [8, 9] and are currently being studied experimentally: i) direct photons [10]; ii) low-mass dileptons [11]; iii) strangeness [12, 13]; iv) charmonium suppression [14]; v) jet-quenching [15]; vi) fluctuations [16, 45]. Other global observables, like the distribution of particles over momentum space, collective flow, and the measurements of effective source sizes via particle interferometry, have also been studied in detail. A description of the ideas behind some of the most promising signatures that will be used in this work is given below.

- **Jet Quenching**

The propagation of partons through a hot and dense medium modifies their transverse momentum due to induced radiative energy loss, a phenomenon called jet quenching [17, 18]. This can be studied by measuring the p_T distribution of hadrons coming from high- p_T jets. When a hard collision, producing two jets, occurs near the surface of the nuclear overlap region, jet quenching might lead to complete absorption of one of the jets, while the other escapes. This signature can be found by studying azimuthal back-to-back correlations of jets. In general, high- p_T partons traveling through the dense medium is probably one of the best probes that can be used to study the medium.

- **Flow**

As the created particles are pushed away from the hot collision region, they acquire a flow velocity pointing outwards. Their momentum increases and the transverse momentum distribution is altered. Since the flow builds up throughout the evolution of the system, it contains information on both the partonic and the hadronic stages. Anisotropic flow [19] appears in a non-central nucleus-nucleus collision. It is most conveniently quantified by the Fourier coefficients in the expansion:

$$\frac{d^2N}{dp_T d\phi} = \frac{dN}{dp_T} (1 + 2v_1 \cos(\phi) + 2v_2 \cos(2\phi) + 2v_4 \cos(4\phi) + \dots) \quad (2.7)$$

displaying only the most contributing terms. Here, the ϕ angle is measured with respect to the reaction plane. The v_2 coefficient is often referred to as elliptic flow.

- **Event-by-Event Fluctuations**

Making use of high particle multiplicities in the heavy systems at SPS and higher energies, we can extract thermodynamic properties of the system by studying several observables on an event-by-event basis. Such measurements present a clear advantage over the averaging of many events. They enable categorization of individual events into groups according to

thermodynamic properties and could potentially lead to the isolation of events with special properties associated with quark-gluon plasma formation. Phase transitions are normally associated with large fluctuations. The QGP phase transition may yield anomalous fluctuations in e.g. particle multiplicities, ratios and transverse momenta. This signature will be discussed in detail in section 2.4.

2.3 Searching for the QCD critical point

Thermodynamical information is often presented in the form of a **phase diagram**, in which the different manifestations or phases of a substance occupy different regions of a plot whose axes are calibrated in terms of the external conditions or control parameters [20]. The system under consideration is a region occupied by strongly interacting matter, described by QCD, in thermal and chemical equilibrium, characterized by the given values of temperature T and baryo-chemical potential μ_b .

Our present understanding [23] of the phases of strongly interacting matter is sketched as a $T - \mu_b$ diagram in Fig. 2.2. The exotic region of low temperatures and high densities (high μ_b) is of relevance to astrophysical phenomena (neutron star physics). The region of high temperatures is the part which is being explored in ultrarelativistic nucleus-nucleus collisions. Theorists expect that this region has an interesting feature: the end point of the first order phase transition line. The critical point is marked as triangle in Fig. 2.2. The arguments leading to such picture can be summarized as follows: 1) First-principle lattice simulations indicate that no phase transition (in a strict thermodynamic sense) occurs as a function of temperature at zero baryo-chemical potential. 2) Non-lattice models indicate that transition from nuclear fluid to quark-matter (with approximate chiral symmetry restored) occurs via a strong first order transition. 3) The last step of the argument is a logical consequence of the previous two. Since the first order line originating at zero T cannot end at the vertical axis $\mu_b = 0$, the line must end somewhere in the midst of the phase diagram [24].

The location of this endpoint is not yet known since the lattice predictions vary wildly. Nevertheless, the available theoretical estimates strongly indicate

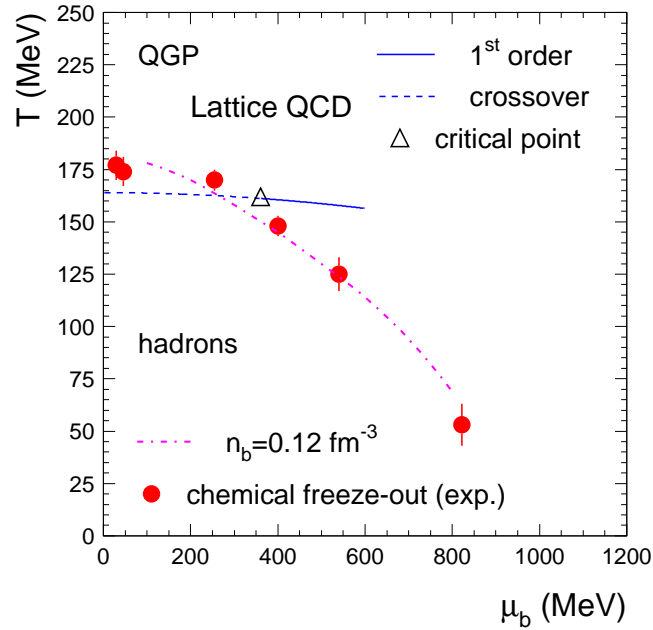


Figure 2.2: Phase diagram of nuclear matter in the temperature - baryon chemical potential plane. Experimental points for hadro-chemical freeze-out are shown together with a recent lattice QCD calculation [21] and a curve of constant total baryon density. Figure taken from ref. [22].

that the point is within the region of the phase diagram probed by the heavy-ion collision experiments. The strategy is to scan the QCD phase diagram by changing the beam energy \sqrt{s} . It is known empirically [22] that with increasing collision energy, \sqrt{s} , the resulting fireballs tend to freezeout at decreasing values of the chemical potential, since the amount of generated entropy (heat) grows with \sqrt{s} while the net baryon number is limited by that number in the initial nuclei. The freeze-out points for different heavy-ion collision experiments with a recent lattice calculation superimposed can also be seen in Fig. 2.2.

2.4 Transverse momentum fluctuations

In general, every physical system fluctuates and in many cases these fluctuations reveal important information about the properties of the system. The magnitude of fluctuations is given by the so-called susceptibilities, which control the response of the system to the application of small external forces. Fluctuations are also closely related to phase transitions. Considering the richness of the QCD phase-diagram the study of fluctuations [25] in heavy ions physics could lead to a rich set of phenomena. The most efficient way to address fluctuations of a system created in a heavy ion collision is via the study of event-by-event (E-by-E) fluctuations, where a given observable is measured on an event-by-event basis and the fluctuations are studied over the ensemble of the events. In most cases (namely when the fluctuations are Gaussian) this analysis is equivalent to the measurement of two particle correlations over the same region of acceptance.

The passage of a system through a second order transition or close to a critical point may lead to critical phenomena, long range correlations and large fluctuations. The study of event-by-event fluctuations therefore provides a novel probe to explore the QCD phase diagram, searching for the quark-gluon plasma (QGP) and the QCD critical point. Such measurements became possible with large acceptance experiments at SPS and RHIC, where the high multiplicity of charged particles produced in collisions of lead and gold nuclei allows a precise determination of global observables on an event-by-event basis.

Transverse momentum fluctuations (p_T fluctuations) should be sensitive to temperature/ energy fluctuations. These in turn provide a measure of the heat capacity of the system. Since the QCD phase transition is associated with a maximum of the specific heat, the temperature fluctuations should exhibit a minimum in the excitation function. It has also been argued that these fluctuations may provide a signal for the long range fluctuations associated with the critical point of the QCD phase diagram. In the vicinity of the critical point the transverse momentum fluctuations should increase, leading to a maximum of the fluctuations in the excitation function. It was predicted that mean p_T fluctuations can be enhanced if the system passes through the QCD critical point, where long wave length fluctuations of the sigma field develop, leading to fluctuations of pions

through the strong $\sigma - \pi - \pi$ coupling [26].

In the next two Chapters 3 and 4, the proposed measures of mean p_T fluctuations and the latest published results will be discussed.

Chapter 3

Measures of Mean p_T Fluctuations

When measuring event-by-event fluctuations in heavy ion collisions, one should consider the influence of trivial sources of fluctuations. Even for tight centrality cuts there are fluctuations in the impact parameter (event-by-event fluctuations of the collision geometry) which may mask the fluctuations of interest. In the thermal language, these impact parameter fluctuations correspond to volume fluctuations. The way out is to study so called intensive variables, i.e. variables which do not scale with the volume, such as temperature, energy density etc. Another issue is the presence of statistical fluctuations due to the finite number of particles observed. These need to be subtracted in order to access the dynamical fluctuations of the system. Finally, there are fluctuations induced by the measurement/detector, which also contribute to the signal. Those need to be understood and removed/subtracted as well. In this situation, a suitable choice of statistical tools for the study of event-by-event fluctuations is really important.

3.1 Φ_{p_T} and $\sigma_{p_T, dyn}^2$

There are numerous observables which can be used to quantify p_T fluctuations in high energy collisions. A natural one is the distribution of the average transverse

momentum of the events defined as:

$$M(p_T) = \frac{\sum_{i=1}^N p_{Ti}}{N}, \quad (3.1)$$

where N is the multiplicity of accepted particles in a given event and p_{Ti} is the transverse momentum of the i -th particle. The distribution of $M(p_T)$ is usually compared to the corresponding distribution obtained for mixed events in which the particles are independent from each other and follow the experimental inclusive spectra (mixed events are constructed such that the multiplicity distribution is the same as for the data). A difference between the two distributions signals the presence of dynamical fluctuations.

In the following, we briefly review quantities which have been proposed as measures for event-wise mean p_T fluctuations and summarize notations used in this study.

The notations of various means and variances are defined as follows. With a measure x of each particle, the mean of x over particles within the acceptance in an event is defined as:

$$[x] \equiv \frac{\sum_{i=1}^N x_i}{N}, \quad (3.2)$$

where i and N indicate the particle index and the multiplicity, respectively.

With a measure defined in each event, X , the mean over all the events is defined as:

$$\langle X \rangle \equiv \frac{\sum_{j=1}^n w_j X_j}{n}, \quad (3.3)$$

where j and n indicate the event index and the number of events, respectively. The weighting factor for each event, w_j is defined to be N_j for $X = [x]$ (see below), and 1 otherwise.

The event-by-event variance of X is defined as:

$$\langle \Delta X^2 \rangle \equiv \langle X^2 \rangle - \langle X \rangle^2. \quad (3.4)$$

The inclusive mean (the mean over all particles in all events) and variance of the measure x of each particle are defined as:

$$\bar{x} \equiv \frac{\sum_{j=1}^n \sum_{i=1}^{N_j} x_i}{\sum_{j=1}^n N_j}, \quad (3.5)$$

and

$$\overline{\Delta x^2} \equiv \overline{x^2} - \bar{x}^2, \quad (3.6)$$

where N_j represents N in event j . The mean and the variance of $[x]$ are defined by replacing X with $[x]$ in the above equations and including the event multiplicities as appropriate weighting factors:

$$\langle [x] \rangle \equiv \frac{\sum_{j=1}^n N_j \frac{\sum_{i=1}^{N_j} x_i}{N_j}}{n \langle N \rangle} = \bar{x} \quad (3.7)$$

and

$$\langle \Delta [x]^2 \rangle \equiv \frac{\sum_{j=1}^n N_j \frac{([x] - \langle [x] \rangle)^2}{N_j^2}}{n \langle N \rangle}. \quad (3.8)$$

This weighting procedure provides the most precise estimate of the variance of the parent distribution in case of finite mean multiplicity [35].

In the present event-by-event analysis, we search for dynamical mean p_T fluctuations beyond those expected in a purely statistical scenario. Dynamical mean $[p_T]$ fluctuations would therefore result in an event-by-event distribution of $M(p_T)$ which is wider than that expected from the inclusive p_T distribution and the finite event multiplicity. Measures for the mean p_T fluctuations are constructed as a difference or a quadratic difference between the standard deviation of the $[p_T]$ distribution and the inclusive p_T distribution normalized with the square-root of mean multiplicity.

In previous analyses, the measure Φ_{p_T} has been used to quantify non-statistical mean p_T fluctuations, defined as [36]:

$$\Phi_{p_T} \equiv \sqrt{\frac{\langle Z^2 \rangle}{\langle N \rangle}} - \sqrt{z^2}, \quad (3.9)$$

where z and Z are defined as $z \equiv p_T - \bar{p}_T$ for each particle, and $Z \equiv \sum_{i=1}^M z_i$ for each event, respectively. There is an approximate expression for Φ_{p_T} in terms of the variances of the event-wise $M(p_T)$ and the r.m.s. of the inclusive $[p_T]$ distributions [37]:

$$\Phi_{p_T} \cong \sqrt{\langle N \rangle} \sqrt{\langle \Delta [p_T]^2 \rangle} - \sqrt{\Delta p_T^2}. \quad (3.10)$$

A different measure for dynamical mean p_T fluctuation has been proposed in [37]:

$$\sigma_{p_T, dyn}^2 \equiv \langle \Delta[p_T]^2 \rangle - \frac{\overline{\Delta p_T^2}}{\langle N \rangle}. \quad (3.11)$$

This expression provides a direct relation between the variance of the inclusive $[p_T]$ distribution, the mean multiplicity and the variance of the event-by-event mean $[p_T]$ distribution. In case of vanishing non-statistical fluctuations and correlations, $\sigma_{p_T, dyn}^2$ is equal to zero.

There is an important relation between the above two measures [37]:

$$\sigma_{p_T, dyn}^2 \cong \frac{2\Phi_{p_T} \overline{\Delta p_T^2}}{\langle N \rangle}. \quad (3.12)$$

It has also been shown that $\sigma_{p_T, dyn}^2$ is the mean of covariances of all the possible pairs between two different particles [37]:

$$\sigma_{p_T, dyn}^2 \cong \frac{1}{n_{events}} \sum_{k=1}^{n_{events}} \left[\frac{1}{N_k(N_k - 1)} \sum_{i \neq j}^{N_k} (p_{Ti} - \overline{p_T})(p_{Tj} - \overline{p_T}) \right]. \quad (3.13)$$

3.2 The average momentum correlator $\langle \overline{\Delta p_{t,1}} \overline{\Delta p_{t,2}} \rangle$

The second part of the equation 3.13, provides the main measure that is used in the present study. The **average momentum correlator** $\langle \overline{\Delta p_{t,1}} \overline{\Delta p_{t,2}} \rangle$ is defined as:

$$\langle \overline{\Delta p_{t,1}} \overline{\Delta p_{t,2}} \rangle \equiv \frac{1}{n_{events}} \sum_{k=1}^{n_{events}} \left[\frac{1}{\frac{1}{2}N_k(N_k - 1)} \sum_{i \neq j}^{N_k} (p_{Ti} - \overline{p_T})(p_{Tj} - \overline{p_T}) \right] \cong \sigma_{p_T, dyn}^2 \quad (3.14)$$

where $\overline{p_T}$ is the inclusive mean p_T , n_{events} is the number of analyzed events, N_k is the number of particles from the event ‘k’, p_{Ti} and p_{Tj} are the transverse momentums of the i^{th} and j^{th} particle in an event, respectively.

The average momentum correlator is a covariance [38] and an integral of 2-body correlations [67]. Due to the central limit theorem [39], in a pure statistical distribution it equals zero in the absence of dynamical fluctuations and is defined to be positive for correlation and negative for anticorrelation. We define the sign of the fluctuation as the sign of the measure. It is also considered to be independent of random detection inefficiencies. The main advantage of that measure

is that it allows to select pairs by charge sign, as well as to make differential studies as a function of the angular pair separation, $\Delta\phi$, and of the separation in pseudo-rapidity, $\Delta\eta$.

The transverse momentum covariance $\langle\langle\delta p_{t_i}\delta p_{t_j}\rangle\rangle_{i\neq j}$ [38] is defined as:

$$\langle\langle\delta p_{t_i}\delta p_{t_j}\rangle\rangle_{i\neq j} \equiv \frac{\sum_{k=1}^{n_{events}} \left[\sum_{i\neq j}^{N_k} (p_{Ti} - \overline{p_T})(p_{Tj} - \overline{p_T}) \right]}{\sum_{k=1}^{n_{events}} \frac{1}{2} N_k (N_k - 1)} \quad (3.15)$$

The two aforementioned measures are approximately equal:

$$\langle\overline{\Delta p_{t,1}}\overline{\Delta p_{t,2}}\rangle \cong \langle\langle\delta p_{t_i}\delta p_{t_j}\rangle\rangle_{i\neq j} \quad (3.16)$$

In addition to the transverse momentum fluctuations given by the previous equation 3.14 for all charged particles, one can investigate the p_T fluctuations of the negative and positive charges independently, as well as the cross correlation between them. For like-sign particles, the average momentum correlation is:

$$\langle\overline{\Delta p_{t,1}^\pm}\overline{\Delta p_{t,2}^\pm}\rangle \equiv \frac{1}{n_{events}} \sum_{k=1}^{n_{events}} \left[\frac{1}{\frac{1}{2} N_k^\pm (N_k^\pm - 1)} \sum_{i\neq j}^{N_k^\pm} (p_{Ti}^\pm - \overline{p_T^\pm})(p_{Tj}^\pm - \overline{p_T^\pm}) \right] \quad (3.17)$$

For the unlike-sign pairs we get:

$$\langle\overline{\Delta p_{t,1}^+}\overline{\Delta p_{t,2}^-}\rangle \equiv \frac{1}{n_{events}} \sum_{k=1}^{n_{events}} \left[\frac{1}{N_k^+ N_k^-} \sum_{i,j}^{N_k^+, N_k^-} (p_{Ti}^+ - \overline{p_T^+})(p_{Tj}^- - \overline{p_T^-}) \right] \quad (3.18)$$

3.3 The normalized dynamical fluctuation Σ_{p_T}

In order to account for a possible change of mean p_T at different beam energies, we define a dimensionless measure, the "normalized dynamical fluctuation" Σ_{p_T} [40], as:

$$\Sigma_{p_T} = \sigma_{p_T, dyn} / \overline{p_T} \equiv \text{sgn}(\sigma_{p_T, dyn}^2) \frac{\sqrt{|\sigma_{p_T, dyn}^2|}}{\overline{p_T}}. \quad (3.19)$$

where $\text{sgn}(x) = 1$ if $x > 0$, $\text{sgn}(x) = -1$ if $x < 0$, and $\text{sgn}(x) = 0$ if $x = 0$.

The measure Σ_{p_T} expresses the magnitude of non-statistical fluctuations in percent of the inclusive mean transverse momentum $\overline{p_T}$.

The best way for a quantitative determination of mean p_T fluctuations is the use of a dimensionless measure. In addition, a comparison between different experiments should be possible. In this context Φ_{p_T} is neither dimensionless nor independent of the event multiplicity. This makes a comparison between experiments and to theory difficult because multiplicity depends on the acceptance window of the experiment and on beam energy. Since different contributions to the fluctuation signal have different multiplicity dependences, the multiplicity dependence of Φ_{p_T} is *a priori* unknown.

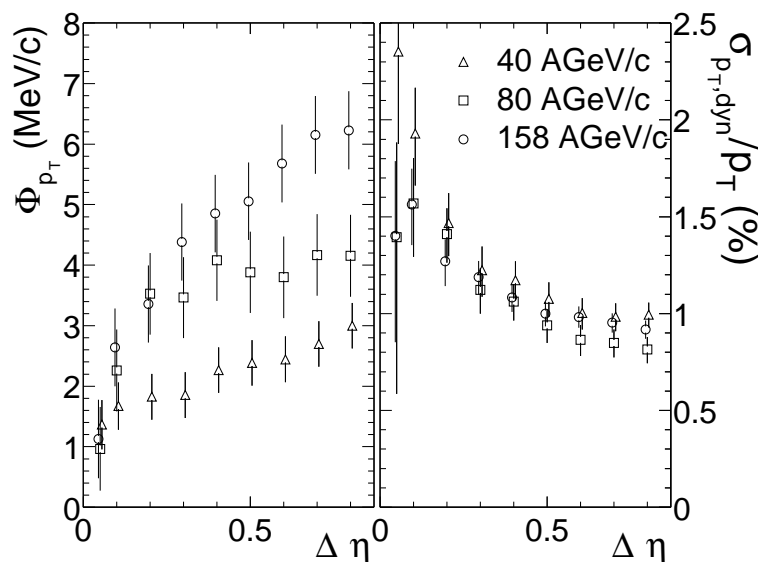


Figure 3.1: The Φ_{p_T} [MeV/c] (left panel), and $\sigma_{p_T,dyn}/\overline{p_T}$ [%] (right panel) at 40, 80, and 158 A·GeV/c in the 6.5 % most central events as a function of η bin size $\Delta\eta$ with the η center fixed to 2.45 [45].

Fig. 3.1 [45] shows Φ_{p_T} and $\sigma_{p_T,dyn}/\overline{p_T}$ as a function of η bin size $\Delta\eta$ at 40, 80, and 158 A·GeV/c. The Φ_{p_T} increases as a function of $\Delta\eta$, while $\sigma_{p_T,dyn}/\overline{p_T}$ decreases at small $\Delta\eta$ and tends to saturate at $\Delta\eta \geq 0.5$. The $\sigma_{p_T,dyn}/\overline{p_T}$ roughly agrees among the three beam energies at all $\Delta\eta$ bins, while Φ_{p_T} varies among the beam energies, which can be understood due to the scaling with mean multiplicity shown in Eq. 3.12. This clearly shows $\sigma_{p_T,dyn}/\overline{p_T}$ ($=\Sigma_{p_T}$) is a universal measure independent of multiplicity within the acceptance.

3.4 $\Delta\sigma_{\langle p_T \rangle}$ and F_{p_T}

Another measure is $\Delta\sigma_{\langle p_T \rangle}$ [39], defined as:

$$\Delta\sigma_{\langle p_T \rangle} \equiv \sqrt{\langle N \rangle} \sigma_{\langle p_T \rangle} - \sigma_{p_T}, \quad (3.20)$$

where $\sigma_{\langle p_T \rangle}$ is the r.m.s. of the event-by-event $\langle p_T \rangle$ distribution, σ_{p_T} is the r.m.s. of the inclusive(track-by-track) p_T distribution. There is an approximation

$$\Phi_{p_T} \cong \Delta\sigma_{\langle p_T \rangle} \quad (3.21)$$

The last measure, introduced by Stephanov *et. al.* [35], is defined as follows:

$$F \equiv \frac{\langle N \rangle \sigma_{\langle p_T \rangle}^2}{\sigma_{p_T}^2}. \quad (3.22)$$

F can be related to a 2-particle correlation function;

$$F = \frac{1}{\langle N \rangle} \sum_p^{N_{bin}} \sum_k^{N_{bin}} \langle \Delta n_p \Delta n_k \rangle \frac{(p_T - \bar{p}_T)(k_T - \bar{k}_T)}{\sigma_{p_T}^2}, \quad (3.23)$$

where p, k are indices for a bin (e.g. η bin).

$$F - 1 = \frac{1}{\langle N \rangle} \sum_{p \neq k} \langle \Delta n_p \Delta n_k \rangle' \frac{\Delta p_T \Delta k_T}{\sigma_{p_T}^2} \quad (3.24)$$

The relation between F and Φ_{p_T} is as follows:

$$\Phi_{p_T} = \sigma_{p_T} (\sqrt{F} - 1) \quad (3.25)$$

3.5 Discussion

A quantitative event-by-event study requires an appropriate formalism which facilitates a comparison of results among different experiments and to theory. Unfortunately, most of the experiments use different measures for fluctuations. These measures have very different sensitivities to particular experimental conditions, such as track quality cuts, tracking efficiency and acceptance. In this sense, measures which are most closely related to single- and two-particle densities appear preferable since they are the least sensitive to trivial efficiency effects

[41]. In this case, it is mandatory that experiments provide all the information necessary for an approximative conversion of one measure into another.

In this work, the measures $\sigma_{p_T, dyn}^2$, Σ_{p_T} , and $\langle \overline{\Delta p_{t,1}} \overline{\Delta p_{t,2}} \rangle$ are used to study mean p_T fluctuations.

When studying the centrality dependence, the following approximate relations can be used:

$$\langle N \rangle \sigma_{p_T, dyn}^2 \propto F_{p_T} \propto \Phi_{p_T}. \quad (3.26)$$

Implying that particle production at SPS is approximately proportional to the number of participating nucleons, the multiplicity $\langle N \rangle$ can be replaced by the mean number of participating nucleons $\langle N_{part} \rangle$ which can be calculated much easier and does not depend on the acceptance.

Chapter 4

Previous Results on Event-by-Event Mean p_T Fluctuations at SPS energies

4.1 Introduction

In this chapter, results obtained previously by the CERES collaboration from Pb-Au collisions at 40, 80, and 158 A·GeV/c [46] are presented.

Fig. 4.1 shows a comparison between event-by-event mean p_T distributions obtained from real and mixed Pb-Au events at 40, 80, and 158 A·GeV/c. Both distributions exhibit very similar Gamma distribution shapes [47]. However, the ratio of real to mixed events in the tails of the distributions shows enhancement at extreme- p_T regions. This is an evidence for the non-statistical fluctuations and wider distributions of real compared to statistical distributions. Their small difference demonstrates that dynamical fluctuations are small compared to statistical ones. Moreover, no distinct class of events with unusual fluctuations is observed.

The main objectives are to quantify magnitudes of the observed p_T fluctuations, and to observe how the fluctuation pattern changes with increasing number of nucleons participating in a collision, i.e. with system size, and what is the collision energy dependence.

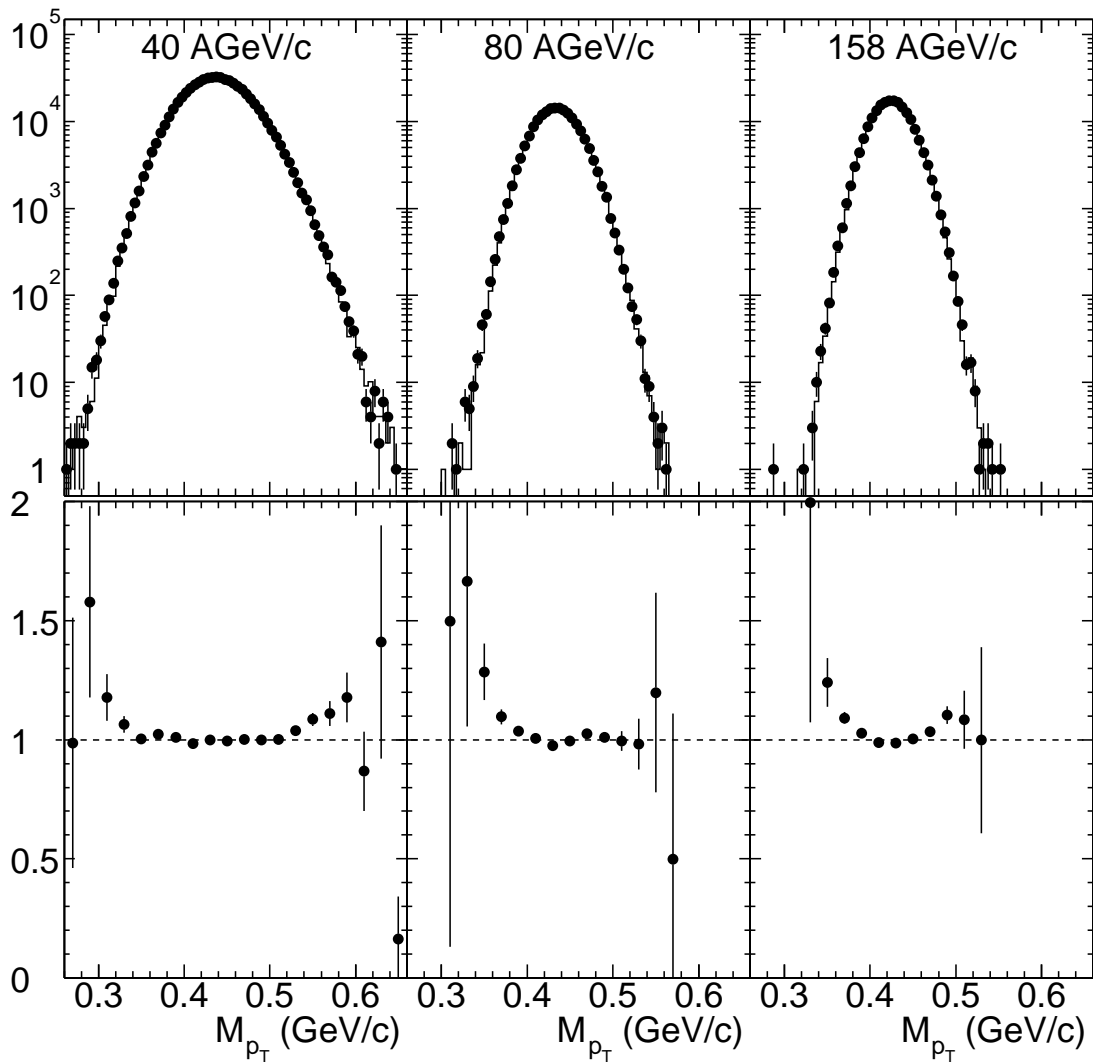


Figure 4.1: Top : event-by-event mean p_T distributions for 40 (left), 80 (middle), and 158 A·GeV/c (right) data. Circles show real data, and solid lines show mixed events. Bottom: ratio of distributions from real events to those from mixed events for 40 (left), 80 (middle), and 158 A·GeV/c (right) data.

4.2 Beam energy dependence

The robust measure Σ_{p_T} (see section 3.19) is used to investigate the collision energy dependence. As it was pointed out previously, the measure Σ_{p_T} is dimensionless and specifies the dynamical contribution to event-by-event $M(p_T)$ fluctuations in fractions of $\overline{p_T}$. In the case of independent particle emission from single parent distribution, Σ_{p_T} is zero.

The finite two-track separation of the TPC leads to a suppression of particle pairs with small momentum difference and consequently to a slight anti-correlation of particles in momentum space. In the case of CERES-TPC, the effect on Σ_{p_T} is negligible [45], hence no correction has been applied. Positive correlations may arise due to quantum statistics, flow, jets and other *physics* effects which have also not been corrected for.

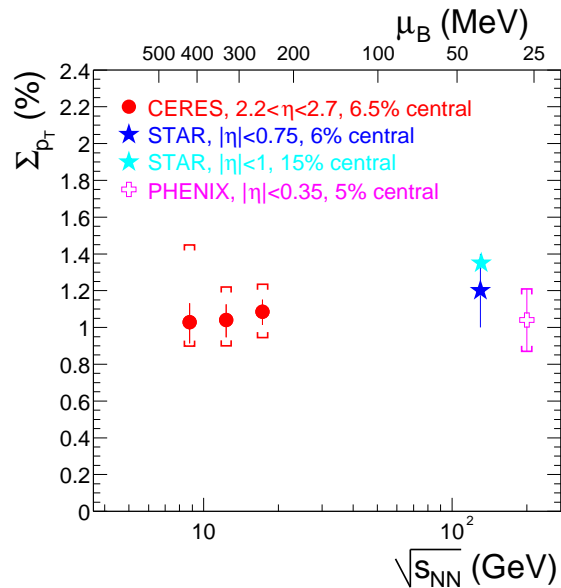


Figure 4.2: The normalized dynamical fluctuation, Σ_{p_T} [%], as a function of nucleon-nucleon center-of-mass energy $\sqrt{s_{NN}}$ [GeV].

A compilation of the normalized dynamical fluctuation, Σ_{p_T} , measured at mid-rapidity and at different beam energies is shown in Fig. 4.2. The upper scale indicates the baryon chemical potential μ_B at chemical freeze-out, related to $\sqrt{s_{NN}}$ via a phenomenological parametrization given in [48]. The Σ_{p_T} that are

measured by CERES at beam energy of 40, 80 and 158 A·GeV/c, in $2.2 < \eta < 2.9$ and $0.1 < p_T < 2$ GeV/c in 6.5 % central events are compared to RHIC data at $\sqrt{s_{NN}} = 130$ GeV [49, 50] and 200 GeV [51].

The observed fluctuations at SPS and at RHIC are similarly about 1 %. The evolution of Σ_{p_T} with beam energy looks smooth and does not show any indication of unusually large fluctuations at any beam energy.

Models predict enhanced mean p_T fluctuations if the system has passed close to the critical point of the QCD phase diagram. At SPS energies and for the finite rapidity acceptance window of the CERES experiment, the fluctuations should reach values of about 2 %, i.e. more than two times larger than observed in the present data [35, 52]. However, no indication for a non-monotonic behaviour as function of the beam energy has been observed. This suggests that the critical point may not be located in the μ_B regime below 450 MeV.

4.3 Centrality dependence

As a reference for the centrality dependence of Σ_{p_T} , the measurements in hadron-hadron collisions are employed. In p - p interactions, particles are produced in a correlated way which leads to large non-statistical fluctuations. At the ISR, dynamical mean p_T fluctuations have been measured in p - p reactions at $\sqrt{s_{NN}} = 30.8$ -63.0 GeV [53]. Independent of beam energy, a value of 12 % of $\overline{p_T}$ was observed for Σ_{p_T} . In α - α reactions, the observed dynamical fluctuation is reduced to about 9 % of $\overline{p_T}$. If particle production in α - α collisions acts like an independent superposition of p - p collisions, the fluctuations may scale with the multiplicity of produced particles:

$$\Sigma_{p_T}^{AA} = \Sigma_{p_T}^{pp} \left(\frac{\langle N_{pp} \rangle}{\langle N_{AA} \rangle} \right)^{1/2}. \quad (4.1)$$

Since the number of charged particles was found to scale close to linear with the number of participants $\langle N_{part} \rangle$ at SPS [54, 55, 56], the ratio of multiplicities in Eq. 4.1 can be replaced:

$$\Sigma_{p_T}^{AA} = \Sigma_{p_T}^{pp} (\langle N_{part} \rangle)^{-1/2}. \quad (4.2)$$

As demonstrated in Fig. 4.3 [57], the data agree with this extrapolation for very peripheral and central events. In contrast, a pronounced deviation is observed

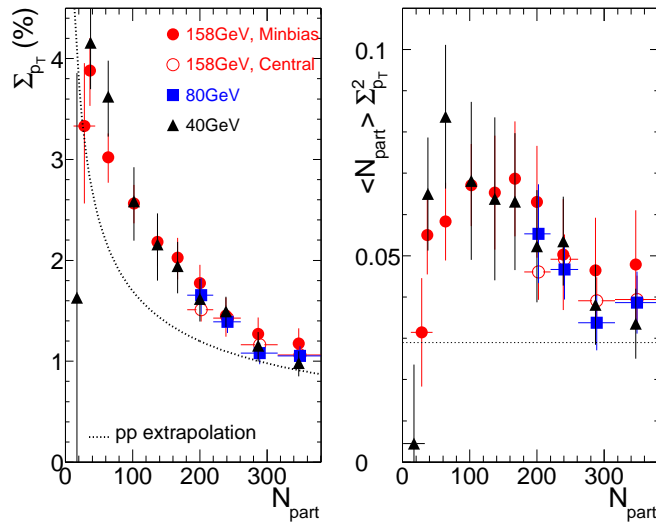


Figure 4.3: Centrality dependence of Σ_{p_T} at 40, 80 and 158 A·GeV/c [57]

in semi-peripheral events. In the right panel of Fig. 4.3, the product $\langle N_{part} \rangle \Sigma_{p_T}^2$ is plotted as function of $\langle N_{part} \rangle$. In this representation, the $p-p$ extrapolation becomes a constant ($=0.03$), while the data exhibit a broad maximum around $N_{part} = 120$. This observation is in qualitative agreement with previous findings at SPS and RHIC. Other experiments like NA49, PHENIX and STAR [50, 51, 58, 59] also observe $M(p_T)$ fluctuations which are significantly increased over the $p-p$ extrapolation in semi-central events. PHENIX attributed the non-monotonic centrality dependence of the measure F_{p_T} [51] to jet production in peripheral events, combined with jet suppression in more central events, causing a decrease of fluctuations. Other interpretations were given in terms of thermalization effects [60, 61], or in the framework of a string percolation model [62, 63].

4.4 Conclusions

The existence of non-statistical event-by-event fluctuations of the mean transverse momentum $M(p_T)$ at SPS and RHIC is by now well established. However, these dynamical fluctuations are small in central collisions, typically about 1 % of the

inclusive mean transverse momentum $\overline{p_T}$ and only weakly depend on $\sqrt{s_{NN}}$. In particular, no indication for a non-monotonic beam energy dependence has been found so far. The p_T fluctuations also violate the trivial $1/N$ scaling expected for nuclear collisions consisting of independent nucleon-nucleon interactions.

Despite the absence of a ‘smoking gun’ signature for the phase transition or the critical point, the systematic study of $M(p_T)$ fluctuations gives valuable insight into the particle production mechanism and the dynamic evolution of the system which cannot be extracted from inclusive distributions.

Although the mean p_T fluctuations are not as large as anticipated, there remains the possibility that the observed fluctuations are reduced from their expected value due to some final thermal effects, or because only a small fraction of the system actually produces a QGP. A ‘differential’, scale-dependent analysis of $M(p_T)$ fluctuations is an essential tool that could shed light on their origin, providing more information.

Chapter 5

The CERES Experiment and the Data Analysis

5.1 The CERES Experiment

The CERES/NA45 experiment is optimized for di-electron measurements in proton and ion induced collisions at CERN-SPS [27, 28]. The spectrometer covers a broad range of p_T close to midrapidity. Until 1996 the experiment consisted of two Ring Imaging Cherenkov detectors (RICH's) for electron identification, two silicon radial drift detectors (SDD's), and a pad chamber. A superconducting magnet (solenoid) between the RICHes provided a deflection field for the determination of the particle's charge and momentum. The silicon detectors together with the pad chamber were used as tracking devices. With this setup CERES measured a significant enhancement of low-mass e^+e^- pairs in heavy ion collisions compared to contributions from hadronic decays, extrapolated from nucleon-nucleon collisions. In 1998 the spectrometer was upgraded by a tracking detector downstream of the existing setup, a cylindrical Time Projection Chamber (TPC) with radial drift field, which replaced the pad chamber in order to improve the di-electron invariant mass resolution [29]. The addition allowed CERES to serve as a hadron spectrometer.

All subdetectors have a common acceptance in the polar angle range of $8^\circ < \theta < 15^\circ$ at full azimuth, corresponding to a pseudorapidity acceptance of $2.1 < \eta < 2.65$. Fig. 5.1 shows a sketch of the setup.

In this analysis, only the two SDD's and the TPC were used for charged particle track reconstruction. The SDD's are located about 12 cm downstream of the target system. Each SDD has uniform drift field in the radial direction, with 360 anodes at the out-most radial position arranged azimuthally in 1° pitch. The TPC is located at 3.8 m downstream of the target system. In the TPC, the ionization electrons drift outward in the radial direction, with a drift field changing as $\sim 1/r$. Electron signals are detected in the Multi-Wire Proportional Chambers (MWPC's) at the outer radial position [29]. The magnetic field formed by two opposite-polarity solenoidal coils, which are placed around the TPC, deflects charged particle trajectories in the ϕ direction. The position resolutions are about $40 \mu\text{m}$ both in r and $r\phi$ directions in the cylindrical coordinate system. The momentum resolution of the spectrometer reached after the final calibration is

$$\frac{\Delta p}{p} = 2\% \oplus 1\% \cdot p/\text{GeV} \quad (5.1)$$

both from residuals of hits with respect to fitted tracks, and from invariant mass of Λ and K_s^0 . Such resolution results in $\frac{\Delta m}{m} = 0.038$ for the ϕ meson in the e^+e^- channel. Particle identification is possible to a certain degree using the energy loss in the TPC gas with $\frac{\Delta(dE/dx)}{(dE/dx)} = 0.10$ [30]. The following sections of this chapter describe the main features of all detectors.

5.1.1 Target Area, Trigger and the Two Silicon Drift Detectors

The target system used during the beam-time 2000 (158 A·GeV/c Pb-beam period) consists of thirteen $25\text{-}\mu\text{m}$ thick Au discs, separated by 2 mm in beam direction, with a total thickness of 1.33% of a hadronic interaction length. The distance between the discs was chosen such that particles coming from a collision in a given target disc and falling into the spectrometer acceptance do not hit any other of the discs. This helps to minimize the conversion of γ 's into e^+e^- -pairs which is essential for the analysis of electron pairs.

To start the read-out sequence of the detectors the occurrence of a collision has to be detected. This is done with a system of beam/trigger detectors, shown in Fig. 5.2 in a simplified view. The beam counters BC1 to BC3 are used to

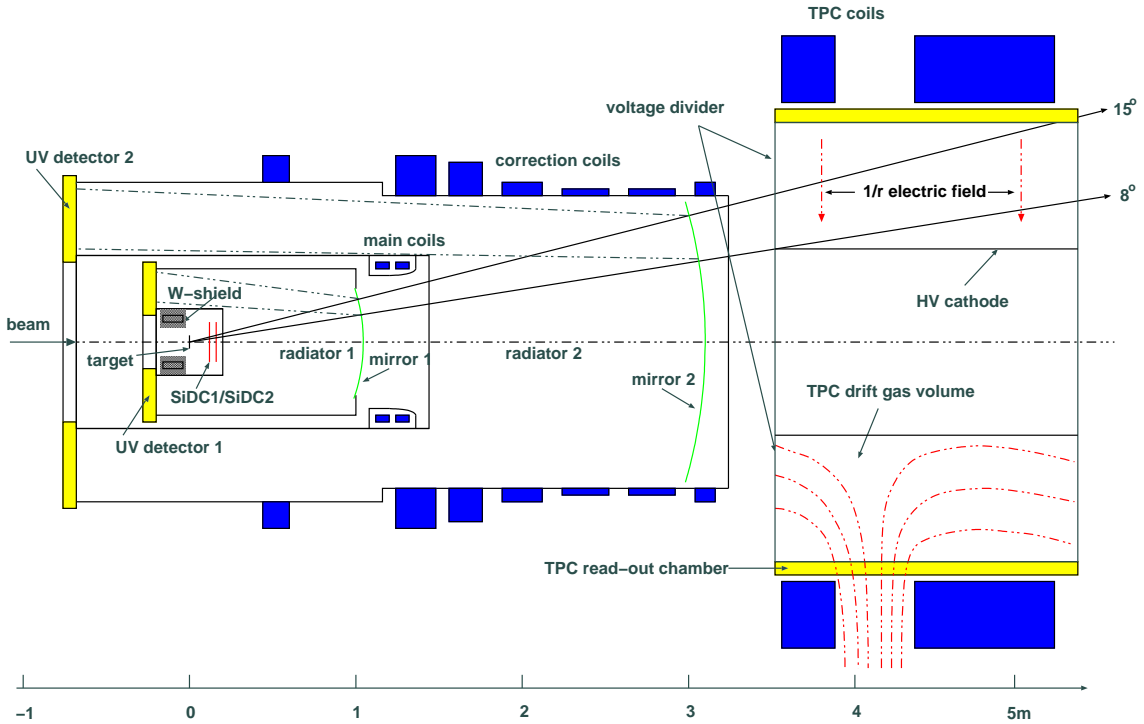


Figure 5.1: Schematic view CERES spectrometer.

detect collisions between projectile and target nuclei. These detectors are gas Cherenkov-counters with air as radiator, located on the beam-line. The beam trigger (BEAM) is defined by the coincidence of two beam counters (BC1 and BC2) located in front of the target, and the minimum bias trigger (MINB) is defined as BEAM and no signal in the beam counter (BC3) located after the target ($T_{MINB} = BC1 \times BC2 \times \overline{BC3}$). The charged particle multiplicity is often used as a measure for the centrality of the collision. The MC or the MD detector can be used to select events with a certain multiplicity. These detectors are scintillation detectors and their output signal is approximately proportional to the number of ionizing particles passing through them. The central collision trigger is defined as $CENT = MINB \times MC$.

The veto detectors VW and VC are both plastic scintillators. They can be used to discard interactions which happened before the target.

The silicon drift detectors (SDD's) are placed approximately 10 cm behind the target. Both detectors are realized on 4 inch silicon wafers with a thickness of

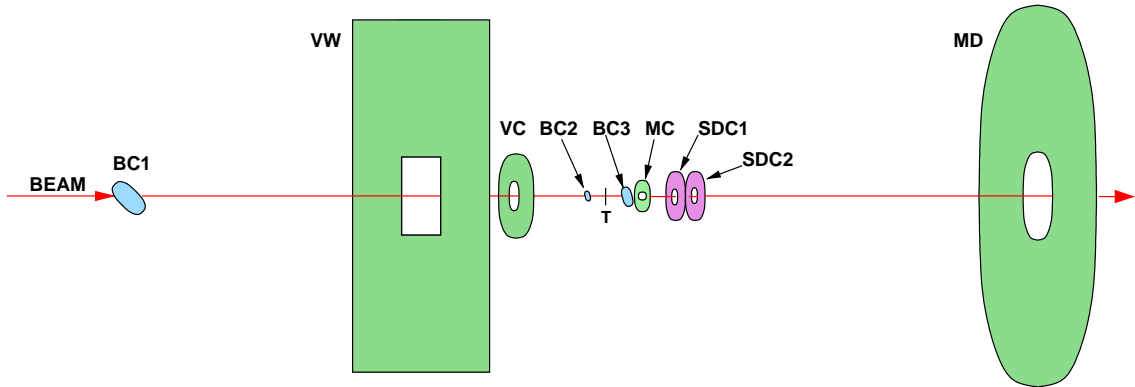


Figure 5.2: Schematic view of the target region with the trigger detectors.

280 μm . The sensitive area covers the region between the radii 4.5 mm and 42 mm with full azimuthal acceptance. They form a vertex telescope, which is a central part of the event and track reconstruction. These detectors provide a very precise reconstruction of an interaction vertex, a measurement of energy loss and coordinates of hundreds of charged particles with high spatial resolution and interaction rate, a track segment reconstruction before the magnetic field. The principle of operation, as well as details about the silicon drift detectors used in CERES and their performance, can be found in [32].

5.1.2 The RICH Detectors

Two Ring Imaging Cherenkov counters (RICH) are used to measure the velocity of the particle and their trajectory. If the momentum of the particle is known the mass can be determined. These detectors are invented by Seguinot and Ypsilantis [31] and rely on the position sensitive measurement of the emitted Cherenkov light. Inside a radiator Cherenkov-light is emitted under a constant angle θ_C with respect to the trajectory of the charged particle.

A ring imaging Cherenkov detector is schematically shown in Fig. 5.3. A spherical mirror reflects the emitted Cherenkov photons into ring images at the focal plane of the mirror. The diameter of these rings then corresponds to a certain Cherenkov angle and thus to the velocity of the particle. Both, the ring radius and the number of Cherenkov photons, depend on particle momentum and mass. Knowing the particle momentum, such detector can be used for particle identi-

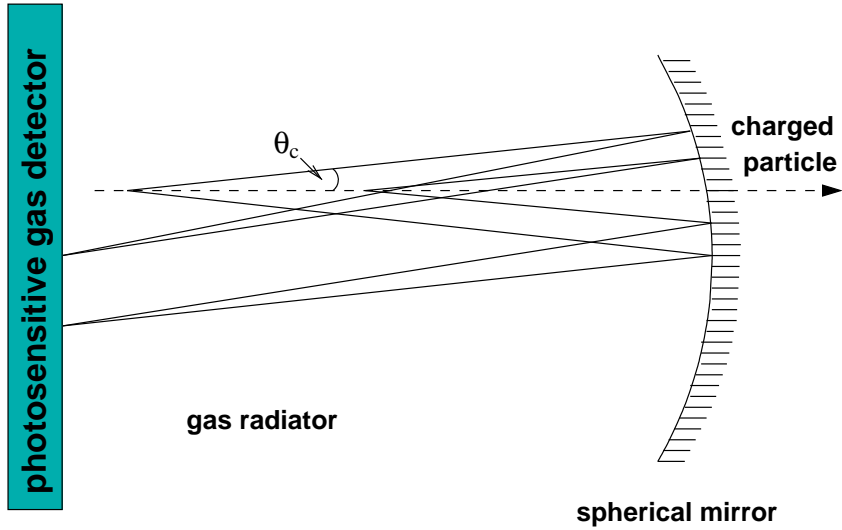


Figure 5.3: Schematic view of a RICH detector with a spherical mirror. The particle enters from the left, the emitted Cherenkov photons are reflected backward into a photon detector.

fication, or the other way around, knowing the particle mass, we can measure its momentum. The RICH detectors in the CERES spectrometer operate with CH_4 at atmospheric pressure as radiator gas. The threshold for light emission is thereby fixed to $\gamma_{th} = 32$. Practically all electrons produce light at the asymptotic angle whereas most hadrons, except pions with a momentum of more than 4.5 GeV, produce no signal at all. The detector is therefore practically hadron blind, which is very important for the dilepton measurement and also offers an excellent tool to study high- p_T pions. The UV detectors used for the position sensitive measurement of the photons are gas counters with a gas composition of 94% helium and 6% methane. They are located at the focal plane of the mirrors.

5.1.3 The Time Projection Chamber

In 1998, the spectrometer was upgraded by an additional tracking detector, a **Time Projection Chamber (TPC)** with radial drift field, which replaced the pad chamber. The aim of the upgrade was to achieve the mass resolution of $\frac{\Delta m}{m} = 2\%$ at $m \sim 1$ GeV which would allow a precise spectroscopy of ρ/ω and ϕ vector mesons. The CERES TPC (shown in a perspective view in Fig. 5.4) is a cylin-

drical drift chamber filled with Ne/CO₂ gas mixture in ratio 80/20. This composition was chosen after optimization on diffusion, multiple scattering, Lorentz angle, primary ionization and drift velocity. The sensitive volume is about 9 m³ and the length 2 m. It has 16 readout chambers with segmented pad-readout placed in a polygonal structure. Along the beam axis, the TPC is divided into 20 planes, each with $16 \times 48 = 768$ readout channels on the circumference. In total, 15360 individual channels with 256 time samples each can be read out, allowing a three-dimensional reconstruction of particle tracks. The electric field is approximately radial and is defined by the inner electrode, which is an aluminum cylinder at a potential of -30 kV, and the cathode wires of the readout chambers at ground potential. The avalanche produced close to the anode wires induces a signal in the chevron-type cathode pads [29].

The magnetic field in the sensitive detection volume is generated by two warm coils with current flowing in opposite directions. The radial component of this field is maximal between the two coils and the deflection of charged particles is mainly in azimuthal direction.

Principle of Operation

The Time Projection Chamber [33] is an essentially three-dimensional tracking detector capable of providing information on many points of a particle track along with information on the specific energy loss, dE/dx , of the particle.

A charged particle produces electron ion pairs along its path through the detector. The electrons drift in the electric field towards a plane of proportional wires close to the pad plane. At distances of a few wire diameters the electron starts an avalanche process which creates free charges. Because the electrons are created very close to the wire they are captured by it and neutralized in a very short time. The movement of the much slower ions is responsible for the creation of the induced signal which is detected by the readout electronics. Moving charges lead to an induced current on the pads. This current is detected and recorded with the help of charge sensitive amplifiers attached to each pad. The measurement of the time between the start of the drift (which is essentially the time of the collision between a projectile and a target nucleus) and the arrival of the charge cloud at the wires combined with the knowledge of the drift velocity

enables the reconstruction of the radial coordinate of the tracks. The other two spatial coordinates are determined by the location of the pad. Due to the chevron shape of the pads the charge cloud is shared between adjacent pads. This allows for a precise reconstruction of the charge centroid in the azimuthal direction. Since the collected charge is proportional to the energy loss of the particle, the signal amplitudes from the anode also provide information on the dE/dx of the particle. If the momentum of the particle is known from the curvature of its trajectory in the magnetic field, for example, then this information can be used to identify the particle.

Details about the TPC used in CERES as well as the readout system with the

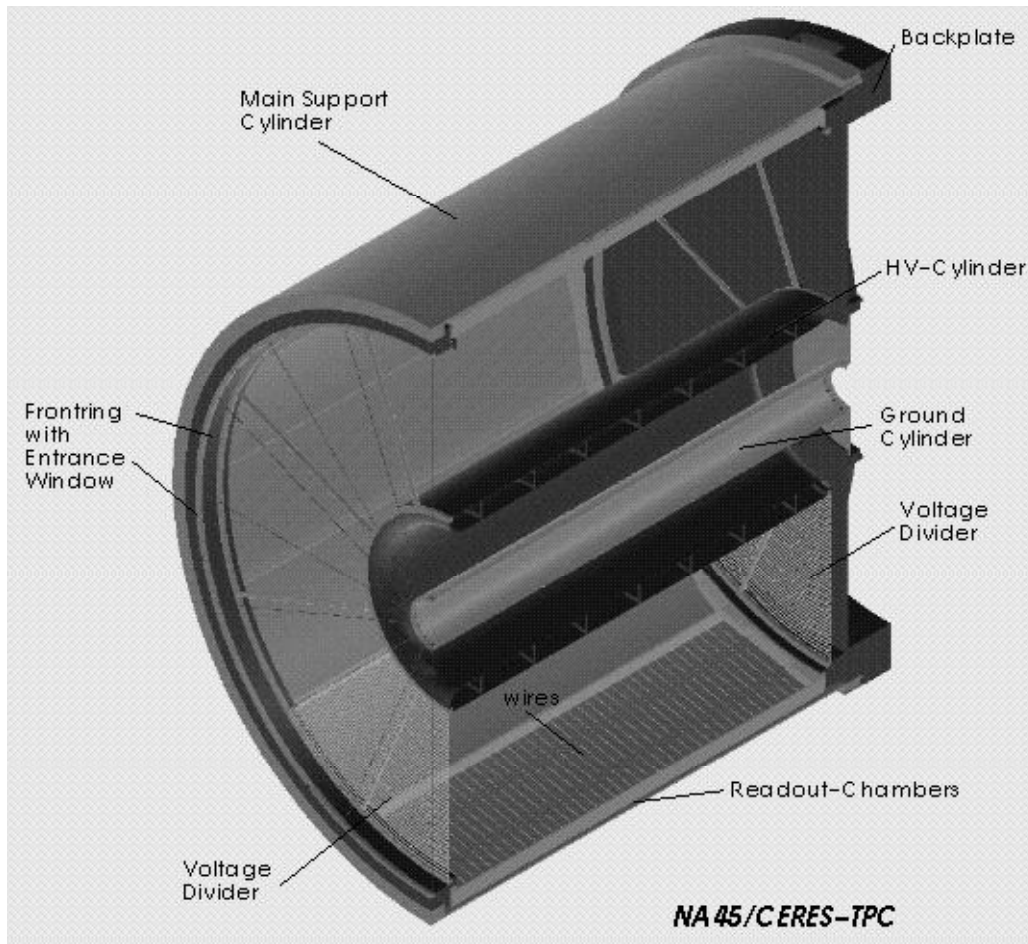


Figure 5.4: Perspective view of the TPC.

front-end, control and back-end electronics, can be found in [34].

5.2 Data Analysis

In the framework of this thesis, data samples of Pb-Au collisions taken at beam energy of 158 AGeV/c at the CERN SPS have been analyzed. A typical Pb beam intensity was 1×10^6 particles per burst. About 30 million Pb+Au collisions at 158 AGeV/c having a centrality of the upper 8 % of the total geometric cross section, and 3 million of 20 % have been collected during the beam period of the year 2000. In this analysis, we use 2 SDD's and a TPC for charged particle track reconstruction. The data taking rate in 2000 was $300 \sim 500$ events/burst.

5.2.1 Event Selection

The following event selection cuts were applied to exclude two superimposed Pb-Au collisions (pile-up events) or a collision of Pb-beam with non-target nucleus, which could have very different multiplicity and p_T distributions compared to a single Pb+Au collision and could change magnitude of event-by-event fluctuations.

- Rejection of events with the number of TPC tracks less than 30 (defined below) to reject non-target interactions.
- Before- and after-protection cuts. In the trigger logic, a minimum time separation to another beam particle with respect to the triggered beam particle was required. It was set to $\pm 2 \mu s$ at 158 AGeV/c.
- Requirement of dE/dx of 2 beam counters (BC1, BC2) to be within $\pm 4\sigma$ from the peak values.

5.2.2 Centrality Determination

The collision centrality was determined via the charged particle multiplicity around midrapidity $y_{\text{beam}}/2=2.91$. Two variables, the amplitude of the Multiplicity Counter (MC) (single scintillator covering $2.3 < \eta < 3.4$) and the track

multiplicity in the TPC ($2.1 < \eta < 2.8$), were alternatively used as the centrality measure (Fig. 5.5). Knowing the DAQ dead time factor (which describes the loss of events due to a busy DAQ) and the target thickness, and assuming that all beam particles were hitting the target, the event counts can be translated to the cross section for collisions with a given multiplicity. The integrated cross section, divided by the geometrical cross section $\sigma_G = 6.94$ barn, is shown as the additional axis in Fig. 5.5.

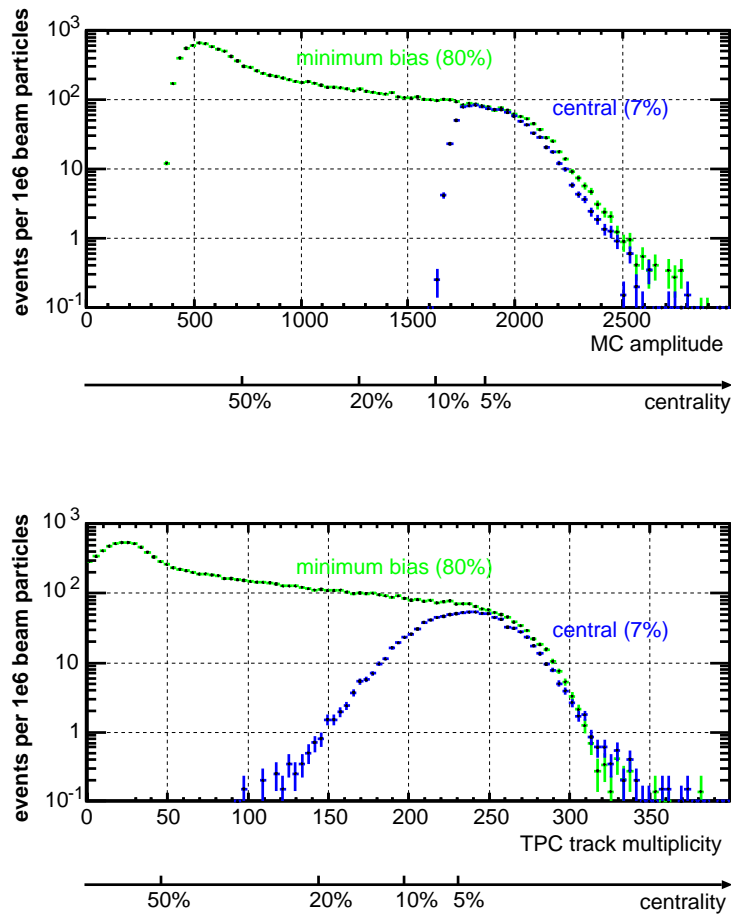


Figure 5.5: Distributions of the pulse height of the MC scintillator detector (top) and the TPC track multiplicity (bottom) used for centrality determination. The MC detector was used in the trigger. The distributions shown are before the run-by-run correction.

The centrality calibration of the CERES' 2000 data was done in two steps. First, a low beam-intensity minimum bias run is used to find the relation between the MC counter amplitude and the centrality. Second, the run-by-run variations

of the MC amplitude are corrected. Details can be found in [64].

In the present analysis we have applied an offline centrality selection of the upper 50 % of the total geometric cross section. The corresponding mean number of participating nucleons $\langle N_{part} \rangle$ and mean number of nucleon-nucleon collisions $\langle N_{coll} \rangle$ was derived from a geometric nuclear overlap model using $b = \sqrt{\sigma/\pi}$ and resulting, with $\sigma_{NN} = 30$ mb, in a total cross section of $\sigma_G = 6.94$ b [66]. Our classification of central events comprises the 8 % most central fraction of the total geometric cross section. For the centrality dependent studies we have subdivided our sample into five centrality classes (see Table 5.1).

σ/σ_{geo} [%]	0 – 8	10 – 20	20 – 30	30 – 40	40 – 50
$\langle N_{part} \rangle$	328	221	153	102	64
$\langle N_{coll} \rangle$	754	454	280	163	88

Table 5.1: Definition of centrality classes

5.2.3 Track Selection

A TPC track is reconstructed as an array of TPC hits on subsequent TPC z -planes, where the initial track-seed vector is required to point to the vertex. Depending on the polar angle, a TPC track consists of up to 20 hits. An initial track seed is reconstructed in middle planes, and it is extended to outer planes. In $\rho - z$ plane in the cylindrical coordinate system, hits are required to be on a straight line originating from the main vertex. In $\phi - z$ plane, a hit position on a plane is predicted from the projection of a local vector with previously found planes. Momentum is calculated as a fit parameter of hit positions of a track in the $r\phi - z$ plane to a track template which is generated with a Monte Carlo simulation. The vertex is reconstructed from all SDD1 hits and SDD2 hits, whose position resolution is about $6 \mu\text{m}$. A SDD-track is required to have a SDD1 hit and a SDD2 hit which are on a straight line passing through the vertex. Association of a TPC track with a SDD track is done using the projections of the 2

tracks on the spherical surface of the RICH2 mirror where the multiple scattering is most probable. This inclusion of SDD track information leads to a powerful rejection of non-vertex tracks, if only TPC tracks with a match to the SDD are used in the analysis. The matching window is set to 10 mrad in a calibrated function of both θ and ϕ , respectively.

In addition, a number of fiducial and quality cuts have been applied to provide stable tracking conditions and to reject tracks from secondary particles:

- The pseudo-rapidity cut of $2.2 < \eta < 2.7$, which corresponds to full-length TPC track acceptance, is applied in the mean p_T fluctuations analysis to keep high momentum resolutions.
- The transverse momentum cut is defined as $0.1 < p_T < 1.5$ GeV/c for p_T fluctuation analysis to keep high momentum resolutions. The minimum p_T cut is set to exclude soft tracks with low efficiency and large contamination from non-vertex tracks. The maximum p_T cut is necessary to suppress high momentum tracks which would dominate the calculation of the mean momentum and for which the momentum resolution is poor.
- The minimum number of fitted hits per track is 12 in the full-length TPC track acceptance.
- To suppress secondary particles it is required that the back-extrapolation of the particle trajectory into the target plane, given by r_0 , misses the interaction point by no more than 10 cm in transverse direction. More technical information about the tracking in the CERES TPC can be found in [65].

Fig. 5.6 shows the inclusive p_T distribution, the η distribution, as well as those of the number of fitted hits in the TPC and r_0 .

The results shown in the following chapter refer to *accepted* particles, i.e., particles that are accepted by the detector and pass all kinematic cuts and track selection criteria.

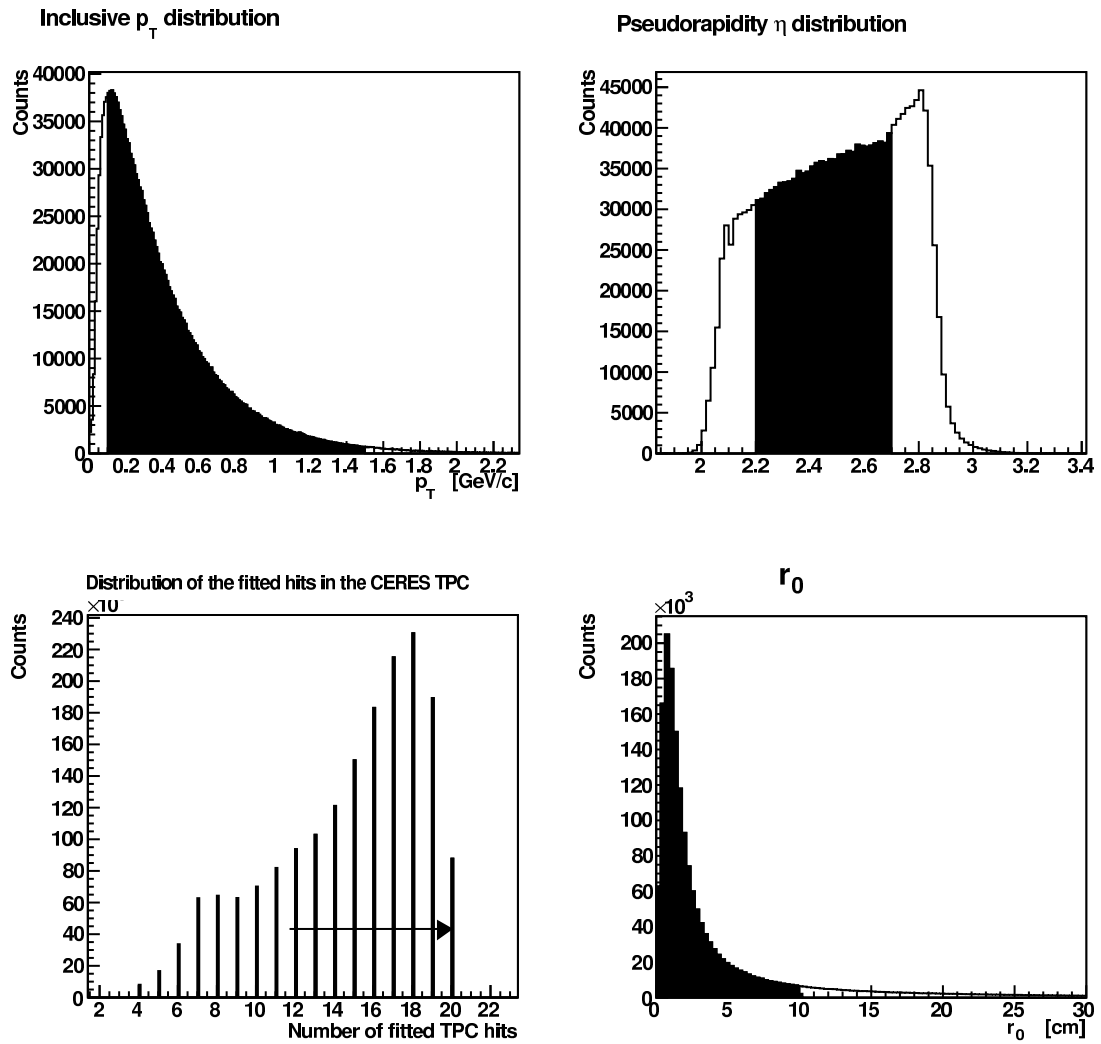


Figure 5.6: Distributions of p_T , η , number of fitted hits in the TPC and r_0 .

Chapter 6

Scale dependence of Mean Transverse Momentum Fluctuations in $\Delta\eta$ - $\Delta\phi$ space

Significant non-statistical event-by-event fluctuations and a characteristic centrality dependence have been observed over a wide range of beam energies. These results have been discussed in the context of QGP formation and the possibility to observe the QCD critical point.

It is important to note, that observation of a large magnitude of fluctuations would not by itself constitute the signal of the critical point. Since fluctuations were characterized so far by one single number, it was difficult to estimate the many possible contributions to them.

Taking into account the high available statistics offered by the CERES experiment combined with the full azimuthal acceptance, we perform a differential study of mean p_T fluctuations. Here, we present recent results of our analysis of data from the CERES collaboration on event-by-event fluctuations of the mean transverse momentum in Pb-Au collisions at 158 AGeV/c, obtained with a sample of about 10 million central events. For the first time at SPS energy, the charge-dependent mean p_T fluctuations have been analyzed as a function of the angular pair separation, $\Delta\phi$, and of the separation in pseudorapidity, $\Delta\eta$. Apart from (expected) HBT correlations the data show a significant dependence on $\Delta\eta$ and $\Delta\phi$ that will be studied to shed light on their origin.

6.1 Inclusive results

Ten million central events are analyzed after all the quality cuts that are described in the previous chapter.

The resulting average momentum correlator $\langle \overline{\Delta p_{t,1}} \overline{\Delta p_{t,2}} \rangle$, the normalized dynamical fluctuation Σ_{p_T} , the $\sigma_{p_T, dyn}^2$, the mean multiplicity $\langle N_{part} \rangle$, and the inclusive mean transverse momentum $\overline{p_T}$ for all pairs, as well as for different charge combinations are given in Table 6.1. The fluctuations are not corrected for two-track resolution and HBT/Coulomb correlations.

For the calculation of Σ_{p_T} , the $\sigma_{p_T, dyn}^2$ was used, via the equations 3.11 and 3.19. The average momentum correlator $\langle \overline{\Delta p_{t,1}} \overline{\Delta p_{t,2}} \rangle$ is calculated using the formula 3.14.

We find that the expected approximation $\langle \overline{\Delta p_{t,1}} \overline{\Delta p_{t,2}} \rangle \cong \sigma_{p_T, dyn}^2$ holds very well. In addition, the measured Σ_{p_T} is about 1 % and agrees with the previous measurements of finite non-statistical fluctuations of transverse momentum that are reported in chapter 4.2. Since $\langle \overline{\Delta p_{t,1}} \overline{\Delta p_{t,2}} \rangle$ and Σ_{p_T} are global observables, a small value of them does not necessarily imply the absence of any strong correlation. It is also possible that contributions of two effects just cancel out each other.

After these consistency checks which verify the measures we use to study mean p_T fluctuations, we perform a ‘differential’ scale-dependent analysis in order to re-evaluate our need for more sensitivity.

Beam energy [A·GeV/c]	158
All pairs	
$\langle \overline{\Delta p_{t,1}} \overline{\Delta p_{t,2}} \rangle [MeV^2]$	22.71 ± 0.32
Σ_{p_T} [%]	1.04 ± 0.01
$\sigma_{p_T, dyn}^2 [MeV^2]$	21.98 ± 0.44
n	10003672
$\langle N \rangle$	154.83 ± 0.01
$\overline{p_T}$ [MeV/c]	449.82 ± 0.01
Positive pairs	
$\langle \overline{\Delta p_{t,1}} \overline{\Delta p_{t,2}} \rangle [MeV^2]$	21.59 ± 0.63
$\sigma_{p_T, dyn}^2 [MeV^2]$	20.65 ± 0.61
n	9009425
$\langle N \rangle$	84.21 ± 0.01
$\overline{p_T}$ [MeV/c]	479.78 ± 0.01
Negative pairs	
$\langle \overline{\Delta p_{t,1}} \overline{\Delta p_{t,2}} \rangle [MeV^2]$	26.63 ± 0.61
$\sigma_{p_T, dyn}^2 [MeV^2]$	26.16 ± 0.54
n	9009425
$\langle N \rangle$	70.63 ± 0.01
$\overline{p_T}$ [MeV/c]	414.10 ± 0.01
Unlike-sign pairs	
$\langle \overline{\Delta p_{t,1}} \overline{\Delta p_{t,2}} \rangle [MeV^2]$	24.71 ± 0.43
n	9009425

Table 6.1: Summary of mean p_T fluctuations for all pairs and different charge combinations at $0.1 < p_T < 1.5$ GeV/c, $2.2 < \eta < 2.7$ and full ϕ acceptance at 158 A·GeV/c in the 8 % most central events. Errors are statistical only. The fluctuations are not corrected for two-track resolution and HBT/Coulomb correlations.

6.2 Differential analysis

A central goal in Event-by-Event analysis has been to develop global comparison measures sensitive to excess variance which might signal residual correlations due to incomplete equilibration – possibly structure remaining from a phase transition. The present treatment makes it clear that global-variables analysis based on average values (integrals) is rather limited in its sensitivity, interpretability and power to discriminate among various correlation sources. Thus, there is a need to resolve these global measures in a way that could provide us more information related to the ‘origin’ of the observed fluctuations.

It was pointed out in the previous chapter, that the pseudo-rapidity of accepted particles is restricted to the interval $2.2 < \eta < 2.7$ and there is a full azimuthal acceptance.

Particle pairs (i, j) can be separated on axial *difference variables* as follows:

$$0 \leq \Delta\phi = |\phi_i - \phi_j| \leq 180^\circ \quad (6.1)$$

and:

$$0 \leq \Delta\eta = |\eta_i - \eta_j| \leq 0.5 \quad (6.2)$$

Where i and j are the particle indices.

The bin size in $\Delta\phi$ should be approximately equal to that in $\Delta\eta$, in terms of solid angle. In our case, this means:

Our θ acceptance is about 120 mrad, corresponding to $\Delta\eta$ about 0.5. Making a bin size of $\Delta\eta=0.1$, this corresponds to about 24 mrad. At this θ , the Jacobian is about 5 ($\sim 1/\sin\theta$), leading to a $\Delta\phi$ of 120 mrad, or 7 degrees.

Therefore, we divide the $\Delta\eta$ - $\Delta\phi$ space into 120 bins in total. 5 bins in $\Delta\eta$ and 24 in $\Delta\phi$ corresponding to an angle of 7.5 degrees.

6.2.1 Mixed event analysis

As a baseline of the statistical distribution, and also for a consistency check of our analysis procedure for statistical distributions, we construct mixed events. To ensure that there is no correlation between any pair of particles, we pick up every track randomly from a different real event, using exactly the same

multiplicity distributions as the real data. The $\langle \overline{\Delta p_{t,1}} \overline{\Delta p_{t,2}} \rangle$ value calculated for the sample of mixed events was consistent with zero. The obtained average value is $\langle \overline{\Delta p_{t,1}} \overline{\Delta p_{t,2}} \rangle_{mixed} = -0.049 \pm 0.314 \text{ MeV}^2$.

In the second step, for each bin in $\Delta\eta$ - $\Delta\phi$ space, we calculate the $\langle \overline{\Delta p_{t,1}} \overline{\Delta p_{t,2}} \rangle$ value.

In order to visualize the full correlation structure for all charged pairs in the four-dimensional momentum subspace $(\eta_i, \eta_j, \phi_i, \phi_j)$ we construct the $\langle \overline{\Delta p_{t,1}} \overline{\Delta p_{t,2}} \rangle$ map as it can be seen in Fig.6.1.

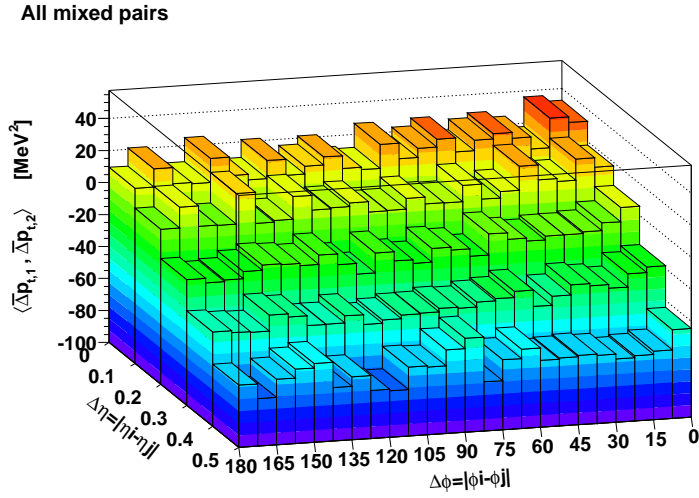


Figure 6.1: The $\langle \overline{\Delta p_{t,1}} \overline{\Delta p_{t,2}} \rangle$ map in $\Delta\eta$ - $\Delta\phi$ space for all mixed pairs.

We observe a declination of the $\langle \overline{\Delta p_{t,1}} \overline{\Delta p_{t,2}} \rangle$ values with increasing $\Delta\eta$, leading to negative values (anticorrelation), showing a rather trivial effect of $p_T(\eta)$ dependence. As it can be seen in Fig.6.2, tracks with large separation in η are anticorrelated in mean p_T .

Constructing the $\langle \overline{\Delta p_{t,1}} \overline{\Delta p_{t,2}} \rangle$ and the Σ_{p_T} map for true pairs, as it is shown in Fig. 6.3, we also note the declination of the signal at finite $\Delta\eta$ which was reproduced with event mixing. The $\langle \overline{\Delta p_{t,1}} \overline{\Delta p_{t,2}} \rangle$ map was transformed to a Σ_{p_T} map using the equations 3.14 and 3.19.

Thus, we should correct the maps taking into account the abovementioned $p_T(\eta)$ dependence by subtracting the map of the mixed pairs from that of true pairs. The results that will follow in the next sections present corrected $\langle \overline{\Delta p_{t,1}} \overline{\Delta p_{t,2}} \rangle$

and Σ_{p_T} maps.

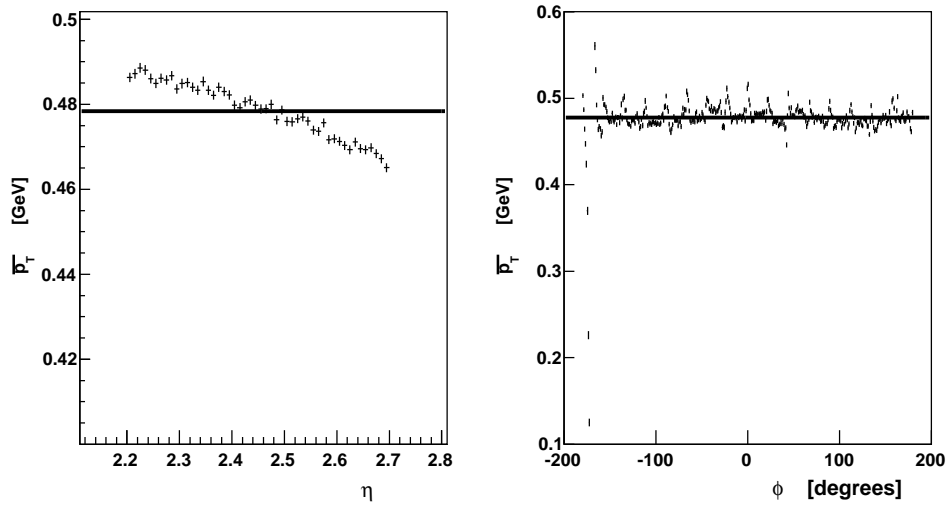


Figure 6.2: The dependence of the inclusive mean p_T of positive particles, on η and ϕ respectively.

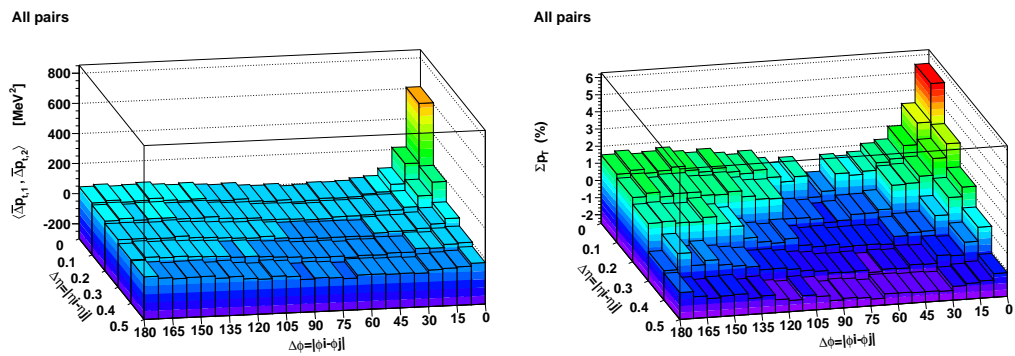


Figure 6.3: The $\langle \bar{\Delta}p_{t,1} \bar{\Delta}p_{t,2} \rangle$ (left panel) and the Σ_{p_T} map (right panel) in $\Delta\eta$ - $\Delta\phi$ space, for all true pairs uncorrected.

Error estimates

For each bin, we calculate the average momentum correlator $\langle \overline{\Delta p_{t,1}} \overline{\Delta p_{t,2}} \rangle$ using the formula 3.14, because it provides a relatively easy way of estimating the statistical error compared to the transverse momentum covariance $\langle \langle \delta p_{t_i} \delta p_{t_j} \rangle_{i \neq j} \rangle$ which is a pair-measure (Eq. 3.15).

The statistical error on $\langle \overline{\Delta p_{t,1}} \overline{\Delta p_{t,2}} \rangle$ was estimated as follows. The value of $\langle \overline{\Delta p_{t,1}} \overline{\Delta p_{t,2}} \rangle$ was evaluated for each event of the whole sample of analyzed events and the dispersion (D) of the results was then calculated. The statistical error of $\langle \overline{\Delta p_{t,1}} \overline{\Delta p_{t,2}} \rangle$ was taken to be equal to $D/\sqrt{N_{events}}$.

In Fig. 6.4 we see the distributions of the $\langle \overline{\Delta p_{t,1}} \overline{\Delta p_{t,2}} \rangle$ taken from a sample of 3.5 million events and obtained using the mixed event analysis. We note that the obtained mean value is the one we use in the maps and the number of entries is the number of analyzed events.

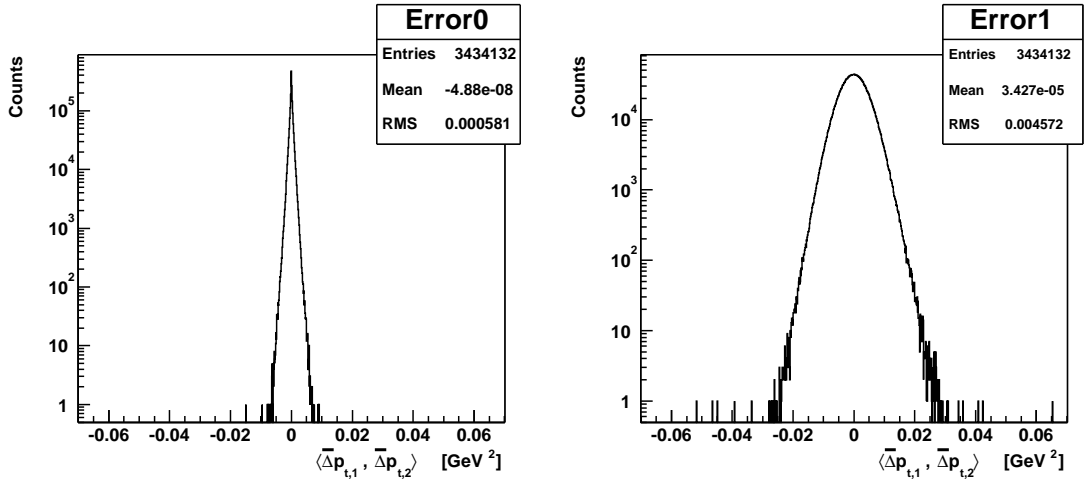


Figure 6.4: Distributions of the $\langle \overline{\Delta p_{t,1}} \overline{\Delta p_{t,2}} \rangle$ obtained using mixed events. The average value (left panel) and the correlator value at $0 < \Delta\eta < 0.1$ and $0 < \Delta\phi < 7.5$ deg. (right panel) are given by the means of the distributions respectively.

Based on our results we find that the relation 3.16 holds extremely well.

Two-track resolution

Detector effects such as the finite two-track resolution influences the measured $\langle \overline{\Delta p_{t,1}} \overline{\Delta p_{t,2}} \rangle$ values. In order to estimate this contribution, an application of a cut in the opening angle distribution of true particle pairs detected in the TPC is needed. The exclusion of pairs with opening angle $\alpha \leq 10$ mrad affects only the magnitude of the signal placed at $0 \leq \Delta\phi \leq 7.5$ and $0 \leq \Delta\eta \leq 0.1$. The value of the correlator in this region drops from 608 MeV² (Fig. 6.3) to 370 MeV², resulting to an average value of 19.03 ± 0.7 MeV². The results that will follow, are not corrected for two-track resolution and HBT/Coulomb correlations.

6.2.2 Same event analysis

The $\langle \overline{\Delta p_{t,1}} \overline{\Delta p_{t,2}} \rangle$ map in $\Delta\eta$ - $\Delta\phi$ space for all pairs is shown in Fig.6.5.

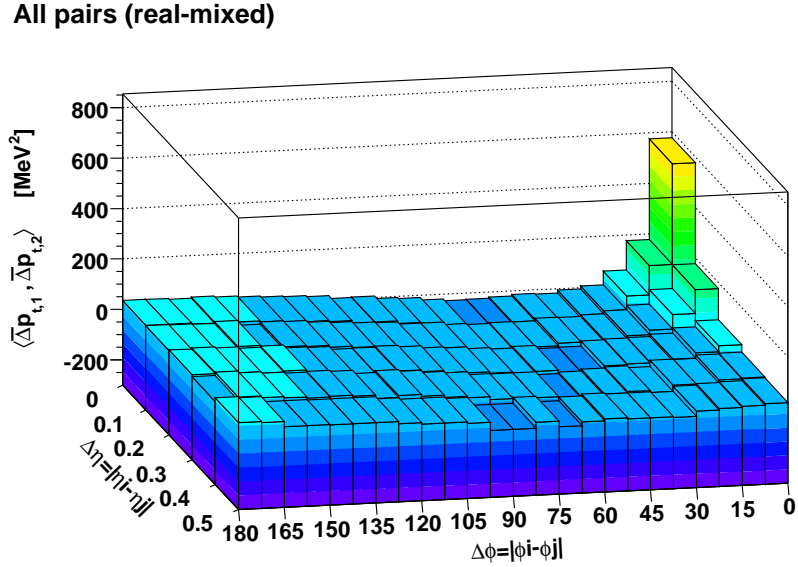


Figure 6.5: The $\langle \overline{\Delta p_{t,1}} \overline{\Delta p_{t,2}} \rangle$ map in $\Delta\eta$ - $\Delta\phi$ space for all true-mixed pairs.

The same $\langle \overline{\Delta p_{t,1}} \overline{\Delta p_{t,2}} \rangle$ map can be plotted in a different way as the $\Delta\phi$ dependence of the $\langle \overline{\Delta p_{t,1}} \overline{\Delta p_{t,2}} \rangle$ in 5 slices of $\Delta\eta$, as can be seen in Fig.6.6. The line is a constant fit which provides the average value of the $\langle \overline{\Delta p_{t,1}} \overline{\Delta p_{t,2}} \rangle$ in the total momentum subspace (η, ϕ) . The average value is consistent with the $\langle \overline{\Delta p_{t,1}} \overline{\Delta p_{t,2}} \rangle$ in

the total subspace as well as with the $\sigma_{p_T, dyn}^2$, as it can be calculated according to the Eq.3.11 (presented in section 6.1). Statistical errors for the $\langle \overline{\Delta p_{t,1}} \overline{\Delta p_{t,2}} \rangle$ map are uniform on $\Delta\phi$ (periodic variable) but as $\Delta\eta$ increases from 0.1 to 0.5 (finite η acceptance), they get values from 3.5 to 11.5 MeV². The error of the corrected $\langle \overline{\Delta p_{t,1}} \overline{\Delta p_{t,2}} \rangle$ for each bin was calculated by adding in squares the statistical error of the real and the statistical error of the mixed value.

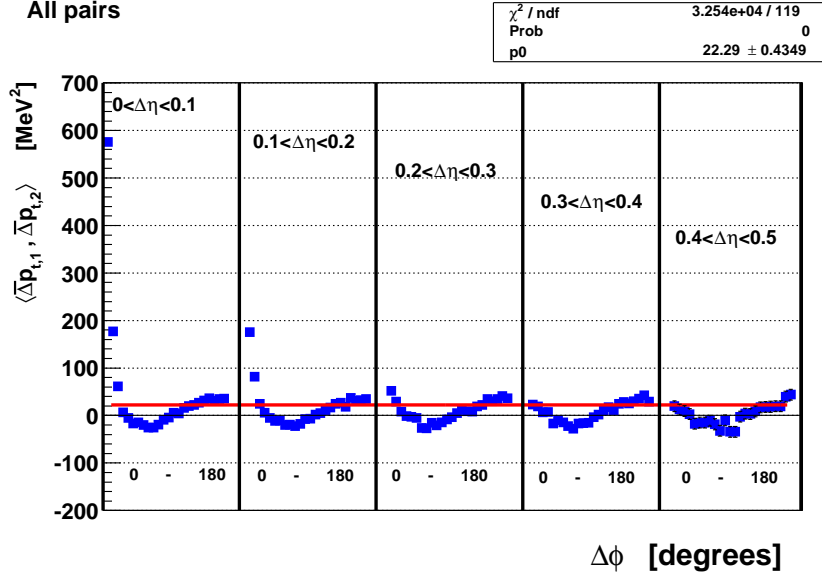


Figure 6.6: The $\Delta\phi$ dependence of the $\langle \overline{\Delta p_{t,1}} \overline{\Delta p_{t,2}} \rangle$ in 5 slices of $\Delta\eta$, for all pairs. The line is a constant fit.

The number of pairs depends strongly on the $\Delta\eta$ while is uniform on $\Delta\phi$, as it can be seen in Fig. 6.7. We note that in the bin of the map at $0 < \Delta\eta < 0.1$ and $0 < \Delta\phi < 7.5$ deg., there are more pairs than in the other bins at the same η range, indicating a correlation.

The $\langle \overline{\Delta p_{t,1}} \overline{\Delta p_{t,2}} \rangle$ map contains two features: a rather narrow **near-side** component ($\Delta\phi \leq 30$ and $\Delta\eta \leq 0.3$) and a broad **away-side** component ($135 \leq \Delta\phi \leq 180$ and $\Delta\eta \leq 0.4$). The near-side peak is probably dominated by HBT (quantum) and Coulomb correlations. Bose and Fermi statistics, final state interactions and experimental effects such as the finite two-track resolution are the origin of short-range (anti-) correlations (SRC). SRC correlations show up

at small momentum differences q and contribute significantly in the part of the map where $\Delta\phi \leq 45$ (this has been confirmed by applying a cut at pairs with $q_{inv} < 70$ MeV/c, where the four-momentum difference $q_{inv} \equiv \sqrt{\mathbf{q}^2 - q_0^2}$, is the momentum difference in the pair rest frame, \mathbf{q} and q_0 , are the differences in three-momentum and energy of a particle pair assuming the pion mass for each particle).

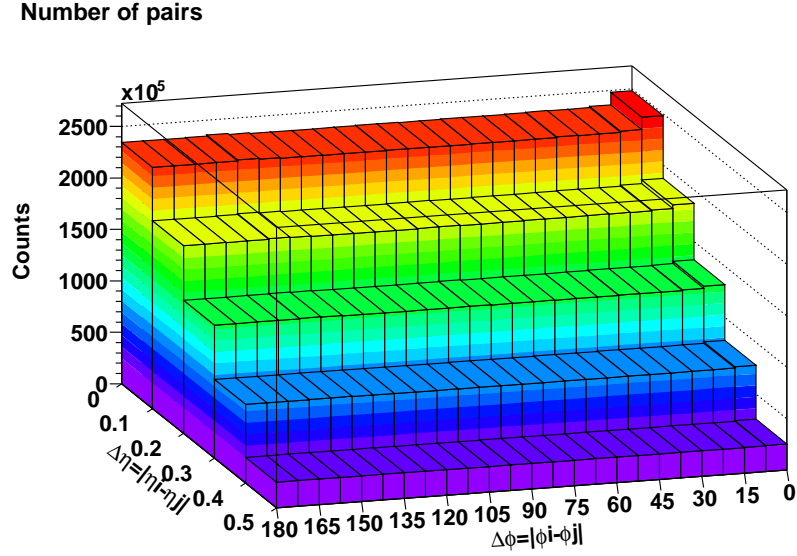


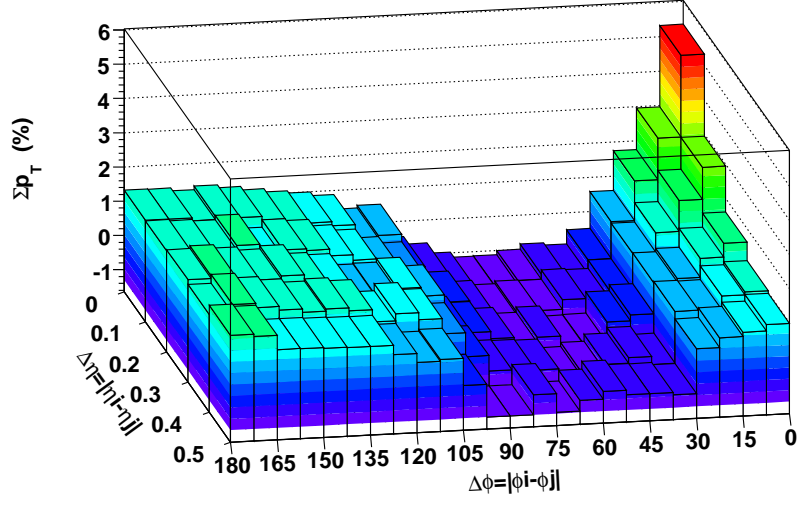
Figure 6.7: The number of pairs in $\Delta\eta$ - $\Delta\phi$ space.

Long-range correlations (LRC) occur as a consequence of energy and momentum conservation and they are not localized at the origin. In the observed away-side peak, contribution by mini-jets and elliptic flow [70] is expected.

Fig.6.8 shows how the normalized fluctuation Σ_{p_T} looks like in $\Delta\eta$ - $\Delta\phi$ space for all pairs. Thus, the observed fluctuations at SPS which are about 1 % on average, have also a rich structure in momentum subspace, providing a signal that varies from -1 to 5.5 %. The landscape is dominated by a near-side peak symmetric about $\Delta\eta = \Delta\phi = 0$ and a broad $\Delta\eta$ independent away-side ridge.

Since particles from jet fragmentation cluster together in phase space, the two-particle correlation is expected to be enhanced. In particular, two-particle correlation at large p_T in the azimuthal angle difference $\Delta\phi$ should be strongly peaked

All pairs (real-mixed)

Figure 6.8: The Σ_{p_T} map in $\Delta\eta$ - $\Delta\phi$ space for all pairs.

at both forward (‘near-side’) $\Delta\phi = 0$, and backward (‘back-to-back’) $\Delta\phi = \pi$ directions. That mini-jet component should be invariant on $\Delta\eta$ (characteristic of back-to-back jet fragments).

$\langle \overline{\Delta p_{t,1}} \overline{\Delta p_{t,2}} \rangle$ maps for different charge combinations.

The inclusive results of mean p_T fluctuations for different charge combinations were presented in Table 6.1 (section 6.1).

In order to visualize the full correlation structure for like-sign and unlike-sign pairs in the four-dimensional momentum subspace $(\eta_i, \eta_j, \phi_i, \phi_j)$, we construct the $\langle \overline{\Delta p_{t,1}} \overline{\Delta p_{t,2}} \rangle$ map as it can be seen in Fig. 6.9. For the calculation of $\langle \overline{\Delta p_{t,1}} \overline{\Delta p_{t,2}} \rangle$ we used the Eq.3.17 and 3.18

The fact that the maps of positively and negatively charged particles look similar in strength and shape at small $\Delta\phi$ and $\Delta\eta$, can be related to their common origin (HBT/Coulomb correlations). On the contrary, unlike-sign pairs have a peak at that region which is weaker and narrower, where we can expect contribution from Coulomb, resonances and e^+e^- decays (conversion electron pairs).

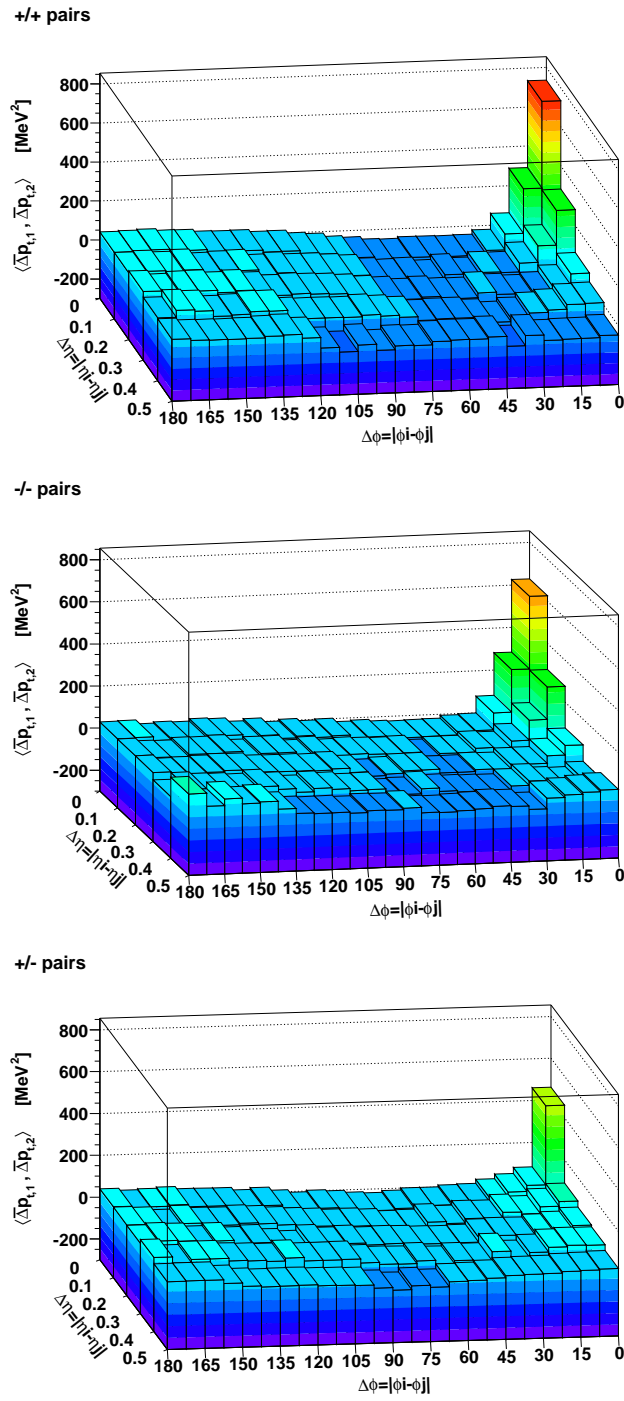


Figure 6.9: The $\langle \overline{\Delta p_{t,1}} \overline{\Delta p_{t,2}} \rangle$ map in $\Delta\eta$ - $\Delta\phi$ space for positive, negative and unlike-sign pairs respectively.

6.2.3 Centrality dependence

Fig.6.10 (left panel) presents our measurement of $\langle \overline{\Delta p_{t,1}} \overline{\Delta p_{t,2}} \rangle$ in 158 A·GeV/c Pb-Au collisions as function of the mean number of participating nucleons $\langle N_{part} \rangle$. One observes that the correlator $\langle \overline{\Delta p_{t,1}} \overline{\Delta p_{t,2}} \rangle$ is finite and positive at this energy and that it exhibits a qualitative inverse proportionality to $\langle N_{part} \rangle$. This qualitative dependence is known to arise from the progressive dilution of the correlation with increased number of particle sources.

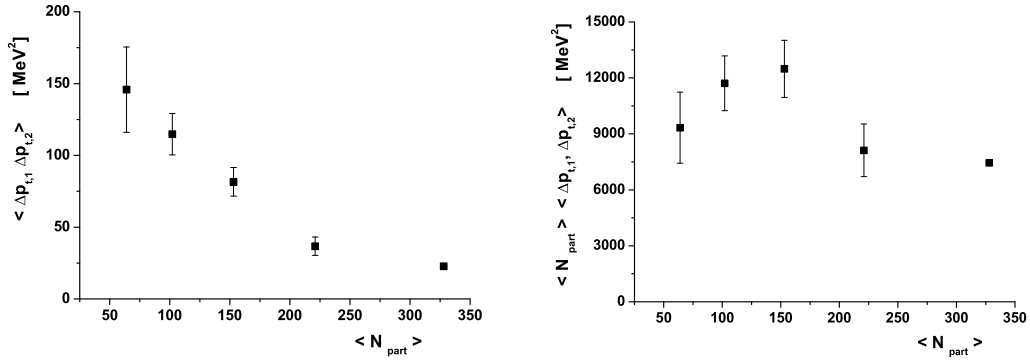


Figure 6.10: Measured correlator $\langle \overline{\Delta p_{t,1}} \overline{\Delta p_{t,2}} \rangle$ versus centrality and $\langle \overline{\Delta p_{t,1}} \overline{\Delta p_{t,2}} \rangle$ scaled by number of participating nucleons.

We next study the monotonic decrease of the correlator $\langle \overline{\Delta p_{t,1}} \overline{\Delta p_{t,2}} \rangle$ with increasing number of participating nucleons. As it was discussed in section 4.3, considering that if Pb-Au collisions consisted of a superposition of independent *nucleon-nucleon* interactions, with no rescattering of secondaries, the correlator measured at a given centrality in *A-A* should be proportional to the correlator measured in *p-p* and inversely proportional to the number of *nucleon-nucleon* interactions at the given centrality. In such collision scenario, the produced particle multiplicity should be strictly proportional to the number of interactions.

Thus, we scale the measured correlator $\langle \overline{\Delta p_{t,1}} \overline{\Delta p_{t,2}} \rangle$ by $\langle N_{part} \rangle$ to remove the $1/N$ correlation dilution, implying the assumption that the number of produced particles is roughly proportional to $\langle N_{part} \rangle$. Fig.6.10 (right panel) presents the scaled correlation $\langle N_{part} \rangle \langle \overline{\Delta p_{t,1}} \overline{\Delta p_{t,2}} \rangle$ as a function of participating nucleons. As a first observation, we note that, at variance with expectations based on an indepen-

dent *nucleon-nucleon* collision scenario, the scaled correlator $\langle N_{part} \rangle \langle \overline{\Delta p_{t,1}} \overline{\Delta p_{t,2}} \rangle$ varies strongly with collision centrality. Therefore, violation of the ‘1/N’ scaling has been established and reveals a dramatic change that occurs in the collision dynamics of central Pb-Au collisions relative to peripheral Pb-Au and *p-p* collisions. This observation is in qualitative agreement with previous findings at RHIC using the same measure [67].

A summary of mean p_T fluctuations for all pairs at $0.1 < p_T < 1.5$ GeV/c, $2.2 < \eta < 2.7$ and full ϕ acceptance at 158 A·GeV/c for five centrality classes is presented in Table 6.2.

The $\langle \overline{\Delta p_{t,1}} \overline{\Delta p_{t,2}} \rangle$ maps in $\Delta\eta$ - $\Delta\phi$ space for these centrality classes are shown in Fig.6.11. We note that the peak structure is enhanced with centrality but the poor statistics of the data that come from the minimum bias run lead to a large fluctuation of the signal. Therefore, we examine the $\Delta\phi$ dependence of the correlator $\langle \overline{\Delta p_{t,1}} \overline{\Delta p_{t,2}} \rangle$ at $\Delta\phi = 30$ degrees and $0 < \Delta\eta < 0.5$, for true and mixed pairs respectively, as it can be seen in Fig.6.12. At $0 < \Delta\phi < 30$ and $120 < \Delta\phi < 180$, we observe a positive increase of the measured correlator with centrality (using mixed pairs there is a consistency to zero).

The centrality dependence of the measured correlator $\langle \overline{\Delta p_{t,1}} \overline{\Delta p_{t,2}} \rangle$, scaled by number of participating nucleons, for several regions of $\Delta\phi$ is shown in Fig.6.13. Since the overall fluctuations seem to be dominated by the short range and the away-side two-particle correlations, we can analyse separately these two components and observe their non-monotonic centrality dependence (two upper sets of points in Fig. 6.13).

The region of $30^\circ < \Delta\phi < 60^\circ$ is free of the influence of the two mentioned components and elliptic flow does not matter. The p_T fluctuations in this region turn out to be close to zero and independent on centrality within the error bars. We also note an anticorrelation for all centrality classes in the region of $60^\circ < \Delta\phi < 90^\circ$.

It has been shown that $\langle \overline{\Delta p_{t,1}} \overline{\Delta p_{t,2}} \rangle$ is a nonmonotonic function of centrality. Such a behavior strongly resembles the dependence of the magnitude of collective flow –*directed*(v_1) and *elliptic*(v_2)– on $\langle N_{part} \rangle$. Thus, there is a natural suggestion that the p_T fluctuations measured by $\langle \overline{\Delta p_{t,1}} \overline{\Delta p_{t,2}} \rangle$ may be caused by the collective flow. This suggestion is checked in the next subsection 6.2.4.

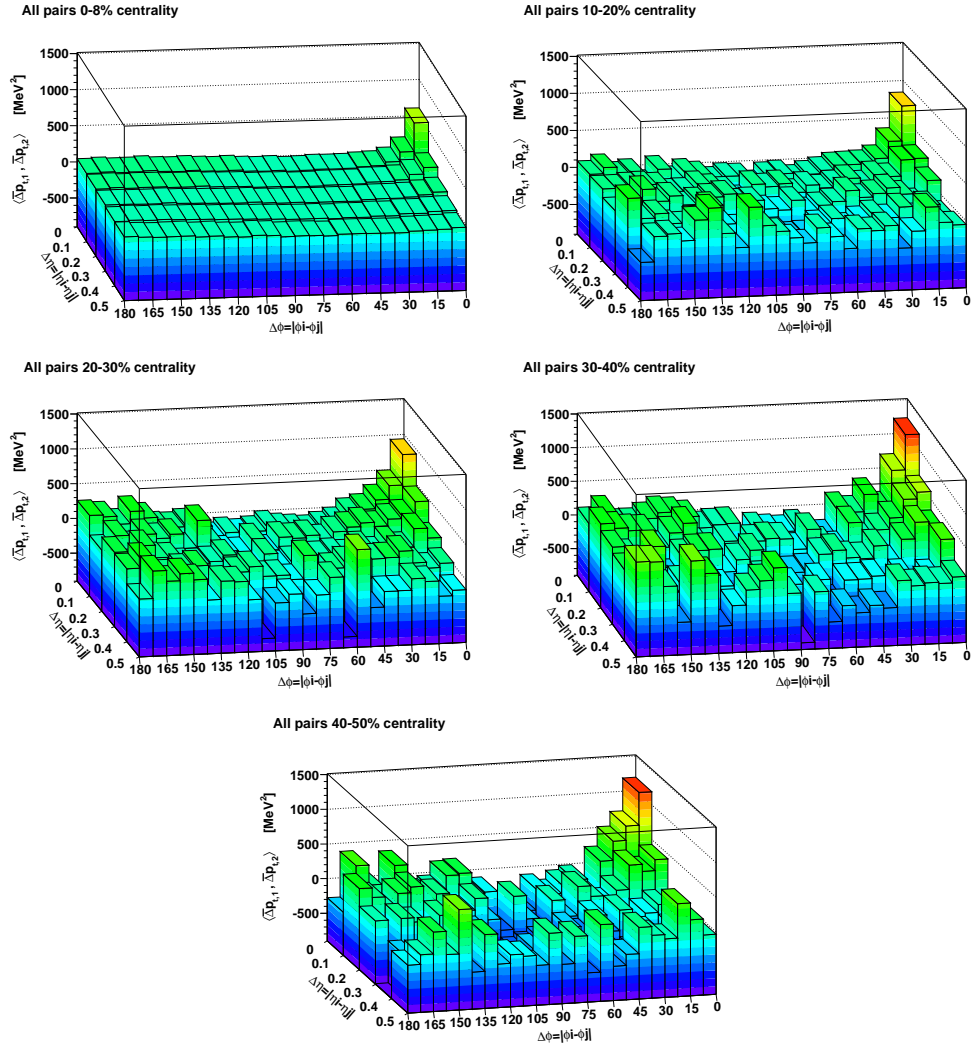


Figure 6.11: $\langle \overline{\Delta p_{t,1}} \overline{\Delta p_{t,2}} \rangle$ maps in $\Delta\eta$ - $\Delta\phi$ space for five centrality classes.

Centrality[%]	0 – 8
$\langle \overline{\Delta p_{t,1}} \overline{\Delta p_{t,2}} \rangle [MeV^2]$	22.71 ± 0.32
$\sigma_{p_T, dyn}^2 [MeV^2]$	21.98 ± 0.44
n	10003672
$\langle N \rangle$	154.83 ± 0.01
$\overline{p_T} [MeV/c]$	449.82 ± 0.01
Centrality[%]	10 – 20
$\langle \overline{\Delta p_{t,1}} \overline{\Delta p_{t,2}} \rangle [MeV^2]$	36.74 ± 6.39
$\sigma_{p_T, dyn}^2 [MeV^2]$	35.52 ± 8.61
n	40146
$\langle N \rangle$	104.81 ± 0.1
$\overline{p_T} [MeV/c]$	448.52 ± 0.14
Centrality[%]	20 – 30
$\langle \overline{\Delta p_{t,1}} \overline{\Delta p_{t,2}} \rangle [MeV^2]$	81.61 ± 9.99
$\sigma_{p_T, dyn}^2 [MeV^2]$	68.62 ± 12.7
n	39496
$\langle N \rangle$	73.37 ± 0.08
$\overline{p_T} [MeV/c]$	445.31 ± 0.17
Centrality[%]	30 – 40
$\langle \overline{\Delta p_{t,1}} \overline{\Delta p_{t,2}} \rangle [MeV^2]$	114.81 ± 14.41
$\sigma_{p_T, dyn}^2 [MeV^2]$	95.81 ± 18.81
n	39763
$\langle N \rangle$	50.07 ± 0.07
$\overline{p_T} [MeV/c]$	441.57 ± 0.2
Centrality[%]	40 – 50
$\langle \overline{\Delta p_{t,1}} \overline{\Delta p_{t,2}} \rangle [MeV^2]$	145.79 ± 29.73
$\sigma_{p_T, dyn}^2 [MeV^2]$	129.62 ± 35.69
n	38197
$\langle N \rangle$	32.72 ± 0.06
$\overline{p_T} [MeV/c]$	436.17 ± 0.25

Table 6.2: Summary of mean p_T fluctuations for all pairs at $0.1 < p_T < 1.5$ GeV/c, $2.2 < \eta < 2.7$ and full ϕ acceptance at 158 A·GeV/c for five centrality classes. Errors are statistical only. The fluctuations are not corrected for two-track resolution and HBT/Coulomb correlations.

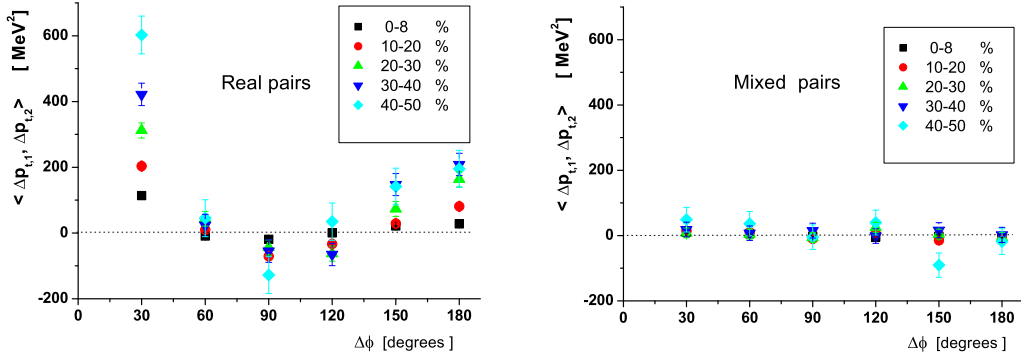


Figure 6.12: The $\Delta\phi$ dependence of the correlator $\langle \overline{\Delta p_{t,1}} \overline{\Delta p_{t,2}} \rangle$ for five centrality classes, for real and mixed pairs respectively.

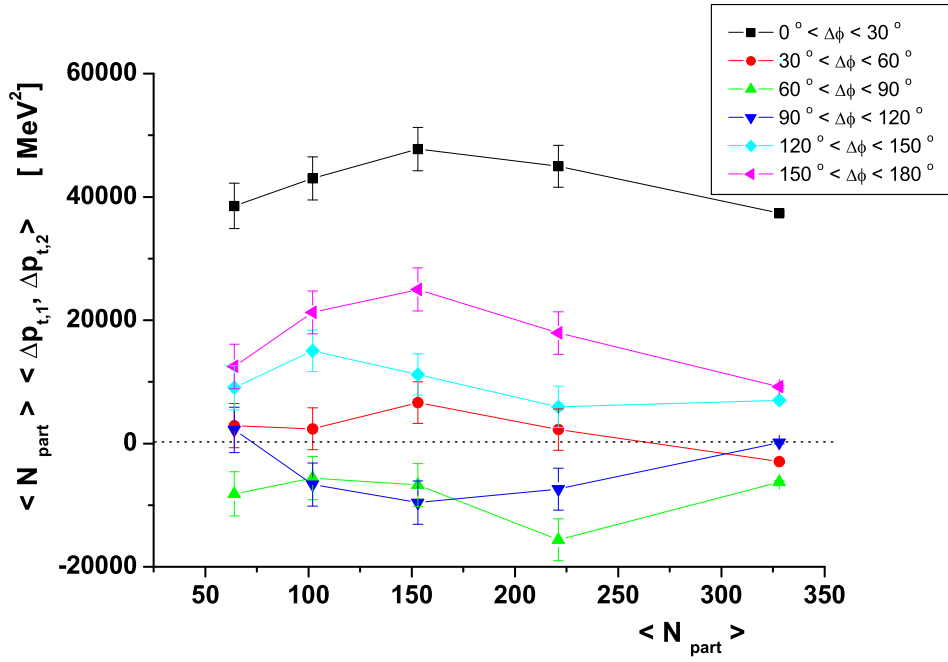


Figure 6.13: Centrality dependence of the measured correlator $\langle \overline{\Delta p_{t,1}} \overline{\Delta p_{t,2}} \rangle$, scaled by number of participating nucleons, for several regions of $\Delta\phi$.

6.2.4 Elliptic flow contribution

In addition to correlations due to SRC and jets, the two-particle azimuthal distributions expressed via the momentum correlator in MeV^2 , exhibit a structure attributable to an elliptic flow anisotropy of single particle production relative to the reaction plane [68, 69]. This leads to a two-particle azimuthal distribution of the form of the Eq. 6.3

$$\frac{dN}{d\Delta\phi} \equiv B[1 + 2v_2^2 \cos(2\Delta\phi)] \quad (6.3)$$

where v_2 is the elliptic flow parameter and B a normalization constant [70]. Previous measurements [69] using several methods have shown that sizable v_2 values persist to high p_T .

The value of v_2 as a function of centrality and p_T has been measured by the CERES experiment [71].

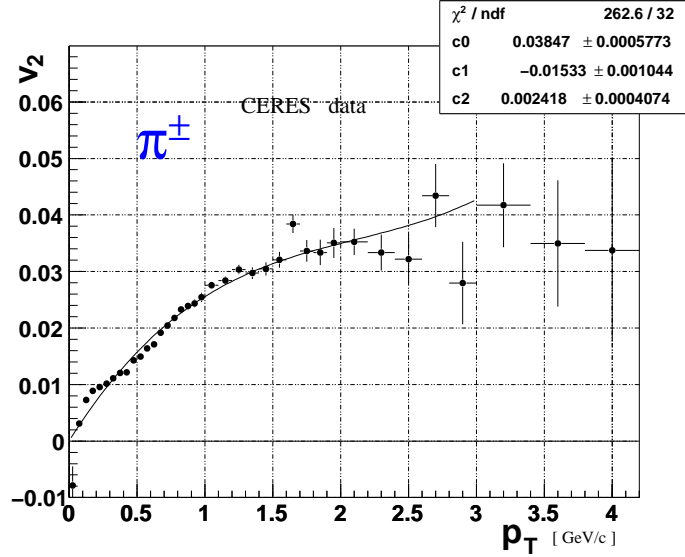


Figure 6.14: π elliptic flow measured by CERES at $\langle\sigma/\sigma_{geo}\rangle = 8.9\%$ [72].

The elliptic flow of pions measured by CERES at $\langle\sigma/\sigma_{geo}\rangle = 8.9\%$ [72] is shown in Fig. 6.14. Since v_2 can be expressed as a function of p_T , we introduce the measure $f_{i,j}$ as:

$$f_{i,j} \equiv 1 + 2v_2(p_{Ti})v_2(p_{Tj})\cos(2|\phi(i) - \phi(j)|) \quad (6.4)$$

Then, we calculate the average momentum correlator $\langle \overline{\Delta p_{t,1}} \overline{\Delta p_{t,2}} \rangle$ for mixed events, multiplying the p_T covariance with $f_{i,j}$ and weighting the numbers of pairs [73] as follows:

$$\langle \overline{\Delta p_{t,1}} \overline{\Delta p_{t,2}} \rangle_{mixed+flow} \equiv \frac{1}{n_{events}} \sum_{k=1}^{n_{events}} \left[\frac{\sum_{i \neq j}^{N_k} (p_{Ti} - \overline{p_T})(p_{Tj} - \overline{p_T}) f_{i,j}}{\sum_{i \neq j}^{N_k} f_{i,j}} \right] \quad (6.5)$$

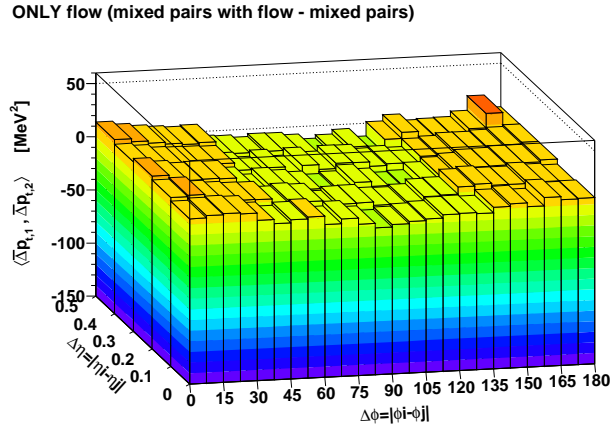


Figure 6.15: The $\langle \overline{\Delta p_{t,1}} \overline{\Delta p_{t,2}} \rangle$ map in $\Delta\eta$ - $\Delta\phi$ space for all pairs assuming there is only flow, as can be obtained by subtracting the corresponding map of mixed pairs from the map of mixed pairs that have elliptic flow.

Subtracting the corresponding map of mixed pairs in the momentum subspace, from the map of mixed pairs that have elliptic flow calculated by Eq. 6.5, we can evaluate the elliptic flow expressed in units of MeV^2 as it can be seen in Fig. 6.15. The $\cos(2\Delta\phi)$ modulation introduced by the elliptic flow obtained at $0 < \Delta\eta < 0.1$ where the statistical error is smaller, is shown in the left panel of Fig. 6.16. In case the average value of v_2 ($\sim 1.5\%$ at this p_T range and centrality) is used for the evaluation of $f_{i,j}$ and not the parametrized one, the $\langle \overline{\Delta p_{t,1}} \overline{\Delta p_{t,2}} \rangle$ does not change. The expected $\cos(2\Delta\phi)$ modulation comes through the p_T dependence.

In order to confirm this effect, a Monte Carlo analysis was performed [74], generating events with independent particles, following the measured inclusive p_T distribution where the uniform azimuthal angle distribution of the events was modified by the elliptic flow expected by CERES according to the parametrization of $v_2(p_T)$ shown in Fig. 6.14 (right panel of Fig. 6.16). Both methods are in a good agreement but for our study we will use the value of the elliptic flow obtained by the calculation of $\langle \overline{\Delta p_{t,1}} \overline{\Delta p_{t,2}} \rangle_{mixed+flow}$.

Fig. 6.17 shows the $\Delta\phi$ dependence of the $\langle \overline{\Delta p_{t,1}} \overline{\Delta p_{t,2}} \rangle$ at $0 < \Delta\eta < 0.1$ with the expected elliptic flow superimposed, for all pairs. We can subtract the CERES flow from the $\langle \overline{\Delta p_{t,1}} \overline{\Delta p_{t,2}} \rangle$ map as it can be seen in Fig. 6.18 and correct as well as the normalized fluctuation Σ_{p_T} (see Fig. 6.19).

Thus, one concludes that the effect of the azimuthal anisotropy caused by the elliptic flow is not responsible for the observed dynamical p_T fluctuations. The question that remains is what is the origin of the observed broad away-side peak and whether is a low or a high p_T effect.

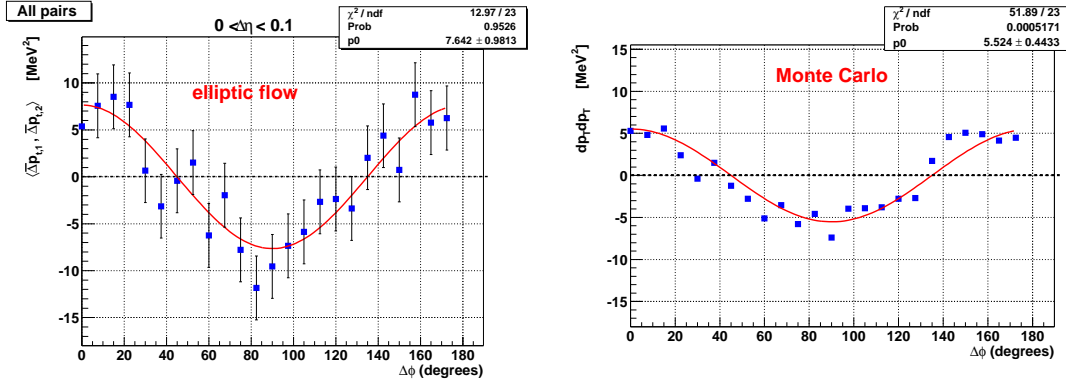


Figure 6.16: Estimation of the elliptic flow expected by CERES using mixed-event analysis (left panel) and Monte Carlo evaluation [74] (right panel).

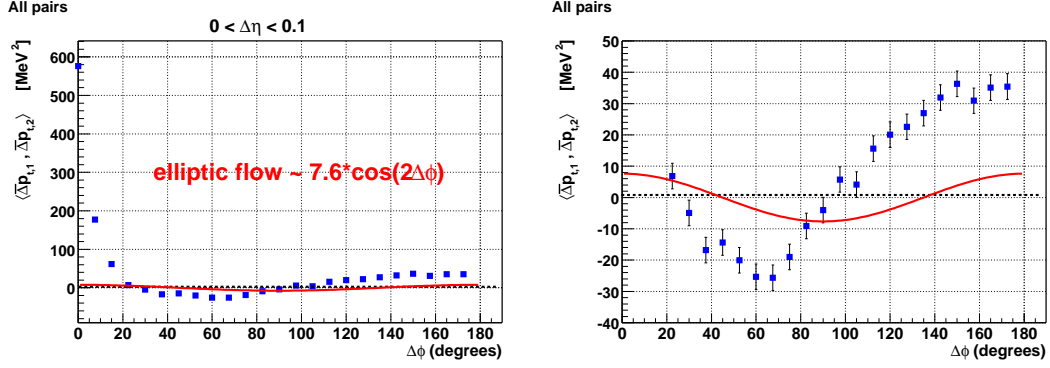


Figure 6.17: The $\Delta\phi$ dependence of the $\langle \overline{\Delta p_{t,1}} \overline{\Delta p_{t,2}} \rangle$ at $0 < \Delta\eta < 0.1$ with the expected elliptic flow superimposed, for all pairs.

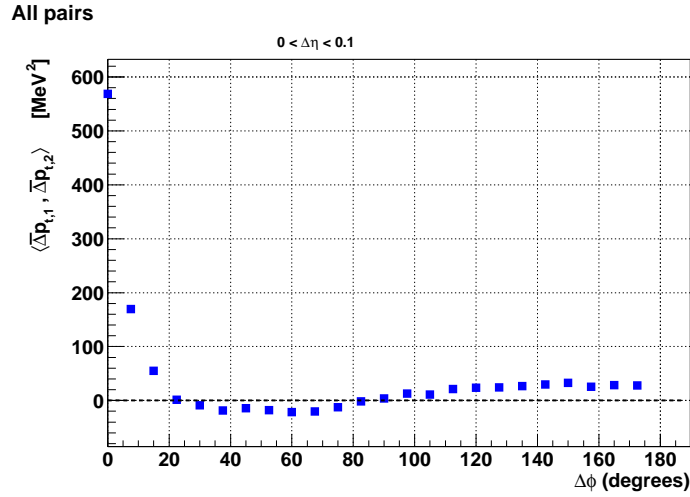
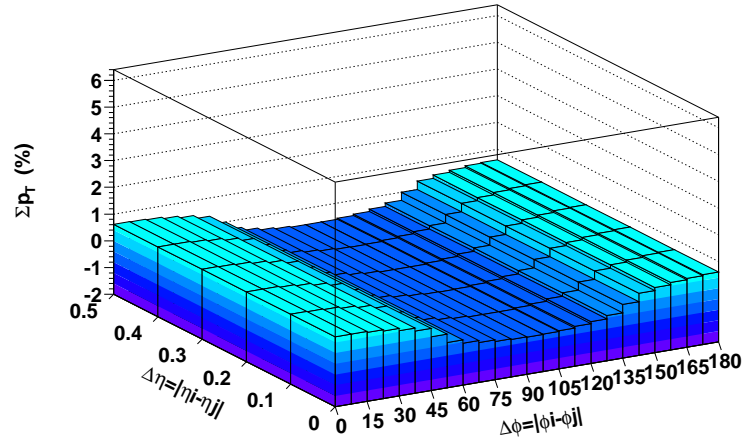


Figure 6.18: The $\Delta\phi$ dependence of the $\langle \overline{\Delta p_{t,1}} \overline{\Delta p_{t,2}} \rangle$ at $0 < \Delta\eta < 0.1$, for all pairs, after subtraction of the expected elliptic flow.

elliptic flow



subtracting flow

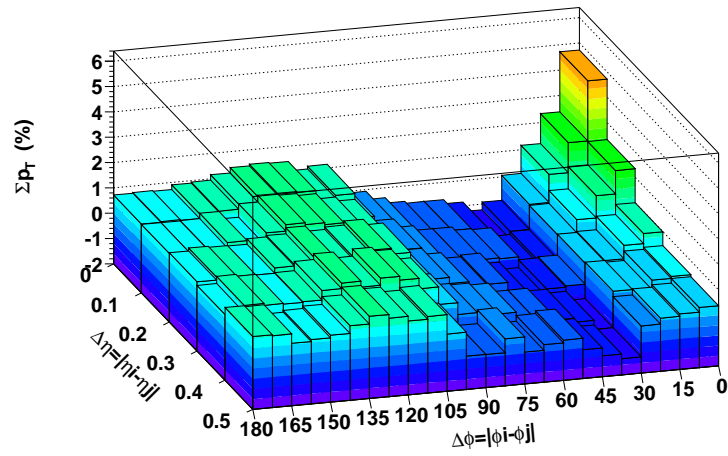


Figure 6.19: The Σp_T map in $\Delta\eta$ - $\Delta\phi$ space for all pairs, when only elliptic flow is present (top panel) and the total Σp_T , after subtraction of the expected elliptic flow (bottom panel).

6.3 Two-particle correlation analysis using the cumulant p_T variable x

In order to achieve a better understanding of the fluctuation structure one needs to apply a more differential method. The correlations can be studied by plotting the cumulative p_T variables of particle pairs. Namely, for a given particle, instead of its p_T one introduces the variable x defined as [42, 43, 44]:

$$x(p_T) = \int_0^{p_T} \rho(p'_T) dp'_T \quad (6.6)$$

where $\rho(p'_T)$ is the inclusive p_T distribution, normalized to unity, which is obtained from all particles used in the analysis. By construction, the x variable varies between 0 and 1 with a flat probability distribution. The Fig.6.20 shows the inclusive p_T distribution and the corresponding p_T variable x , for all pairs. Thus, a high p_T value corresponds to a high x (close to 1). We have also prepared the cumulant p_T variable x for different charge combinations.

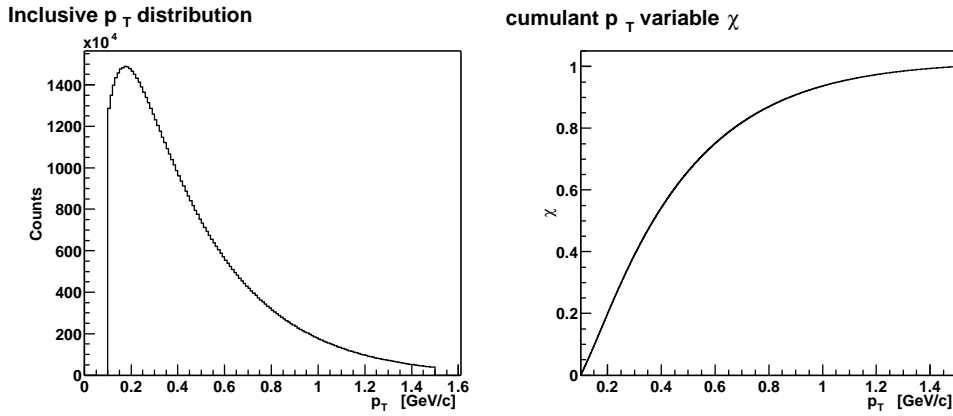


Figure 6.20: The inclusive p_T distribution (left panel) and the corresponding p_T variable x (right panel), for all pairs.

The two-particle correlation plots, as presented in this work, are obtained by plotting (x_1, x_2) points for all possible particle pairs within the same event. The number of pairs in each (x_1, x_2) bin is divided by the mean number of pairs in a

bin (averaged over all (x_1, x_2) bins). This two-dimensional plot is uniform when no inter-particle correlations are present in the system. Correlations due to the Bose statistics produce a ridge along the diagonal of the (x_1, x_2) plot, which starts at $(0, 0)$ and ends at $(1, 1)$, whereas temperature fluctuations lead to a saddle shaped structure [39]. As will be seen in this section, the distribution of x_1 or x_2 obtained from the two-dimensional (x_1, x_2) plots by projecting on the x_1 or x_2 axis is not flat. This is due to the method by which the plots are constructed. Namely, each pair of particles is represented by a point on the plot. Therefore, the events with higher multiplicities are represented by a larger number of pairs than those with smaller multiplicities. It should be stressed that in the absence of any correlations the (x_1, x_2) plot is uniformly populated and the x_1 and x_2 projections are flat.

6.3.1 Two-particle correlation plots in several $\Delta\phi$ regions

A study of two-particle correlation plots from a sample of about seven millions events, having a centrality of the upper 8 % of the total geometric cross section, is performed in several $\Delta\phi$ regions.

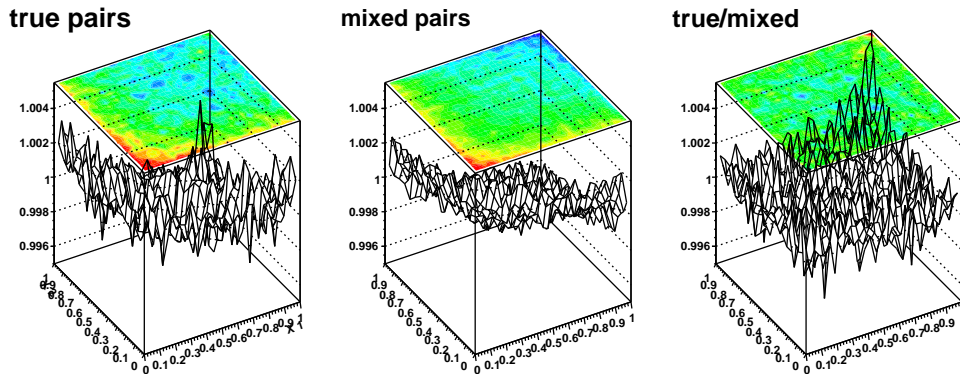


Figure 6.21: The two-particle correlation plots for all pairs, mixed pairs and true versus mixed, at $0 < \Delta\eta < 0.5$ and $142.5 < \Delta\phi < 150$ deg.).

The two-particle correlation plots for mixed pairs as it can be seen in Fig. 6.21 are not completely flat as it is expected by definition. Therefore, to mini-

6.3. TWO-PARTICLE CORRELATION ANALYSIS USING THE CUMULANT P_T VARIABLE X

mize instrumental effects and to reveal possibly the origin of the away-side peak that was observed using the $\langle \overline{\Delta p_{t,1}} \overline{\Delta p_{t,2}} \rangle$ measure, we construct the two-particle correlation plots for all pairs corrected, by dividing real versus mixed.

After each charged particle pair (x_1, x_2) was entered into the plot, the bin contents were normalized by dividing with the average number of entries per bin. The data in these figures, are plotted with same colour scales and are symmetric about the diagonal by construction. All the next plots are corrected after a division with the corresponding mixed ones.

Two-particle correlation plots using the cumulant p_T variable x for all pairs, in several $\Delta\phi$ regions, are given in Fig. 6.22. We note that the plots are not uniformly populated. Contributions to them include, but are not limited to, quantum statistics, Coulomb effects, resonances decays, instrumental effects and ‘dynamical’ fluctuations. At $0^\circ < \Delta\phi < 30^\circ$, one observes a prominent ridge along the main diagonal. At $30^\circ < \Delta\phi < 120^\circ$, the plots seem to be rather flat. At $120^\circ < \Delta\phi < 180^\circ$, we see a high- p_T correlation given as a sharp narrow peak as an enhancement in the region close to $x_1 = x_2 = 1$. It was already presented before (see Fig. 6.12 for 0-8 % centrality) that the average momentum correlator $\langle \overline{\Delta p_{t,1}} \overline{\Delta p_{t,2}} \rangle$ in the same region ($120^\circ < \Delta\phi < 180^\circ$) is positive. This observation attributes the away-side peak of the $\langle \overline{\Delta p_{t,1}} \overline{\Delta p_{t,2}} \rangle$ in that $\Delta\phi$ region to high- p_T correlations.

A separate treatment of positive, negative and unlike-signed pairs is generally necessary in order to extract complete information, since different physics may affect each combination. Two-particle correlation plots for all charged combinations are presented in Figs. 6.23, 6.24, 6.25. One observes a ridge along the main diagonal for the like-signed pairs corresponding to quantum correlations and a peak in the unlike-signed pairs ($x_1 = x_2 = 0$) due to the Coulomb interaction.

In order to see how the elliptic flow influences the two-particle correlation plots, we use the same procedure described in 6.2.4. Thus, the flow is evaluated by giving a weight to mixed particle pairs equal to $f_{i,j}$ according to Eq. 6.4 and divide the resulting plots with the corresponding ones of mixed pairs. The results are presented in Fig. 6.26. The plots are flat indicating that the elliptic flow that is measured at CERES, is too weak to be visible. An abnormally large value of $3v_2$, where v_2 gets the measured by CERES parametrized value [72],

results to two-particle correlation plots with much bigger high- p_T enhancement at $x_1 = x_2 = 1$, as can be seen in Fig. 6.27,

Two-particle correlation plots for all pairs in smaller $\Delta\phi$ bins, 24 in total, corresponding to an angle of 7.5 degrees (the bin index follows the increase of $\Delta\phi$, i.e., 1 bin corresponds to $0 < \Delta\phi < 7.5$, 2 bin corresponds to $7.5 < \Delta\phi < 15$, 24 bin corresponds to $172.5 < \Delta\phi < 180$, allowing a comparison with the measured $\langle \overline{\Delta p_{t,1}} \overline{\Delta p_{t,2}} \rangle$) can be found in appendix A.

6.3. TWO-PARTICLE CORRELATION ANALYSIS USING THE CUMULANT P_T VARIABLE X_C

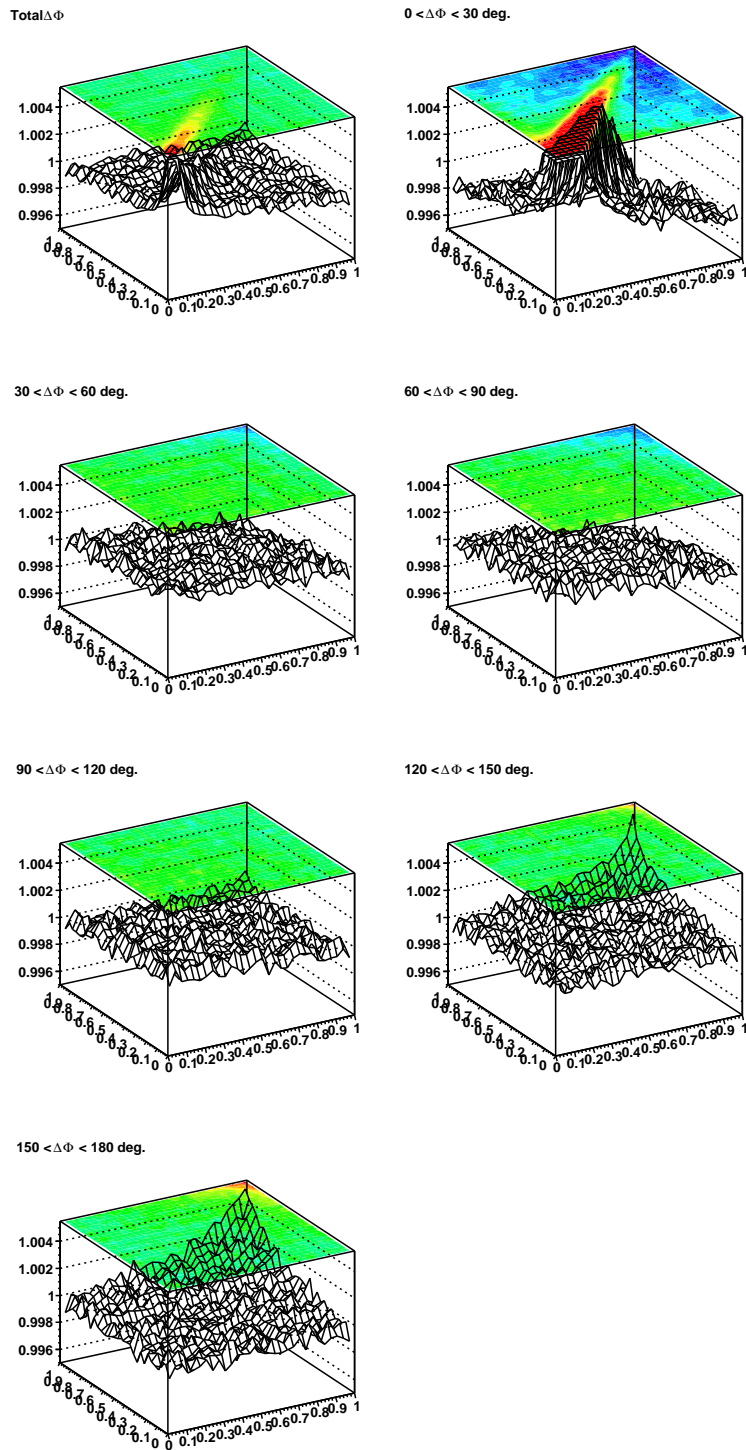


Figure 6.22: Two-particle correlation plots using the cumulant p_T variable x for all pairs, in several $\Delta\phi$ regions.

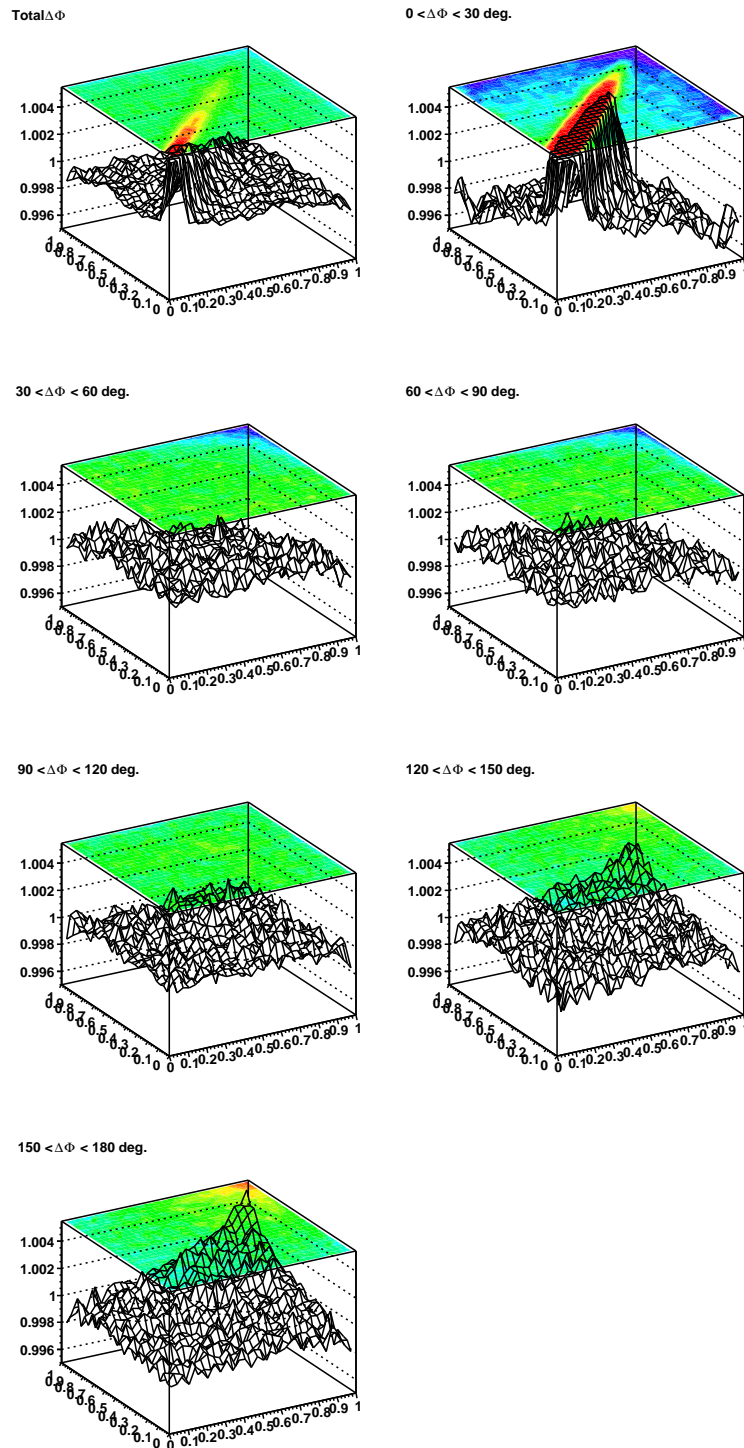


Figure 6.23: Two-particle correlation plots using the cumulant p_T variable x for positive pairs, in several $\Delta\phi$ regions.

6.3. TWO-PARTICLE CORRELATION ANALYSIS USING THE CUMULANT p_T VARIABLE x

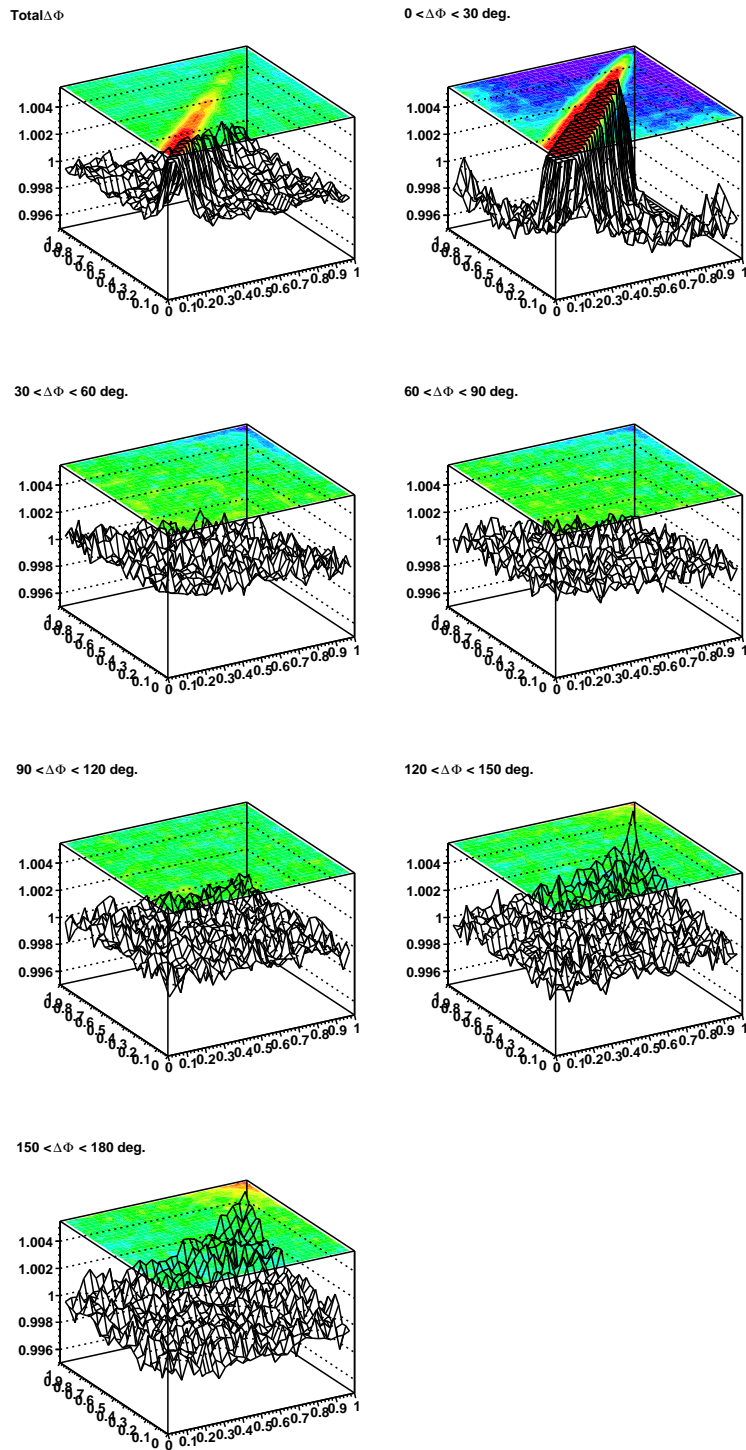


Figure 6.24: Two-particle correlation plots using the cumulant p_T variable x for negative pairs, in several $\Delta\phi$ regions.

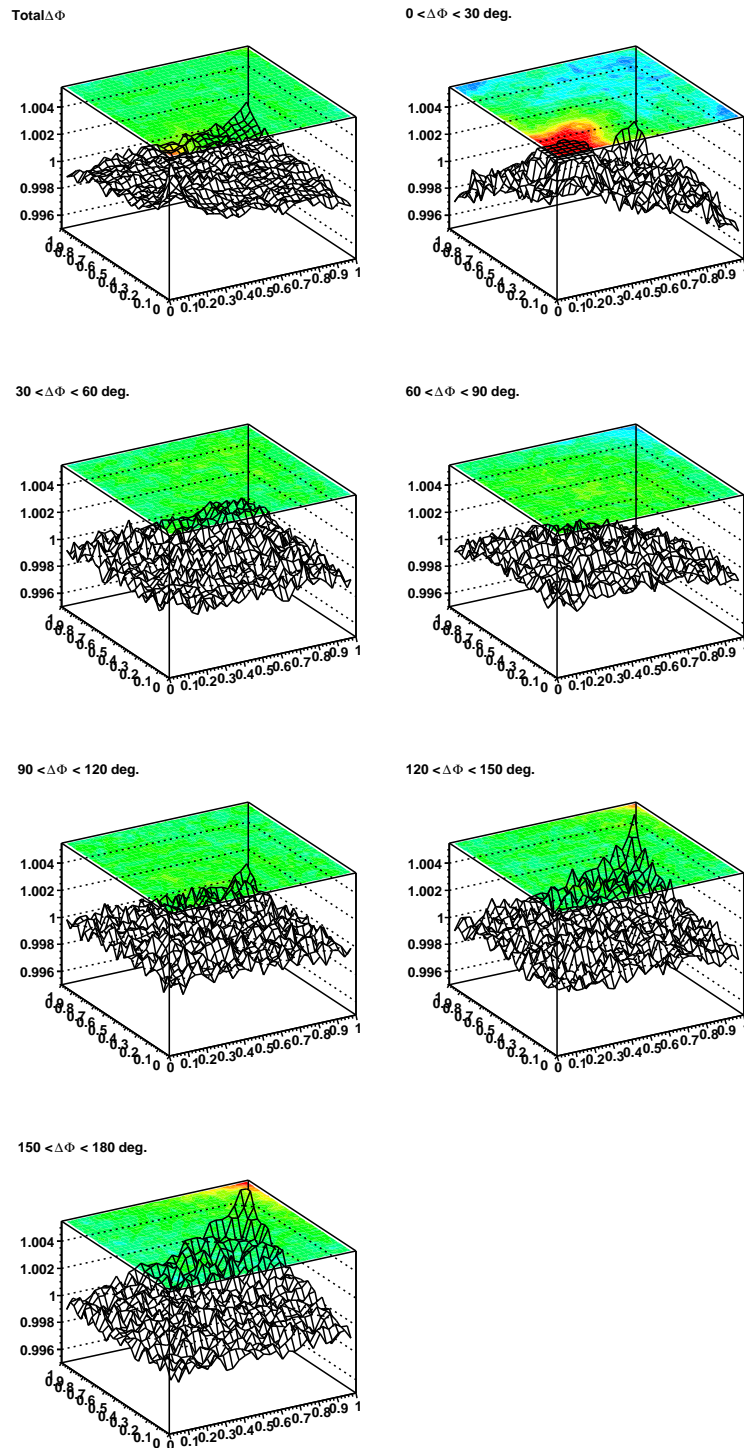


Figure 6.25: Two-particle correlation plots using the cumulant p_T variable x for unlike-sign pairs, in several $\Delta\phi$ regions.

6.3. TWO-PARTICLE CORRELATION ANALYSIS USING THE CUMULANT P_T VARIABLE X_T

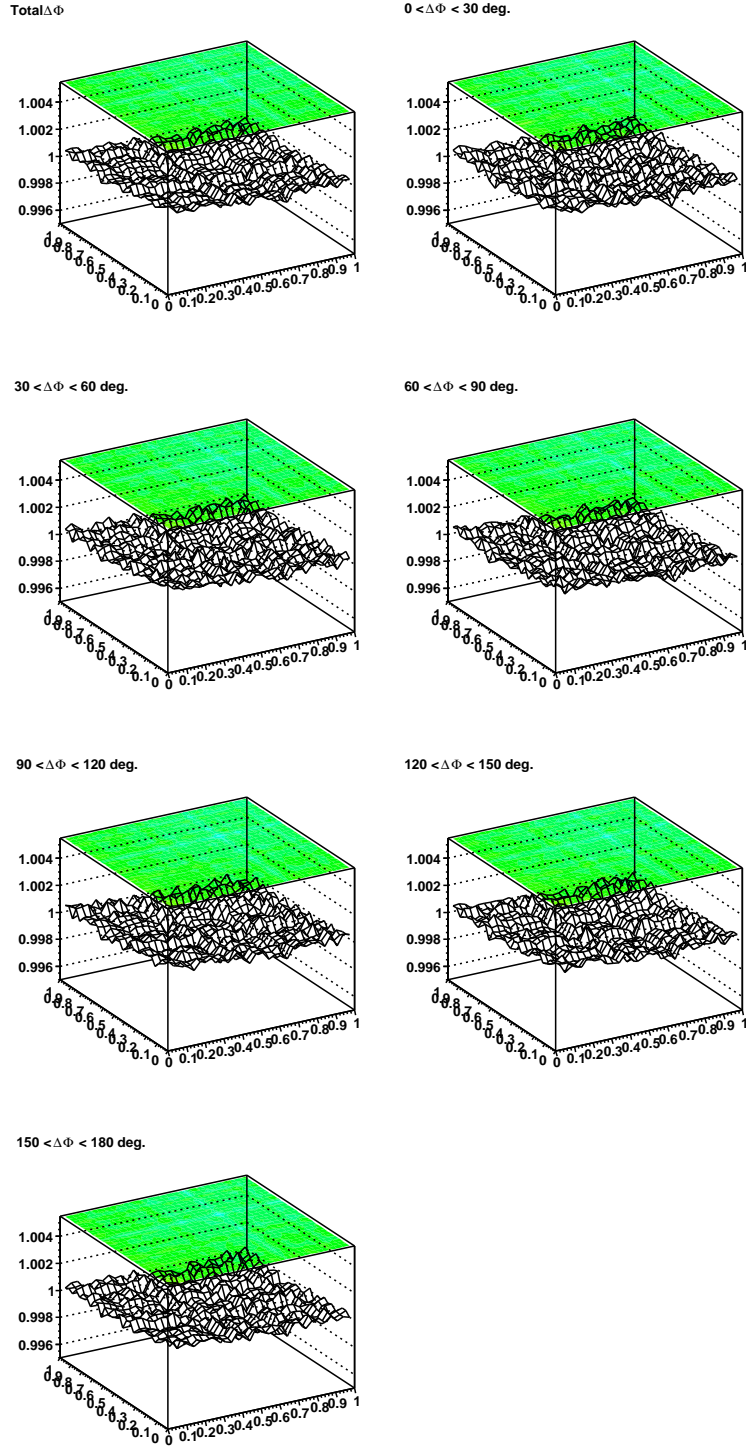


Figure 6.26: Two-particle correlation plots using the cumulant p_T variable x for all pairs that have only the elliptic flow expected by CERES (corrected by dividing mixed with flow versus mixed), in different $\Delta\phi$ regions.

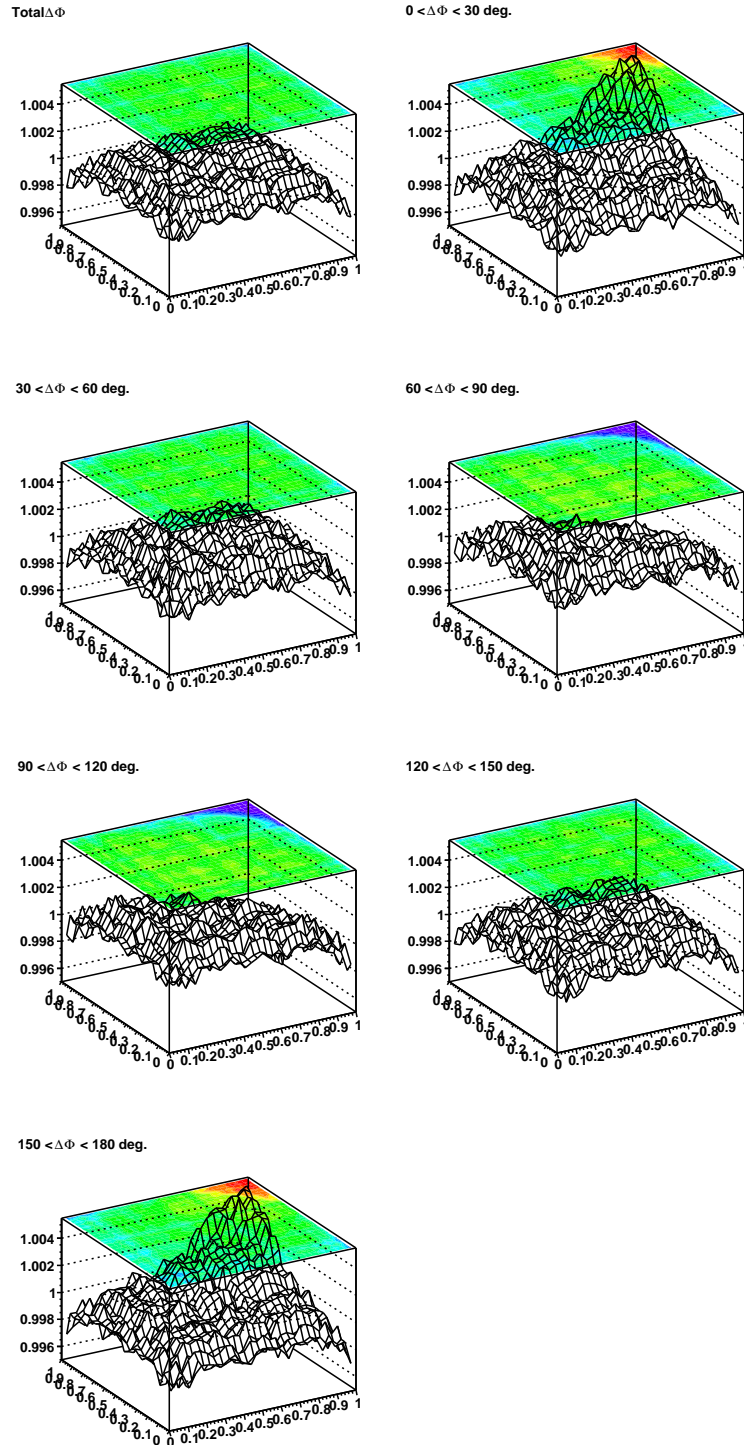


Figure 6.27: Two-particle correlation plots using the cumulant p_T variable x for all pairs that have only elliptic flow with $3v_2$, where v_2 gets the expected by CERES value (corrected by dividing mixed with flow versus mixed), in several $\Delta\phi$ regions.

6.4 Discussion

Enhanced event-by-event fluctuations of transverse momenta are considered to be one of the signatures of the vicinity to the critical point of the QCD phase transition. The fluctuations observed so far turned out to be rather independent of beam energy [45]. On the other hand, the fluctuations seem to be a non-monotonic function of centrality.

More insight into the origin of the observed fluctuations is gained by studying the average momentum correlator $\langle \overline{\Delta p_{t,1}} \overline{\Delta p_{t,2}} \rangle$ between pairs of tracks of a given opening angle. The covariance map (Fig. 6.5) reveals several structures and demonstrates that if the fluctuations were to be characterized by one single number the result would depend on the experiment's acceptance. The observed nonzero p_T fluctuations indicate that particle p_T is drawn event-wise from an effective parent distribution which deviates, as a function of $\Delta\phi$, $\Delta\eta$ and differently in each event, from the inclusive p_T distribution.

The landscape is dominated by the short range correlation peak at small opening angles, most probably originating from Bose-Einstein and Coulomb effects between pairs of particles emitted with similar velocities, and the broad maximum at $\Delta\phi=180^\circ$ which contains back-to-back correlations like those observed at RHIC and the SPS [75]. The elliptic flow measured by CERES cannot explain the observed dynamical p_T fluctuations. The non-monotonic centrality dependence of the overall fluctuations is indeed visible in the separate analysis of these two components. Since the critical point fluctuations should be present for all opening angles the best strategy seems to be to focus on the fluctuations in the region of $30^\circ < \Delta\phi < 60^\circ$, free of the influence of the two mentioned components, and where the elliptic flow cancels out. The p_T fluctuations in this region turn out to be close to zero and independent on centrality.

Concerning the observed away-side peak, we demonstrated that it comes from high- p_T correlations that cannot be attributed to the elliptic flow. The cumulative two-particle correlation study provides results that are consistent with those of the average momentum correlator $\langle \overline{\Delta p_{t,1}} \overline{\Delta p_{t,2}} \rangle$. Thus, we incline to consider the event-by-event fluctuations of mean transverse momentum mostly related to two-particle correlations.

The event and track selection criteria reduce the possible systematic bias of the measured $\langle \overline{\Delta p_{t,1}} \overline{\Delta p_{t,2}} \rangle$ values. Anyway, the remaining systematic uncertainty should be estimated varying the values of cut parameters within a reasonable range. It would also be interesting to analyze the beam energy dependence of this quantity, as well as following a similar procedure, like in case of elliptic flow, to remove Bose-Einstein and Coulomb effects and provide a ‘clean’ map from known correlations.

Part II

Chapter 7

The ALICE experiment

7.1 Introduction

ALICE (A Large Ion Collider Experiment) [152] is the dedicated heavy-ion experiment designed to exploit the unique physics opportunities which will be offered by nucleus-nucleus collisions at the LHC. ALICE is going to study nuclear matter under extreme conditions of energy density, at a centre-of-mass energy per nucleon pair of 5.5 TeV. The physics motivation is the study of QGP in a new energy regime and characterizing it in particular by so-called ‘rare probes’.

The ALICE detector is conceived as a general-purpose detector, sensitive to the majority of known observables including hadrons, electrons, muons and photons. It will allow the study of a number of specific signals in the same experiment together with global information about the events. The observables accessible include:

- global event features;
- production cross-section of J/Ψ and Υ families coupled with the measurement of D and B mesons;
- prompt photons and lepton pairs;
- cross-section of high- p_T hadrons;
- strangeness production;

- multiplicity fluctuations;
- particle correlation;
- particle ratios and transverse-momentum distributions.

The LHC will start to collide protons at $\sqrt{s} = 14$ TeV in the middle of 2007 and will provide the first heavy ion collisions (Pb–Pb) at the end of its first year of operation at $\sqrt{s} = 5.5$ TeV.

7.2 The ALICE detector layout

The estimated high multiplicities (up to 8000 charged particles per rapidity unit), the relatively low event rate which will characterize Pb–Pb collisions at LHC and the need of a large acceptance for event-by-event analysis and HBT interferometry play a crucial role in the design of ALICE.

The strategy of ALICE is to combine a nearly exclusive measurement of particle production in the central region with spectroscopy of quarkonia state at central and intermediate rapidities and global event characterization. Therefore the experimental setup combines three major components: (a) the central barrel, contained in the L3 magnet, where most charged particles are detected including electron identification and photon measurements; (b) the forward muon spectrometer [23], dedicated to the study of muon pairs from quarkonia decays in the interval $2.5 \leq n \leq 4.0$; and (c) the forward detectors, dedicated to global event characterization based on photon and charged particle multiplicity counters and forward calorimetry.

A longitudinal view of the ALICE detector is shown in Fig. 7.1. The central barrel detectors cover $\pm 45^\circ$ ($|\eta| \leq 0.9$) over the full azimuth and are embedded in a large magnet with a solenoidal field up to 0.5 T, where the charged particle tracking is performed. Tracking starts in the Inner Tracking System (ITS), with six layers of high-resolution silicon detectors, located around the interaction point, for precision tracking and primary as well as secondary vertex reconstruction; it extends the central barrel acceptance for multiplicity measurements up to $|\eta| < 2.0$. It is followed by a large Time Projection Chamber (TPC), the

main tracking device, for momentum determination and particle identification via dE/dx . A layer of Transition Radiation Detectors (TRD), for electron identification, enhances in addition the tracking capabilities at high- p_T and is used for high- p_T triggering. Hadrons are identified via dE/dx in the TPC and ITS in the range $\sim 100 - 550$ MeV/c, and up to ~ 900 MeV/c for protons. A Time-Of-Flight array (TOF) over the TPC geometrical acceptance provides hadron identification in the intermediate p_T range, while high- p_T is covered over a limited acceptance at mid-rapidity by an array of ring-imaging Cherenkov counters, the High Momentum Particle Identification Detector (HMPID): up to 3 GeV/c for K/π and up to 5 GeV/c for p/K separation. Photons and neutral mesons are measured in the electromagnetic calorimeter (PHOS). This central barrel will be complemented at pseudorapidities of $2.5 \leq \eta \leq 4.0$ by a muon spectrometer with a dipole magnet and finally an iron wall to select muons.

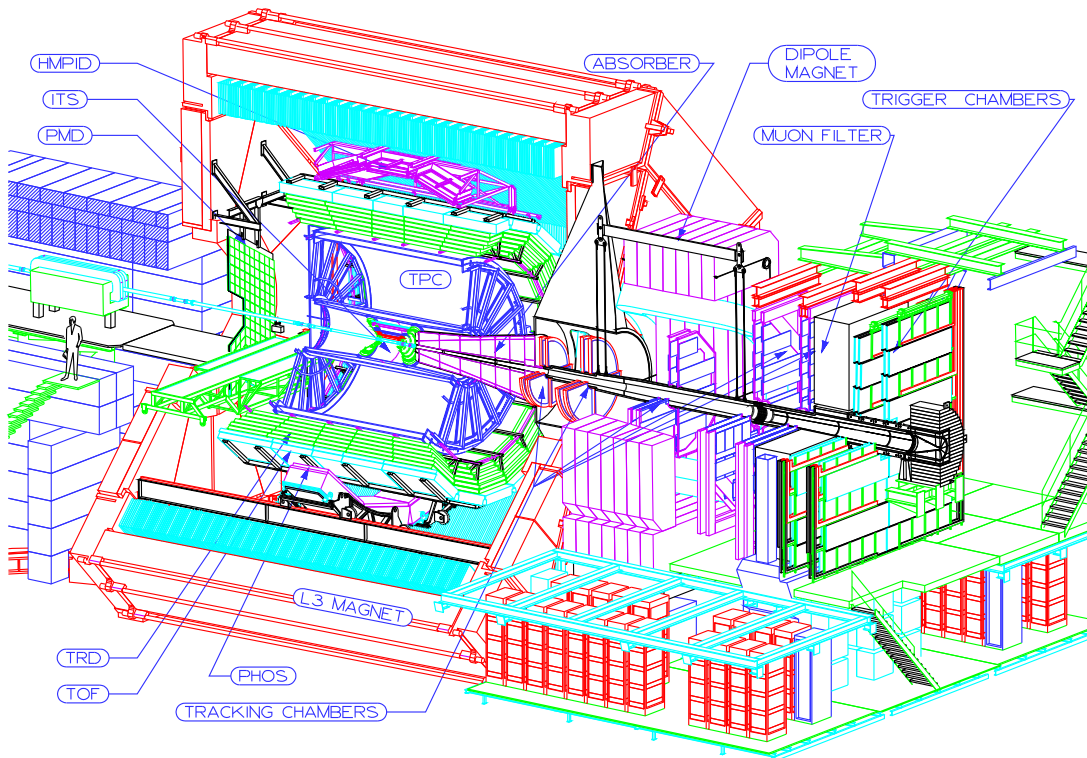


Figure 7.1: Longitudinal view of the ALICE detector.

7.3 Studies of gas properties for the ALICE central detectors

ALICE will consist of large-volume gaseous detectors which are expected to operate continuously for a long period of time. The design of these detectors is optimized with the precise knowledge of their gas properties as well as of the radiation load on their various parts.

In the next two chapters we study the drift velocity and gain in argon- and xenon-based mixtures and estimate the radiation background in the ALICE TRD.

Chapter 8

Drift velocity and gain in argon- and xenon-based mixtures

Measurements of drift velocities and gains in gas mixtures based on Ar and Xe, with CO₂, CH₄, and N₂ as quenchers, are presented. The dependence of Ar- and Xe-CO₂ drift velocities and gains on the amount of nitrogen contamination in the gas is also shown. In addition, a quantification of the Penning mechanism which contributes to the Townsend coefficients of a given gas mixture is proposed. The measured velocities are compared with calculations using the Magboltz code.

8.1 Introduction

For ionization detectors, an understanding of the motion of the electrons and ions in gases is extremely important as these factors influence many operating characteristics of the detector. For the most part, this motion is described by the classical kinetic theory of gases. In the presence of an electric field, the electrons and ions freed by radiation are accelerated along the field lines towards the anode and cathode respectively. This acceleration is interrupted by collisions with the gas molecules which limit the maximum average velocity which can be attained by the charge along the field direction. The average velocity attained is known as the *drift velocity* of the charge and is superimposed upon its normal random movement.

The *drift velocity* u_D in an electric field is given by :

$$u_D = \frac{e\tau E}{2m} \quad (8.1)$$

Where e is the charge, E is the electric field, m is the mass of the particle and τ is the mean time between the collisions. Compared to their thermal velocities, the drift speed of the ions is slow, however, for electrons this can be much higher since they are much lighter. In position sensitive ionization detectors, u_D is typically arranged to be of the order of several cm/ μ s.

The essential component in a drift chamber is usually one of the noble gases (such as argon or xenon) plus a second component, the quencher, which could be any other gas with large number of degrees of freedom, such as poly-atomic or organic compounds. The addition of a quencher fraction to a noble gas increases the macroscopic drift velocity u_D of free electrons and decreases the diffusion at a given drift field, temperature and pressure.

Modern detectors such as those being constructed for the Large Hadron Collider (LHC) include large-volume gaseous detectors which are expected to operate continuously for several months every year. The design of these detectors and their read-out electronics can be optimized with precise knowledge of the drift velocity and of the gas gain. These relevant gas parameters depend on the detector field configuration and on the gas components, composition, density, and purity.

The ALICE Transition Radiation Detector (TRD) will be used for electron identification and particle tracking in the high multiplicity environment of heavy-ion collisions at LHC. This requires accurate pulse height measurements in drift chambers filled with Xe, CO₂ (15%) gas mixture over the drift time of the order of 2 μ s. Details related to the development of the ALICE-TRD Readout Chambers as well as to the required gas mixture and its properties can be found in [85, 86]. Due to the large volume (28 m³) of this barrel detector and the high cost of xenon, the drift gas will be recirculated in a closed loop, with a modest rate of fresh gas injection. A certain fraction of contamination (O₂, N₂, H₂O) is entering into the gas volume through leaks. While oxygen can be readily removed by appropriate filters, the known methods for nitrogen removal are complex and tedious, and lead to further losses of the main gas and to the modification of its composition. The latter circumstance is particularly undesirable during data

taking periods. Thus, nitrogen gradually builds up into the mixture. After a running period of 8 months, the nitrogen content of the TRD gas rises up to 8 % and can be cryogenically distilled and removed from the mixture during the shutdown periods, at a moderate loss of xenon.

The needs of the ALICE TRD xenon-based gas mixture in terms of regeneration from nitrogen contamination are discussed in [76]. We have shown that the separation of N_2 from Xe- CO_2 mixture by cryogenic distillation performs satisfactorily. Most of the nitrogen has been successfully removed from the mixture at a moderate loss of xenon. Two existing cryogenic plants have been thoroughly tested and nitrogen levels down to 1% have been achieved. During the running time, the increasing amount of nitrogen influences the drift velocity. Therefore, systematic studies of the influence of N_2 on the gas properties become very important.

We have also performed measurements [77] of pulse height distributions in drift chambers operated with Xe, CO_2 mixtures. After studying the general behavior of these distribution under clean conditions, we have investigated the effect of oxygen and SF_6 contamination on the detection gas. A small signal loss due to attachment is seen for O_2 impurities up to a few hundred ppm. In case of SF_6 , a contamination even at the level below 1 ppm produces a dramatic loss of signal over the drift length of about 3 cm. Attachment on SF_6 is studied here for the first time concerning its practical implications for gas detectors. As the SF_6 was found accidentally in some xenon supplies, it is important to have a careful monitoring of the SF_6 contamination when precision measurements are performed using Xe-based gas mixtures in drift chambers. We have used ECD gas chromatography analysis to detect and quantify small traces of SF_6 . We have shown that measurements of ^{55}Fe signals in monitor detectors are very sensitive to SF_6 contamination, thus allowing an inexpensive in situ check of the gas quality. Thus, using xenon supplies as SF_6 -free as possible is an important requirement. In the following we used clean xenon.

The experimental set-up which is used to measure both the drift velocity and the gain of various gas mixtures, is described in the next section, followed by the measurement procedure. In section 8.3 the measured drift velocities are shown. Measurements of drift velocities in some binary and ternary Xe-based mixtures

(without nitrogen) have been published earlier [87, 88, 89, 90]. The results are compared to existing data where available and to simulations, in order to validate our method. The gain measurements, together with results from simulations, are presented in section 8.4. We finally draw our conclusions.

8.2 Experimental setup

Several methods have been described in the literature to measure drift velocities in gases [78, 79, 80, 81, 82, 83, 84]. They differ in the technique applied to generate free electrons. In some setups electrons are released from a photocathode through illumination with UV light or from radioactive β -sources, like ^{90}Sr . In recent experiments UV-laser beams are widely used to ionize molecules in the gas mixtures. The experiments also vary in the way they measure the drift time of the electrons.

In the present work, we have chosen a small drift chamber with a geometry similar to that anticipated for the final ALICE TRD [85], but with a much smaller active area ($10 \times 10 \text{ cm}^2$). The chamber has a drift region of 31.5 mm and an amplification region of 6.4 mm. The anode wires (W-Au, 20 μm diameter) have a pitch of 5 mm. For the cathode wires (Cu-Be, 75 μm diameter) the pitch is 2.5 mm. The signal is read out on a cathode plane segmented into rectangular pads of area 6 cm^2 each. The drift electrode is made of a 25 μm aluminized Kapton foil, which also serves as gas barrier. The electric field thus created is sufficiently uniform over the full active area of the pad plane. The mass flowmeters were calibrated for each gas mixture.

A schematic view of the set-up used for the drift velocity measurements is shown in Fig. 8.1. Two sets of slits, 0.75 mm wide, are machined into the stesalit side walls of the drift region and covered with Kapton foils. Electrons from a collimated ^{90}Sr radioactive source enter the drift volume through either of these slits, and ionise the gas. Some of these particles cross the corresponding slit at the other side of the drift enclosure, behind which a scintillator is placed for triggering purposes. Triggered events will show signals in the 8 pads, with a drift time corresponding, on average, to the distance from the selected set of slits to the anode plane. A 2 mm thick lead absorber is placed behind the opposite outlet

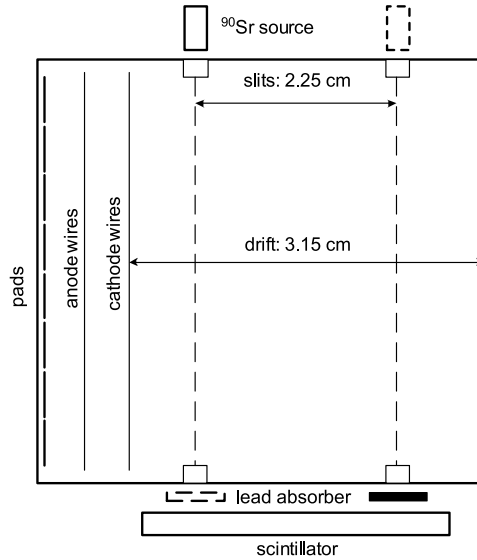


Figure 8.1: Schematics of the modified drift chamber used for the drift velocity measurements.

slit to prevent triggers from particles going at an angle through the detector. For each set of slits, we record on FADCs the pulse height distributions on the pads as a function of the drift time of the tracks. The corresponding average times are evaluated and then subtracted for a constant value of the electric field as it is shown in Fig. 8.2. Measuring the arrival time difference Δt and knowing Δx , provides $u_D = \Delta x / \Delta t$, the drift velocity component parallel to the electric field E . In this way, the contribution to the drift time of the amplification region, where the electric field is not uniform, is cancelled. The anode voltage is adjusted for each mixture to achieve a gain near 10^4 , and ranges between 1450 V and 1800 V. Both the pad plane and the cathode wires are kept at ground potential. The amplification field leaks through the cathode wire plane and effectively increases the drift field. In order to correct for this effect, the position of the 0 Volts equipotential line, relative to the position of the cathode wires, is computed with the Garfield simulation package [91] for each set of anode and drift voltages. This shift, which depends on both the drift and anode voltages, ranges in our case from 0.02 mm to 6 mm. The reduced electric field is finally evaluated taking

into account the recorded atmospheric pressure. The oxygen and water vapour in the gas was monitored during the measurements, and varied, depending on the gas flow, between 10 and 50 ppm O₂, and 300 to 500 ppm H₂O. This experimental set-up allows the determination of electron drift velocities as a function of the reduced electric field E/p with a systematic uncertainty estimated to be lower than 10 % .

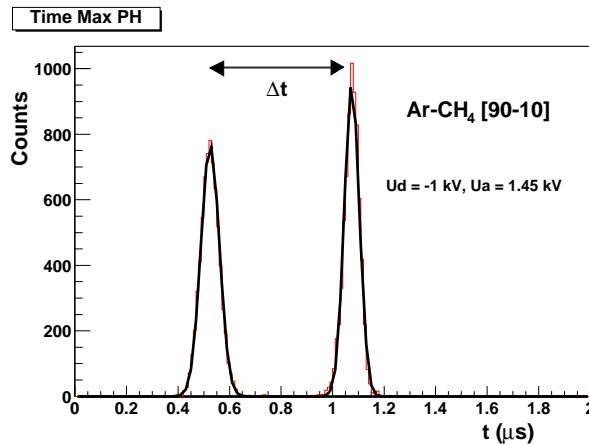


Figure 8.2: Pulse height distributions on the pads as a function of the drift time.

We use a prototype of the charge-sensitive preamplifier/shaper (PASA) especially designed and built for TRD prototypes with discrete components. It has a noise on-detector of about 2000 electrons r.m.s. and the FWHM of the output pulse is about 120 ns for an input step function. The nominal gain of the PASA is 3 mV/fC. The FADC has an 8-bit non-linear conversion and adjustable baseline, and runs at 100 MHz sampling frequency.

8.3 Drift velocity measurements

In order to check and validate how reliable is the experimental method we used, we first measured the drift velocity of a well known mixture, Ar-CH₄ [90-10], and compared our results with existing data [90] that we refer to as MIT data. We also compare the measurements with Magboltz [93] calculations. Magboltz is a simulation program, which calculates electron transport parameters such as

drift velocity, diffusion coefficients, Lorentz angle and electron energy for arbitrary values of electric and magnetic fields. Input parameters are temperature, pressure, electric and magnetic field settings and composition of the desired gas.

Our results are compared without and with the correction of the reduced field due to the leakage of the anode field into the drift region. This correction is higher at lower drift fields. As can be seen in Fig. 8.3, the agreement between this work and the calculation is good only after the correction of the drift field values. On the other hand, a clear discrepancy with the MIT data is visible at low fields, and reaches 10 %. The argon data showed no difference, within 2 %, in the results obtained from any pad, meaning that the drift field is uniform enough in the regions above the pads at the edges of the active area.

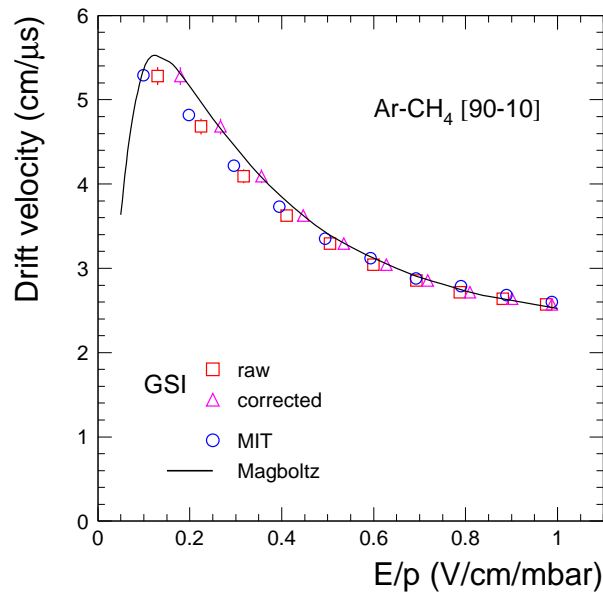


Figure 8.3: Drift velocity measurements and calculations in Ar-CH₄ [90-10]. The effect of the anode potential on the configuration of the electric drift field manifests itself (square data points) especially at low fields, and is corrected for (triangles).

In case of xenon mixtures, we should expect a significant multiple scattering of electrons coming from the ⁹⁰Sr source. To evaluate this effect, we measured the

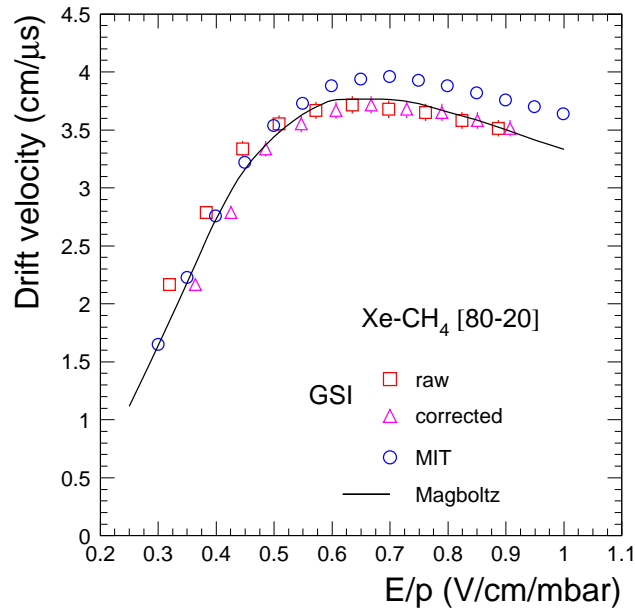


Figure 8.4: Drift velocity in Xe-CH₄ [80-20], with (triangles) and without (squares) drift field correction as measured in this work, together with other measurements and a calculation.

drift velocity of Xe-CH₄ [80-20], which the MIT group has also measured. We have observed that the multiple scattering, combined with the asymmetric gas volume available for tracks emerging from either slit, biases the measurement towards larger drift velocities by, in this case, as much as 15 %. In order to avoid that overestimation, we work with drift time distributions measured on the pad closest to the entrance slit only, for which multiple scattering is minimal. The resulting drift velocity and its comparisons are shown in Fig. 8.4.

There is again a significant discrepancy between our measurement and the MIT results at fields above drift velocity saturation. However, the calculations of the drift velocity in this region are compatible with our measurements. At low fields, on the contrary, the MIT data agree well with the calculation, whereas our results underestimate the calculated values by 7 % near 0.45 V/cm/mbar.

The next set of measurements were undertaken for Ar-CO₂ [85-15] and admixtures of 0, 10 and 20 % N₂. Adding, for example, 10 % N₂ into the mixture

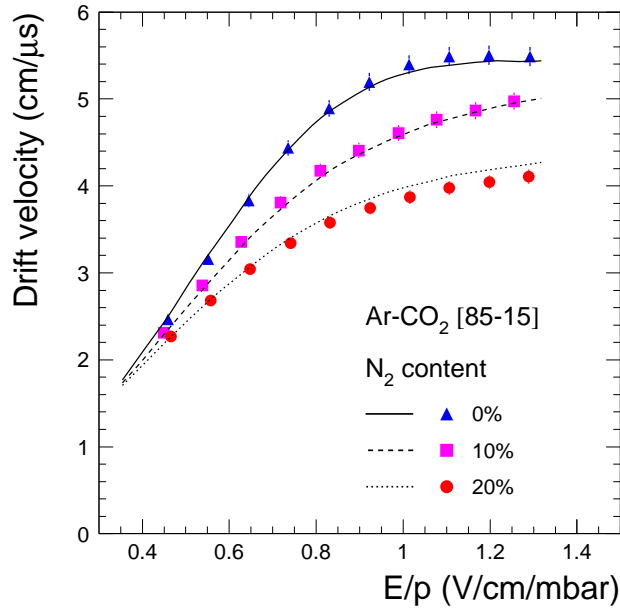


Figure 8.5: Drift velocity in Ar-CO₂ [85-15] with N₂ additions. The measurements (symbols) are compared to simulations (lines).

results in an Ar-CO₂-N₂ [76.5-13.5-10] mixture. As can be seen in Fig. 8.5, the drift velocity decreases with increasing concentration of nitrogen, and there is a reasonable agreement between measurements and simulation. Due to the saturation of the drift velocity at lower values with increasing N₂ content, keeping the drift velocity constant would require higher and higher drift voltages as the gas composition changes, and to maintain a fast mixture would eventually become impossible.

Finally, the results for Xe-CO₂ [85-15] mixtures with 0, 10 and 20 % N₂ admixtures, shown in Fig. 8.6, exhibit a weak dependence on the nitrogen concentration. We notice deviations of up to 12 % with respect to the calculations at intermediate fields. The calculated drift velocities exhibit a crossing of the three curves at a field near 800 V/cm. The measurements show very little dependence of the drift velocity on the N₂ concentration at fields up to this value. Since, for example, the anticipated electric field of the ALICE TRD is 700 V/cm, this circumstance should be welcome: no large drift velocity variation is expected due

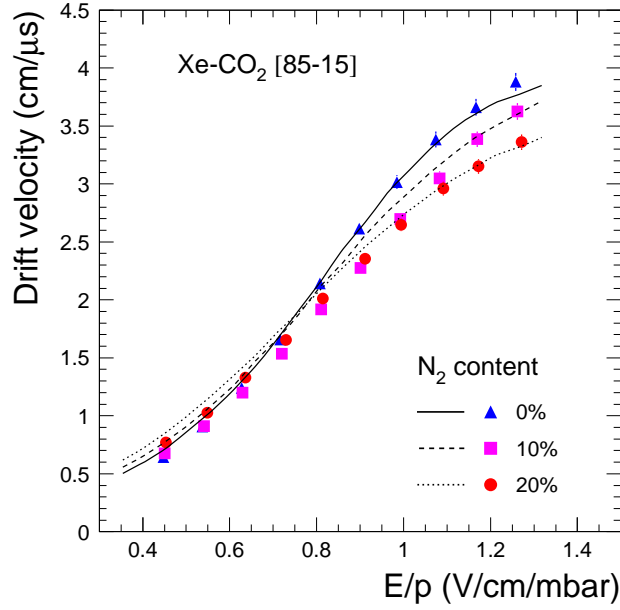


Figure 8.6: Drift velocity in Xe-CO₂ [85-15] with N₂ additions.

to substantial accumulations of nitrogen.

8.4 Gain measurements

The gain is measured with an ⁵⁵Fe source, by counting the number of signals produced by X-rays absorbed in the gas, and measuring the currents drawn by the anode high voltage power supply due to these photons. Typical rates are 60 kHz in a projected area of order 1 cm². The number of primary electrons per photon produced in the gas is derived for each mixture separately using the work functions given in [92]. The drift voltage during these measurements was set at -2 kV.

The general formula that we used to estimate the *Gain* G in an electric field is given by :

$$G = \frac{I(nA)}{Rate_{Fe}(Hz) \times Ne \times 1.6 \times 10^{-10}(nA/e^-)} \quad (8.2)$$

Where I is the measured current in the detector, $Rate_{Fe}$ the number of signals

produced by X-rays absorbed in the gas, Ne the number of primary electrons per photon produced in the gas¹ (if W is the energy needed to release a free electron and $E_{Fe}=5.96$ keV, $Ne^- = E_{Fe}/W$).

As explained above, the absolute gain as a function of the anode voltage is measured with the use of a ^{55}Fe source, which is placed in front of the entrance window of the chamber. We have also carried out calculations of the gain with the use of the package Magboltz 2 [93]. This program computes the Townsend and attachment coefficient for a given gas mixture and electric field. By introducing this information, together with the chamber geometry and voltages, into Garfield [91], one can calculate the gain of the detector for each mixture and anode voltage. The multiplication factor obtained in this way accounts for the electrons produced in the avalanche by collisions of atoms or molecules with other energetic electrons. In addition, Magboltz 2 provides information about the excited and ionised species produced in the avalanche. This information can be used to scale up the Townsend coefficients, according to the ionisation of gas species due to collisions with other excited metastable gas states (Penning effect) [94, 95, 96]. Since this energy transfer rate is a priori not known, the experimental data are used as a guide to tune one parameter, the so-called Penning fraction, for matching the calculations to the measurements. The Penning fraction refers to the amount of a given excited species which effectively ionise an atom or molecule, normalised to the abundance of such species and provided the energy balance of the process allows for the reaction. It should be noted, though, that this parameter is unique for a given gas mixture, i.e. it does not depend on the electric field nor the high voltage, and that it is expected to vary according to the characteristics of the quencher(s) and noble gas used in the mixture. In other words, the Penning transfer can be regarded as a measure of how well a quencher works: light noble gases tend, through their excited states, to ionise quenchers such as CO_2 , and therefore the Penning fraction in these mixtures are expected to be relatively large. On the other hand, heavy noble gases will tend to be ionised, probably to a lower extent, by excited molecules of certain quenchers (Penning mixtures).

¹The numbers of primary electrons for different gas components are [92] : $Ne_{Ar} = 227$, $Ne_{Xe} = 268$, $Ne_{N_2} = 169$, $Ne_{CO_2} = 179$

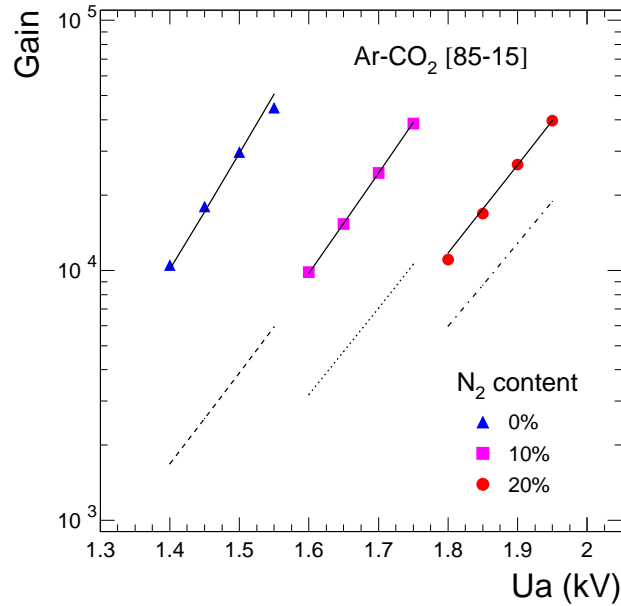


Figure 8.7: Gain in Ar-CO₂ [85-15] with N₂ additions. The dotted lines are calculations with Magboltz 2 and no Penning transfer. The tuning of the Penning transfer parameter to the data yields 37, 20, and 8 %, for 0, 10, and 20 % N₂, respectively (solid lines).

In the case of Ar-CO₂-N₂ mixtures, the suggested Penning mechanism to provide extra gain is the reaction $\text{Ar}^* + \text{CO}_2 \rightarrow \text{Ar} + \text{CO}_2^+ + e^-$, where the average excitation energy of the Ar D-levels is 14.0 eV and the ionisation potential of CO₂ is 13.773 eV. Fig. 8.7 shows the measured and calculated gain as a function of anode voltage for the three argon-based mixtures. As can be observed, after tuning of the Penning fraction to the second highest point in each curve, the slopes are properly matched by the calculations. The Penning fraction decreases from 37 % in the case of no nitrogen to 8 % when the N₂ admixture is 20 %. This means that nitrogen limits the Penning ionisation of CO₂. This effect may occur by quenching of the excited argon states by N₂ or by the occasional excitation of the nitrogen molecule thus leaving the argon atom unexcited. The highest excitation level in N₂ used in the calculations corresponds to 13.0 eV. The difference in voltage for equal gain in this series of mixtures is about 200 V, and apparently

this gap increases with the gain.

Shown also in Fig. 8.7 are the calculated gains with no Penning effects, which fail to reproduce the measurements. In addition, the slopes, at least for the nitrogen free case, are less steep than the experimental ones, and the disagreement of the calculations with the measurements decreases with increasing N_2 concentrations. Thus, the effect of nitrogen in this mixture, apart from lowering the gain at a given voltage, is to reduce the Penning effect by providing more effective quenching.

The case of the Xe-CO₂-N₂ mixtures is, from the Penning transfer point of view, different from argon. In this case, the highest energy level of excited Xe is 11.7 eV, insufficient to ionise CO₂. Levels in CO₂ between the Xe ionisation energy, 12.13 eV, and the CO₂ ionisation at 13.773 eV have sufficient energy to cause xenon ionisation. Unfortunately, due to the lack of data, all CO₂ excitations above 10.5 eV have been combined into a single level at 10.5 eV [97, 98] in the simulation program. This does not exclude an analysis similar to the previous mixture since only a fraction of the excitation of the 10.5 eV level representing levels above 12.13 eV are used in the simulation. In conclusion we assume that the Penning transfer occurs from CO₂^{*}(10.5) onto ionisation of xenon. The effect of N₂ on the Xe-CO₂ mixture is quite complex. There are possible energy transfer channels from CO₂^{*} to N₂ as in the Ar-CO₂ mixture but also from N₂^{*} to ionisation of Xe. The nitrogen excited states are produced less copiously than the CO₂ excited states according to calculations done with Magboltz 2. Therefore as an approximation we assume the dominating transfer is from CO₂^{*} to Xe.

As can be seen in Fig. 8.8, the experimental gain measurements, and the calculations performed under these assumptions, give an approximately constant Penning fraction (22 %). All slopes are correctly reproduced, with and without Penning transfer. The voltage gaps between the curves is about 50 Volts. The deviation of the data from the calculation -tuned at the middle point of each curve- at high gains is probably an indication of space charge effects within the amplification region due to the high X-ray rates. It is interesting to note that this measured deviation from exponential behaviour seems to decrease with increasing N₂ concentration, probably due to the higher anode fields involved. This also implicates space charge as the cause.

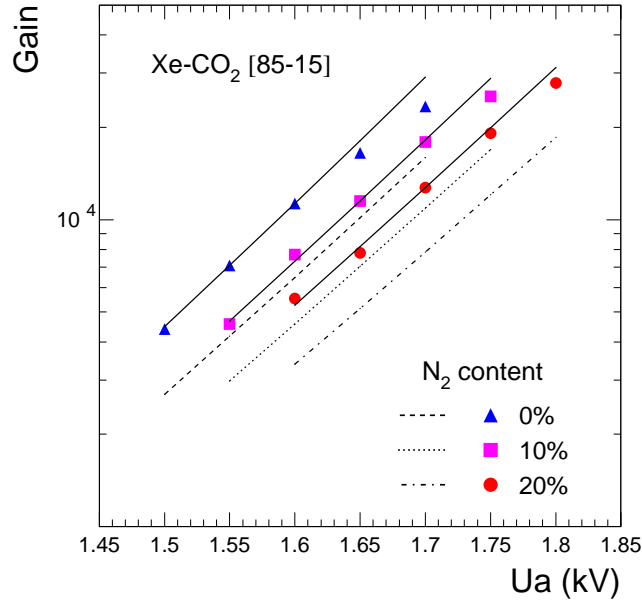


Figure 8.8: Gain in Xe-CO₂ [85-15] with N₂ additions. The tuned Penning transfer rates are 24 % for the N₂-free mixture, and 22 % for the mixtures with N₂.

8.5 Conclusions

Drift velocity and gain measurements have been performed for a number of gas mixtures in order to assess the effect of nitrogen admixture in the gas. In particular, the drift velocity measurements presented in this work show a reasonable agreement with calculations performed with Magboltz, although significant discrepancies are clearly visible in some cases. Our measurements have been corrected for the effect of the amplification field leaking between the cathode wires. The effect of the multiple scattering of sub-MeV electrons in xenon has been reduced to a negligible level. In the case of Xe-CO₂ mixtures, the variation of the drift velocity as a function of the N₂ admixture turns out to practically vanish at fields below 800 V/cm.

Gain measurements have been performed with mixtures with CO₂ and admixtures of N₂. A phenomenological quantification of the Penning mechanism, namely further ionisation from excited species formed in the avalanche, has been

proposed and calculated with the Magboltz 2 simulation program. The measured gain curves are only reproduced by the calculations including this mechanism. Penning transfer is somewhat inhibited by the presence of N_2 in the argon-based mixtures. In the case of the heavier xenon mixtures, the role of N_2 in this respect seems to be negligible. The results can also be found in [99].

Chapter 9

Background in the ALICE TRD based on FLUKA calculations

ALICE, the dedicated heavy-ion experiment at the CERN LHC, will study a variety of colliding systems ranging from pp and pA to light and heavy nuclei. The main focus of the experiment is to study central Pb–Pb collisions at nucleon-nucleon center-of-mass energy of 5.5 TeV which are expected to result in very high particle multiplicities and a luminosity of $10^{27} \text{ cm}^{-2}\text{s}^{-1}$.

Due to such experimental conditions a high background of thermal neutrons is expected to build up as the particles shower and get stopped in the material of the detectors, magnets, support structures and in particular in the concrete of the experimental cavern.

The Transition Radiation Detector (TRD) is located in the ALICE central barrel inside the solenoidal L3 magnet and will be used for electron identification and triggering on high p_t particles. It consists of 6 layers of Xe gas with a total volume of 27.2 m^3 in the sensitive part of the detector (see chapter 8). Some of the Xe natural isotopes have resonance peaks with very high neutron capture cross-sections (up to 50 kbarn) that lead to multi-gamma deexcitation cascades which can then produce low energy electrons through Compton scattering in the Xe gas, photo-effect and conversion to electron-positron pairs. These electrons will thus create an event uncorrelated background during the active gating time of the TRD readout chambers which is $3 \mu\text{s}$. The aim of the present study is to estimate the level of this background. The simulations were based on the FLUKA interaction

and transport Monte Carlo code as it provides the best treatment of low energy neutron transport. The energy and intensity of gammas produced by thermal neutron capture in Xenon must be known in order to simulate the background in the ALICE TRD detector. Because such information is missing from the available evaluated nuclear data files, it has been necessary to reconstruct it by comparing the few existing experimental data with a NNDC database of adopted energy levels. An algorithm based on the resulting data has been implemented in the FLUKA code to simulate the full gamma cascade in all stable Xenon isotopes. The estimation of the steady state hit rates from late neutrons in the ALICE TRD detector and the effect of the thermal neutron capture in Xenon in the radiation background are presented. In addition, neutron fluences and the energy deposition in the TRD are calculated as well as the induced radioactivity of the active gas system of ALICE TRD.

9.1 Radiation transport code (FLUKA)

The FLUKA program [100, 101] is well-established in studies of cascades induced by high-energy particles in matter. Hadronic and electromagnetic cascades can be simulated from TeV energies down to keV energies (except neutrons which can be transported down to thermal energies). Hadron inelastic interactions are described in FLUKA by three models depending on the energy. Above 4 GeV the dual parton model is used [102]. Between 2.5 GeV and 4 GeV a resonance production and decay model is employed [103], modified to take into account correlations among cascades particles and nuclear effects. Between 20 MeV and 2.5 GeV the pre-equilibrium-cascade model (PEANUT) [104] is used. All three models include evaporation and gamma deexcitation of the residual nucleus [105, 106]. Light residual nuclei are not evaporated but fragmented into a maximum of 6 bodies according to a Fermi break-up model. FLUKA has been benchmarked against experimental data over a wide energy range for both hadronic and electromagnetic showers [107, 108, 109, 110].

FLUKA is used for the radiation environment simulations of ALICE. It has a full treatment of low and high energy nuclear, hadronic and electromagnetic physics processes and provides similar accuracy for the radiation due to hadrons,

muons, electrons, photons and low energy neutrons. Some FLUKA features which are of main importance for our studies are:

- Hadron-hadron and hadron-nucleus elastic and inelastic interactions from 20 MeV up to 20 TeV including evaporation, gamma nuclear deexcitation and Fermi breakup.
- Pre-equilibrium cascade model for inelastic interactions below 1.3 GeV and for capture reactions.
- Electromagnetic and μ interactions in the range 0-100 TeV including pair production, Bremsstrahlung, multiple Coulomb scattering, magnetic field transport and delta ray production.
- Particle transport for all stable hadrons, e^\pm , muons, photons.
- Neutron multigroup transport and interactions in the range 0-20 MeV.
- Neutron capture reactions with explicit photon emission.
- Accurate and detailed ionization energy loss.
- Efficient model for multiple scattering for all charge particles based on Molière's theory.

Although the thermal neutron group of FLUKA ranges from 10^{-5} eV to 0.414 eV, the corresponding cross sections have been averaged over a Maxwellian spectrum with the most probable energy at 0.025 eV corresponding to a room temperature of 293 K. Anti-neutron transport is stopped at 50 MeV, which is dictated by the available cross-section data. The transport cut for charged hadrons was set to 10 keV. Energy cuts for electromagnetic particles are more problematic, because of the increase of computing time when the cuts are set too low. Therefore the energy thresholds for electrons and photons were set to 50 keV and 30 keV, respectively.

9.1.1 Radiation units used in FLUKA

In radiation background calculations, the rates of particles in a given detector region are quantified in terms of *flux*, or *current*. These two quantities have the dimensions of number/unit-time/unit-area, but they do not have the same meaning. *Flux* counts the rate of arrivals per unit area independent of the particle direction and its real physical meaning is that of path density, whereas *current* counts the rate crossing through a given plane, referred to area elements in the surface of the plane.

The importance of flux is that if one considers lengths in mean free paths for a given reaction, then the path density is just equal to the reaction density. *To measure lengths in mean free paths* means to multiply the lengths in cm by the cross section and by the atom density. Thus, every time we want to score a quantity which is proportional to any effect which has a cross section, or a mean free path, we must score flux. Current is meaningful only for counting particles independent of any effect they may produce in matter.

In FLUKA *flux* is defined either as the track-length of a particle per unit of volume, or as the number of particles hitting a sphere of unit cross-section per unit time and its unit can be expressed as ($\text{cm}^{-2}\text{s}^{-1}$). *Fluence* is the time integral of flux expressed in units of (cm^{-2}). Only in the special case of normal incidence on a flat surface the flux is equal to the number of particles crossing a unit surface. For particles arriving at an angle to a flat surface the flux is the number of particles crossing a unit surface per unit of time weighted by $(1/\cos\theta)$, where θ is the angle with respect to the normal of the surface [111].

A *star* is a hadronic inelastic interaction (spallation reaction) at an energy higher than a user-defined threshold (or by default higher than the transport threshold of the interacting particle). Star scoring (traditionally used in most high-energy shielding codes) can therefore be considered as a form of crude collision estimator: multiplication of the star density by the asymptotic value of the inelastic nuclear interaction length gives the fluence of hadrons having energy higher than the current threshold.

Selecting star scoring is meaningful for hadrons, photons and muons (if their energy is sufficiently high). Any other particle will not produce any star. More-

over, in FLUKA stars do not include spallations due to annihilating particles. The results are expressed in stars/cm³/primary particle.

The scoring by regions enables the calculation of the *energy deposition* in different detectors represented by different regions. Energy deposition is expressed in GeV/cm³/primary particle. To obtain *doses* (in Gy per unit primary particle), the results must be multiplied by $(10^{12} \times e / \rho \times V)$, where ρ is the material density in g/cm³, e the electron charge in C and V the volume of the region in cm³. The fluence of charged particles and the absorbed dose, are correlated for a given particle type and energy in a given medium. Assume a minimum ionizing particle passing through an object and interacting only by dE/dX energy loss due to ionization. The damage will depend on accumulated track-length, even in the case of very thin detectors, and the damage scales with the flux, since the accumulated track-length does not depend on orientation. For charged particles, track-length is proportional to the energy deposited ($E_{\text{dep}} = L \times S$, where L is the tracklength and $S = dE/dX$ is the stopping power).

To sum up, star density by producing particle and region as well as energy deposition by region, total or from electrons/photons only can be scored. Moreover, fluence and current scoring as a function of energy can be done via boundary-crossing, collision and track-length estimators coincident with regions or region boundaries.

9.2 Implementation of Xenon capture gammas in FLUKA

The ALICE Transition Radiation Detector (TRD) [112, 113] will be a 6-layer barrel detector surrounding the interaction point at radial distances from 2.9 to 3.7 meters. Each layer will include radiator and a drift chamber filled with a gas mixture containing 85% of Xenon.

The TRD has been designed to provide a separation of pions and electrons with momenta larger than 0.5 GeV/c, based on Transition Radiation (TR) photons which are produced by electrons when traversing the radiator. Such photons, with typical energies between 4 and 30 keV, have an absorption length of the

order of 1 cm in Xenon at STP.

Nominal rejection factors for pions have also been measured experimentally [114] in test beams with prototype and real size detectors [115, 116, 117], but the actual separation power will depend in a complex way on the intensity, composition and time structure of the radiation background which will be present in the real LHC environment.

To predict the characteristics of such background, accurate Monte Carlo simulations are needed, taking into account the particles issued from the initial collision as well as their secondaries, and the interaction of the latter not only with the different parts of the experiment but also with the accelerator structure and with the concrete walls of the tunnel.

Some of the secondaries are neutrons which become thermalized by repeated scattering in the surrounding structures and after a relatively long time (typically several milliseconds) are eventually captured by a nucleus. The resulting nucleus is left in an excited state, generally about 7 or 8 MeV above the ground level, and de-excites by releasing its excitation energy as a cascade of gamma rays. These interact in turn by releasing electrons and producing a signal uncorrelated with the initial particles. Such noise, which tends to hide the signal of the particles issued directly from the collision, needs to be evaluated by detailed Monte Carlo calculations.

9.2.1 Neutron transport and (n,γ) reactions in FLUKA

In the FLUKA Monte Carlo program [100], the transport of neutrons with energies lower than 20 MeV is performed by a multigroup algorithm. In the standard FLUKA cross-section library [118], the energy range up to 20 MeV is divided into 72 energy groups of approximately equal logarithmic width, one of which is thermal. The angular probabilities for inelastic scattering are obtained by a discretization of a P5 Legendre polynomial expansion of the actual scattering distribution which preserves its first 6 moments.

In general, gamma generation (but not transport) is also treated in the frame of a multigroup scheme. A so-called “downscattering matrix” provides the probability, for a neutron in a given energy group, to generate a photon in each of 22

gamma energy groups, covering the range 10 keV to 20 MeV. With the exception of a few important gamma lines, such as the 2.2 MeV transition of Deuterium, the actual energy of the generated photon is sampled randomly in the energy interval corresponding to its gamma group. Note that the gamma generation matrix does not include only capture gammas, but also gammas produced in other inelastic reactions such as (n,n') .

The gamma generation probabilities, as well as the neutron total and differential cross sections, kerma factors and information on production of residual nuclei, are derived from Evaluated Nuclear Data Files, distributed by specialized Centres such as the NEA Data Bank [119], RSICC [120] and the IAEA [121], by processing them with an appropriate code [122]. Since several evaluated cross section sets are available, with variable degrees of completeness and reliability, an effort is constantly being made to include in the FLUKA library the best data available at a particular time. Presently, the library includes about 120 different materials (elements or isotopes, in some cases with the possible choice of different molecular bindings, temperatures or degrees of self-shielding). However, while transport cross sections are available for all materials of the library, for a few of them it has not been possible so far to find evaluated data concerning some of the complementary information (gamma production, kerma factors or residual nuclei).

As stressed above, a proper simulation of capture gammas in Xenon is an essential ingredient of any background prediction for the ALICE TRD, but unfortunately gamma generation information is missing in the Xenon entry of the FLUKA neutron cross section library, since no corresponding evaluated data have been found. However, much of the basic information is available in the form of recommended level energies, published regularly on the journal Nuclear Data Sheets and available also on-line [123]. These recommended levels have not been identified necessarily only in (n,γ) reactions, but have been derived also from experiments on beta decay, heavy ion reactions, etc. And indeed, many of them don't play any role in neutron capture because of quantum selection rules, but in most cases it is possible to select the relevant ones by a cross check with Xenon capture gamma energies reported by experimental papers and by following all the possible paths of the gamma cascade from the capture level (easily calculated by

an energy-mass balance) down to the ground state. Combining all this material together, and making some reasonable physical assumption about the information which is still missing, it has been possible to write a FLUKA subroutine providing an acceptable description of $\text{Xe}(n,\gamma)$ reactions.

A similar work was done some time ago to implement in FLUKA capture gammas from another important nuclide for which evaluated data were missing, ^{113}Cd . However, the approach has not been identical in the two cases. First, in the case of Cadmium only the most important isotope was considered, while in the case of Xenon all 9 stable isotopes have been taken into account. In addition, the type of available experimental data was different for the two elements: for Cadmium, in addition to level energies and relative intensities, gamma energies and absolute gamma ray intensities (probabilities per neutron capture) were available. However, since the existence of unobserved transitions was evident from the intensity balance, a simple deexcitation model has been applied to complete the decay scheme.

9.2.2 Basic nuclear data for Xenon

Element Xenon (atomic number 54) has 9 stable isotopes, with mass number 124, 126, 128, 129, 130, 131, 132, 134, 136 (^{124}Xe and ^{136}Xe are actually unstable, but with an extremely long half-life). Their abundances [124] and their nuclear masses [125] are reported in Table 9.1. In the same Table are reported also the atomic masses¹ of the nuclei formed by neutron capture in those nuclei.

The respective Q-values for (n,γ) reaction, as given by the formula:

$$Q = u \left({}_{54}^A M + M_n - {}_{54}^{A+1} M \right)$$

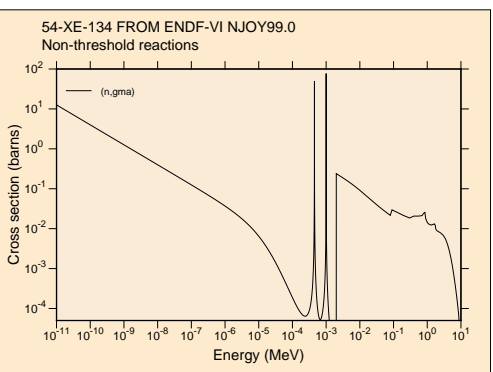
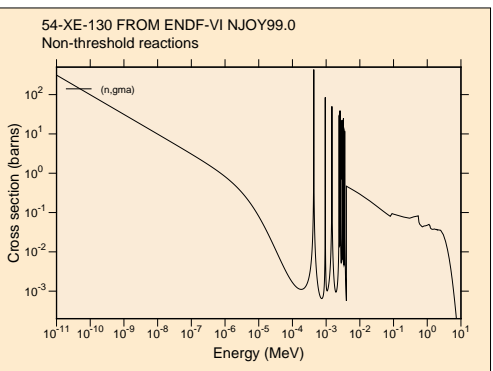
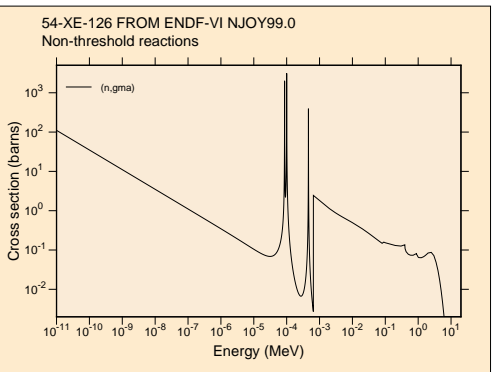
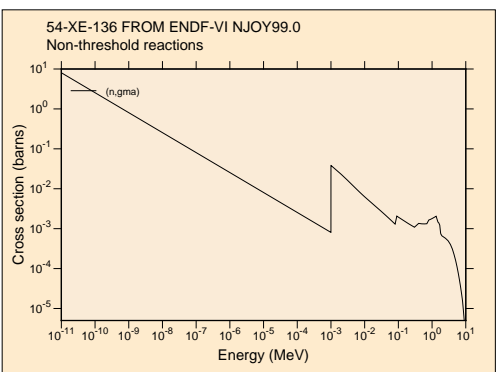
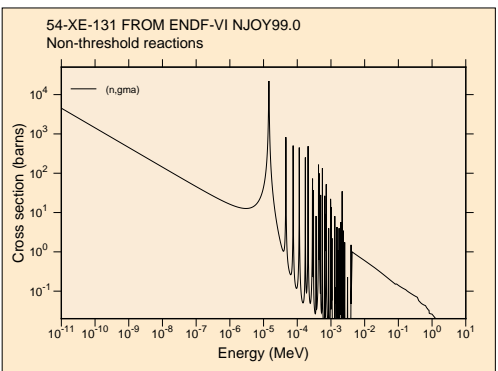
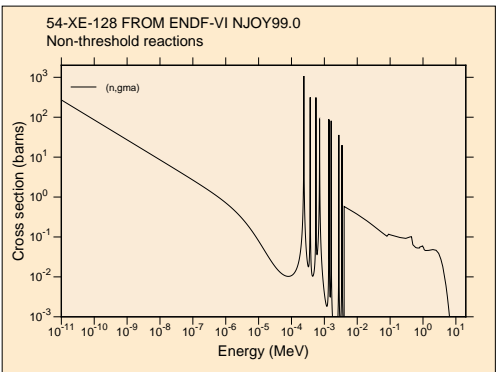
where u is the atomic mass unit (931.494013 MeV), and M_n is the neutron mass (939.56533 MeV). Plots of (n,γ) cross sections as a function of energy for the 9 natural isotopes of Xenon, derived from ENDF/B-VI files [126] are shown in Fig. 9.1.

¹The evaluated data refer to *atomic* masses, but internally FLUKA uses *nuclear* masses obtained by the latter by subtracting the electron masses and adding the electron binding energies

9.2. IMPLEMENTATION OF XENON CAPTURE GAMMAS IN FLUKA105

Xenon isotope	A ${}_{54}^A M$ (amu)	$A+1$ ${}_{54}^{A+1} M$ (amu)	Abundance %
${}^{124}\text{Xe}$	123.9058958	124.9063982	0.09
${}^{126}\text{Xe}$	125.9042689	126.9051796	0.09
${}^{128}\text{Xe}$	127.9035304	128.9047795	1.92
${}^{129}\text{Xe}$	128.9047795	129.9035079	26.44
${}^{130}\text{Xe}$	129.9035079	130.9050819	4.08
${}^{131}\text{Xe}$	130.9050819	131.9041545	21.18
${}^{132}\text{Xe}$	131.9041545	132.9059057	26.89
${}^{134}\text{Xe}$	133.9053945	134.907207	10.44
${}^{136}\text{Xe}$	135.907220	136.911563	8.87

Table 9.1: Masses and abundances of naturally occurring Xenon isotopes, and masses of the nuclei formed by neutron capture



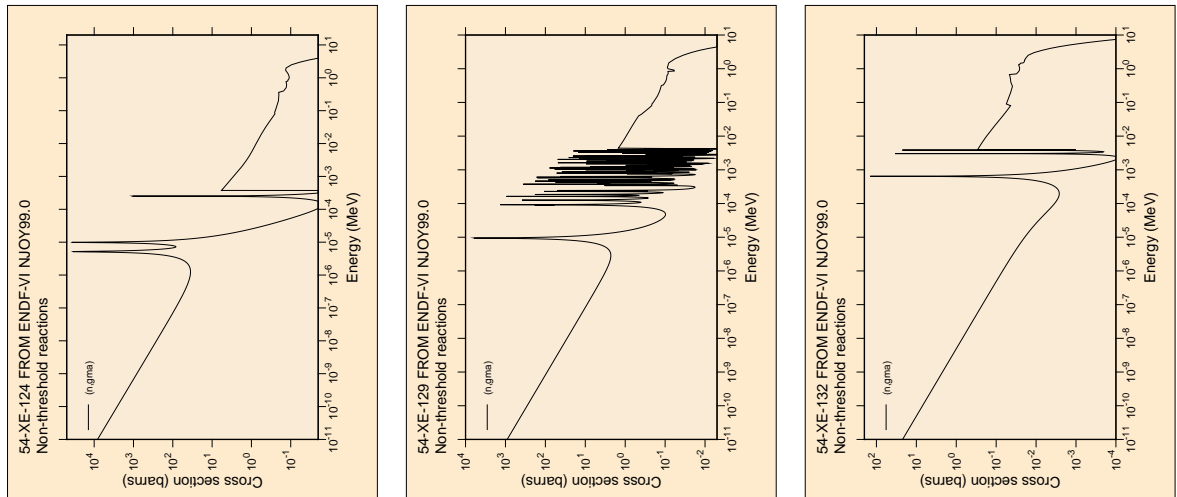


Figure 9.1: ENDF/B-VI (n, γ) cross sections of Xenon isotopes

9.2.3 Available information on energy levels

Measured and recommended values for the energy levels of all known nuclides are reported monthly on the journal Nuclear Data Sheets [127]. The same data and decay schemes can be retrieved on-line from the Evaluated Nuclear Structure Data File (ENSDF) [128]. The NuDat program [123] provided by NNDC (National Nuclear Data Center at the Brookhaven National Laboratory), allows to extract the recommended values in the form of tables which can be easily read and processed by a user program. For each level, recommended gamma energies, intensities and multiplicities are listed, as well as the level half-life and the spin and parity, when known.

These recommended levels and gamma transitions, which have been derived from a variety of nuclear reaction and decay experiments, do not include virtual

excitation levels populated by neutron capture. The energy of latter is easily calculated anyway by adding the Q-value (see Table 9.1) and the kinetic energy of the captured neutron, but the energies and intensities of gammas emitted from the virtual levels can be obtained only from published experiments on neutron capture (all rather old in the case of Xenon). Such data are reported on Nuclear Data Sheets, but exactly as they were published, without any evaluation of the gamma energies to make them consistent with the adopted energies of all other levels. Also, only measurements made on single isotopes are considered. Such experimental data are available for ^{130}Xe [129, 130], ^{132}Xe [129, 131] and ^{137}Xe [132, 133] but not for the other six Xenon isotopes.

With some difficulty, additional information can be extracted also from experimental data obtained with Xenon of natural isotopic composition. The popular “Lone-Catalog” [134] is a compilation of energies and relative intensities of capture gamma rays for all elements up to $Z = 83$. For Xenon, 161 gamma lines are reported. However, a comparison with presently recommended values and with the available single-isotope data mentioned above shows that the compilation cannot be considered as very reliable, despite the fact that it is still proposed as a reference by NNDC [135] (for a discussion of the quality of these data see [136]).

A much better source for Xenon capture gammas is a paper by Hamada *et al.* [137], where 273 gamma lines are reported. The authors have assigned some of these lines to ^{130}Xe and ^{132}Xe , but a systematic comparison with differences between adopted levels has allowed to assign practically each gamma line to one of the stable isotopes of Xenon. Several of the gamma energies reported in [137] have also been found to correspond, within small uncertainties, to transitions from the virtual level of one of the Xenon isotopes to one of the corresponding adopted levels.

9.2.4 Implementation in FLUKA

As can be understood from the previous survey of available data, it is impossible at the present time to establish a complete database of capture gamma lines for Xenon. However, a large number of gamma lines (820) have been identified, corresponding to transitions between 335 levels. More details are given in Table 9.2.

The implementation in FLUKA has been based on the relative branching ratios within each level, which are well established, rather than on the poorly known absolute intensities (number of gammas per capture) or even than on relative intensities over all levels. Gamma lines from a given level for which no relative intensity was reported were assumed to be equally distributed among the known branchings; when the intensity was expressed for instance as “< 80”, one-half of that value was assumed. In a few cases, when different transitions from the same virtual level were reported by two sources, the values were merged after a re-normalisation of intensities based on all those lines which were common to both.

The resulting database does not include explicitly gamma energies, but only level energies and, for each level, the possible transitions to lower levels with the respective cumulative probabilities. In this way, each gamma energy is obtained by difference between its starting and ending level, and exactly the same total gamma energy is emitted for any possible path of the gamma cascade from the virtual to the ground level.

Energy conservation on a more global level is ensured by calculating the recoil of the nucleus in the laboratory frame, based on an accurate balance of all masses concerned. The photon emission is assumed to be isotropic.

Of course, several approximations have been necessary. While the energy of the virtual level is calculated correctly taking into account the kinetic energy of the captured neutron, it has been assumed that the possible transitions and their relative intensities do not depend on the neutron energy. This assumption is unlikely to be valid at energies at which the reaction proceeds predominantly through p-wave capture, but a rigorous analysis to identify these energies has not been made. First of all, there is no sufficient experimental or theoretical information which would allow to establish different transitions and intensities. On the contrary, some of the published gamma transitions we have used were not obtained at thermal energies but at some resonance energy [130, 131], because this is the simplest way to study transitions in an individual isotope. But even if such information would exist, its implementation in FLUKA should take into account a different situation for each of the 9 Xenon isotopes, making the database and the dedicated routine exceedingly complex. Also, it could be possible to avoid

Xenon isotope	Number of levels		Number of gammas			
	adopted in NuDat	used in FLUKA	adopted in NuDat	used in FLUKA, from:		
				lower levels	virtual level	total
^{124}Xe	234	80	633	175	24	199
^{126}Xe	108	46	233	81	12	93
^{128}Xe	58	28	109	45	9	54
^{129}Xe	103	72	207	144	45	189
^{130}Xe	43	19	66	24	6	30
^{131}Xe	75	30	200	87	18	105
^{132}Xe	29	13	56	24	4	28
^{134}Xe	29	15	86	38	3	41
^{136}Xe	164	32	213	53	28	81

Table 9.2: Number of Xenon energy levels and gammas: adopted in NuDat and implemented in FLUKA

the problem by implementing gamma production only for thermal neutrons and epithermals with energies lower than any resonance, but it has been judged better to produce some gammas with the wrong energy or probability rather than producing none at all: at least, the total excitation energy will be correctly accounted for as gamma radiation and the overall energetic balance will be satisfied.

On the other hand, the implementation would be too grossly incorrect — or too complicated to do correctly — if it would extend also above the threshold for inelastic neutron scattering. Therefore, an upper limit of 39 keV (isotope-independent for the sake of simplicity) has been set for the energy of any neutron which can be captured in with gamma emission in Xenon. Table 9.3 shows the different thresholds for (n,n') reaction in Xenon isotopes, obtained from the ENDF/B-VI evaluated file [126].

It is also possible, as it was found in the case of Cadmium, that not all transitions from the virtual level have been identified. However, too little information is available for Xenon concerning absolute gamma emission probabilities. Therefore, no attempt has been made at filling gaps of unknown size.

Xenon isotope	Q (MeV)	nuclide ${}^A_{54}\text{Xe}$	Q (MeV)	nuclide ${}^A_{54}\text{Xe}$	Q (MeV)
${}^{124}\text{Xe}$	-0.357	${}^{129}\text{Xe}$	-0.040	${}^{132}\text{Xe}$	-0.668
${}^{126}\text{Xe}$	-0.389	${}^{130}\text{Xe}$	-0.536	${}^{134}\text{Xe}$	-0.847
${}^{128}\text{Xe}$	-0.443	${}^{131}\text{Xe}$	-0.080	${}^{136}\text{Xe}$	-1.313

Table 9.3: Q-values for neutron inelastic scattering in the naturally occurring isotopes of Xenon

9.2.5 Discussion

Despite the approximations which have been described above, the new FLUKA description of capture gammas from neutron capture in Xenon should give better results than the default multigroup description used for most FLUKA materials. The energy of each photon is determined as the exact difference between two energy levels, instead of being sampled randomly in a certain energy interval; but — even more important — the correlations between photons emitted by the same excited nucleus will be reproduced correctly in most cases. This should be of a particular interest for the simulation of the high-energy physics detector which has triggered this work.

Extensions of the present approach to other nuclides are possible, provided that good data on the transitions from the virtual levels are available. Otherwise, it will be necessary to derive them from a physical model, similar to what has been done for ${}^{113}\text{Cd}$. However, if the number of nuclides considered should increase beyond a certain limit, it could be preferable in future to read the level data from an external data file, rather than having them hard-wired in a routine specific for each element.

By following each possible sequence of level transitions and compounding the product of their respective probabilities with the abundance and with the relative capture cross section of the isotope concerned, it is possible to calculate an absolute intensity for each gamma produced. The 689 gamma energies having an intensity larger than 10^{-3} per 100 neutron captures are reported in an ALICE Internal Note [145] (see appendix B). Here the 28 most intense ones are shown

9.2. IMPLEMENTATION OF XENON CAPTURE GAMMAS IN FLUKA111

in Table 9.4.

Two different tests were done. In one test, many neutron captures in a quasi-infinite Xenon volume were simulated, and the length of the photon tracks versus the photon energy was scored. All the photons produced travelled some distance before being captured or escaping. So, for each capture we get all the energies of the transition tree. In addition, we get also tracks of photons which had been scattered and therefore had not the initial energy anymore. In the second test, we did not do any simulation, but simply traversed each branch of the tree in a separate program. There was no transport, but just a check of all possible transition combinations.

Fig. 9.2 shows a gamma line spectrum obtained in a standalone test of the new FLUKA routine which generates capture gammas in Xenon. The input neutrons energies were randomly sampled from a Maxwellian distribution in the energy range 10^{-5} to 0.4 eV, corresponding to the thermal neutron group of FLUKA and the target nucleus was sampled according both to its abundance and to its thermal neutron capture cross section. As it can be expected from Table 9.4, the most frequent lines belong to ^{132}Xe (667.72, 772.60, 1317.93 and 6466.07 keV, the latter corresponding to a transition from the capture level). The 536.09 keV line is from ^{130}Xe .

A test of the new routine has been done also with a FLUKA run in an idealized geometry: an isotropic 0.025 eV neutron point source in the middle of an “infinite” cube of Xenon. Fig. 9.3 shows the calculated track length of photons as a function of photon energy. Comparing this spectrum with that of Fig. 9.2, the following differences can be noticed:

- the presence of a high 511 keV peak, due to positron annihilation
- a progressive decrease of the gamma line intensity with decreasing energy, due to increasing absorption by photoelectric effect
- a broad Compton background, hiding most of the lower energy lines

Real situations should be more complex, of course, since neutron capture in surrounding structural materials would provide additional gammas of different energies and would even be probably dominant. But, due to the high

energy of most capture gammas and to their ability to create electron pairs, the largest contribution can still be expected to be that of the annihilation peak.

Appendix: Preparation of FLUKA input

To activate the new scheme of capture gammas in Xenon, two things are required. Command LOW-NEUT must be issued with `WHAT(6) = 1.0` (or 11.0 if a special fission biasing is also requested), and material XENON must be defined as a `COMPOUND`, consisting of its 9 natural isotopes with the respective abundances (see Table 9.1). Single-isotope materials are defined by setting `WHAT(6) =` the mass number of the isotope in the corresponding `MATERIAL` command.

Example (note the compulsory names of the 9 isotopes as they are now defined in the neutron cross section library):

```
*...+...1...+...2...+...3...+...4...+...5...+...6...+...7...+...
LOW-NEUT      72.0    22.0  0.0196    0.0    1.0    1.
MATERIAL      54.0   123.9 5.4854E-3  26.0    0.0   124. 124-XE
MATERIAL      54.0   125.9 5.4854E-3  27.0    0.0   126. 126-XE
MATERIAL      54.0   127.9 5.4854E-3  28.0    0.0   128. 128-XE
MATERIAL      54.0   128.9 5.4854E-3  29.0    0.0   129. 129-XE
MATERIAL      54.0   129.9 5.4854E-3  30.0    0.0   130. 130-XE
MATERIAL      54.0   130.9 5.4854E-3  31.0    0.0   131. 131-XE
MATERIAL      54.0   131.9 5.4854E-3  32.0    0.0   132. 132-XE
MATERIAL      54.0   133.9 5.4854E-3  33.0    0.0   134. 134-XE
MATERIAL      54.0   135.9 5.4854E-3  34.0    0.0   136. 136-XE
*
MATERIAL      0.0     0.0 5.4854E-3  35.0    0.0    0. XENON
COMPOUND     -0.09   26.0  -0.09   27.0   -1.92   28. XENON
COMPOUND    -26.44   29.0  -4.08   30.0  -21.18   31. XENON
COMPOUND    -26.89   32.0 -10.44   33.0   -8.87   34. XENON
```

9.2. IMPLEMENTATION OF XENON CAPTURE GAMMAS IN FLUKA113

Xenon isotope	Gamma energy (keV)	From level (keV)	To level (keV)	I_γ per 100 captures
^{132}Xe	667.72	667.72	0.0	64.73
^{132}Xe	6466.1	8935.2	2469.1	24.07
^{132}Xe	772.61	1440.3	667.72	22.55
^{130}Xe	536.09	536.09	0.0	16.60
^{132}Xe	1317.9	1985.7	667.72	15.88
^{132}Xe	6379.8	8935.2	2555.4	10.66
^{130}Xe	668.52	1204.6	536.09	10.25
^{132}Xe	483.46	2469.1	1985.7	9.824
^{132}Xe	600.03	2040.4	1440.3	8.355
^{132}Xe	5754.4	8935.2	3180.8	7.847
^{132}Xe	569.75	2555.4	1985.7	7.196
^{132}Xe	1028.8	2469.1	1440.3	6.778
^{132}Xe	1887.7	2555.4	667.72	6.404
^{125}Xe	111.78	111.78	0.0	6.344
^{132}Xe	1140.4	3180.8	2040.4	6.278
^{130}Xe	739.48	1944.1	1204.6	5.859
^{132}Xe	5142.9	8935.2	3792.3	5.783
^{132}Xe	1801.4	2469.1	667.72	5.501
^{130}Xe	752.79	2696.9	1944.1	5.344
^{130}Xe	275.45	2972.3	2696.9	5.225
^{130}Xe	720.84	3693.2	2972.3	4.921
^{125}Xe	140.82	252.60	111.78	4.608
^{132}Xe	630.20	1297.9	667.72	4.384
^{132}Xe	8267.5	8935.2	667.72	4.323
^{132}Xe	5235.7	8935.2	3699.5	4.186
^{130}Xe	854.99	2059.6	1204.6	3.992
^{125}Xe	57.940	310.54	252.60	3.917
^{130}Xe	315.60	2375.2	2059.6	3.666

Table 9.4: Number of gammas per 100 thermal neutron captures in ^{nat}Xe

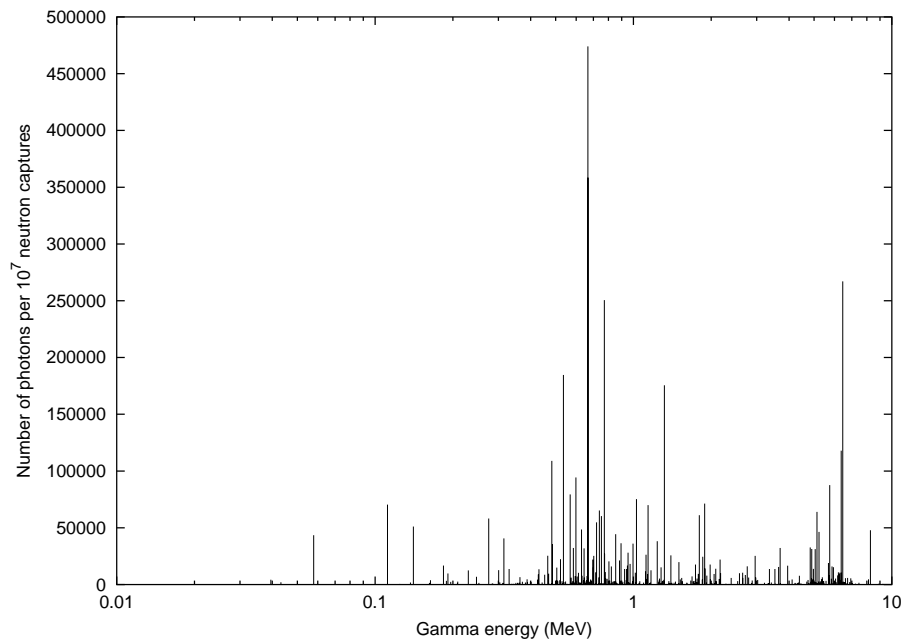


Figure 9.2: Gamma lines generated in 10^7 neutron captures in Xenon

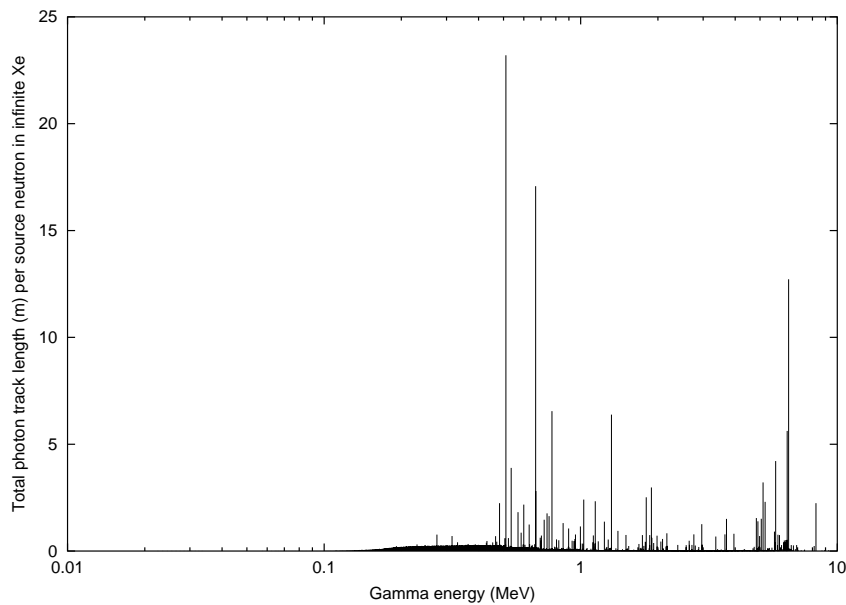


Figure 9.3: Photon track length spectrum calculated by FLUKA for a thermal neutron source in an infinite Xenon volume

9.3 Background from thermal neutrons

9.3.1 Description of the detector geometry and material

FLUKA uses the combinatorial geometry in order to describe general three dimensional material configurations by considering unions, differences and intersections of simple bodies such as spheres, boxes, cylinders, etc. A flexible tool, the ALIFE [139] editor and parser, was developed in ALICE, to facilitate the preparation of the FLUKA input cards which are used to define the geometry, material, as well as tracking and scoring options.

The ALICE experimental area as simulated in FLUKA is shown in Figs. 9.4 and 9.5. All lines represent boundaries between different materials as used in the calculations. The geometry [140] is described in a right handed orthogonal system with origin at the ALICE interaction point, the x -axis vertical, the y -axis pointing towards the centre of the LHC ring and the z -axis along the beam direction.

About 3200 volumes and 1500 regions are needed to describe the ALICE detector and experimental area including the cavern, tunnels, vertical shafts, shielding, inner triplet and separation dipoles, surrounding hall, beam elements and the ALICE detectors racks. Since the aim is to study the background all detectors were described with the appropriate accuracy and correct amount of material on average; however not in the detail required for tracking performance studies and as implemented in AliRoot [141], the Geant [142] based simulation of the experiment. Particle back-scattering in the concrete walls of the caverns and shafts is taken into account by approximating the walls by a 30 cm layer of concrete. Regions behind this layer are treated as ‘black-holes’, i.e. as regions that absorb all particles that enter them. Magnetic fields were taken into account in five different parts of the geometrical setup: the L3 magnet, the muon spectrometer, the dipole magnet compensating the field in the muon spectrometer, the inner quadrupole triplet and separation/recombination dipole magnet D1.

The TRD layout as described in FLUKA is shown in Fig. 9.6. It is approximated by 6 sets of concentric cylindrical layers each one of them consisting of 9 layers of different materials with thickness summarized in Table 9.5 in accordance with the description of the detector in the TRD TDR [113].

Table 9.5: The FLUKA materials in the TRD and their thickness.

FLUKA materials in the TRD	Thickness (cm)
Air	3.923
Polyethylene (Rohacell)	4.8
Mylar	0.005
Xenon	3.5
Copper	0.001
Read out (G10)	0.06
Signal lines (Copper)	0.005
Cooling Al (Aluminum)	0.02
Cooling Water	0.02

9.3.2 Primary event generation and scoring

The radiation environment for this study is based on minimum bias events. The parametrized HIJING event generator [143] was used to generate pions and kaons according to parametrized pseudo-rapidity η and p_t distributions.

The produced events with average multiplicity of 80 000 primary particles were used as input for FLUKA and transported through the material of the experiment and experimental area.

Boundary crossing scoring was used to estimate the number of particles that passed through the 6 Xe layers or were created there by using a user-defined boundary crossing fluence or current estimator for each of the 6 different Xe layers. All particles entering the scoring region are ‘tagged’ to avoid double counting and the particles which leave the scoring volume are ‘untagged’ so they can be detected again. In the case of electrons or

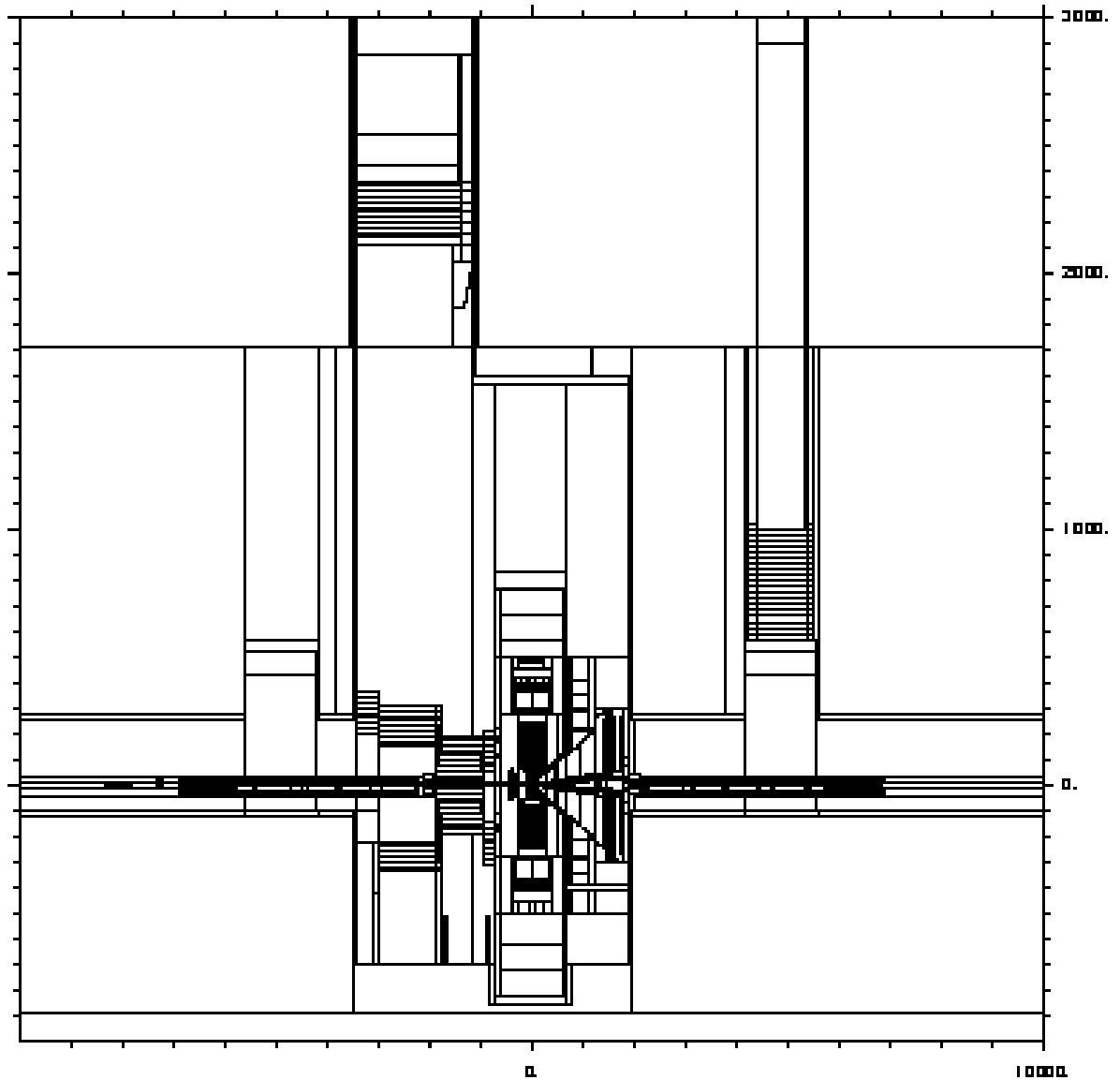


Figure 9.4: The geometry of the ALICE experimental area as implemented in FLUKA (vertical longitudinal section through the main experimental cavern UX25, the counting room shaft PX24 and the shaft PGC2).

positrons from gamma reaction it is the gamma that is actually tagged and the gamma production vertex is scored.

As low energy electrons can interact many times in the gas layer and pro-

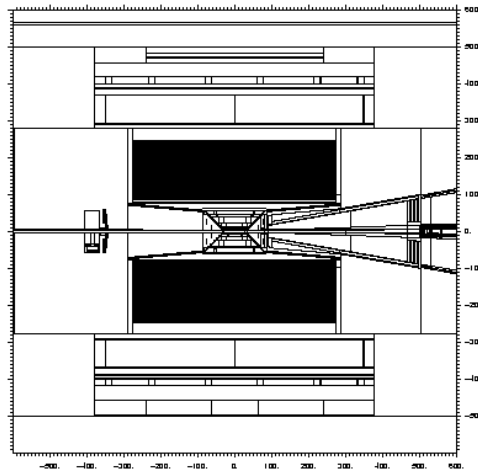


Figure 9.5: The geometry of the central detector as implemented in FLUKA (vertical cross-section).

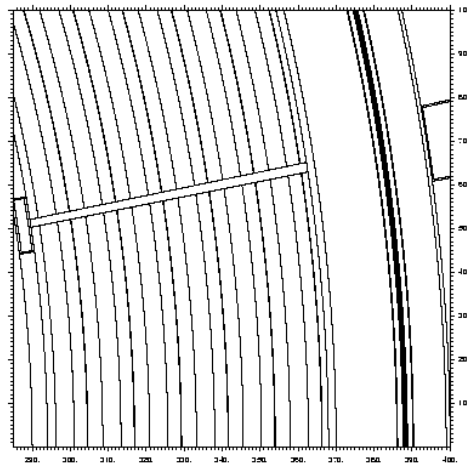


Figure 9.6: The geometry of the TRD detector as implemented in FLUKA.

duce many hits, it was necessary to optimise the electron step length by scoring the energy deposited in many steps along its trajectory. The boundary crossing estimator in conjunction with the energy deposition in steps is a sufficient way to estimate the number of electron hits and the charge deposition from the number of their tracking steps in a given detector.

9.3.3 Particle fluxes and energy deposition in the TRD, with and without neutron capture in Xenon

The way used to calculate particle fluxes in the TRD is via a special tool of FLUKA the track-length estimator. Defining 6 such estimators, each of them pointing on one Xe layer region and taking the average from them during one FLUKA event (a minimum bias event), we calculate the total track-length of electrons, photons and neutrons, normalized per source particle. The results are summarized in Table 9.6 with and without neutron capture in Xenon respectively.

Table 9.6: Total track-length of electrons, photons and neutrons, normalized per source particle with and without neutron capture in Xenon (2nd and 3rd column respectively).

Particles	Track-length (cm/primary)	
electrons	1.74±0.3	1.4±0.15
photons	57.23±2.8	47.98±2.12
neutrons	148.07±9.4	146.05±9.1

The total track-length of electrons and photons is higher **24%** and **19%** respectively taking into account the neutron capture in Xenon. The track-length is more meaningful than the number of particles, because any signal, or any damage, is proportional to the energy deposited, or to the number of collisions which are all proportional to the track-length. Dividing the total track-length with the volume of the scoring region we obtain the total response or *cumulative fluence* expressed as (particles/cm²/primary).

The results of the FLUKA track-length estimator are always given as differential distributions of fluence in energy (cm⁻² GeV⁻¹ per incident primary unit weight). In figures displaying differential fluence versus energy over a large range of energy, the abscissa is often the logarithm of energy [144]. In making the coordinate transformation from linear energy and particle-differential fluence distribution $d\Phi/dE$ to logarithmic energy, it is desirable

to preserve the fact that relative areas in different energy regions represent relative fluences. This can easily be accomplished by multiplying the conventional particle-differential fluence distribution $d\Phi/dE$ by the energy because $d\Phi/d(\log E) = d\Phi/(dE/E) = E d\Phi/dE$.

Figures 9.7, 9.8 and 9.9 are designed to allow visual integration of fluence having the areas under the curves proportional to the fluence (lethargy spectra) and were taken with and without neutron capture in Xenon in one Xenon layer for electrons, photons and neutrons respectively.

Comparing the photon spectra (Fig. 9.8) by activating or not the neutron capture in Xenon, it can be noticed the presence of a much higher 511 keV peak (due to positron annihilation) as well as the most frequent gammas in Xenon from the isotope ^{132}Xe . Concerning the 2.2 MeV peak from the neutron capture in Hydrogen and the 7.9 MeV in Copper, both peaks are there and identical, whether the neutron capture gammas in Xenon are activated or not. Due to the high energy of most capture gammas and to their ability to create electron pairs, the largest contribution is expected to be that of the annihilation peak.

The lethargy spectrum of electrons (Fig. 9.7) indicates that when the neutron capture gammas in Xenon are activated, electrons with energy from 50 keV to 500 keV have greater track-length and energy deposition.

The energy deposition in one Xenon layer, total or from electrons, positrons and photons (all together), by activating the neutron capture in Xenon is:

→ Total energy deposition : $\sim (4.32 \pm 0.31) \times 10^{-5}$ GeV per source particle.

→ Energy deposition from electrons, positrons and photons : $\sim (3.05 \pm 0.22) \times 10^{-5}$ GeV per source particle.

Without including in the simulation the neutron capture in Xenon is:

→ Total energy deposition : $\sim (3.98 \pm 0.3) \times 10^{-5}$ GeV per source particle.

→ Energy deposition from electrons, positrons and photons : $\sim (2.7 \pm 0.13) \times 10^{-5}$ GeV per source particle.

Therefore, all the additional energy deposition that is expected from the neutron capture in Xenon is in fact EM energy about 10 % more.

Due to the high neutron flux in the TRD detector it is important to be aware of the cumulative fluence of the dominating thermal neutrons. Scoring in the six Xenon layers during one event and taking the average value it can be noticed:

→ Total neutron fluence per primary in the TRD is : $\sim (27 \pm 3) \times 10^{-6}$ neutrons/cm².

→ Thermal neutron fluence per primary in the TRD is : $\sim (8 \pm 1) \times 10^{-6}$ neutrons/cm².

To scale up to a ten-year run period we multiply the aforementioned results with a factor of 3.2×10^{15} (80000 primaries \times 8 KHz / $5 \times 2.5 \times 10^6$ sec/year \times 10 years). The following Table 9.7 shows the resulting dose in a Xe layer accumulated during ten years of operation as well as the energy deposition, the neutron and thermal neutron fluence.

Table 9.7: Neutron fluences, energy depositions and absorbed doses in one Xenon layer of the TRD per 10 ALICE years.

Neutron Fluence [cm ⁻²]	$(8.64 \pm 0.96) \times 10^{10}$
Thermal neutron Fluence [cm ⁻²]	$(2.56 \pm 0.32) \times 10^{10}$
Total Edep [GeV]	$(1.38 \pm 0.10) \times 10^{11}$
Edep from e [±] , γ [GeV]	$(0.98 \pm 0.07) \times 10^{11}$
Total Dose [Gy]	$(7.45 \pm 0.54) \times 10^{-1}$
Dose from e [±] , γ [Gy]	$(5.26 \pm 0.38) \times 10^{-1}$

9.3.4 Evaluation of the steady state background hit rate in the TRD

The FLUKA simulations indicate that, for the geometry and materials present in the experiment, thermalization time (the time for the neutron kinetic energy to reach 1/40 eV) is of the order of a few μs .

Neutrons are slowed down inside the detector module and surrounding material, become thermalized and eventually some of them get captured by a nucleus after several μs . Therefore, the start of the neutron capture according to the scope of this study is set 10 μs after the collision. The energy spectra of the early and the delayed neutrons as well as their age vs energy distribution are shown in Figs. 9.10 and 9.11 respectively.

The secondaries inside the TRD after 10 μs are only neutrons, photons, positrons and electrons. Their time spectra are shown in Fig. 9.12. The dashed lines (red curves) have been obtained by activating the neutron capture in Xenon and the solid (blue) without.

By integrating the distributions of the delayed particles for each FLUKA event it can be estimated that due to neutron capture in Xenon we will have:

- $(30\pm 6)\%$ more photons
- $(26\pm 7)\%$ more electrons
- $(19\pm 3)\%$ more positrons

Figure 9.13 shows the energy spectra of the delayed secondaries. The energy of the delayed electrons ranges up to 10 MeV. The energy spectra of the delayed photons with neutron capture in Xenon indicates the presence of two capture lines from ^{132}Xe (667.72 and 6466.07 keV), the most frequent as we have seen before, as well as a high 511 keV peak (because it is due in part to the annihilation of positrons created by capture gammas). Moreover, it should be noticed again the presence of the 2.2 MeV (neutron capture in Hydrogen) as well as the 7.9 MeV (in Copper).

A comparison between the energy distributions of electrons and photons, delayed and not, with and without neutron capture, has been done and shows the contribution of the neutron capture in the kinetic energy of all, as it is shown in Fig. 9.14.

Fig. 9.15 gives an idea of the topology of the tracks in the scored volume of TRD, as well as their spiral direction due to the magnetic field. The tracking topology of electrons and muons seems to indicate a significant difference. In fact, the momentum of the electrons is of the order of hundreds of keV/c compared with that of muons which are coming from pion decays and is hundreds of MeV/c. Therefore, electrons are curled around the magnetic field having trajectory which is a much closer helix compared with that of muons.

In the ‘detailed’ TRD response simulation as implemented in AliRoot , charged particles losing energy in the chamber gas produce primary and secondary electrons from ionization. Each electron produces a ‘hit’ from which the digitized signal for every pad is derived.

As stressed above, the geometry simulated with FLUKA has a less detailed description of the layout. In fact, there are no pads at all. Thus, it has been necessary to find a ‘virtual’ segmentation and define pads as volumes inside the scored gas layers that are in accordance with the almost rectangular shape of the real ones.

The procedure that was followed is:

- We define in the TRD layer a volume of the average area of a pad ($7.25 \times 87.5 \text{ mm}^2$) and the length in the drift direction of 0.3 cm. This volume is attached to the first ‘hit’ of an electron and any additional hit in this volume from this electron is not counted. In this way it is counted, how many such volumes are occupied by signal.
- We add the time distributions of the delayed electrons from 6 FLUKA events (sum $\sim 1281940 \text{ e}^-$ or $\sim 213000 \text{ e}^-$ per event) that fulfill the previous statement.
- We fit the final time spectra with a sum of exponential functions as

shown in Fig. 9.16.

- We do the right normalization (every function should be multiplied by $dN/dy / 6 \times 8000$), assuming 8 kHz interactions and adding randomly each of them in a histogram with bins-size= $3 \mu s$ with an average $dt \sim 125 \mu s$.
- We superimpose all of them in the same histogram for about 8500 interactions which correspond to 1 s.

Figure 9.17 shows the TRD background in both cases, including and not in the simulation the neutron capture in Xenon. From this histogram we extract the average number of hits in a $3 \mu s$ window. In addition, we estimate the number of extra hits due to the neutron capture in Xenon by subtracting the 2 distributions.

Applying the same procedure we estimate the total number of hits from all the electrons independent of their age in order to find out the contribution of the background.

The distribution of hits from all electrons and from the delayed electrons (background) in a $3 \mu s$ window as well as the distribution of the extra hits from delayed electrons due to neutron capture in Xenon are shown in Fig 9.18.

9.3.5 Results and conclusions

The results can be summarized as follows :

- Random e^- -background : ~ 1856 hits/layer/ $3\mu s$ (RMS=907)
- Random e^- -background without neutron capture in Xenon : ~ 1457 hits/layer/ $3\mu sec$ (RMS=494)
- Electron hits due to neutron capture in Xe : ~ 398 extra hits/layer/ $3\mu s$ (RMS=480)
- All electron hits : ~ 7074 hits/layer/ $3\mu s$ (RMS=15450)

→ The contribution of the background to the total number of hits (from e^-) is $\sim 26\%$ and of the neutron capture less than 6%

The number of extra hits per layer is a broad distribution with a mean value at 398 hits/layer/ $3\mu s$ and a rms of 480 hits. So most of the events will have less than 1000 extra hits/layer/ $3\mu s$. In some rare cases (two or more consecutive central events) this can go up to 4000/layer/ $3\mu s$.

Using a ‘current’ estimator for counting particles by taking into account only the first ‘hit’ position in the TRD, we estimate the number of ‘unique’ electrons that are crossing or are created in that region. The radial distribution of their origin is shown in Fig. 9.19.

The momentum spectra of all electrons as well as of the delayed (background) and of those that are produced in the gas with and without activating the neutron capture in Xenon during one central Pb-Pb collision, are shown in Fig. 9.20.

Applying the same procedure as before we estimate the number of the ‘unique’ delayed secondaries in $3\mu s$ window:

Number of delayed particles in the TRD in a $3\mu s$ window

- Electrons : $\sim 264 e^-$ /layer/ $3\mu sec$ (RMS=144)
- Photons : $\sim 9750 \gamma$ /layer/ $3\mu sec$ (RMS=4434)
- Neutrons : $\sim 43500 n$ /layer/ $3\mu sec$ (RMS=42000)
- Positrons : $\sim 12 e^+$ /layer/ $3\mu sec$ (RMS=6)

Without activating the neutron capture in Xenon the delayed ‘unique’ particles are:

Number of delayed particles in the TRD in a $3\mu s$ window

- Electrons : $\sim 195 e^-$ /layer/ $3\mu sec$ (RMS=63)
- Photons : $\sim 7848 \gamma$ /layer/ $3\mu s$ (RMS=2643)
- Positrons : $\sim 9 e^+$ /layer/ $3\mu s$ (RMS=3)

To conclude, the total number of hits in a central Pb–Pb collision in a $3 \mu\text{s}$ window is a broad distribution with a mean of 7074 hits/layer and an rms of 15450/layer. Of these the random steady-state background contributes 26% as it produces extra hits in the Xe readout chambers with a mean of 1856 hits/layer and an rms of 907/layer. The neutron capture in Xe has as result a 22% increase in the background and a 6% increase in the total number of hits.

The results show that the n-capture in Xe does not increase the background by a big amount but it is not negligible and will be included in the AliRoot simulations.

9.4 Radioactivity in the gas system of ALICE TRD

Due to the high neutron and charged particle fluxes at the ALICE TRD, it is very probable to have radioactive isotopes produced from the circulating gas used in the detector. Depending on the lifetime of the isotope produced, the resulting activity may be quite high, and should be taken into account particularly during the run period, because part of the gas is supposed to be always in accessible areas.

An estimate of the activity levels of the TRD gas system is presented in comparison with CERN safety limits, based on a similar study which was done for ATLAS-ID-TRT [146].

9.4.1 Calculation of activity

Radioactive isotopes can be produced by many reactions like (n,γ) , $(n,2n)$, (π,p) etc. Among them, neutron capture process has the highest significance for the TRD gas activation because of its large cross section at low neutron energies.

Activity is defined as the number of decays per second, but the specific activity, which takes into account the number of particles emitted per decay, is considered here. The specific activity A can be calculated as:

$$A = \Phi \cdot \sigma \cdot N \cdot M \cdot X \cdot (\text{buildup}) \cdot (\text{decay}) \quad (9.1)$$

Where: Φ is the neutron flux (kHz/cm²), σ is the neutron capture cross-section (10²⁴ barn), N is the number of parent atoms per unit mass (atoms/g), M is the mass of element considered (g), and X is the number of particles emitted per decay. The effect of build-up and decay are calculated as:

$$(\text{buildup}) = 1 - e^{-\lambda \cdot T} \quad (9.2)$$

$$(\text{decay}) = e^{-\lambda \cdot t} \quad (9.3)$$

where $\lambda = (\ln 2)/T_{1/2}$, $T_{1/2}$ is the half-life, T is the irradiation time (a maximum running time of 100 days per year is assumed at the LHC), and t is the decay time (the rest of the year ~ 250 days). The build-up factor determines how many isotopes of our interest are produced during the irradiation time which is the run period taken as 100 days for a year. When the beam is off, the decay factor calculates the number of decays for the rest of the year.

The standard unit of activity is Becquerel (Bq) which is the number of particles per second. Relation between often used Curie (Ci), and Becquerel is $1 \text{ Ci} = 3.7 \times 10^{10} \text{ Bq}$ (or $3.7 \times 10^{10} \text{ sec}^{-1}$). The product of the absorbed dose in tissue due to radiation, so called the dose equivalent, is expressed in units of Sievert (Sv: $1 \text{ Sv} = 1 \text{ J/kg}$).

There are two types of decays which should be considered separately, gamma and beta decays. For the gamma decays, so called ‘‘gamma exposure factor’’ (also known as the specific gamma constant) should be taken into account. It relates the activity of a point source with a certain energy to the dose equivalent at a distance. The equivalent dose from $1 \mu\text{C}$ point source at a distance of D meters is $\Gamma/D^2 \mu\text{Sv/h}$ [147, 148]. The CERN safety limits for gamma radiation [149] are summarised in Table 9.8.

Table 9.8: CERN safety limits for gamma radiation.

AREA	MAX DOSE RATE ($\mu\text{Sv/h}$)
NON-DESIGNATED	<0.5
SUPERVISED	<7.5
SIMPLE CONTROLLED	<100

In the ATLAS-TRT study, it is shown that from all the possible radioactive products only Xe has large neutron capture cross-section and should be considered as potentially dangerous element. In calculations, isotopes with cross-sections less than 10^2 barn, or with lifetimes less than a few minutes were ignored (assuming ~ 10 minutes minimum for gas to travel from detector to accessible areas). Beta activity of Xenon was not taken into account because the minimum thickness of any gas system wall is 0.5 mm of stainless steel which will very effectively attenuate the radiation.

The gamma activity of each isotope was calculated separately for 1 kg of the bulk material, so that it is easy to estimate the total activity by scaling to the amount of the material to be used. Summing the activities of all isotopes, at the end of the running period (100 days), it was calculated that for 1 kg of Xenon, activated by slow neutrons, the maximum activity is ~ 0.4 mCi. It was also shown that 6% of the photons have energies above 250 keV and 0.5% above 550 keV.

9.4.2 Scaling ATLAS results to ALICE TRD

The ATLAS SCT aims to operate reliably according to performance specifications over a 10-year period of high luminosity LHC operation. The design LHC luminosity aims for an average peak value of $10^{34} \text{ cm}^{-2}\text{s}^{-1}$ over 10^7 secs per year, giving an annual integrated luminosity of 10^{41} cm^{-2} . Instantaneous rates may exceed this value. These luminosities are achieved using bunch-bunch crossings separated by 25 nsec (40MHz) to result in a particle interaction rate $\sim 10^9$ Hz [150]. The standard running scenario for

particle production in ATLAS and in ALICE respectively, is summarized in Table 9.9

The neutron flux values used throughout the ATLAS study were taken from reference [151].

$$\rightarrow \text{Neutron Fluence} \sim 8 \times 10^{13} [\text{particles}/\text{cm}^2/\text{year}]$$

$$\rightarrow \text{Thermal neutron Fluence} \sim 3 \times 10^{13} [\text{particles}/\text{cm}^2/\text{year}]$$

Table 9.9: Operational scenario for a one year running period ($\langle L \rangle$ stands for mean luminosity and σ_t for inelastic cross section.)

	ATLAS pp	ALICE PbPb
$\langle L \rangle [\text{cm}^{-2}\text{s}^{-1}]$	10^{34}	10^{27}
$\sigma_t[\text{b}]$	0.07	8
Rate [s^{-1}]	10^9	8×10^3
Runtime [s]	10^7	5×10^5
Events/year	10^{16}	4×10^9

According to Eq. 9.1, the specific activity A is proportional to the neutron flux. Assuming for simplicity that the running period is the same, the aforementioned activity of 1 kg of Xenon can be scaled in accordance with the neutron fluence in ALICE TRD as summarized in Table 9.7.

Thus, for 1 kg of Xenon, activated by slow neutrons, the maximum activity is $\sim (0.04-0.1) \mu\text{Ci}$ in ALICE TRD. The volume of the TRD is $\sim 27 \text{ m}^3$. Assuming the worst scenario that 150 kg of Xenon are stored in a cylindrical container with dimensions length=4×diameter, the maximum radiation dose is about $2.3 \mu\text{Sv/h}$ on the surface. Since this value is already below the supervised area limit of $7.5 \mu\text{Sv/h}$, no special shield is required.

9.4.3 Conclusions

The resulting activity and dose rate of Xenon appear to be rather low and safe, especially if compared with the expected general radiation environment. All parts of the TRD gas system have rates below supervised limit

and no special shielding is required. The possible leakage of Xenon into the ALICE cavern does not lead to any safety problems.

9.5 Estimation of the radiation level in the ALICE TPC electronics

The inaccessibility of the ALICE experiment during the entire year of LHC running makes stringent quality tests of the readout electronics mandatory before installation. Here we analyze and present the contributions to the radiation background in the region where the ALICE TPC front-end electronics is situated. The simulations were based on the FLUKA interaction and transport Monte Carlo code.

The Time Projection Chamber (TPC) [154] surrounds the Inner Tracking System (ITS) and is the main tracking detector of the central barrel and together with the ITS, TRD and TOF will provide charged particle momentum measurement, particle identification and vertex determination with sufficient momentum resolution, two track separation and dE/dx resolution for studies of hadronic and leptonic signals in the region $P_t < 10$ GeV/c and pseudorapidities $|\eta| < 0.9$. To cover this acceptance the TPC is of cylindrical design with an inner radius of about 80 cm, an outer radius of about 250 cm and an overall length in the beam direction of 500 cm. A gas mixture of 90% Ne, 10% CO₂ has been chosen for operating the detector. The front-end electronics read out the charge detected by about 570 000 cathode pads located on the readout chambers at the TPC end-plates. Using the FLUKA geometry, we define 4 concentric cylindrical layers of silicon at radial distances from 77.2 up to 278.17 cm with 1 mm width along the beam direction, 10 cm away from the TPC limiting planes. We perform two studies for both end-plates (μ -absorber and non-absorber side). Events with average multiplicity of 80 000 primary pions and kaons were transported through the material of the experiment and experimental area which was described with about 3200 volumes. The neutron fluence in the first Si layer (nearest to the beam axis) in particles/cm²/primary per cen-

Table 9.10: Particle fluences with $E_{\text{kin}} > 10$ MeV and total absorbed doses per 10 ALICE years .

Scoring region	μ -absorber side	non-absorber side
n [cm^{-2}]	$(2.4-8.4) \times 10^9$	$(1.1-2.8) \times 10^9$
p [cm^{-2}]	$(1.2-3.2) \times 10^8$	$(1.1-4.8) \times 10^8$
π [cm^{-2}]	$(0.7-1.4) \times 10^9$	$(0.8-2.9) \times 10^9$
k [cm^{-2}]	$(2.4-7.6) \times 10^7$	$(3.3-19.3) \times 10^7$
Total Dose [Gy]	(0.8-2.5)	(0.3-5.7)

tral event is: $(3.42 \times 10^{-5}) \pm 1.6\%$ and $(1.27 \times 10^{-5}) \pm 1.3\%$ for μ -absorber and non-absorber side respectively, as is shown in Fig. 9.21.

To scale up to a ten-year run period we multiply the aforementioned result of the fluence per central event with a factor of 3.2×10^{15} (80000 primaries \times 8 KHz / $5 \times 2.5 \times 10^6$ sec/year \times 10 years).

The radiation load on the TPC electronics is relatively low, with a neutron flux received over 10 years of $(0.6-1.1) \times 10^{11}$ neutrons/ cm^2 . Thus, standard radiation-soft technologies are suitable for the implementation of this electronics. Nevertheless, some special care should be taken to protect the system against potential damage caused by Single Event Effects (SEEs). Concerning the SEU (Single Event Upset) in the FPGAs probably only the protons above 10-20 MeV can cause bit-flips. Neutrons can contribute to this effect only if they scatter in the plastic of the chip package or in the PCB with a proton and kick the fast proton into the silicon.

The particle fluences with $E_{\text{kin}} > 10$ MeV in both sides of TPC are summarized in Table 9.10.

The aforementioned results of this study [153] concerning the particle rates, fluences and fluxes should be taken into account for evaluating the radiation tolerance of the TPC electronics.

All the study including more details can be found in appendix C.

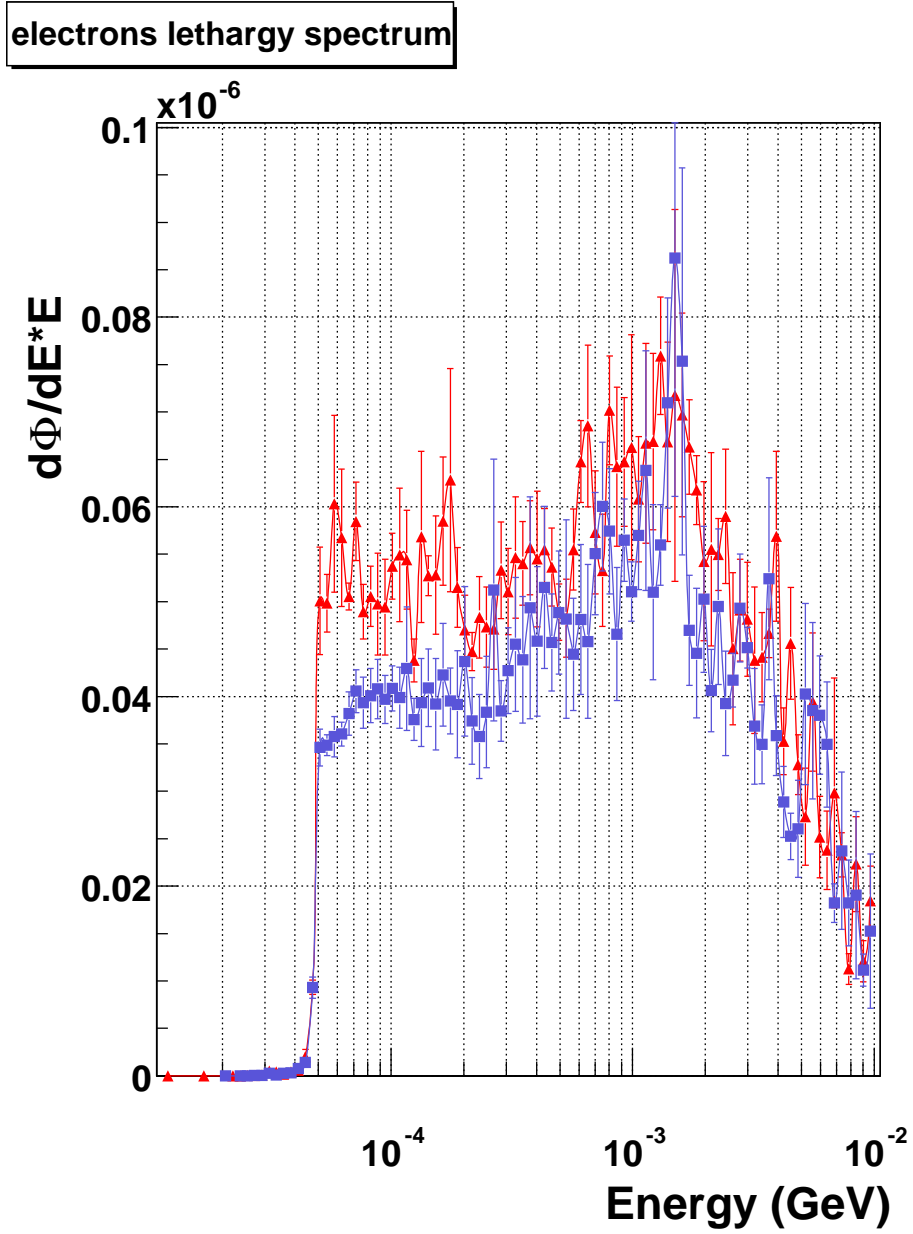


Figure 9.7: Electron fluence spectra in one Xenon layer during one FLUKA event, whereas the red curve (full triangle) has been taken with activated the neutron capture in Xenon and the blue curve (full rectangle) without.

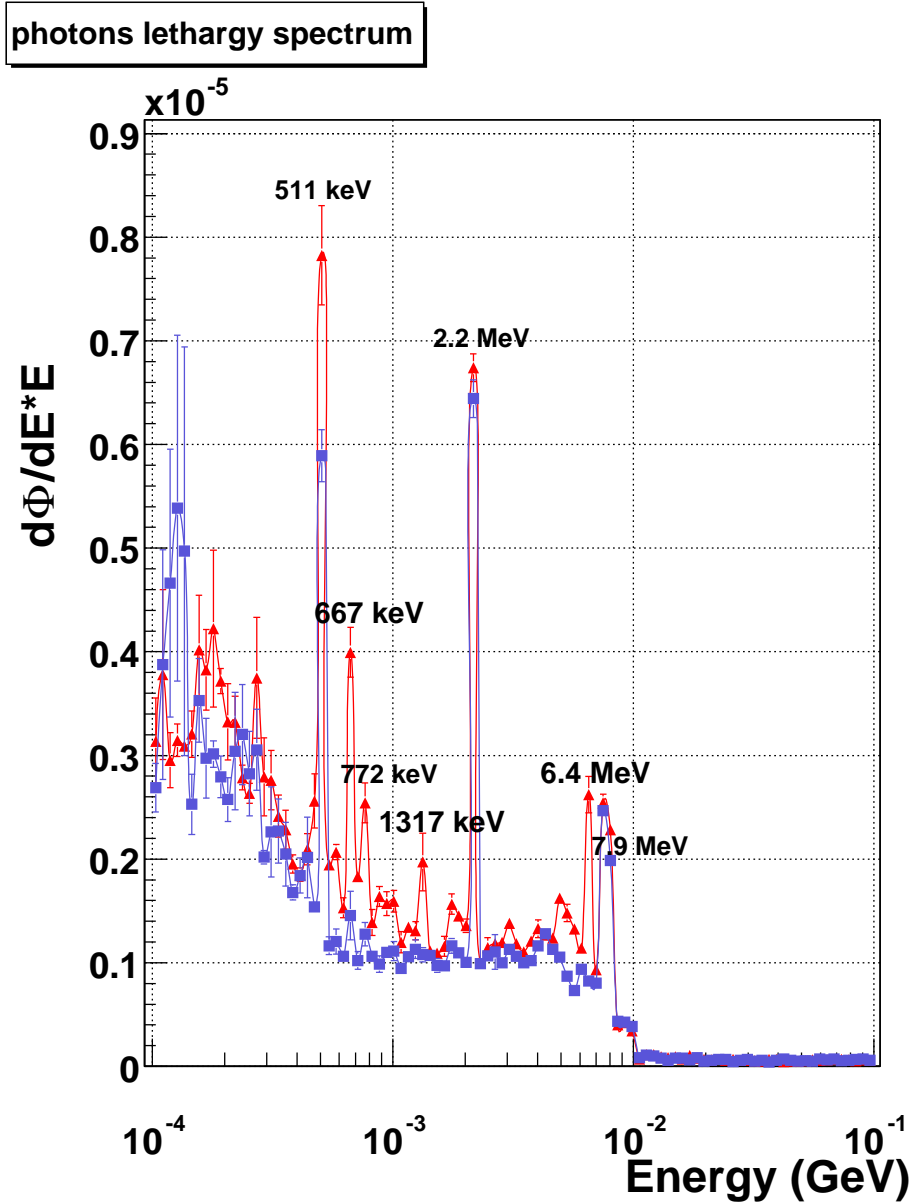


Figure 9.8: Photon fluence spectra in one Xenon layer during one FLUKA event, whereas the red curve (full triangle) has been taken with activated the neutron capture in Xenon and the blue curve (full rectangle) without.

neutrons lethargy spectrum

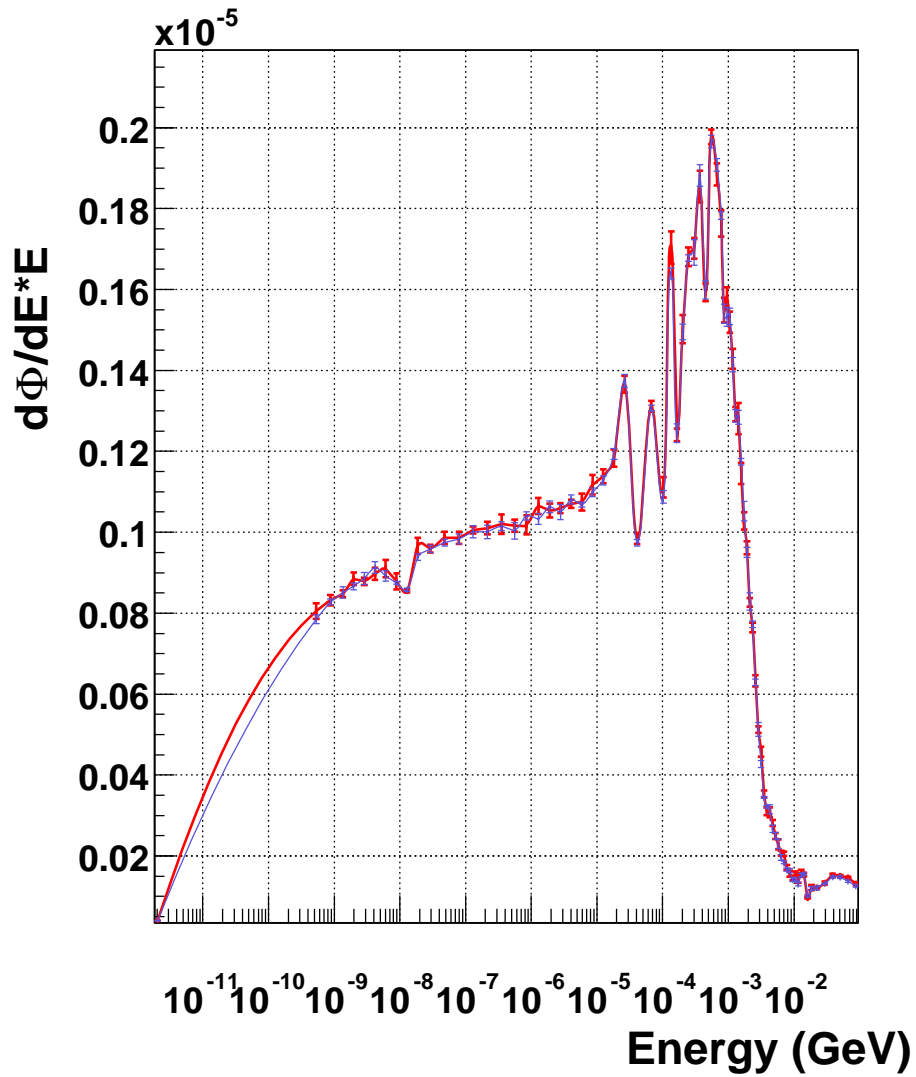


Figure 9.9: Neutron fluence spectra in one Xenon layer during one FLUKA event, whereas the red curve has been taken with activated the neutron capture in Xenon and the blue curve without.

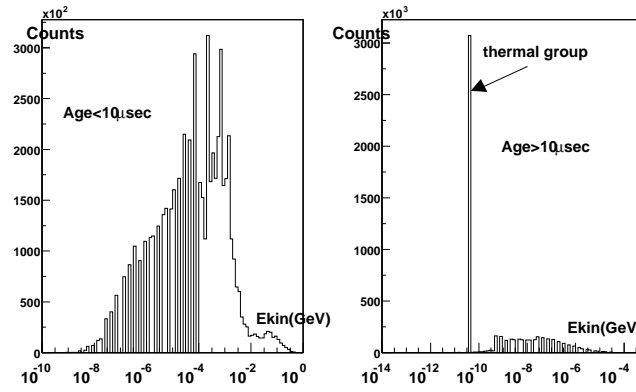


Figure 9.10: Energy spectra of neutrons.

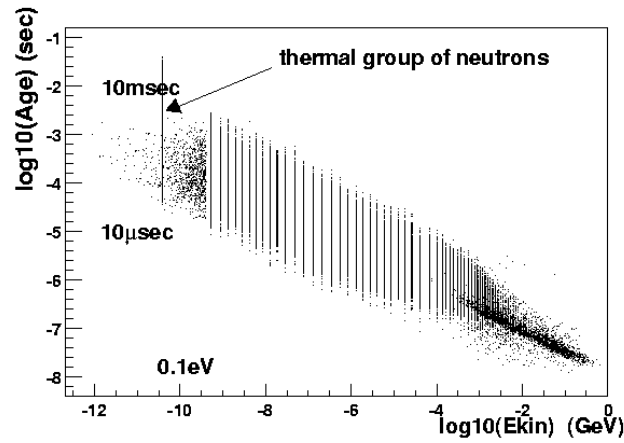


Figure 9.11: Age-Energy distribution of neutrons.

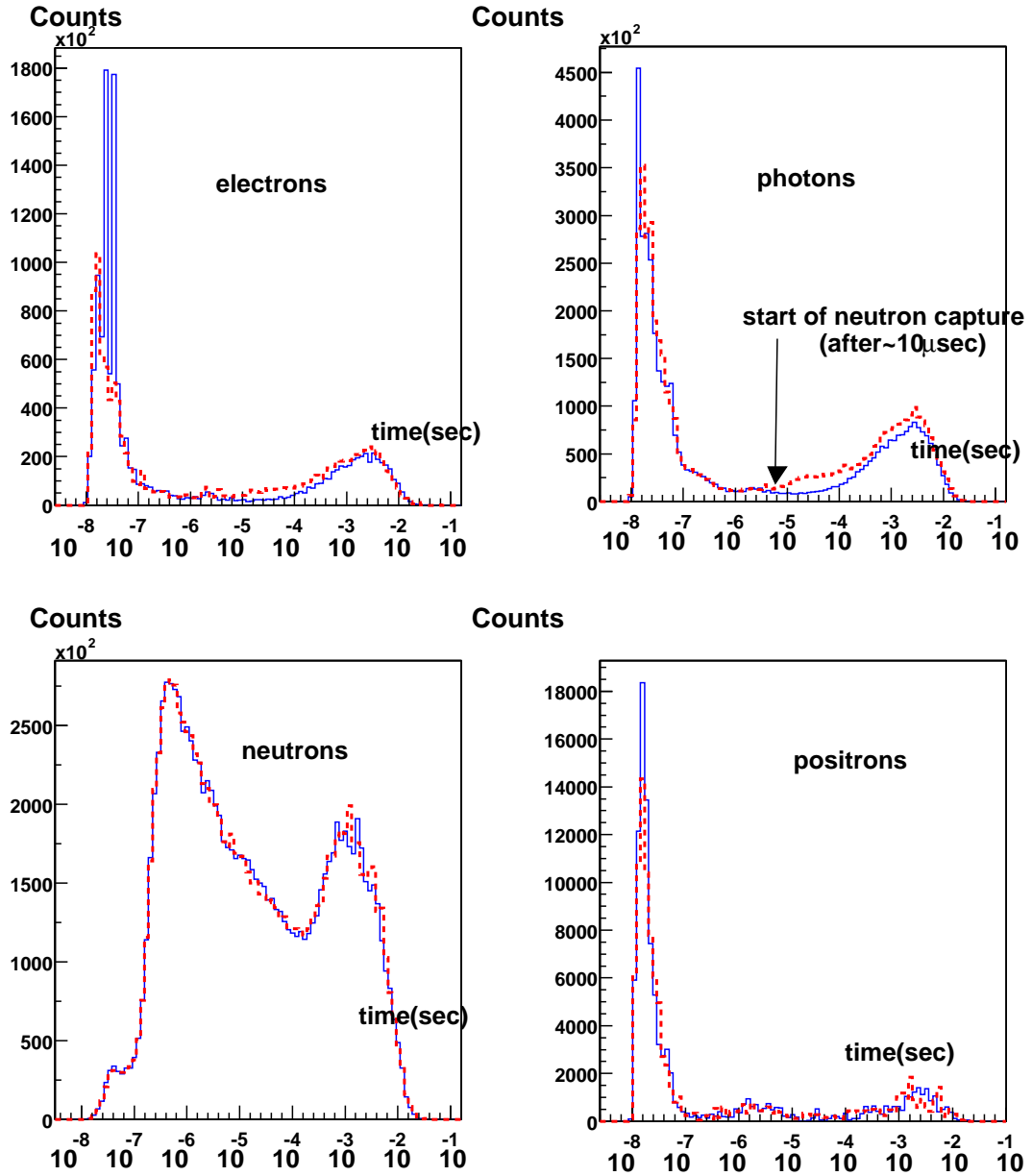


Figure 9.12: Time Spectra of e^- , γ , n and e^+ . The red curves (dashed line) are taken by one event with activated the neutron capture in Xenon. The blue (solid line) without.

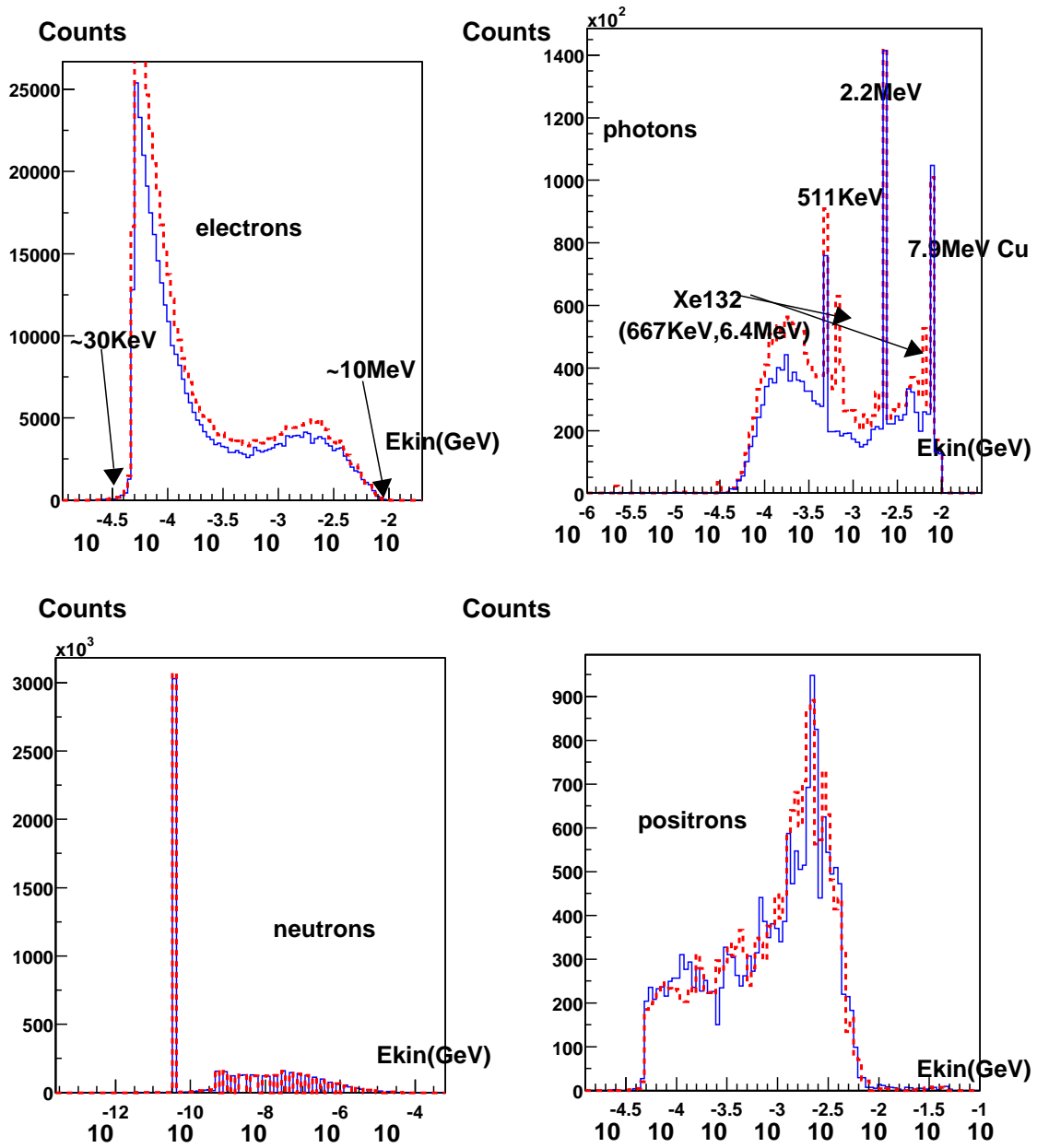


Figure 9.13: Energy Spectra of e^- , γ , n and e^+ . The red curves (dashed line) are taken by one event with activated the neutron capture in Xenon. The blue (solid line) without.

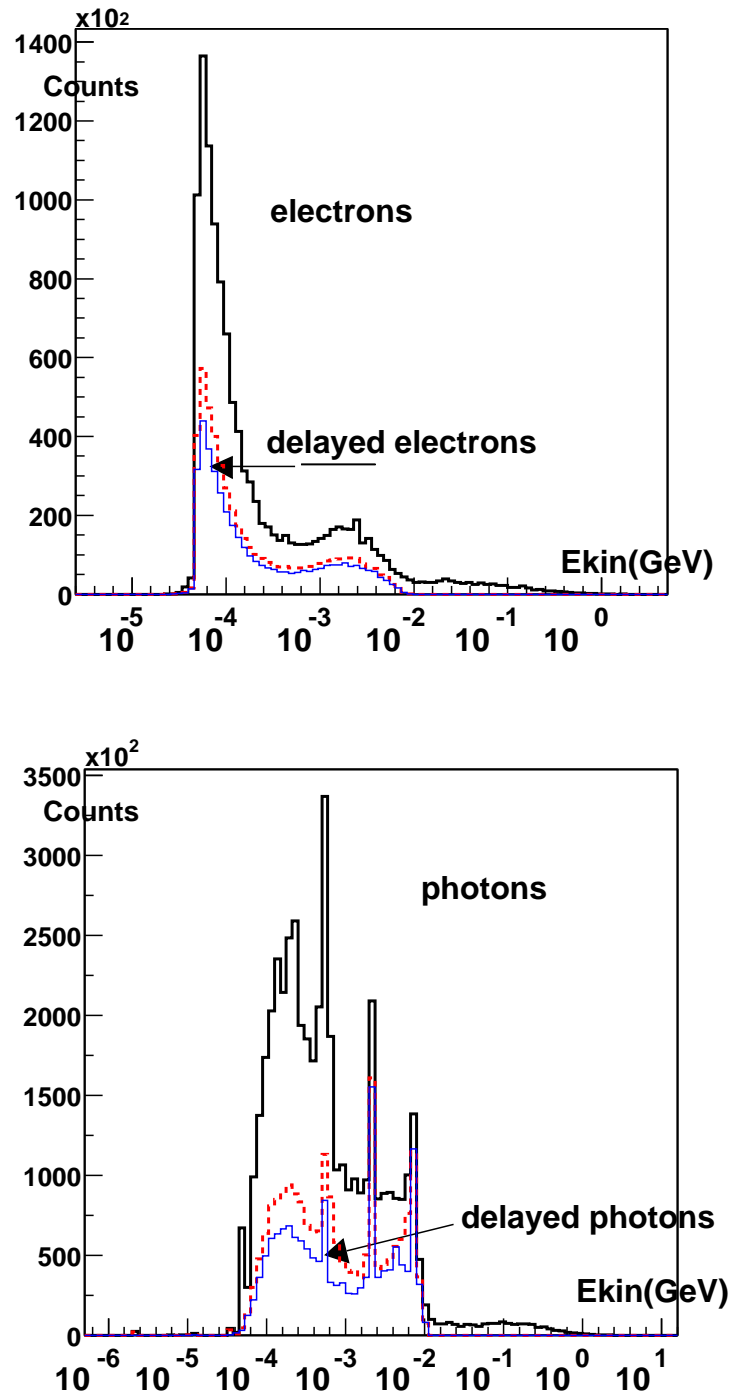


Figure 9.14: Energy Spectra of delayed e^-,γ compared with the Spectra of all e^-,γ respectively during one FLUKA event. The red curves (dashed line) are taken by one event with activated the neutron capture in Xenon. The blue (solid line) without.

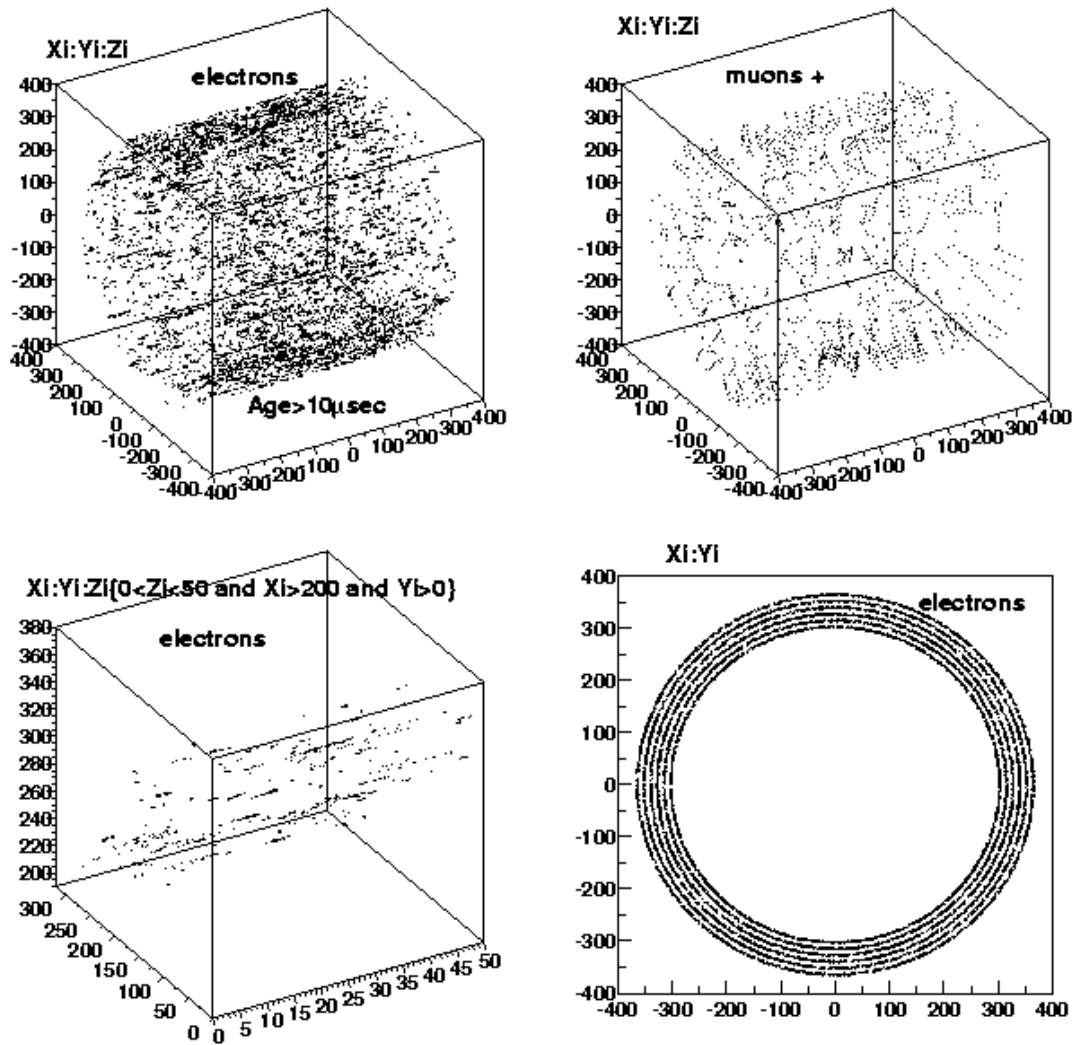


Figure 9.15: Topology of the tracks for e^- and μ^+ respectively.

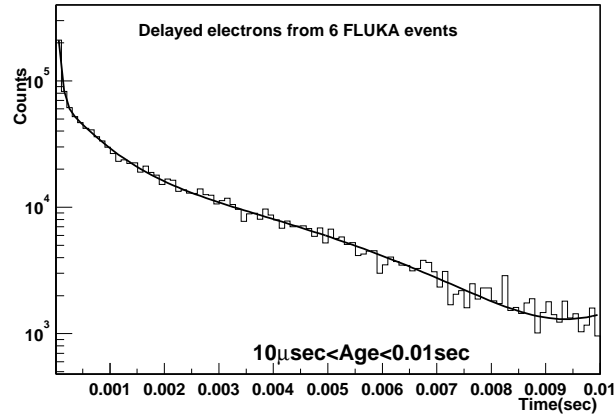


Figure 9.16: The time spectrum of the delayed electrons. The line is a fit with a sum of exponential functions.

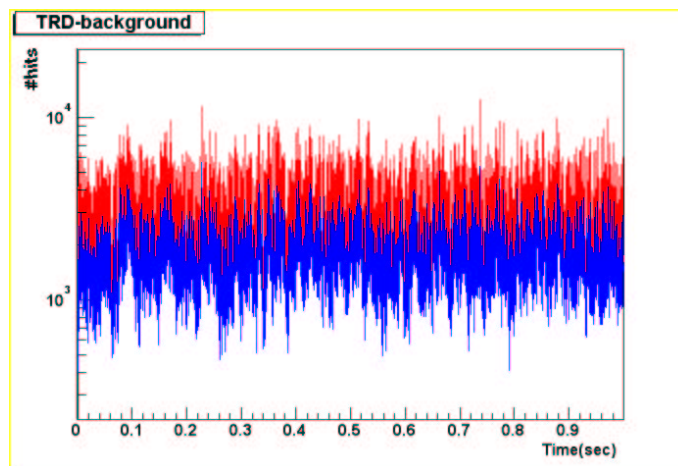


Figure 9.17: TRD-background, where the red shows the fluctuations of the hits with activated the neutron capture in Xenon and the blue without.

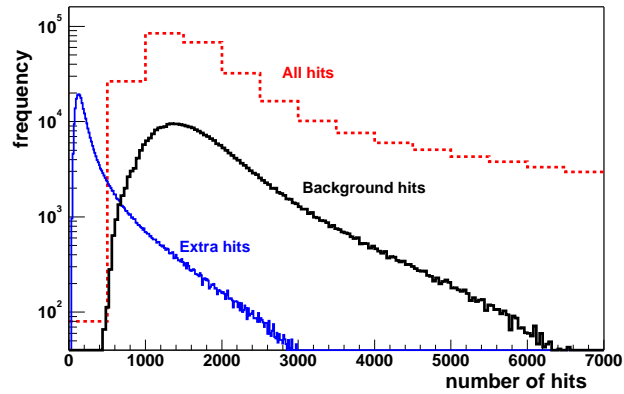


Figure 9.18: The distribution of the number of hits from all e^- and delayed e^- (background) and extra hits (from delayed e^-) in a $3\mu s$ window due to neutron capture in Xenon.

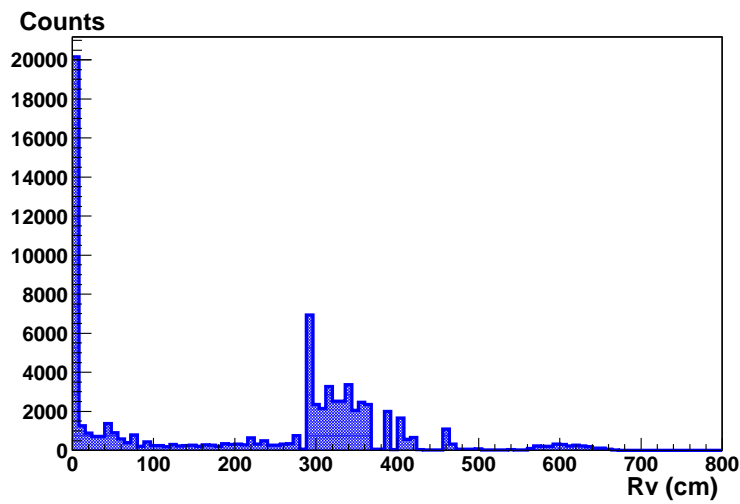


Figure 9.19: Radial distribution of all 'unique' electrons origin that scored in the TRD gas layers

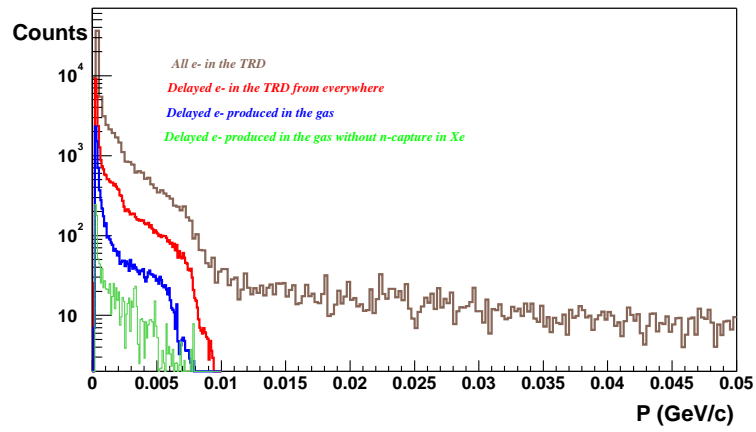


Figure 9.20: Momentum spectra of 'unique' electrons in the TRD

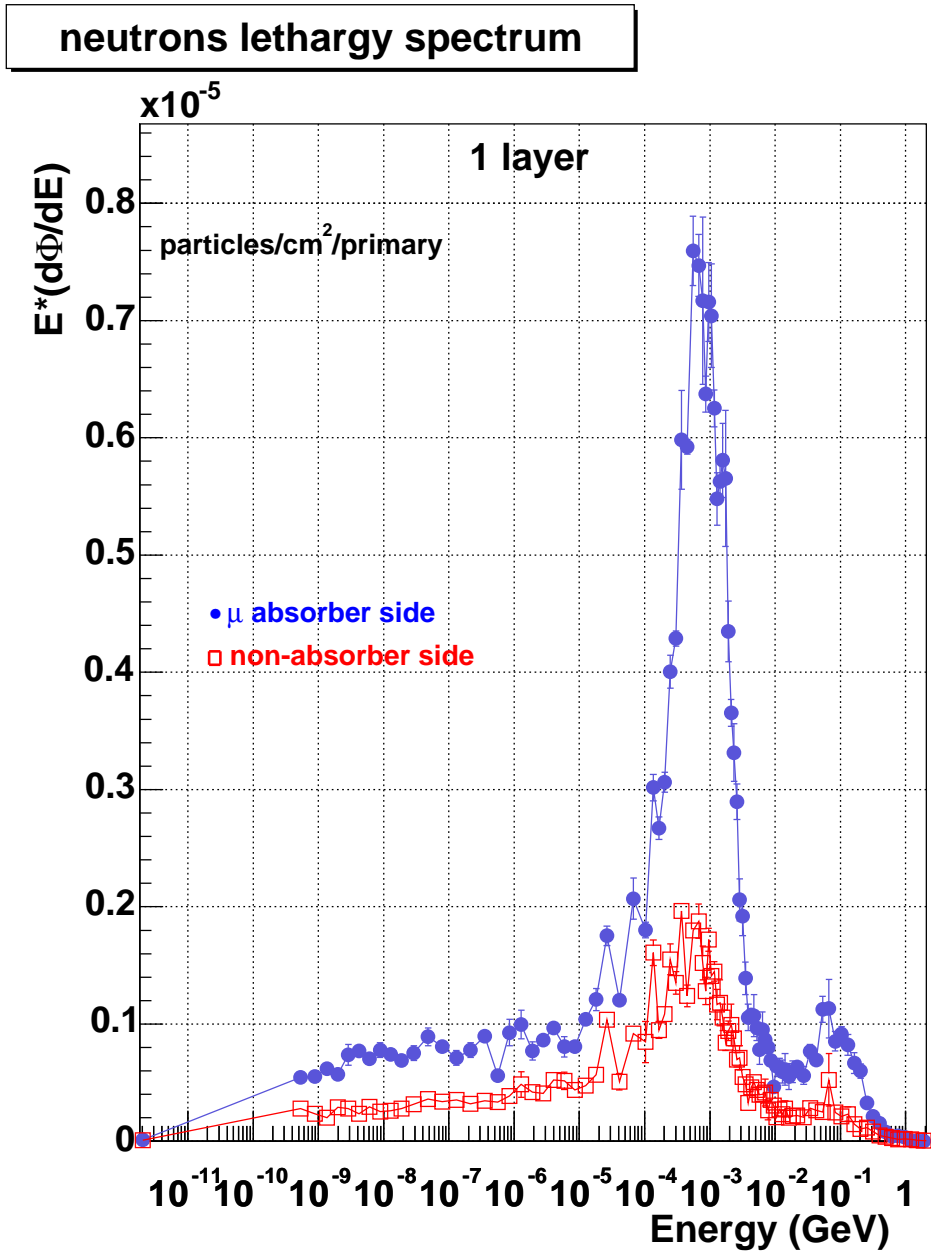


Figure 9.21: Lethargy energy spectra of neutrons in the μ -absorber (full circles) and non-absorber side (empty rectangles) of the TPC (one central event).

Appendix A

Two-particle correlation plots

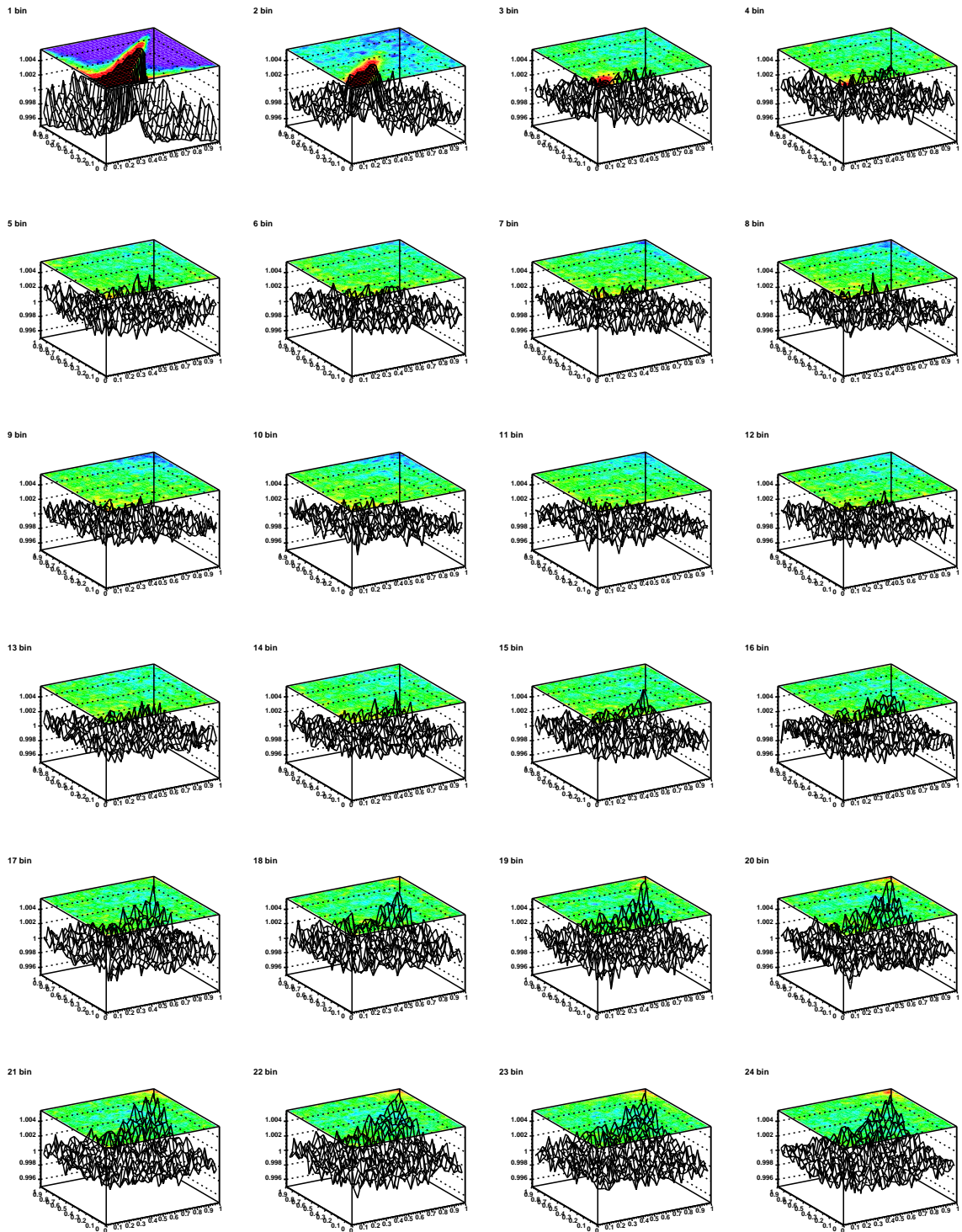


Figure A.1: Two-particle correlation plots using the cumulant p_T variable x for all pairs, in several $\Delta\phi$ regions.

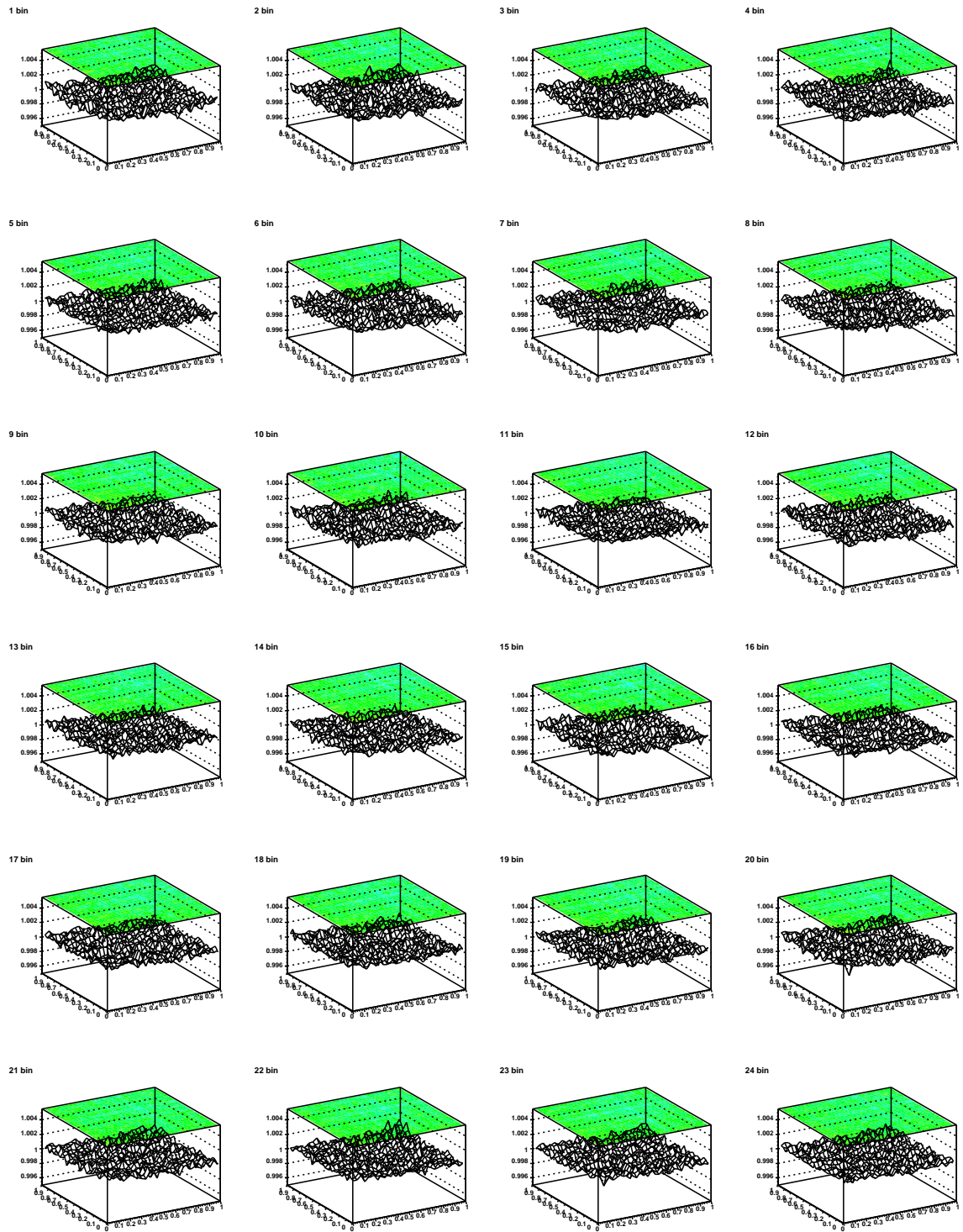


Figure A.2: Two-particle correlation plots using the cumulant p_T variable x for all pairs that have only the elliptic flow expected by CERES (corrected by dividing mixed with flow versus mixed), in different $\Delta\phi$ regions.

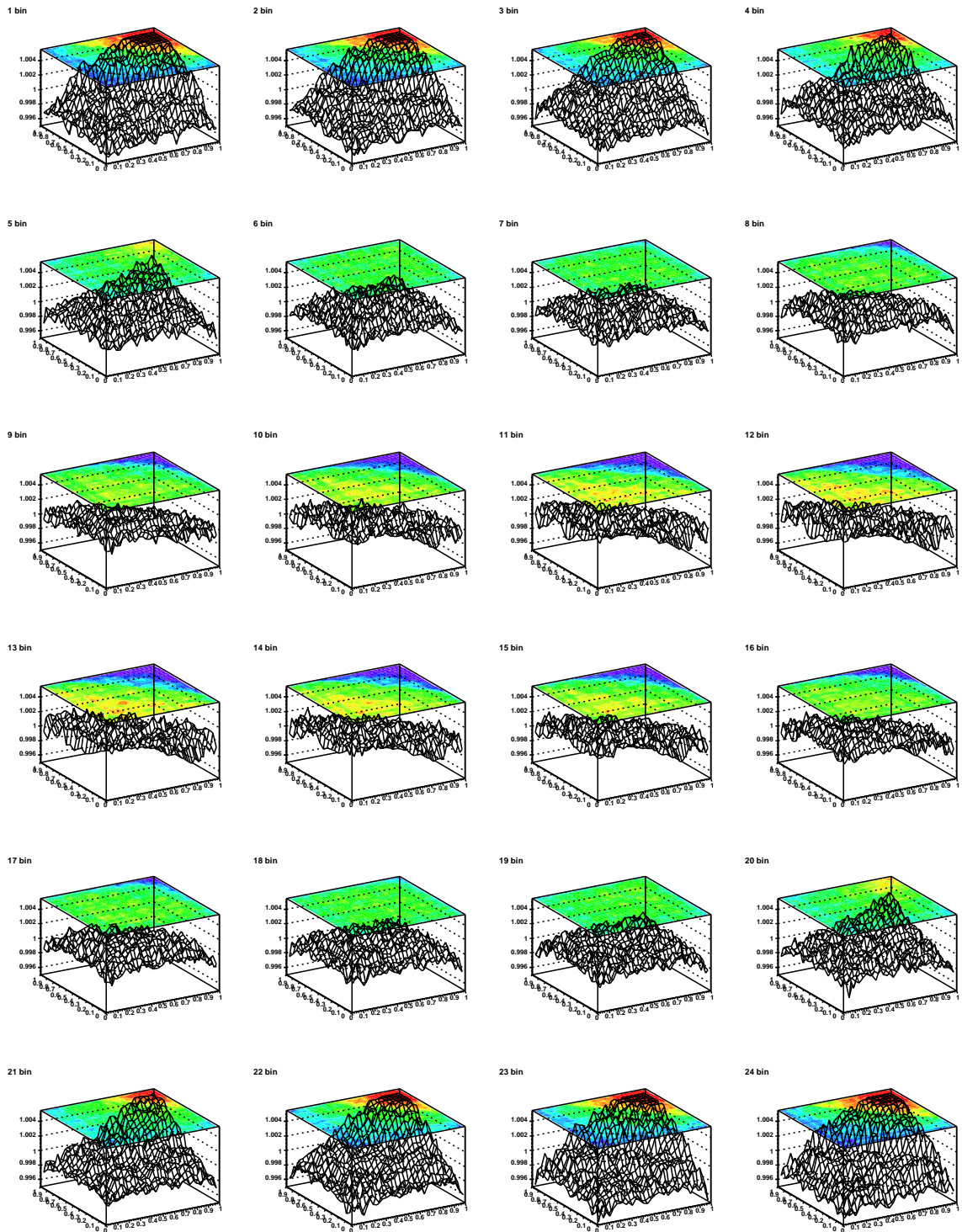


Figure A.3: Two-particle correlation plots using the cumulant p_T variable x for all pairs that have only elliptic flow with $3v_2$, where v_2 gets the expected by CERES value (corrected by dividing mixed with flow versus mixed), in several $\Delta\phi$ regions.

Appendix B

Number of gammas in ^{nat}Xe

Xenon isotope	Gamma energy (keV)	From level (keV)	To level (keV)	I_γ per 100 captures	Xenon isotope	Gamma energy (keV)	From level (keV)	To level (keV)	I_γ per 100 captures
^{132}Xe	667.72	667.72	0.0	64.73	^{125}Xe	644.56	1441.2	796.62	2.876
^{132}Xe	6466.1	8935.2	2469.1	24.07	^{132}Xe	5059.9	8935.2	3875.3	2.808
^{132}Xe	772.61	1440.3	667.72	22.55	^{132}Xe	4908.2	8935.2	4027.0	2.588
^{130}Xe	536.09	536.09	0.0	16.60	^{125}Xe	774.54	2215.7	1441.2	2.445
^{132}Xe	1317.9	1985.7	667.72	15.88	^{132}Xe	1397.4	3792.3	2394.9	2.341
^{132}Xe	6379.8	8935.2	2555.4	10.66	^{130}Xe	702.80	6290.5	5587.7	2.275
^{130}Xe	668.52	1204.6	536.09	10.25	^{130}Xe	2965.3	9255.8	6290.5	2.275
^{132}Xe	483.46	2469.1	1985.7	9.824	^{130}Xe	466.39	2841.6	2375.2	2.269
^{132}Xe	600.03	2040.4	1440.3	8.355	^{132}Xe	1120.9	3875.3	2754.4	2.247
^{132}Xe	5754.4	8935.2	3180.8	7.847	^{132}Xe	1858.2	4027.0	2168.8	2.194
^{132}Xe	569.75	2555.4	1985.7	7.196	^{132}Xe	954.58	2394.9	1440.3	2.177
^{132}Xe	1028.8	2469.1	1440.3	6.778	^{132}Xe	522.67	1963.0	1440.3	1.988
^{132}Xe	1887.7	2555.4	667.72	6.404	^{132}Xe	2168.8	2168.8	0.0	1.972
^{125}Xe	111.78	111.78	0.0	6.344	^{125}Xe	884.18	3099.9	2215.7	1.911
^{132}Xe	1140.4	3180.8	2040.4	6.278	^{130}Xe	696.28	3071.5	2375.2	1.911
^{130}Xe	739.48	1944.1	1204.6	5.859	^{132}Xe	1501.1	2168.8	667.72	1.775
^{132}Xe	5142.9	8935.2	3792.3	5.783	^{132}Xe	5691.8	8935.2	3243.4	1.707
^{132}Xe	1801.4	2469.1	667.72	5.501	^{125}Xe	971.00	4070.9	3099.9	1.639
^{130}Xe	752.79	2696.9	1944.1	5.344	^{132}Xe	1985.7	1985.7	0.0	1.588
^{130}Xe	275.45	2972.3	2696.9	5.225	^{132}Xe	1740.5	3180.8	1440.3	1.569
^{130}Xe	720.84	3693.2	2972.3	4.921	^{130}Xe	804.89	4347.1	3542.2	1.543
^{125}Xe	140.82	252.60	111.78	4.608	^{125}Xe	184.08	295.86	111.78	1.512
^{132}Xe	630.20	1297.9	667.72	4.384	^{130}Xe	949.60	5296.7	4347.1	1.494
^{132}Xe	8267.5	8935.2	667.72	4.323	^{130}Xe	3959.1	9255.8	5296.7	1.494
^{132}Xe	5235.7	8935.2	3699.5	4.186	^{130}Xe	821.87	3893.4	3071.5	1.442
^{130}Xe	854.99	2059.6	1204.6	3.992	^{132}Xe	5877.0	8935.2	3058.1	1.432
^{125}Xe	57.940	310.54	252.60	3.917	^{130}Xe	3651.0	9255.8	5604.8	1.407
^{130}Xe	315.60	2375.2	2059.6	3.666	^{130}Xe	5956.8	9255.8	3299.0	1.375
^{132}Xe	1236.9	3792.3	2555.4	3.442	^{132}Xe	505.80	1803.7	1297.9	1.369
^{125}Xe	486.08	796.62	310.54	3.226	^{130}Xe	700.62	3542.2	2841.6	1.368

continues on next page

Table B.1: Number of gammas per 100 thermal neutron captures in ^{nat}Xe

continued from previous page

Xenon isotope	Gamma energy (keV)	From level (keV)	To level (keV)	I_γ per 100 captures	Xenon isotope	Gamma energy (keV)	From level (keV)	To level (keV)	I_γ per 100 captures
^{130}Xe	997.20	5587.7	4590.5	3.207	^{132}Xe	1280.4	3243.4	1963.0	1.366
^{130}Xe	897.33	4590.5	3693.2	3.207	^{132}Xe	1895.8	3699.5	1803.7	1.273
^{132}Xe	4840.7	8935.2	4094.5	2.946	^{132}Xe	2086.7	2754.4	667.72	1.248
^{132}Xe	3699.5	3699.5	0.0	2.913	^{132}Xe	4981.0	8935.2	3954.2	1.239
^{130}Xe	586.06	1122.1	536.09	2.908	^{125}Xe	3532.4	7603.3	4070.9	1.238
^{130}Xe	941.93	4635.1	3693.2	1.230	^{131}Xe	606.73	971.22	364.49	0.6350
^{130}Xe	925.80	5560.9	4635.1	1.230	^{130}Xe	246.98	2633.2	2386.2	0.6104
^{130}Xe	3364.1	9255.8	5891.7	1.230	^{130}Xe	595.50	4942.6	4347.1	0.5960
^{130}Xe	330.80	5891.7	5560.9	1.230	^{131}Xe	364.49	364.49	0.0	0.5909
^{125}Xe	300.90	596.76	295.86	1.151	^{132}Xe	2577.4	3875.3	1297.9	0.5617
^{130}Xe	229.89	3071.5	2841.6	1.127	^{132}Xe	2796.6	4094.5	1297.9	0.5556
^{132}Xe	1171.2	2469.1	1297.9	1.120	^{130}Xe	646.75	4540.1	3893.4	0.5514
^{130}Xe	2762.6	2762.6	0.0	1.105	^{130}Xe	2978.5	2978.5	0.0	0.5482
^{132}Xe	1115.1	2555.4	1440.3	1.029	^{125}Xe	736.03	2272.2	1536.2	0.5460
^{125}Xe	715.40	1925.3	1209.9	0.9781	^{125}Xe	574.74	870.60	295.86	0.5405
^{132}Xe	6220.8	8935.2	2714.4	0.9639	^{132}Xe	1539.1	4094.5	2555.4	0.5303
^{130}Xe	6369.8	9255.8	2886.0	0.9406	^{125}Xe	665.60	1536.2	870.60	0.5278
^{130}Xe	6301.5	9255.8	2954.3	0.9406	^{132}Xe	2390.4	3058.1	667.72	0.5242
^{125}Xe	778.83	2704.1	1925.3	0.9340	^{132}Xe	6748.0	8935.2	2187.2	0.5232
^{125}Xe	613.15	1209.9	596.76	0.9327	^{130}Xe	2653.0	3189.1	536.09	0.5222
^{130}Xe	2649.9	9255.8	6605.9	0.9320	^{130}Xe	5713.6	9255.8	3542.2	0.5217
^{130}Xe	1018.2	6605.9	5587.7	0.9320	^{130}Xe	431.11	2375.2	1944.1	0.5132
^{130}Xe	2176.9	3299.0	1122.1	0.9135	^{130}Xe	6622.6	9255.8	2633.2	0.5066
^{130}Xe	191.70	2954.3	2762.6	0.8877	^{132}Xe	6949.5	8935.2	1985.7	0.4957
^{130}Xe	470.73	3542.2	3071.5	0.8620	^{132}Xe	791.44	2754.4	1963.0	0.4743
^{132}Xe	1785.4	3954.2	2168.8	0.8545	^{130}Xe	1763.9	2886.0	1122.1	0.4739
^{132}Xe	2054.1	4094.5	2040.4	0.8418	^{130}Xe	6066.7	9255.8	3189.1	0.4703
^{132}Xe	1136.0	1803.7	667.72	0.8353	^{130}Xe	1264.1	2386.2	1122.1	0.4703
^{132}Xe	428.75	2469.1	2040.4	0.8056	^{125}Xe	4899.2	7603.3	2704.1	0.4696
^{130}Xe	6277.3	9255.8	2978.5	0.7960	^{130}Xe	5849.7	9255.8	3406.1	0.4560

continues on next page

Table B.4: Number of gammas per 100 thermal neutron captures in ^{nat}Xe

continued from previous page

Xenon isotope	Gamma energy (keV)	From level (keV)	To level (keV)	I_γ per 100 captures	Xenon isotope	Gamma energy (keV)	From level (keV)	To level (keV)	I_γ per 100 captures
^{130}Xe	453.75	4347.1	3893.4	0.7713	^{130}Xe	1122.1	1122.1	0.0	0.4478
^{132}Xe	2714.4	2714.4	0.0	0.7472	^{132}Xe	388.13	3058.1	2670.0	0.4194
^{130}Xe	6184.3	9255.8	3071.5	0.7235	^{130}Xe	8133.7	9255.8	1122.1	0.4124
^{130}Xe	5720.6	9255.8	3535.2	0.7235	^{125}Xe	5387.6	7603.3	2215.7	0.4124
^{130}Xe	662.20	5604.8	4942.6	0.7033	^{125}Xe	782.96	3487.1	2704.1	0.4064
^{130}Xe	633.20	5604.8	4971.6	0.7033	^{125}Xe	4116.2	7603.3	3487.1	0.4064
^{130}Xe	431.50	4971.6	4540.1	0.7033	^{132}Xe	1519.5	2187.2	667.72	0.3994
^{132}Xe	1925.7	4094.5	2168.8	0.6987	^{131}Xe	683.00	1654.2	971.22	0.3980
^{125}Xe	4392.5	7603.3	3210.8	0.6960	^{131}Xe	4950.9	6605.1	1654.2	0.3980
^{130}Xe	1687.4	2223.5	536.09	0.6544	^{125}Xe	426.31	736.85	310.54	0.3953
^{132}Xe	1986.6	4027.0	2040.4	0.3948	^{130}Xe	841.87	3814.2	2972.3	0.2649
^{130}Xe	1850.1	2386.2	536.09	0.3904	^{130}Xe	5441.6	9255.8	3814.2	0.2649
^{129}Xe	39.578	39.578	0.0	0.3884	^{130}Xe	510.38	1632.5	1122.1	0.2646
^{132}Xe	2150.5	3954.2	1803.7	0.3845	^{125}Xe	5458.8	7603.3	2144.5	0.2612
^{130}Xe	1311.7	3535.2	2223.5	0.3720	^{125}Xe	1547.7	2144.5	596.76	0.2612
^{130}Xe	894.94	2017.1	1122.1	0.3686	^{130}Xe	846.93	4540.1	3693.2	0.2592
^{125}Xe	954.50	4573.5	3619.0	0.3673	^{125}Xe	5301.8	7603.3	2301.5	0.2578
^{125}Xe	3029.8	7603.3	4573.5	0.3673	^{125}Xe	1408.0	2301.5	893.50	0.2578
^{132}Xe	4746.6	8935.2	4188.6	0.3602	^{130}Xe	1059.7	3688.1	2628.4	0.2549
^{132}Xe	6346.5	8935.2	2588.7	0.3597	^{130}Xe	5362.5	9255.8	3893.4	0.2488
^{125}Xe	938.57	3210.8	2272.2	0.3480	^{125}Xe	651.05	1387.9	736.85	0.2444
^{125}Xe	660.05	3210.8	2550.8	0.3480	^{125}Xe	688.32	1718.6	1030.3	0.2424
^{130}Xe	2762.9	3299.0	536.09	0.3426	^{125}Xe	546.55	1030.3	483.70	0.2410
^{132}Xe	2575.7	3243.4	667.72	0.3414	^{130}Xe	1706.9	2243.0	536.09	0.2379
^{131}Xe	163.93	163.93	0.0	0.3390	^{125}Xe	519.10	3619.0	3099.9	0.2376
^{131}Xe	642.00	805.93	163.93	0.3390	^{125}Xe	5218.6	7603.3	2384.7	0.2373
^{130}Xe	2886.0	2886.0	0.0	0.3269	^{132}Xe	1456.5	2754.4	1297.9	0.2371
^{130}Xe	1257.5	1793.5	536.09	0.3209	^{130}Xe	209.00	3535.2	3326.2	0.2344
^{132}Xe	1669.7	4094.5	2424.8	0.3199	^{125}Xe	686.37	1579.9	893.50	0.2344
^{132}Xe	506.11	2469.1	1963.0	0.3145	^{132}Xe	1295.3	1963.0	667.72	0.2326

continues on next page

Table B.4: Number of gammas per 100 thermal neutron captures in ^{nat}Xe

continued from previous page

Xenon isotope	Gamma energy (keV)	From level (keV)	To level (keV)	I_γ per 100 captures	Xenon isotope	Gamma energy (keV)	From level (keV)	To level (keV)	I_γ per 100 captures
^{131}Xe	810.37	1616.3	805.93	0.3102	^{133}Xe	856.28	1386.2	529.87	0.2309
^{125}Xe	5348.4	7603.3	2255.0	0.2974	^{133}Xe	4696.3	6440.1	1743.8	0.2309
^{132}Xe	1297.9	1297.9	0.0	0.2937	^{133}Xe	357.60	1743.8	1386.2	0.2309
^{130}Xe	5567.7	9255.8	3688.1	0.2893	^{130}Xe	399.56	2841.6	2442.0	0.2269
^{131}Xe	189.00	1805.3	1616.3	0.2881	^{125}Xe	591.28	1387.9	796.62	0.2249
^{132}Xe	1314.1	2754.4	1440.3	0.2871	^{130}Xe	677.53	4370.7	3693.2	0.2244
^{125}Xe	640.90	893.50	252.60	0.2840	^{130}Xe	4908.7	9255.8	4347.1	0.2244
^{132}Xe	1719.5	4188.6	2469.1	0.2781	^{130}Xe	4885.1	9255.8	4370.7	0.2244
^{130}Xe	2092.3	2628.4	536.09	0.2775	^{125}Xe	371.92	483.70	111.78	0.2216
^{131}Xe	670.20	1641.4	971.22	0.2726	^{125}Xe	832.18	2550.8	1718.6	0.2207
^{132}Xe	1372.1	2670.0	1297.9	0.2718	^{130}Xe	6493.2	9255.8	2762.6	0.2171
^{125}Xe	996.60	5067.5	4070.9	0.2690	^{132}Xe	910.68	2714.4	1803.7	0.2167
^{125}Xe	2535.8	7603.3	5067.5	0.2690	^{129}Xe	196.56	236.14	39.578	0.2135
^{125}Xe	582.96	893.50	310.54	0.2670	^{125}Xe	5031.2	7603.3	2572.1	0.2054
^{133}Xe	529.87	529.87	0.0	0.2665	^{125}Xe	1130.9	2572.1	1441.2	0.2054
^{125}Xe	804.87	2384.7	1579.9	0.2047	^{132}Xe	363.39	1803.7	1440.3	0.1369
^{132}Xe	621.06	2424.8	1803.7	0.2021	^{125}Xe	1378.1	2819.3	1441.2	0.1369
^{130}Xe	6550.9	9255.8	2704.9	0.2005	^{133}Xe	1052.3	1052.3	0.0	0.1360
^{130}Xe	6869.6	9255.8	2386.2	0.1955	^{129}Xe	534.97	771.11	236.14	0.1343
^{130}Xe	539.11	2171.6	1632.5	0.1896	^{130}Xe	252.80	2886.0	2633.2	0.1340
^{130}Xe	5361.5	9255.8	3894.3	0.1882	^{125}Xe	807.54	3619.0	2811.5	0.1331
^{130}Xe	6012.9	9255.8	3242.9	0.1880	^{125}Xe	312.40	4383.3	4070.9	0.1328
^{130}Xe	1019.9	3406.1	2386.2	0.1824	^{125}Xe	4223.8	7603.3	3379.5	0.1311
^{125}Xe	43.260	295.86	252.60	0.1814	^{130}Xe	351.14	3893.4	3542.2	0.1298
^{130}Xe	6104.5	9255.8	3151.3	0.1810	^{130}Xe	2870.0	3406.1	536.09	0.1295
^{130}Xe	2100.8	3894.3	1793.5	0.1759	^{132}Xe	1290.8	2588.7	1297.9	0.1269
^{130}Xe	961.41	2978.5	2017.1	0.1754	^{132}Xe	947.86	3058.1	2110.3	0.1258
^{130}Xe	1096.4	1632.5	536.09	0.1720	^{129}Xe	624.42	1395.5	771.11	0.1251
^{125}Xe	304.40	3379.5	3075.1	0.1710	^{129}Xe	576.67	1972.2	1395.5	0.1251
^{130}Xe	6596.4	9255.8	2659.4	0.1686	^{129}Xe	4935.6	6907.8	1972.2	0.1251

continues on next page

Table B.4: Number of gammas per 100 thermal neutron captures in ^{nat}Xe

continued from previous page

Xenon isotope	Gamma energy (keV)	From level (keV)	To level (keV)	I_γ per 100 captures	Xenon isotope	Gamma energy (keV)	From level (keV)	To level (keV)	I_γ per 100 captures
^{132}Xe	1760.2	3058.1	1297.9	0.1677	^{132}Xe	2002.3	2670.0	667.72	0.1250
^{132}Xe	1254.4	3058.1	1803.7	0.1677	^{125}Xe	748.80	4268.2	3519.4	0.1238
^{130}Xe	162.70	2386.2	2223.5	0.1646	^{125}Xe	3335.1	7603.3	4268.2	0.1238
^{131}Xe	4963.7	6605.1	1641.4	0.1628	^{125}Xe	4784.1	7603.3	2819.3	0.1228
^{130}Xe	137.10	3326.2	3189.1	0.1615	^{130}Xe	6711.4	9255.8	2544.5	0.1200
^{133}Xe	5387.8	6440.1	1052.3	0.1608	^{130}Xe	967.03	2171.6	1204.6	0.1195
^{131}Xe	444.00	2249.3	1805.3	0.1599	^{130}Xe	764.28	3461.2	2696.9	0.1191
^{131}Xe	4355.8	6605.1	2249.3	0.1599	^{130}Xe	1127.4	3299.0	2171.6	0.1188
^{130}Xe	1610.4	3242.9	1632.5	0.1580	^{130}Xe	2008.4	2544.5	536.09	0.1181
^{131}Xe	991.60	3185.9	2194.3	0.1570	^{130}Xe	1727.0	3535.2	1808.2	0.1172
^{131}Xe	389.00	2194.3	1805.3	0.1570	^{125}Xe	484.25	736.85	252.60	0.1146
^{131}Xe	3419.2	6605.1	3185.9	0.1570	^{132}Xe	812.36	2110.3	1297.9	0.1128
^{130}Xe	382.43	2442.0	2059.6	0.1543	^{130}Xe	599.76	2659.4	2059.6	0.1124
^{125}Xe	1162.9	2550.8	1387.9	0.1500	^{125}Xe	628.89	3519.4	2890.5	0.1115
^{130}Xe	7462.3	9255.8	1793.5	0.1449	^{131}Xe	655.68	2297.1	1641.4	0.1097
^{130}Xe	686.03	1808.2	1122.1	0.1400	^{131}Xe	4308.0	6605.1	2297.1	0.1097
^{125}Xe	3220.0	7603.3	4383.3	0.1394	^{130}Xe	2067.0	3189.1	1122.1	0.1097
^{132}Xe	1921.0	2588.7	667.72	0.1394	^{125}Xe	5094.6	7603.3	2508.7	0.1086
^{125}Xe	5428.5	7603.3	2174.8	0.1384	^{125}Xe	1120.8	2508.7	1387.9	0.1086
^{125}Xe	1438.0	2174.8	736.85	0.1384	^{130}Xe	7012.8	9255.8	2243.0	0.1085
^{130}Xe	7032.3	9255.8	2223.5	0.1084	^{130}Xe	7238.7	9255.8	2017.1	0.07243
^{130}Xe	1154.6	3326.2	2171.6	0.1077	^{125}Xe	3310.7	7603.3	4292.6	0.07235
^{125}Xe	5188.5	7603.3	2414.8	0.1076	^{125}Xe	696.31	2006.4	1310.1	0.07166
^{130}Xe	402.50	4942.6	4540.1	0.1073	^{130}Xe	470.85	2103.4	1632.5	0.06893
^{129}Xe	732.99	1755.3	1022.3	0.1056	^{125}Xe	208.41	3486.3	3277.9	0.06826
^{129}Xe	580.11	1022.3	442.20	0.1056	^{130}Xe	2284.0	3406.1	1122.1	0.06749
^{129}Xe	5152.5	6907.8	1755.3	0.1056	^{129}Xe	712.08	2048.2	1336.1	0.06718
^{129}Xe	402.62	442.20	39.578	0.1056	^{129}Xe	4859.6	6907.8	2048.2	0.06718
^{125}Xe	4452.2	7603.3	3151.1	0.1032	^{130}Xe	937.21	2954.3	2017.1	0.06658
^{130}Xe	1500.3	2704.9	1204.6	0.1023	^{135}Xe	4231.0	6382.5	2151.5	0.06603

continues on next page

Table B.4: Number of gammas per 100 thermal neutron captures in ^{nat}Xe

continued from previous page

Xenon isotope	Gamma energy (keV)	From level (keV)	To level (keV)	I_γ per 100 captures	Xenon isotope	Gamma energy (keV)	From level (keV)	To level (keV)	I_γ per 100 captures
^{130}Xe	5475.3	9255.8	3780.5	0.1013	^{135}Xe	2151.5	2151.5	0.0	0.06603
^{125}Xe	675.09	2255.0	1579.9	0.09913	^{130}Xe	499.78	2886.0	2386.2	0.06537
^{125}Xe	867.06	2255.0	1387.9	0.09913	^{130}Xe	5794.6	9255.8	3461.2	0.06440
^{125}Xe	669.46	2255.0	1585.5	0.09913	^{125}Xe	778.80	2166.7	1387.9	0.06224
^{130}Xe	1272.1	1808.2	536.09	0.09797	^{125}Xe	3550.5	7603.3	4052.8	0.06163
^{132}Xe	669.95	2110.3	1440.3	0.09479	^{125}Xe	4325.4	7603.3	3277.9	0.06112
^{130}Xe	756.04	4217.2	3461.2	0.09403	^{125}Xe	783.25	1579.9	796.62	0.06093
^{130}Xe	5929.6	9255.8	3326.2	0.09403	^{133}Xe	5089.7	6440.1	1350.4	0.05936
^{130}Xe	5267.4	9255.8	3988.4	0.09403	^{132}Xe	431.91	2394.9	1963.0	0.05877
^{130}Xe	5038.6	9255.8	4217.2	0.09403	^{132}Xe	687.73	1985.7	1297.9	0.05875
^{125}Xe	805.02	2811.5	2006.4	0.09400	^{130}Xe	338.65	2442.0	2103.4	0.05865
^{125}Xe	519.20	3898.7	3379.5	0.09296	^{130}Xe	981.10	3959.6	2978.5	0.05791
^{125}Xe	3704.6	7603.3	3898.7	0.09296	^{130}Xe	9255.8	9255.8	0.0	0.05791
^{132}Xe	889.30	2187.2	1297.9	0.08787	^{130}Xe	5296.2	9255.8	3959.6	0.05791
^{130}Xe	806.86	2978.5	2171.6	0.08772	^{130}Xe	5278.5	9255.8	3977.3	0.05791
^{132}Xe	284.63	2394.9	2110.3	0.08707	^{125}Xe	344.16	596.76	252.60	0.05754
^{125}Xe	573.28	1310.1	736.85	0.08668	^{125}Xe	878.89	3151.1	2272.2	0.05687
^{130}Xe	825.02	2633.2	1808.2	0.08546	^{125}Xe	618.28	2890.5	2272.2	0.05651
^{130}Xe	603.57	1808.2	1204.6	0.08118	^{130}Xe	313.40	2659.4	2346.0	0.05619
^{132}Xe	8935.2	8935.2	0.0	0.08032	^{130}Xe	286.36	2346.0	2059.6	0.05619
^{130}Xe	2029.2	3151.3	1122.1	0.07959	^{125}Xe	339.31	1209.9	870.60	0.05596
^{129}Xe	752.69	1576.0	823.31	0.07919	^{125}Xe	858.97	3131.2	2272.2	0.05556
^{129}Xe	587.17	823.31	236.14	0.07919	^{130}Xe	894.50	3780.5	2886.0	0.05519
^{132}Xe	984.45	2424.8	1440.3	0.07679	^{130}Xe	735.52	2978.5	2243.0	0.05482
^{130}Xe	1389.0	3406.1	2017.1	0.07661	^{125}Xe	806.30	4292.6	3486.3	0.05481
^{130}Xe	896.74	2704.9	1808.2	0.05421	^{125}Xe	524.35	3075.1	2550.8	0.03528
^{125}Xe	555.73	2414.8	1859.1	0.05379	^{131}Xe	636.99	636.99	0.0	0.03525
^{125}Xe	1618.2	2414.8	796.62	0.05379	^{130}Xe	1181.6	2386.2	1204.6	0.03480
^{125}Xe	248.30	3379.5	3131.2	0.05303	^{132}Xe	2148.2	4188.6	2040.4	0.03477
^{125}Xe	331.87	3151.1	2819.3	0.05175	^{130}Xe	1054.9	3688.1	2633.2	0.03441

continues on next page

Table B.4: Number of gammas per 100 thermal neutron captures in ^{nat}Xe

continued from previous page

Xenon isotope	Gamma energy (keV)	From level (keV)	To level (keV)	I_γ per 100 captures	Xenon isotope	Gamma energy (keV)	From level (keV)	To level (keV)	I_γ per 100 captures
^{130}Xe	671.39	1793.5	1122.1	0.05134	^{130}Xe	855.20	3151.3	2296.1	0.03382
^{127}Xe	124.75	124.75	0.0	0.05126	^{129}Xe	817.42	1336.1	518.70	0.03359
^{125}Xe	595.74	2811.5	2215.7	0.04982	^{129}Xe	670.70	1336.1	665.42	0.03359
^{132}Xe	2384.9	4188.6	1803.7	0.04728	^{125}Xe	625.44	2550.8	1925.3	0.03310
^{130}Xe	2344.8	3977.3	1632.5	0.04596	^{133}Xe	733.97	1609.3	875.33	0.03263
^{125}Xe	548.94	1859.1	1310.1	0.04539	^{133}Xe	452.70	2062.0	1609.3	0.03263
^{131}Xe	80.185	80.185	0.0	0.04438	^{133}Xe	4378.1	6440.1	2062.0	0.03263
^{131}Xe	284.30	364.49	80.185	0.04438	^{130}Xe	1987.0	3780.5	1793.5	0.03246
^{130}Xe	622.96	2704.9	2082.0	0.04398	^{125}Xe	273.84	870.60	596.76	0.03243
^{132}Xe	784.98	2588.7	1803.7	0.04321	^{130}Xe	1614.1	2150.2	536.09	0.03223
^{130}Xe	2615.2	3151.3	536.09	0.04298	^{133}Xe	875.33	875.33	0.0	0.03190
^{125}Xe	618.54	2006.4	1387.9	0.04228	^{125}Xe	202.79	3277.9	3075.1	0.03168
^{125}Xe	908.40	3075.1	2166.7	0.04150	^{129}Xe	604.00	2180.0	1576.0	0.03160
^{125}Xe	848.65	1585.5	736.85	0.04046	^{129}Xe	4727.8	6907.8	2180.0	0.03160
^{125}Xe	725.52	2166.7	1441.2	0.03983	^{125}Xe	370.96	3075.1	2704.1	0.03154
^{130}Xe	7447.6	9255.8	1808.2	0.03975	^{125}Xe	997.60	4052.8	3055.2	0.03097
^{130}Xe	488.83	3461.2	2972.3	0.03931	^{125}Xe	943.56	2384.7	1441.2	0.03070
^{130}Xe	877.35	2082.0	1204.6	0.03927	^{132}Xe	1148.4	2588.7	1440.3	0.03067
^{132}Xe	1757.1	2424.8	667.72	0.03799	^{125}Xe	952.90	4052.8	3099.9	0.03066
^{130}Xe	1745.4	3988.4	2243.0	0.03791	^{130}Xe	5632.9	9255.8	3622.9	0.02905
^{129}Xe	479.12	518.70	39.578	0.03762	^{130}Xe	1760.0	2296.1	536.09	0.02889
^{130}Xe	908.32	3151.3	2243.0	0.03661	^{131}Xe	794.67	1600.6	805.93	0.02881
^{130}Xe	1176.0	3326.2	2150.2	0.03661	^{131}Xe	204.70	1805.3	1600.6	0.02881
^{125}Xe	335.35	335.35	0.0	0.03650	^{125}Xe	148.35	483.70	335.35	0.02881
^{130}Xe	8719.7	9255.8	536.09	0.03612	^{132}Xe	1442.6	2110.3	667.72	0.02866
^{130}Xe	642.49	4184.7	3542.2	0.03612	^{125}Xe	802.87	3075.1	2272.2	0.02822
^{130}Xe	5071.1	9255.8	4184.7	0.03612	^{132}Xe	1617.8	3058.1	1440.3	0.02727
^{132}Xe	2187.2	2187.2	0.0	0.03594	^{129}Xe	870.30	2446.3	1576.0	0.02724
^{125}Xe	723.81	2890.5	2166.7	0.03560	^{129}Xe	4461.5	6907.8	2446.3	0.02724
^{131}Xe	334.23	971.22	636.99	0.03556	^{125}Xe	458.64	3277.9	2819.3	0.02661

continues on next page

Table B.4: Number of gammas per 100 thermal neutron captures in ^{nat}Xe

continued from previous page

Xenon isotope	Gamma energy (keV)	From level (keV)	To level (keV)	L_γ per 100 captures	Xenon isotope	Gamma energy (keV)	From level (keV)	To level (keV)	L_γ per 100 captures
^{125}Xe	573.75	3277.9	2704.1	0.02598	^{125}Xe	1062.2	3277.9	2215.7	0.01774
^{130}Xe	427.92	1632.5	1204.6	0.02593	^{137}Xe	1218.0	1218.0	0.0	0.01731
^{125}Xe	188.83	796.62	607.79	0.02581	^{125}Xe	898.13	2616.7	1718.6	0.01642
^{135}Xe	3904.6	6382.5	2477.9	0.02563	^{125}Xe	504.04	2819.3	2315.2	0.01642
^{125}Xe	416.63	1310.1	893.50	0.02514	^{125}Xe	202.55	2819.3	2616.7	0.01642
^{125}Xe	692.00	1585.5	893.50	0.02509	^{125}Xe	654.25	919.84	265.59	0.01606
^{125}Xe	888.50	3055.2	2166.7	0.02376	^{127}Xe	670.77	1751.6	1080.8	0.01590
^{135}Xe	288.46	288.46	0.0	0.02316	^{127}Xe	684.83	2307.1	1622.3	0.01546
^{135}Xe	2189.4	2477.9	288.46	0.02307	^{127}Xe	471.80	2778.9	2307.1	0.01546
^{125}Xe	286.22	596.76	310.54	0.02302	^{130}Xe	837.10	3988.4	3151.3	0.01517
^{133}Xe	820.51	1350.4	529.87	0.02293	^{129}Xe	318.18	318.18	0.0	0.01506
^{130}Xe	697.82	3326.2	2628.4	0.02261	^{127}Xe	5189.8	7223.0	2033.2	0.01451
^{127}Xe	217.48	342.23	124.75	0.02260	^{129}Xe	343.71	665.42	321.71	0.01434
^{130}Xe	1481.0	2017.1	536.09	0.02248	^{125}Xe	378.30	2384.7	2006.4	0.01433
^{133}Xe	1350.4	1350.4	0.0	0.02223	^{125}Xe	1518.6	2315.2	796.62	0.01428
^{131}Xe	4988.8	6605.1	1616.3	0.02211	^{137}Xe	1937.5	4025.5	2088.0	0.01416
^{127}Xe	595.94	938.17	342.23	0.02115	^{127}Xe	550.48	1080.8	530.31	0.01407
^{125}Xe	665.66	1585.5	919.84	0.02104	^{130}Xe	132.03	2442.0	2310.0	0.01389
^{130}Xe	1355.2	3988.4	2633.2	0.02085	^{129}Xe	5493.5	6907.8	1414.3	0.01377
^{127}Xe	684.10	1622.3	938.17	0.02081	^{127}Xe	308.98	308.98	0.0	0.01371
^{125}Xe	355.19	607.79	252.60	0.02069	^{130}Xe	826.20	3780.5	2954.3	0.01364
^{125}Xe	268.50	2819.3	2550.8	0.02053	^{125}Xe	674.79	2890.5	2215.7	0.01356
^{129}Xe	5331.8	6907.8	1576.0	0.02036	^{127}Xe	405.56	530.31	124.75	0.01301
^{132}Xe	478.42	2588.7	2110.3	0.01952	^{130}Xe	2544.5	2544.5	0.0	0.01299
^{125}Xe	839.48	3055.2	2215.7	0.01948	^{127}Xe	519.11	828.09	308.98	0.01279
^{129}Xe	347.24	665.42	318.18	0.01937	^{125}Xe	473.40	3959.7	3486.3	0.01261
^{125}Xe	513.51	1310.1	796.62	0.01907	^{125}Xe	332.90	4292.6	3959.7	0.01261
^{130}Xe	1449.4	3242.9	1793.5	0.01896	^{135}Xe	4127.0	6382.5	2255.5	0.01257
^{129}Xe	282.13	321.71	39.578	0.01872	^{125}Xe	561.06	1585.5	1024.4	0.01254
^{133}Xe	262.70	262.70	0.0	0.01843	^{125}Xe	690.36	3075.1	2384.7	0.01245

continues on next page

Table B.4: Number of gammas per 100 thermal neutron captures in ^{nat}Xe

continued from previous page

Xenon isotope	Gamma energy (keV)	From level (keV)	To level (keV)	I_γ per 100 captures	Xenon isotope	Gamma energy (keV)	From level (keV)	To level (keV)	I_γ per 100 captures
^{129}Xe	4871.6	6907.8	2036.2	0.01842	^{133}Xe	789.60	1052.3	262.70	0.01237
^{125}Xe	12.990	265.59	252.60	0.01813	^{130}Xe	915.80	3894.3	2978.5	0.01232
^{125}Xe	255.85	3075.1	2819.3	0.01785	^{125}Xe	464.20	3519.4	3055.2	0.01227
^{125}Xe	859.38	3075.1	2215.7	0.01784	^{125}Xe	565.26	2006.4	1441.2	0.01218
^{125}Xe	812.81	2819.3	2006.4	0.01779	^{130}Xe	363.46	2171.6	1808.2	0.01214
^{125}Xe	466.65	2890.5	2423.9	0.01187	^{137}Xe	870.00	2088.0	1218.0	0.00762
^{125}Xe	269.74	1579.9	1310.1	0.01172	^{125}Xe	192.92	1030.3	837.33	0.00723
^{130}Xe	698.45	3242.9	2544.5	0.01106	^{129}Xe	592.11	1414.3	822.16	0.00688
^{125}Xe	893.94	2819.3	1925.3	0.01095	^{129}Xe	324.79	1414.3	1089.5	0.00688
^{127}Xe	4444.1	7223.0	2778.9	0.01091	^{127}Xe	218.00	3620.8	3402.8	0.00684
^{125}Xe	386.90	870.60	483.70	0.01081	^{133}Xe	680.26	680.26	0.0	0.00680
^{125}Xe	466.43	3277.9	2811.5	0.01077	^{125}Xe	105.10	3075.1	2970.0	0.00664
^{130}Xe	916.92	3988.4	3071.5	0.01062	^{127}Xe	172.35	297.10	124.75	0.00660
^{127}Xe	3820.2	7223.0	3402.8	0.01057	^{127}Xe	5249.4	7223.0	1973.6	0.00657
^{125}Xe	505.95	1536.2	1030.3	0.01056	^{127}Xe	1561.6	1973.6	411.97	0.00657
^{125}Xe	326.29	1536.2	1209.9	0.01056	^{137}Xe	867.93	2088.0	1220.1	0.00655
^{130}Xe	1814.7	3622.9	1808.2	0.01037	^{129}Xe	570.78	1089.5	518.70	0.00652
^{130}Xe	206.62	2310.0	2103.4	0.01029	^{133}Xe	670.12	1350.4	680.26	0.00642
^{133}Xe	522.43	1052.3	529.87	0.01020	^{127}Xe	637.21	1283.1	645.90	0.00639
^{137}Xe	1220.1	1220.1	0.0	0.01010	^{130}Xe	765.08	3151.3	2386.2	0.00637
^{127}Xe	680.60	1508.7	828.09	0.00990	^{127}Xe	734.68	2243.4	1508.7	0.00627
^{125}Xe	771.84	1024.4	252.60	0.00980	^{127}Xe	411.97	411.97	0.0	0.00624
^{132}Xe	559.73	2670.0	2110.3	0.00978	^{125}Xe	387.38	3277.9	2890.5	0.00602
^{135}Xe	1131.5	1131.5	0.0	0.00960	^{127}Xe	746.14	2497.7	1751.6	0.00601
^{135}Xe	1124.0	2255.5	1131.5	0.00958	^{133}Xe	438.93	1350.4	911.45	0.00596
^{130}Xe	1764.9	3988.4	2223.5	0.00948	^{137}Xe	1925.5	4025.5	2100.0	0.00589
^{127}Xe	4979.6	7223.0	2243.4	0.00947	^{129}Xe	500.45	822.16	321.71	0.00584
^{129}Xe	1265.1	2036.2	771.11	0.00921	^{137}Xe	2034.3	4025.5	1991.2	0.00581
^{129}Xe	1213.2	2036.2	823.05	0.00921	^{125}Xe	422.41	3075.1	2652.7	0.00581
^{125}Xe	501.98	837.33	335.35	0.00884	^{127}Xe	1446.1	2033.2	587.07	0.00580

continues on next page

Table B.4: Number of gammas per 100 thermal neutron captures in ^{nat}Xe

continued from previous page

Xenon isotope	Gamma energy (keV)	From level (keV)	To level (keV)	L_γ per 100 captures	Xenon isotope	Gamma energy (keV)	From level (keV)	To level (keV)	L_γ per 100 captures
^{130}Xe	1451.3	3622.9	2171.6	0.00882	^{127}Xe	1321.6	2033.2	711.61	0.00580
^{130}Xe	3977.3	3977.3	0.0	0.00873	^{127}Xe	127.00	3402.8	3275.8	0.00580
^{132}Xe	684.36	2670.0	1985.7	0.00870	^{127}Xe	434.10	3402.8	2968.7	0.00580
^{125}Xe	965.57	1859.1	893.50	0.00862	^{127}Xe	120.00	3402.8	3282.8	0.00580
^{132}Xe	1727.2	2394.9	667.72	0.00826	^{125}Xe	732.30	2970.0	2237.7	0.00577
^{129}Xe	278.60	318.18	39.578	0.00813	^{137}Xe	601.05	601.05	0.0	0.00569
^{127}Xe	3940.2	7223.0	3282.8	0.00786	^{127}Xe	5471.4	7223.0	1751.6	0.00564
^{127}Xe	952.30	2968.7	2016.4	0.00779	^{130}Xe	985.38	3622.9	2637.5	0.00550
^{127}Xe	733.29	2016.4	1283.1	0.00779	^{130}Xe	2101.4	2637.5	536.09	0.00550
^{127}Xe	251.90	2968.7	2716.8	0.00779	^{132}Xe	1097.0	2394.9	1297.9	0.00545
^{129}Xe	321.71	321.71	0.0	0.00543	^{125}Xe	764.30	4383.3	3619.0	0.00332
^{125}Xe	126.77	3277.9	3151.1	0.00539	^{125}Xe	1283.4	4383.3	3099.9	0.00332
^{125}Xe	705.29	2423.9	1718.6	0.00526	^{127}Xe	375.46	375.46	0.0	0.00327
^{127}Xe	303.67	645.90	342.23	0.00503	^{127}Xe	935.00	4136.8	3201.8	0.00327
^{125}Xe	667.24	919.84	252.60	0.00498	^{127}Xe	889.70	3201.8	2312.1	0.00327
^{125}Xe	157.90	4292.6	4134.7	0.00493	^{127}Xe	803.41	2312.1	1508.7	0.00327
^{132}Xe	147.28	2110.3	1963.0	0.00485	^{127}Xe	3086.2	7223.0	4136.8	0.00327
^{125}Xe	433.49	1030.3	596.76	0.00482	^{130}Xe	826.00	3977.3	3151.3	0.00322
^{130}Xe	1545.9	2082.0	536.09	0.00471	^{127}Xe	776.62	2243.4	1466.8	0.00320
^{137}Xe	773.18	1991.2	1218.0	0.00465	^{125}Xe	279.20	1859.1	1579.9	0.00318
^{125}Xe	1036.0	2423.9	1387.9	0.00458	^{127}Xe	462.31	587.07	124.75	0.00307
^{127}Xe	503.90	3282.8	2778.9	0.00455	^{132}Xe	1126.9	2424.8	1297.9	0.00303
^{127}Xe	785.10	3282.8	2497.7	0.00455	^{137}Xe	1302.7	1302.7	0.0	0.00303
^{127}Xe	314.10	3282.8	2968.7	0.00455	^{137}Xe	2100.0	2100.0	0.0	0.00302
^{137}Xe	1512.2	1512.2	0.0	0.00450	^{125}Xe	887.66	2423.9	1536.2	0.00295
^{130}Xe	736.90	3622.9	2886.0	0.00436	^{127}Xe	390.06	711.61	321.55	0.00293
^{132}Xe	591.19	2394.9	1803.7	0.00435	^{127}Xe	1908.4	2033.2	124.75	0.00290
^{137}Xe	608.37	4025.5	3417.1	0.00435	^{125}Xe	297.25	607.79	310.54	0.00290
^{137}Xe	3417.1	3417.1	0.0	0.00435	^{125}Xe	784.38	3000.1	2215.7	0.00285
^{127}Xe	3602.2	7223.0	3620.8	0.00426	^{125}Xe	277.79	3277.9	3000.1	0.00285

continues on next page

Table B.4: Number of gammas per 100 thermal neutron captures in ^{nat}Xe

continued from previous page

Xenon isotope	Gamma energy (keV)	From level (keV)	To level (keV)	I_γ per 100 captures	Xenon isotope	Gamma energy (keV)	From level (keV)	To level (keV)	I_γ per 100 captures
^{127}Xe	45.130	342.23	297.10	0.00407	^{130}Xe	1028.1	2150.2	1122.1	0.00280
^{137}Xe	2513.3	4025.5	1512.2	0.00403	^{125}Xe	856.81	4134.7	3277.9	0.00273
^{125}Xe	757.02	2237.7	1480.7	0.00401	^{137}Xe	2229.4	4025.5	1796.1	0.00267
^{127}Xe	965.24	2716.8	1751.6	0.00390	^{129}Xe	548.96	588.53	39.578	0.00259
^{127}Xe	1094.5	2716.8	1622.3	0.00390	^{125}Xe	643.35	1480.7	837.33	0.00259
^{127}Xe	4254.3	7223.0	2968.7	0.00377	^{135}Xe	2477.9	2477.9	0.0	0.00256
^{129}Xe	196.99	518.70	321.71	0.00376	^{127}Xe	587.07	587.07	0.0	0.00254
^{125}Xe	1485.4	2926.6	1441.2	0.00374	^{125}Xe	325.32	3277.9	2952.6	0.00254
^{125}Xe	148.50	3075.1	2926.6	0.00374	^{125}Xe	146.69	3277.9	3131.2	0.00253
^{130}Xe	2296.1	2296.1	0.0	0.00370	^{125}Xe	1264.8	2652.7	1387.9	0.00243
^{129}Xe	411.55	823.05	411.50	0.00362	^{127}Xe	348.80	645.90	297.10	0.00241
^{129}Xe	504.87	823.05	318.18	0.00362	^{127}Xe	321.55	321.55	0.0	0.00239
^{129}Xe	234.52	823.05	588.53	0.00362	^{127}Xe	468.00	4088.8	3620.8	0.00236
^{130}Xe	250.40	2310.0	2059.6	0.00360	^{133}Xe	372.04	1052.3	680.26	0.00231
^{125}Xe	793.62	2652.7	1859.1	0.00338	^{133}Xe	648.75	911.45	262.70	0.00228
^{125}Xe	187.84	483.70	295.86	0.00222	^{133}Xe	417.56	680.26	262.70	0.00161
^{125}Xe	648.40	4134.7	3486.3	0.00221	^{129}Xe	411.50	411.50	0.0	0.00159
^{125}Xe	223.57	335.35	111.78	0.00219	^{130}Xe	2150.2	2150.2	0.0	0.00151
^{129}Xe	371.92	411.50	39.578	0.00218	^{137}Xe	2722.7	4025.5	1302.7	0.00146
^{132}Xe	707.01	2670.0	1963.0	0.00217	^{127}Xe	880.73	3275.8	2395.1	0.00145
^{127}Xe	638.66	1466.8	828.09	0.00216	^{127}Xe	778.10	3275.8	2497.7	0.00145
^{137}Xe	3424.4	4025.5	601.05	0.00215	^{127}Xe	772.80	2395.1	1622.3	0.00145
^{127}Xe	3134.2	7223.0	4088.8	0.00215	^{127}Xe	611.20	3275.8	2664.6	0.00145
^{125}Xe	1005.1	2315.2	1310.1	0.00214	^{127}Xe	307.10	3275.8	2968.7	0.00145
^{137}Xe	881.97	2100.0	1218.0	0.00211	^{137}Xe	576.01	1796.1	1220.1	0.00142
^{137}Xe	2309.9	4025.5	1715.6	0.00208	^{127}Xe	344.94	1283.1	938.17	0.00140
^{125}Xe	342.20	607.79	265.59	0.00207	^{125}Xe	163.46	3486.3	3322.8	0.00137
^{137}Xe	385.15	986.20	601.05	0.00193	^{137}Xe	1534.3	1534.3	0.0	0.00134
^{137}Xe	748.75	4025.5	3276.7	0.00191	^{137}Xe	1416.7	4025.5	2608.8	0.00134
^{132}Xe	866.29	2670.0	1803.7	0.00190	^{127}Xe	586.86	711.61	124.75	0.00129

continues on next page

Table B.4: Number of gammas per 100 thermal neutron captures in ^{nat}Xe

continued from previous page

Xenon isotope	Gamma energy (keV)	From level (keV)	To level (keV)	I_γ per 100 captures	Xenon isotope	Gamma energy (keV)	From level (keV)	To level (keV)	I_γ per 100 captures
^{137}Xe	1715.6	1715.6	0.0	0.00188	^{129}Xe	303.46	822.16	518.70	0.00127
^{125}Xe	1633.9	3075.1	1441.2	0.00187	^{137}Xe	2216.7	4025.5	1808.8	0.00126
^{133}Xe	911.45	911.45	0.0	0.00187	^{137}Xe	1808.8	1808.8	0.0	0.00126
^{125}Xe	713.90	1024.4	310.54	0.00186	^{130}Xe	1174.0	2296.1	1122.1	0.00124
^{127}Xe	183.16	1080.8	897.63	0.00183	^{125}Xe	785.87	2952.6	2166.7	0.00122
^{133}Xe	381.58	911.45	529.87	0.00182	^{127}Xe	154.85	530.31	375.46	0.00117
^{133}Xe	1087.7	1350.4	262.70	0.00181	^{137}Xe	1991.2	1991.2	0.0	0.00116
^{125}Xe	1441.1	2237.7	796.62	0.00176	^{137}Xe	893.25	2608.8	1715.6	0.00112
^{127}Xe	522.17	897.63	375.46	0.00172	^{137}Xe	578.08	1796.1	1218.0	0.00107
^{130}Xe	227.55	2171.6	1944.1	0.00171	^{127}Xe	292.27	938.17	645.90	0.00106
^{129}Xe	4735.8	6907.8	2172.0	0.00165	^{127}Xe	674.38	1466.8	792.37	0.00104
^{129}Xe	1349.0	2172.0	823.05	0.00165	^{125}Xe	272.44	607.79	335.35	0.00103
^{137}Xe	1573.1	4025.5	2452.4	0.00163	^{137}Xe	2058.7	3276.7	1218.0	0.00102
^{137}Xe	1466.2	2452.4	986.20	0.00163	^{132}Xe	306.56	2110.3	1803.7	0.00102
^{135}Xe	2255.5	2255.5	0.0	0.00163					

Table B.4: Number of gammas per 100 thermal neutron captures in ^{nat}Xe

Appendix C

Radiation level in the TPC electronics

ALICE, the dedicated heavy-ion experiment at the CERN LHC [152], will study a variety of colliding systems ranging from pp and pA to light and heavy nuclei.

High beam energy ($Z/A \times 7$ TeV/nucleon) at the LHC combined with high luminosities result in a high primary particle production rate. Many of these particles produce secondaries through hadronic and electromagnetic cascades in the absorbers and structural elements of ALICE. They produce particle fluxes even far away from the interaction point and in shielded regions. Detailed particle transport simulations are needed to calculate the doses and neutron fluences in these regions. These quantities are needed to evaluate the risk of radiation damage and activation of detectors and electronics equipment. Here we will analyze and present the contributions to the radiation background in the region where the ALICE TPC front-end electronics is located concerning the expected particle fluences, fluxes and number of total particles, for a 10 years standard running scenario including Pb–Pb runs.

We also quantify the slow proton background that would originate from a small admixture of CH₄ or N₂ to the 90% Ne, 10% CO₂ TPC gas. All these results were obtained from simulations using the FLUKA transport code.

C.1 TPC detector and front-end electronics

The Time Projection Chamber (TPC) [154], surrounds the Inner Tracking System (ITS) and is the main tracking detector of the central barrel and together with the ITS, TRD and TOF has to provide charged particle momentum measurement, particle identification and vertex determination with sufficient momentum resolution, two track separation and dE/dx resolution for studies of hadronic and leptonic signals in the region $P_t < 10$ GeV/c and pseudorapidities $|\eta| < 0.9$. To cover this acceptance the TPC is of cylindrical design with an inner radius of about 80 cm, an outer radius of about 250 cm and an overall length in the beam direction of 500 cm. A gas mixture of 90% Ne, 10% CO₂ has been chosen for operating the detector. The front-end electronics have to read out the charge detected by all these pads located on the readout chambers at the TPC end-plates.

The ALICE TPC [155] is a 88 m³ cylinder filled with a gas and divided in two drift regions by the central electrode located at its axial centre. A field cage creates a uniform electric field along each half of the chamber. Charged particles traversing the TPC volume ionise the gas along their path, liberating electrons that drift towards the end plates of the chamber. The necessary signal amplification is provided through avalanche effect in the vicinity of the anode wires. Moving from the anode wire towards the surrounding electrodes, the positive ions created in the avalanche induce a positive current signal on the pad plane. This current signal, which is characterised by a fast rise time (less than 1 ns) and a long tail with a rather complex shape, carries a charge that, for the minimum ionising particle, is of 4.8fC.

The readout of the signal is done by the 570132 pads that form the cathode plane of conventional multi-wire proportional chambers located at the TPC end plates. The signals from the pads are processed by 4356 front-end cards located some 10 cm away from the pad plane via flexible capton cables. In the front-end card a custom made charge sensitive amplifier transforms the charge induced in the pads in a differential semi-gaussian signal that is fed to the input of the ALTRO chip. Each ALTRO contain 16 channels

operating concurrently that digitize and process the input signals. Upon arrival of a first level trigger, the data stream is stored in a memory. The maximum number of samples that can be continuously processed for each trigger (event data stream) is 1000. When the second level trigger (accept or reject) is received, the latest event data stream is either frozen in the data memory, until its complete readout takes place, or discarded. The data memory has the capacity to store up to 8 event data streams. The readout can take place any time, at a speed of 200MByte/sec through a 40-bit wide backplane bus linking the Front End Cards to the Readout Control Unit.

The theoretical predictions for the charged particle multiplicity expected in such collisions range from 2000 up to 8000 charged particles per rapidity unit at mid-rapidity resulting in 80 000 primary charged particles in the central barrel acceptance for the worst case scenario. The expected luminosity of $10^{27} \text{ cm}^{-2}\text{s}^{-1}$ will lead to an inelastic event rate of 8 kHz.

The inaccessibility of the ALICE experiment during the entire year of LHC running makes stringent quality tests of the readout electronics mandatory before installation. The radiation load on the TPC is relatively low with a neutron flux received over 10 years of less than 10^{11} neutrons/cm². Thus, standard radiation-soft technologies are suitable for the implementation of this electronics. Nevertheless, some special care should be taken to protect the system against potential damage caused by Single Event Effects (SEEs). Concerning the SEU (Single Event Upset) in the FPGAs probably only the protons above 10-20 MeV can cause bit-flips. Neutrons can contribute to this effect only if they scatter in the plastic of the chip package or in the PCB with a proton and kick the fast proton into the silicon.

C.1.1 Detector geometry and scoring

The TPC volume as described in FLUKA is shown in Fig. 9.5 of the Chapter 9. The TPC gas volume is approximated by a cylinder with an inner radius of about 79.25 cm, an outer radius of about 278 cm and an overall length in the beam direction of 550 cm ($-275 < Z < 275\text{cm}$). The TPC gas mixture

Table C.1: Dimensions of the scoring layers.

Layers	Outer radial distance [cm]	Volume [cm ³]	Area [cm ²]
1	127.20	3210.7	32107
2	177.20	4781.5	47815
3	227.20	6352.3	63523
4	278.17	8092.3	80923

consists of 90% Ne, 10% CO₂. There is a correspondence between FLUKA materials and low-energy neutron cross-sections. Since FLUKA low-energy neutron library does not include neon, fluorine has been chosen instead due to its similar properties.

Since the front-end electronics will be placed on the readout chambers at the TPC end-caps, we define 4 concentric cylindrical layers of silicon at radial distances from 77.2 up to 278.17 cm with 1 mm width along the beam direction ($-296.1 < Z < -296\text{cm}$ and $284 < Z < 284.1\text{cm}$), 10 cm away from the TPC limiting planes. The dimensions of the layers are summarized in Table C.1. We perform two studies for both end-plates (muon-aborber and non-aborber side) considering that are made by aluminium of 1 cm width ($-276 < Z < -275\text{cm}$ and $275 < Z < 276\text{cm}$). The two scoring regions (muon-aborber and non-aborber side, the right and left group of rings respectively) are shown in Fig. C.1.

Events with average multiplicity of 80 000 primary pions and kaons were transported through the material of the experiment and experimental area which was described with about 3200 volumes.

C.1.2 Particle fluences based on FLUKA calculations

Firstly we estimate the number of particles in both sides per central event. The results are presented in Tables C.2 and C.3 for the absorber and non-aborber side respectively. In the muon-aborber side there are 45% more neutrons and 40% less charged particles. In both cases most of the neutrons

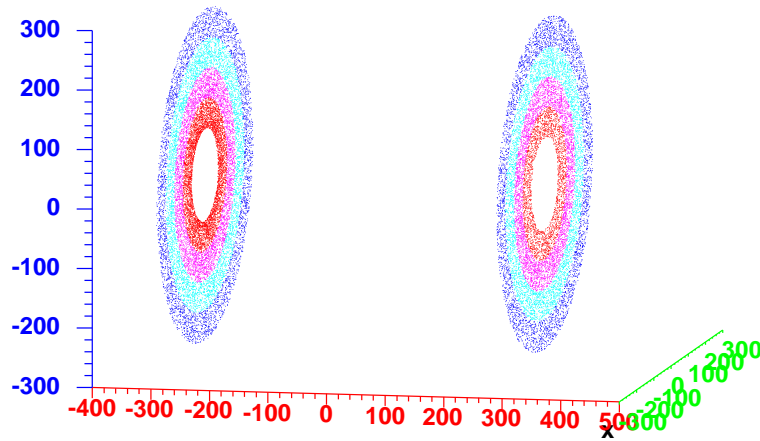


Figure C.1: The two scoring regions (four silicon layers).

come from the muon absorber side as shown in Fig. C.3. The age and energy spectra of the particles that are of main importance for this study can be seen in Figs. C.2 and C.4 respectively.

The way used to calculate particle fluxes in the TPC is via a special tool of FLUKA, the track-length estimator. Defining 4 such estimators, each of them pointing on one silicon layer and taking the average from them during one FLUKA event (one central event), we calculate the total track-length. The track-length is more meaningful than the number of particles, because any signal, or any damage, are proportional to the energy deposited, or to the number of collisions which are all proportional to the track-length. Dividing the total track-length with the volume of the scoring region we obtain the total response or *cumulative fluence* expressed as (particles/cm²/primary).

The results of the FLUKA track-length estimator are always given as differential distributions of fluence in energy (cm⁻² GeV⁻¹ per incident primary unit weight). In figures displaying differential fluence versus energy over a

large range of energy, the abscissa is often the logarithm of energy [144]. In making the coordinate transformation from linear energy and particle-differential fluence distribution $d\Phi/dE$ to logarithmic energy, it is desirable to preserve the fact that relative areas in different energy regions represent relative fluences. This can easily be accomplished by multiplying the conventional particle-differential fluence distribution $d\Phi/dE$ by the energy because $d\Phi/d(\log E) = d\Phi/(dE/E) = E d\Phi/dE$.

Figures C.5, C.6, C.7, C.8, C.9 and C.10 show the lethargy and kinetic energy spectra of neutrons, all charged particles, protons, pions, kaons and photons respectively. The lethargy spectra are designed to allow visual integration of fluence having the areas under the curves proportional to the fluence. As can be observed, protons, pions and kaons of $E_{\text{kin}} > 10$ MeV can contribute in the fluence. Their respective kinetic energy spectra (same points but both axes are logarithmic) are not very useful but we provide them since is the method of plotting neutron-energy spectra generally chosen.

The particle fluences per central event are shown in Tables C.4 and C.5.

The fluxes (particles/cm²/s) can be obtained from the cumulative fluences by multiplying them with (80000 primaries \times 8 KHz / 5) for minimum bias Pb–Pb running. The results can be seen in Tables A.6 and A.7 for both sides of the TPC.

To scale up to a ten-year run period we multiply the aforementioned results of the fluences per central event with a factor of 3.2×10^{15} (80000 primaries \times 8 KHz / 5 \times 2.5 $\times 10^6$ sec/year \times 10 years). The results are presented in Table C.8 where the range in the values comes from the lower and upper limit of the 4 layers for both sides of the TPC.

C.1.3 Admixture of CH₄ or N₂ in the TPC gas.

The ideal gas mixture for a particular TPC varies with the environment in which that TPC will operate. The necessity of having a low diffusion gas has led to the choice of Ne-CO₂ as operating gas of the ALICE TPC.

However, this choice has a number of serious consequences for the operation and design of the TPC. The most obvious disadvantage is the drastically increased temperature dependence of the drift velocity as compared to Ar-CH₄. Moreover, CO₂ is known as a bad quencher, which contradicts the need of a high gas gain to achieve a reasonable signal to noise ratio [156, 157].

Recent investigations [158, 159] have indicated a possible improvement of the above problems. A small admixture of N₂ ($\approx 5\%$) as additional quencher increases the stability of the gas mixture significantly without lowering the drift velocity (and gain) to an intolerable extent as increase in the CO₂ content would do.

Nitrogen is however sensitive to neutrons. ¹⁴N can capture a thermal neutron to become ¹⁵N which sometimes emits a 10.8 MeV photon. Although this mechanism has a numerous useful applications (detection of explosives, measuring protein contents in living beings) it is not desired in ALICE since the photon can be absorbed by the gas yielding ionisation electrons thus making the TPC sensitive to the background neutron radiation.

To enhance the effect of the admixture, we added 10% N₂ in the normal TPC gas (Ne-CO₂, 90-10) and did a simulation using the FLUKA transport code. Comparing the lethargy photon spectra, as it is shown in Fig.C.12, with and without the N₂ admixture, one can be notice the presence of a 511 keV peak (due to positron annihilation), the 2.2 MeV peak from the neutron capture in Hydrogen and the 7.9 MeV in Copper. In both cases the spectra look similar and there is no sign of the 10.8 MeV photon peak.

However, we should expect a small proton background from the ¹⁴N(n,p)¹⁴C which is a very important reaction, especially in dosimetry (it contributes substantially to the person dose from low energy neutrons). For this reason, in FLUKA that reaction is simulated in detail, and each proton is tracked individually. In Fig.C.13 we can see that the (n,p) cross section of ¹⁴N is more than one order of magnitude larger than the (n, γ). (By the way, that is the same reaction which produces ¹⁴C in the atmosphere, and which is used to date ancient wooden artifacts: plants assimilate CO₂ containing

Table C.2: Number of particles per central event (**absorber side**).

Layers	1	2	3	4	Sum
Protons	113	147	134	147	541
Protons with $E_{\text{kin}} > 10$ MeV	109	144	128	143	524
Electrons	1097	971	854	954	3876
Positrons	464	586	334	281	1665
Photons	16530	34581	22930	28187	102228
Neutrons	41502	49600	50853	57780	199735
Neutrons with $E_{\text{kin}} > 10$ MeV	3600	2700	2100	2200	10600
Muons $^{\pm}$	234	348	368	300	1250
Pions $^{\pm}$	492	1449	1495	1030	4466
Pions $^{\pm}$ with $E_{\text{kin}} > 10$ MeV	492	1447	1493	1029	4461
Kaons $^{\pm}$, all with $E_{\text{kin}} > 10$ MeV	19	91	72	51	233
Primaries	103	197	567	435	1302
Charged	2419	3592	3257	2763	12031

^{14}C while they are alive, and of course stop when they die. From then on, the ^{14}C they have assimilated starts to decay, and from what is left one can calculate how many years have passed since the plant died.).

Anyway, the proton background from the admixture of 10% N_2 in the normal TPC gas, is much smaller compared to that which is expected after the addition of 5% CH_4 as it can be seen in Fig.C.11. In case of CH_4 , prompt neutrons can scatter on hydrogen and produce a significant knockout proton background which is an additional big disadvantage to the ageing effect that it also has [160]. Analyzing one central FLUKA event, it can also be calculated the number of protons that are created in the gas. In case of 10% N_2 , we have a factor of 2 more produced protons and each of them deposit on average ~ 0.85 MeV in a 2 cm track length (about 200 mips in one pad). With the addition of 5% CH_4 in the normal TPC gas, we have a factor of 10 more produced protons in the gas.

Table C.3: Number of particles per central event (**non-absorber side**).

Layers	1	2	3	4	Sum
Protons	292	200	155	156	803
Protons with $E_{\text{kin}} > 10$ MeV	289	198	151	151	789
Electrons	4476	1551	1070	584	7681
Positrons	1897	906	339	309	3451
Photons	58286	60649	29010	67192	215137
Neutrons	17796	35758	34999	49756	138349
Neutrons with $E_{\text{kin}} > 10$ MeV	1800	2000	1300	1700	6800
Muons $^{\pm}$	390	457	368	325	1540
Pions $^{\pm}$	2140	1664	1452	1109	6365
Pions $^{\pm}$ with $E_{\text{kin}} > 10$ MeV	2138	1664	1451	1109	6362
Kaons $^{\pm}$, all with $E_{\text{kin}} > 10$ MeV	164	106	84	53	407
Primaries	85	171	519	474	1249
Charged	9359	4884	3468	2536	20247

Table C.4: Particle fluences (particles/cm²/primary) per central event (**absorber side**).

Layers	1	2	3	4
p	$(1.03 \times 10^{-7}) \pm 26.7\%$	$(6.04 \times 10^{-8}) \pm 6.9\%$	$(3.93 \times 10^{-8}) \pm 10.6\%$	$(4.01 \times 10^{-8}) \pm 10.6\%$
p with $E_{\text{kin}} > 10 \text{ MeV}$	9.96×10^{-8}	5.89×10^{-8}	3.79×10^{-8}	3.88×10^{-8}
e [±]	$(1.01 \times 10^{-6}) \pm 26.4\%$	$(6.10 \times 10^{-7}) \pm 6.8\%$	$(4.50 \times 10^{-7}) \pm 26.0\%$	$(3.16 \times 10^{-7}) \pm 9.7\%$
n	$(3.42 \times 10^{-5}) \pm 1.6\%$	$(2.57 \times 10^{-5}) \pm 0.3\%$	$(2.13 \times 10^{-5}) \pm 0.9\%$	$(1.85 \times 10^{-5}) \pm 0.5\%$
n with $E_{\text{kin}} > 10 \text{ MeV}$	2.61×10^{-6}	1.60×10^{-6}	1.05×10^{-6}	7.49×10^{-7}
Thermal n	2.82×10^{-6}	2.58×10^{-6}	2.44×10^{-6}	2.54×10^{-6}
γ	$(1.66 \times 10^{-5}) \pm 10.5\%$	$(1.31 \times 10^{-5}) \pm 7.0\%$	$(1.04 \times 10^{-5}) \pm 9.1\%$	$(8.06 \times 10^{-6}) \pm 15.4\%$
μ [±]	$(1.47 \times 10^{-7}) \pm 9.0\%$	$(1.51 \times 10^{-7}) \pm 7.3\%$	$(1.31 \times 10^{-7}) \pm 13.7\%$	$(8.22 \times 10^{-8}) \pm 5.0\%$
π [±]	$(2.92 \times 10^{-7}) \pm 5.7\%$	$(4.37 \times 10^{-7}) \pm 3.1\%$	$(3.71 \times 10^{-7}) \pm 2.4\%$	$(2.23 \times 10^{-7}) \pm 2.8\%$
π [±] with $E_{\text{kin}} > 10 \text{ MeV}$	2.91×10^{-7}	4.36×10^{-7}	3.71×10^{-7}	2.23×10^{-7}
k [±] with $E_{\text{kin}} > 10 \text{ MeV}$	$(7.54 \times 10^{-9}) \pm 14.0\%$	$(2.37 \times 10^{-8}) \pm 15.1\%$	$(1.59 \times 10^{-8}) \pm 12.5\%$	$(9.85 \times 10^{-9}) \pm 27.9\%$
Charged	$(1.55 \times 10^{-6}) \pm 17.3\%$	$(1.28 \times 10^{-6}) \pm 3.6\%$	$(1.01 \times 10^{-6}) \pm 12.5\%$	$(6.72 \times 10^{-7}) \pm 5.3\%$

Table C.5: Particle fluences (particles/cm²/primary) per central event (**non-absorber side**).

Layers	1	2	3	4
p	$(1.52 \times 10^{-7}) \pm 9.6\%$	$(7.22 \times 10^{-8}) \pm 11.5\%$	$(6.34 \times 10^{-8}) \pm 19.3\%$	$(3.61 \times 10^{-8}) \pm 8.5\%$
p with $E_{\text{kin}} > 10 \text{ MeV}$	1.50×10^{-7}	7.10×10^{-8}	6.18×10^{-8}	3.54×10^{-8}
e [±]	$(3.50 \times 10^{-6}) \pm 23.0\%$	$(1.10 \times 10^{-6}) \pm 25.1\%$	$(4.61 \times 10^{-7}) \pm 15.5\%$	$(3.08 \times 10^{-7}) \pm 7.3\%$
n	$(1.27 \times 10^{-5}) \pm 1.3\%$	$(1.28 \times 10^{-5}) \pm 2.1\%$	$(1.27 \times 10^{-5}) \pm 1.2\%$	$(1.27 \times 10^{-5}) \pm 1.3\%$
n with $E_{\text{kin}} > 10 \text{ MeV}$	8.70×10^{-7}	5.80×10^{-7}	4.47×10^{-7}	3.56×10^{-7}
Thermal n	1.87×10^{-6}	1.75×10^{-6}	1.77×10^{-6}	1.86×10^{-6}
γ	$(4.59 \times 10^{-5}) \pm 11.7\%$	$(2.91 \times 10^{-5}) \pm 13.8\%$	$(1.46 \times 10^{-5}) \pm 6.5\%$	$(1.09 \times 10^{-5}) \pm 15.6\%$
μ [±]	$(2.81 \times 10^{-7}) \pm 12.4\%$	$(2.14 \times 10^{-7}) \pm 2.2\%$	$(1.45 \times 10^{-7}) \pm 8.6\%$	$(1.06 \times 10^{-7}) \pm 7.1\%$
π [±]	$(8.94 \times 10^{-7}) \pm 1.0\%$	$(5.13 \times 10^{-7}) \pm 2.5\%$	$(3.65 \times 10^{-7}) \pm 4.0\%$	$(2.42 \times 10^{-7}) \pm 3.0\%$
π [±] with $E_{\text{kin}} > 10 \text{ MeV}$	8.93×10^{-7}	5.11×10^{-7}	3.64×10^{-7}	2.42×10^{-7}
k [±] with $E_{\text{kin}} > 10 \text{ MeV}$	$(6.03 \times 10^{-8}) \pm 3.5\%$	$(2.80 \times 10^{-8}) \pm 13.3\%$	$(1.83 \times 10^{-8}) \pm 9.3\%$	$(1.02 \times 10^{-8}) \pm 6.9\%$
Charged	$(4.89 \times 10^{-6}) \pm 17.0\%$	$(1.92 \times 10^{-6}) \pm 14.3\%$	$(1.05 \times 10^{-6}) \pm 7.3\%$	$(7.03 \times 10^{-7}) \pm 2.2\%$

Table C.6: Particle fluxes (particles/cm²/s) for minimum bias Pb–Pb running (**absorber side**). Same errors with their respective fluences in accordance with a previous table.

Layers	1	2	3	4
Neutron Flux [cm ⁻² s ⁻¹]	4377.6	3289.6	2726.4	2368
Neutron Flux [cm ⁻² s ⁻¹] with $E_{\text{kin}} > 10$ MeV	334.1	204.8	134.4	95.9
Proton Flux [cm ⁻² s ⁻¹]	13.2	7.7	5.0	5.1
Proton Flux [cm ⁻² s ⁻¹] with $E_{\text{kin}} > 10$ MeV	12.7	7.5	4.9	5.0
Pion [±] Flux [cm ⁻² s ⁻¹]	37.4	55.9	47.5	28.5
Pion [±] Flux [cm ⁻² s ⁻¹] with $E_{\text{kin}} > 10$ MeV	37.2	55.8	47.5	28.5
Kaon [±] Flux [cm ⁻² s ⁻¹], all with $E_{\text{kin}} > 10$ MeV	1.0	3.0	2.0	1.3

Table C.7: Particle fluxes (particles/cm²/s) for minimum bias Pb–Pb running (**non-absorber side**). Same errors with their respective fluences in accordance with a previous table.

Layers	1	2	3	4
Neutron Flux [cm ⁻² s ⁻¹]	1625.6	1638.4	1625.6	1625.6
Neutron Flux [cm ⁻² s ⁻¹] with $E_{\text{kin}} > 10$ MeV	111.4	74.2	57.2	45.6
Proton Flux [cm ⁻² s ⁻¹]	19.5	9.2	8.1	4.6
Proton Flux [cm ⁻² s ⁻¹] with $E_{\text{kin}} > 10$ MeV	19.2	9.1	7.9	4.5
Pion [±] Flux [cm ⁻² s ⁻¹]	114.4	65.7	46.7	31.0
Pion [±] Flux [cm ⁻² s ⁻¹] with $E_{\text{kin}} > 10$ MeV	114.3	65.4	46.6	31.0
Kaon [±] Flux [cm ⁻² s ⁻¹], all with $E_{\text{kin}} > 10$ MeV	7.7	3.6	2.3	1.3

Table C.8: Particle fluences and total absorbed doses per 10 ALICE years.

Scoring region of TPC electronics	Absorber side	Non-absorber side
Neutron Fluence [cm^{-2}]	$(0.6-1.1) \times 10^{11}$	0.4×10^{11}
Neutron Fluence [cm^{-2}] with $E_{\text{kin}} > 10 \text{ MeV}$	$(2.4-8.4) \times 10^9$	$(1.1-2.8) \times 10^9$
Proton Fluence [cm^{-2}] with $E_{\text{kin}} > 10 \text{ MeV}$	$(1.2-3.2) \times 10^8$	$(1.1-4.8) \times 10^8$
Pion Fluence [cm^{-2}] with $E_{\text{kin}} > 10 \text{ MeV}$	$(0.7-1.4) \times 10^9$	$(0.8-2.9) \times 10^9$
Kaon Fluence [cm^{-2}] with $E_{\text{kin}} > 10 \text{ MeV}$	$(2.4-7.6) \times 10^7$	$(3.3-19.3) \times 10^7$
Total Dose [Gy]	$(0.8-2.5) \times 10^0$	$(0.3-5.7) \times 10^0$

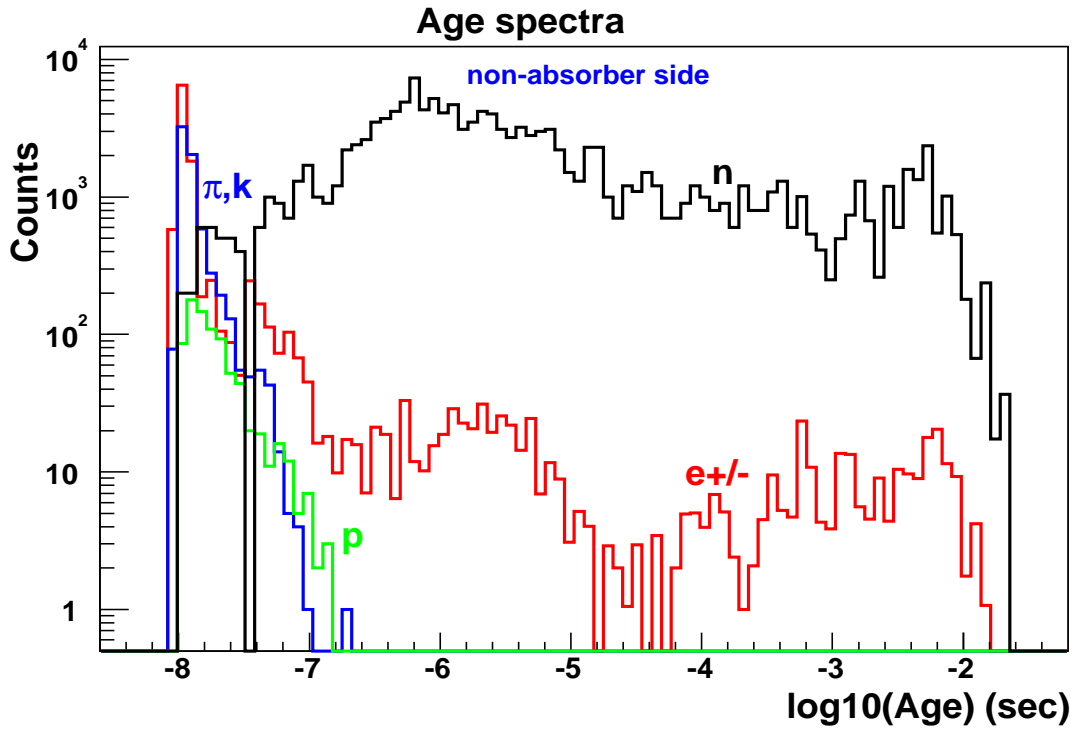


Figure C.2: Age spectra of neutrons, electrons and positrons, pions and kaons, protons in the non-absorber side (one central event).

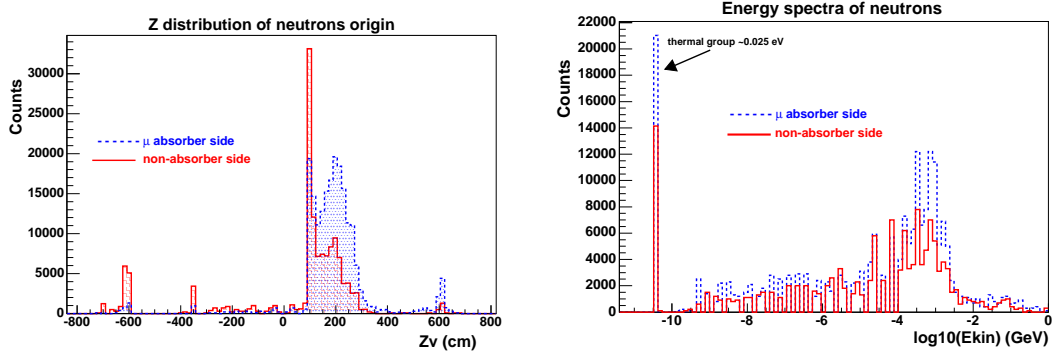


Figure C.3: Z distribution and kinetic energy of neutrons in the absorber side (dashed line) and non-absorber side (solid line) of the TPC respectively (one central event)

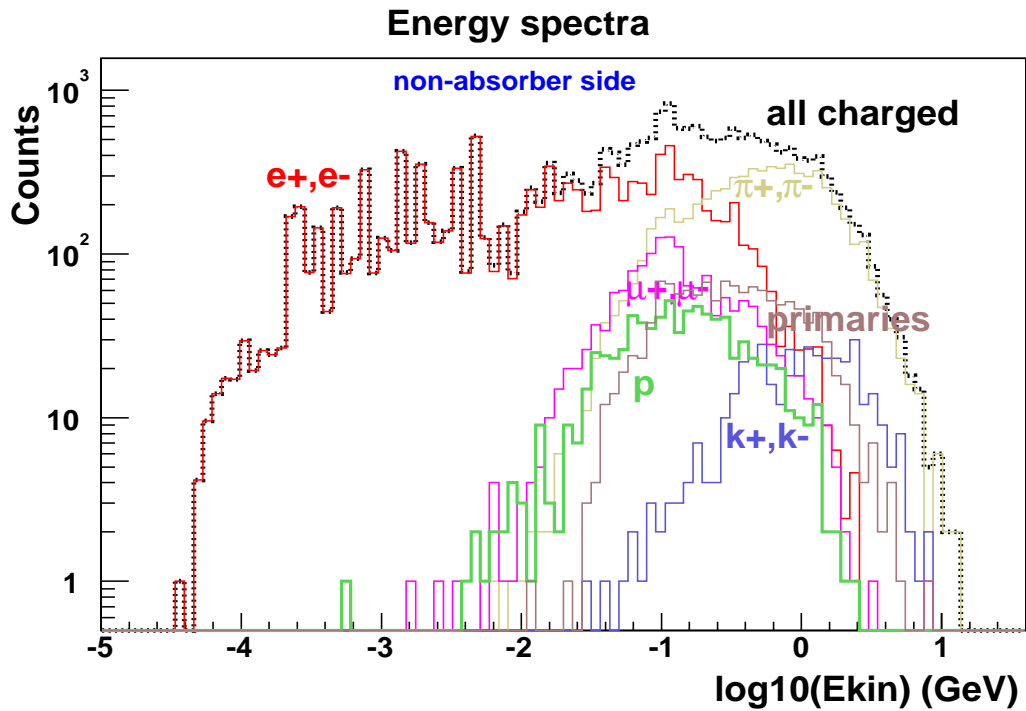


Figure C.4: Energy spectra of all charged particles in the non-absorber side (one central event).

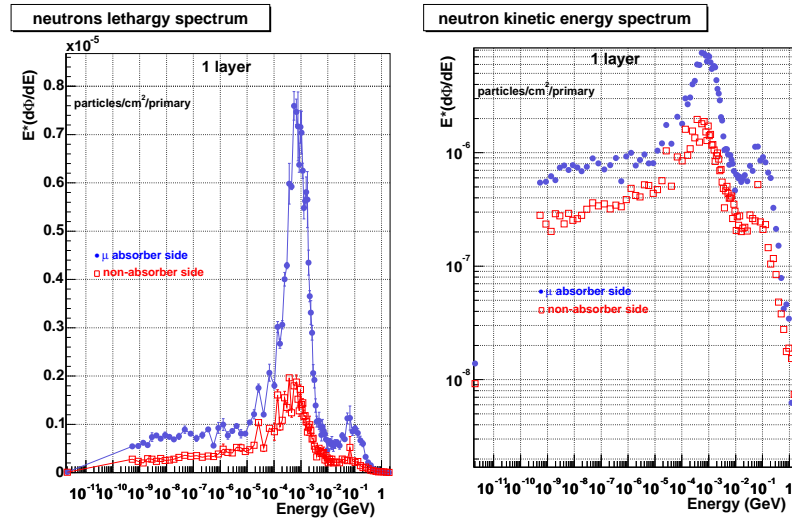


Figure C.5: Lethargy and kinetic energy spectra of neutrons in the absorber side (full circles) and non-absorber side (empty rectangles) of the TPC respectively (one central event).

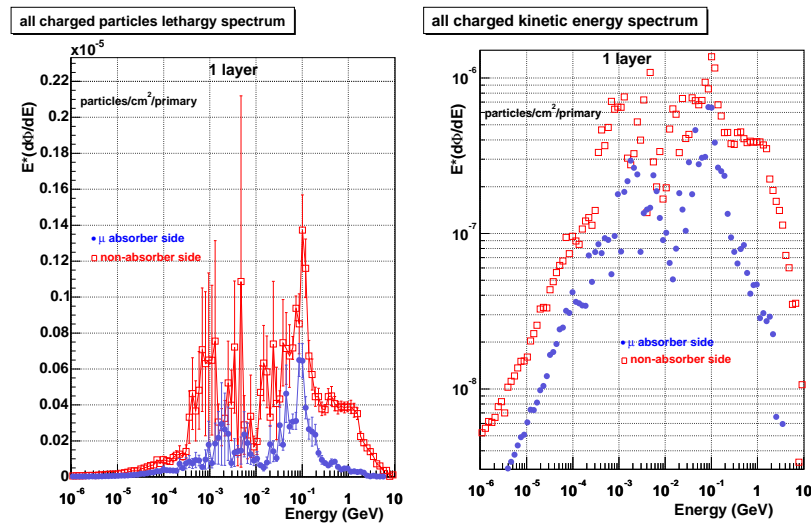


Figure C.6: Lethargy and kinetic energy spectra of all charged particles in the absorber side (full circles) and non-absorber side (empty rectangles) of the TPC respectively (one central event).

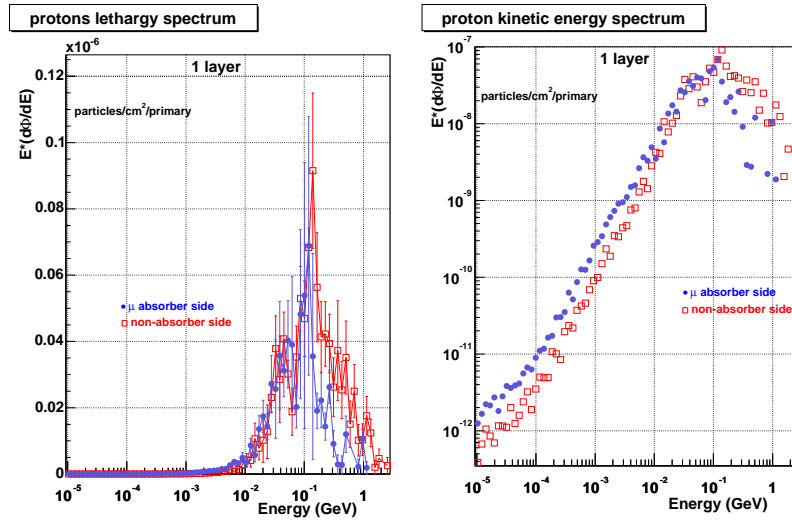


Figure C.7: Lethargy and kinetic energy spectra of protons in the absorber side (full circles) and non-absorber side (empty rectangles) of the TPC respectively (one central event).

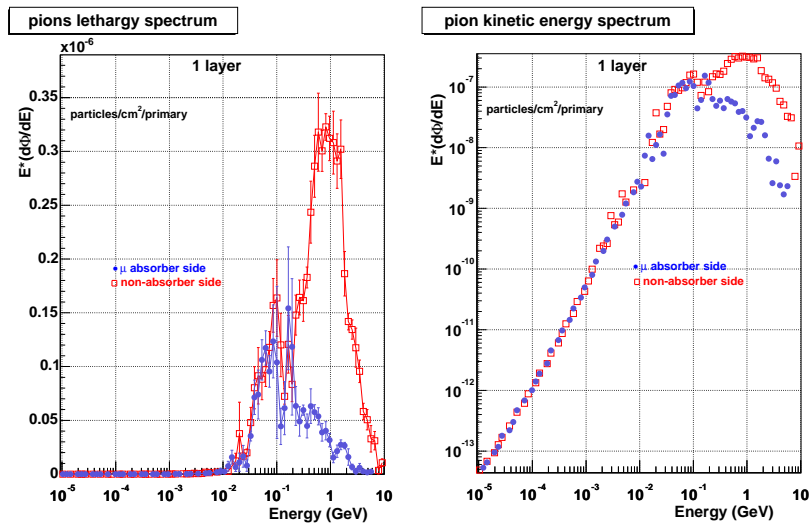


Figure C.8: Lethargy and kinetic energy spectra of all pion particles in the absorber side (full circles) and non-absorber side (empty rectangles) of the TPC respectively (one central event).

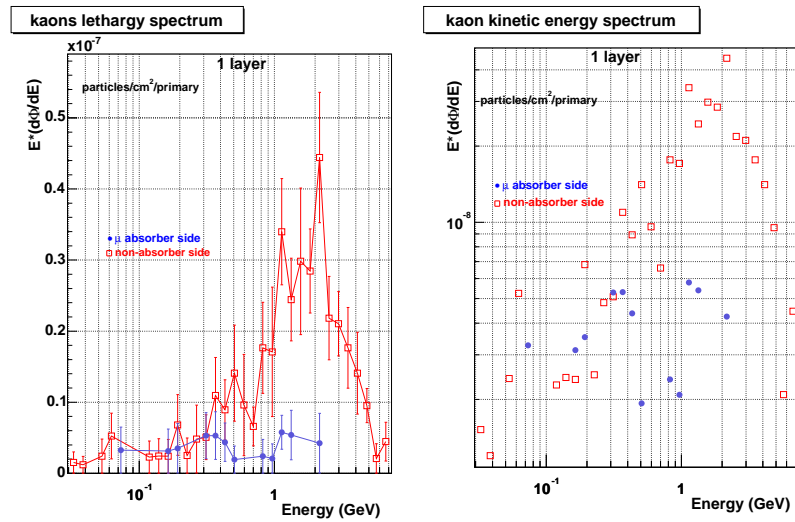


Figure C.9: Lethargy and kinetic energy spectra of kaons in the absorber side (full circles) and non-absorber side (empty rectangles) of the TPC respectively (one central event).

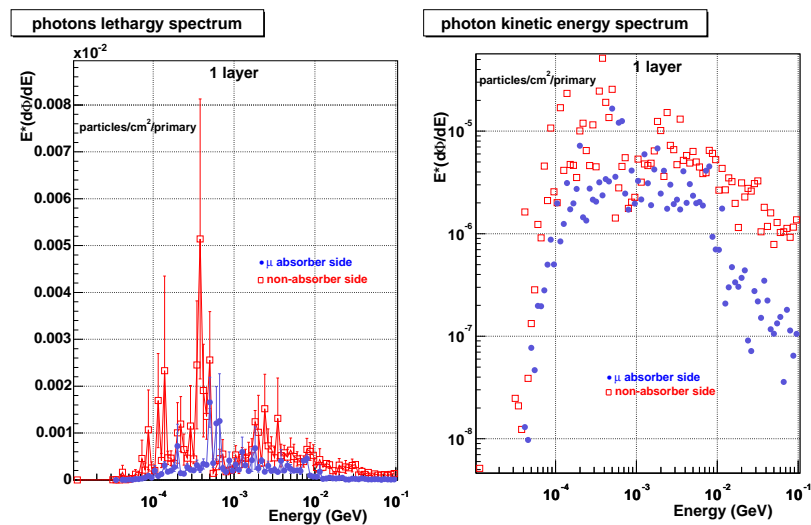


Figure C.10: Lethargy and kinetic energy spectra of all photon particles in the absorber side (full circles) and non-absorber side (empty rectangles) of the TPC respectively (one central event).

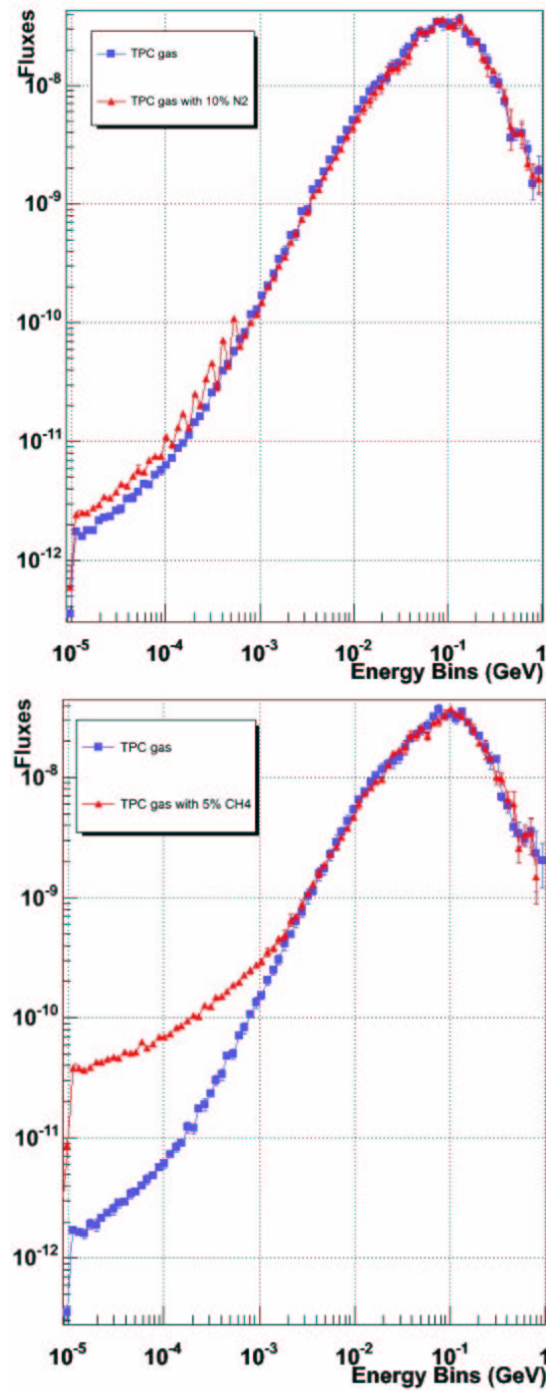


Figure C.11: Kinetic spectra of protons in the normal TPC gas (blue rectangles) and after the addition of 10% N₂ or 5% CH₄ respectively (red triangles).

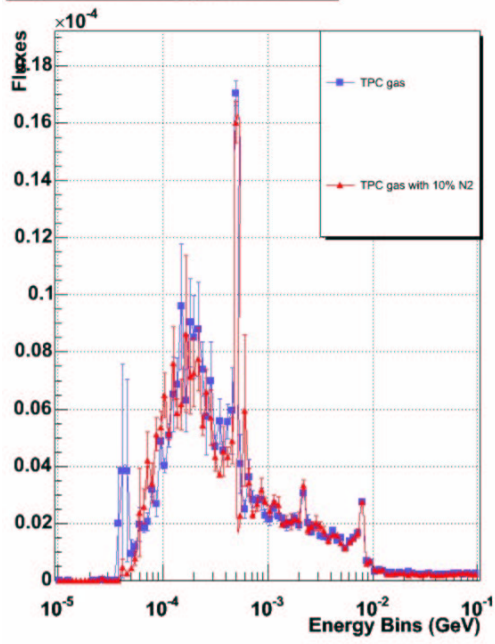


Figure C.12: Lethargy spectra of photons in the normal TPC gas (blue rectangles) and after the addition of 10% N₂ respectively (red triangles).

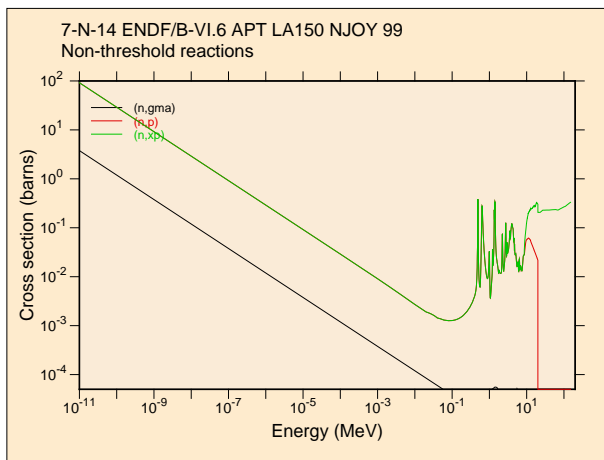


Figure C.13: (n,p) and (n, γ) cross sections of ¹⁴N.

Bibliography

- [1] B. Müller, *Physics of the Quark Gluon Plasma* nucl-th/9211010 (1992).
- [2] K.G. Wilson, Phys. Rev. **D10** (1974) 2445.
- [3] A. Andronic and P. Braun-Munzinger, *Ultrarelativistic nucleus-nucleus collisions and the quark-gluon plasma*, VIII Hispalensis International Summer School, Oromana (Seville, Spain), June 9-21, 2003, hep-ph/0402291 (2004).
- [4] F. Karsch and E. Laermann *Thermodynamics and in-medium hadron properties from lattice QCD*, hep-lat/0305025 (2003).
- [5] See e.g. H. Satz, Nucl. Phys. **A715** (2003) 3, hep-ph/0209181.
- [6] <http://www.bnl.gov/RHIC>
- [7] G.D. Westfall, *et al.*, Phys. Rev. Lett. **37** (1976) 1202.
- [8] J.D. Bjorken, Phys. Rev. D 27 (1983) 140.
- [9] K. Kajantie, L. McLerran, Ann. Rev. Nucl. Part. Sci. 37 (1987) 293. J.W. Harris, B. Müller, Ann. Rev. Nucl. Part. Sci. 46 (1996) 71 [hep-ph/9602235]; S.A. Bass, M. Gyulassy, H. Stöcker, and W. Greiner, J. Phys. G25 (1999) R1 [hep-ph/9810281].
- [10] T. Peitzmann and M.H. Thoma, Phys. Rep. 364 (2002) 175 [hep-ph/0111114].
- [11] R. Rapp, J. Wambach, Adv. Nucl. Phys. 25 (2000) 1 [hep-ph/9909229]; J.P. Wessels et al. (CERES), Nucl. Phys. A 715 (262c) 2003, [nucl-ex/0212015] and ref. therein.

- [12] J. Rafelski, Nucl. Phys. **A418** 215c (1984).
- [13] J. Rafelski, J. Letessier, J. Phys. G 30 (2004) S1 [hep-ph/0305284]; R. Stock, hep-ph/0312039.
- [14] H. Satz, Rep. Prog. Phys. 63 (2000) 1511 [hep-ph/0007069].
- [15] S.S. Adler et al. (PHENIX), Phys. Rev. Lett. 91 (2003) 072301 [nucl-ex/0304022], Phys. Rev. Lett. 91 (2003) 072303 [nucl-ex/0306021], nucl-ex/0308006; J. Adams et al. (STAR), Phys. Rev. Lett. 91 (2003) 172302 [nucl-ex/0305015], Phys. Rev. Lett. 91 (2003) 072304 [nucl-ex/0306024]; B.B. Back et al. (PHOBOS), Phys. Rev. Lett. 91 (2003) 072302 [nucl-ex/0306025]; I. Arsene et al. (BRAHMS), Phys. Rev. Lett. 91 (2003) 072305 [nucl-ex/0307003]; G. Agakichiev et al. (CERES), Phys. Rev. Lett. 92 (2004) 032301 [nucl-ex/0303014].
- [16] M. Asakawa, U. Heinz, B. Müller, Phys. Rev. Lett. 85 (2000) 2072 [hep-ph/0003169]; S. Jeon, V. Koch, Phys. Rev. Lett. 85 (2000) 2076 [hep-ph/0003168].
- [17] M. Gyulassy and M Plümer, Phys. Lett. **B243** (1990) 432.
- [18] X.N. Wang and M. Gyulassy, Phys. Rev. Lett. **68** (1992) 1480.
- [19] U. Heinz, *Concepts of Heavy-Ion Physics*, CERN-2004-001, pp.127-178, hep-ph/0407360 (2004)
- [20] S. Hands *The Phase Diagram of QCD*, physics/0105022 (2001)
- [21] Z. Fodor, S.D. Katz, J. High Ener. Phys. 404 50, hep-lat/0402006 (2004).
- [22] updated version of Figure in P. Braun-Munzinger, J. Stachel, J. Phys. G 28 1971 (2002), taken from A. Andronic, P. Braun-Munzinger, J. Stachel, to be published.
- [23] J. Stachel *Has the Quark Gluon Plasma been seen?*, nucl-ex/0510077 (2005).
- [24] M. Stephanov *QCD phase diagram and the critical point*, hep-ph/0402115 (2005).

- [25] S. Jeon, V. Koch, *Event-by-Event Fluctuations*, review for "Quark-Gluon Plasma 3", eds. R.C. Hwa and X.-N. Wang, World Scientific, Singapore, [hep-ph/0304012](#), (2003).
- [26] M.A. Stephanov, K. Rajagopal, and E.V. Shuryak, *Phys. Rev. Lett.* **81** (1998) 4816.
- [27] G. Agakichiev, *et al.*, (CERES Collaboration), *Eur. Phys. J.* **C4** (1998) 231. G. Agakichiev, *et al.*, (CERES Collaboration), *Eur. Phys. J.* **C4** (1998) 249.
- [28] G. Agakichiev et al. (CERES), *Phys. Rev. Lett.* **75** (1995) 1272 and [nucl-ex/0506002](#).
- [29] A. Marin, *et al.*, (CERES Collaboration), *Nucl. Phys.* **A661** (1999)
- [30] D. Miśkowiec (CERES Collaboration), *Recent Results from CERES*, Proceedings of Quark Matter 2005, Budapest, in print.
- [31] J. Seguinot and T. Ypsilantis, *Nucl. Instr. Meth.* **1977** (142) .
- [32] J. Slivova, "Azimuthal Correlations of High- p_T Pions in 158 A-GeV/c Pb-Au Collisions Measured by the CERES Experiment", PhD thesis, University of Heidelberg, 2003.
- [33] W. R. Leo, *Techniques for Nuclear and Particle Physics Experiments*, Springer-Verlag, 1993.
- [34] H. Tilsner, "Two-particle Correlations at 40, 80, and 158 A-GeV/c Pb-Au Collisions Measured by the CERES Experiment", PhD thesis, University of Heidelberg, 2002.
- [35] M. Stephanov, K. Rajagopal, and E. Shuryak, *Phys. Rev.* **D60** (1999) 14028.
- [36] M. Gazdzicki and S. Mrowczynski, *Z. Phys.* **C54** (1992) 127.
- [37] S. Voloshin, V. Koch, and H. Ritter, *Phys. Rev.* **C60** (1999) 024901.
- [38] S. Voloshin, *Mean p_T fluctuations from 2- and 4-particle correlations.*, [nucl-th/0206052](#) (2002).
- [39] T.A. Trainor, *Event-by-Event Analysis and the Central Limit Theorem*, [hep-ph/0001148](#) (2000).

- [40] R. L. Ray *et al.* (STAR Collaboration), Nucl. Phys. **A715** (2003) 45.
- [41] C. Pruneau, S. Gavin, and S. Voloshin, Phys. Rev. **C66** (2002) 044904.
- [42] A. Bialas, and M. Gazdzicki, Phys. Lett. **B252** (1990) 483.
- [43] NA49 Collaboration, *Transverse Momentum Fluctuations at 158 A·GeV/c*, hep-ph/0001148 (2000).
- [44] NA49 Collaboration, *Transverse Momentum Fluctuations in nuclear collisions at 158 A·GeV/c*, Phys. Rev. **C70** (2004) 034902.
- [45] H. Appelshäuser *et al.* (CERES Collaboration), Nucl. Phys. **A727** (2003) 97, nucl-ex/0305002 (2000).
- [46] H. Sako and H. Appelshäuser for the CERES Collaboration, *Event-by-event fluctuations in 40, 80, and 158 A·GeV/c Pb+Au collisions*, (Quark Matter 04, Proc. Int. Conf. on Ultra-Relativistic Nucleus-Nucleus Collisions, Oakland, 2004) J. Phys. G 30 (2004) S1371-1375, nucl-ex/0403037, preprint.
- [47] M. Tannenbaum, Phys. Lett. **B498** (2001) 29.
- [48] P. Braun-Munzinger *et al.*, Nucl. Phys. **A697** (2002) 902.
- [49] STAR Collaboration, S. Voloshin *et al.*, nucl-ex/0109006 (2001).
- [50] STAR Collaboration, J. Adams *et al.*, nucl-ex/0308033 (2003).
- [51] PHENIX Collaboration, S. Adler *et al.*, nucl-ex/0310005 (2003).
- [52] M. Stephanov, Phys. Rev. **D65** (2002) 096008.
- [53] K. Braune, *et al.*, Phys. Lett. **B123** (1983) 467.
- [54] WA98 Collaboration, M.M. Aggarwal, *et al.*, Eur. Phys. J. **C18** (2001) 651.
- [55] CERES Collaboration, D. Miśkowiec, *et al.*, in *Proceedings of the International Workshop XXX on Gross Properties of Nuclei and Nuclear Excitations*, Hirschegg, Austria, January 13-19, 2002.
- [56] WA97 Collaboration, W. Andersen, *et al.*, Phys. Lett. **B449** (1999) 401.

- [57] H. Appelshäuser *et al.* (CERES Collaboration), J. Phys. G: Nucl. Part. Phys. **30** (2004) S1376.
- [58] NA49 Collaboration, T. Anticic *et al.*, [hep-ex/0311009](#) (2000).
- [59] G.D. Westfall *et al.* (STAR Collaboration), J. Phys. G: Nucl. Part. Phys. **30** (2004) S1389.
- [60] S. Gavin, J. Phys. G: Nucl. Part. Phys. **30** (2004) S1385.
- [61] S. Gavin, Phys. Rev. Lett. **92** (2004) 162301.
- [62] E.G. Ferreira, J. Phys. G: Nucl. Part. Phys. **30** (2004) S1159.
- [63] E.G. Ferreira, F. del Moral and C. Pajares, Phys. Rev. **C69** (2004) 034901.
- [64] D. Miśkowiec and D. Antończyk, *Centrality calibration of the CERES' 2000 data*, CERES note, January 31, 2005
- [65] O. Busch, *Track Fitting in the CERES TPC*, CERES note, March 29, 2005
- [66] K.J. Eskola, K. Kajantie, J. Lindfors, Nucl. Phys. **B323** (1989) 37, for implementation see <http://www.gsi.de/~misko/overlap>.
- [67] C. Pruneau (STAR Collaboration), *Excitation Function of mean p_T and Net Charge Fluctuations at RHIC*, Proceedings of Quark Matter 2004, Oakland, [nucl-ex/0401016](#).
- [68] A.M. Poskanzer and S. Voloshin, *Methods of analyzing anisotropic flow in relativistic nuclear collisions*, Phys. Rev. **C58** (1998) 1671.
- [69] C. Adlair, Phys. Rev. Lett. 90 (2003) 032301.
- [70] C. Adlair, Phys. Rev. Lett. 90 (2003) 082302.
- [71] J. Milošević (CERES Collaboration), *Strange and charged particle elliptic flow in Pb-Au collisions at 158 GeV*, Proceedings of Quark Matter 2005, Budapest, in print.
- [72] J. Milošević, private communication.
- [73] D. Miśkowiec, private communication.
- [74] H. Appelshäuser, private communication.

- [75] G. Agakichiev et al. (CERES), Phys. Rev. Lett. 92 (2004) 032301.
- [76] C. Garabatos, F. Hahn, G. Tsileidakis and A. Wasem, *TRD gas regeneration by cryogenic distillation*, ALICE Internal NOTE 37-2002 (2002).
- [77] A. Andronic et al., Nucl. Instr. Meth. Phys. Res. A **498** (2003) 143.
- [78] O. Kiselev et al., Nucl. Instr. Meth. Phys. Res. A **367** (1995) 306.
- [79] U. Becker et al., Nucl. Instr. Meth. Phys. Res. A **306** (1991) 194.
- [80] Th. Berghofer et al., Nucl. Instr. Meth. Phys. Res. A **525** (2004) 544.
- [81] P. Bernardini et al., Nucl. Instr. Meth. Phys. Res. A **355** (1995) 428.
- [82] U. von Hagel et al., Nucl. Instr. Meth. Phys. Res. A **420** (1999) 429.
- [83] E. Oettinger et al., Nucl. Instr. Meth. Phys. Res. A **412** (1998) 355.
- [84] W. Walkowiak et al., Nucl. Instr. Meth. Phys. Res. A **449** (2000) 299.
- [85] *ALICE TRD Technical Design Report*, CERN/LHCC 2001-021, October 2001; <http://www-alice.gsi.de/trd/trd>.
- [86] T. Mahmoud, "*Development of the Readout Chambers of the Alice TRD and evaluation of its physics performance in the quarkonium sector*", PhD thesis, University of Heidelberg, 2004.
- [87] L.G. Christophorou et al, Nucl. Instr. Meth. **171** (1980) 491.
- [88] B. Dolgoshein et al., Nucl. Instr. Meth. Phys. Res. A **294** (1990) 473.
- [89] T. Kunst, B. Götz and B. Schmidt, Nucl. Instr. Meth. Phys. Res. A **324** (1993) 127.
- [90] U. Becker et al., Nucl. Instr. Meth. Phys. Res. A **421** (1999) 54; <http://cyclo.mit.edu/drift/www>.
- [91] R. Veenhof, Nucl. Instr. Meth. Phys. Res. A **419** (1998) 726; <http://consult.cern.ch/writeup/garfield/>.
- [92] F. Sauli, CERN Yellow Report 77-09 (1977).

- [93] S.F. Biagi, Nucl. Instr. Meth. Phys. Res. A **421** (1999) 234. Magboltz 2, version 5.3, is available from the author (sfb@hep.ph.liv.ac.uk).
- [94] W.H. Miller and H. Morgner, J. Chem. Phys. 67, 4923 (1977).kis
- [95] J.E. Velazco, J.H. Kolts, and D.W. Setser, J. Chem. Phys. 69, 4357 (1978).
- [96] P. Cwetanski, Proc. IEEE Nuclear Science Symposium and Medical Imaging Conference, Lyon, France, Oct. 2000, 5/39-43.
- [97] B.R. Bulos and A.V.Phelps, Phys. Rev. A14, 615 (1976).
- [98] Y.Nakamura, Aust. J. Phys. 48, 357 (1995).
- [99] A.Andronic, S.Biagi, P.Braun-Munzinger, C.Garabatos and G.Tsileidakis, Nucl. Instr. Meth. Phys. Res. A **523** (2004) 302.
- [100] A. Ferrari, J. Ranft and P.R. Sala, "The FLUKA radiation transport code and its use for space problems", Physica Medica, **XVII**, Suppl. 1, 72-80 (2001)
A. Fassò, A. Ferrari, J. Ranft and P.R. Sala, "FLUKA: Status and Prospective for Hadronic Applications", Proceedings of the MonteCarlo 2000 Conference, Lisbon, October 23–26 2000, A.Kling, F.Barao, M.Nakagawa, L.Tavora, P.Vaz - eds. , Springer-Verlag Berlin, p.955-960 (2001).
A. Fassò, A. Ferrari, P.R. Sala, "Electron-photon transport in FLUKA: status", Proceedings of the MonteCarlo 2000 Conference, Lisbon, October 23–26 2000, A.Kling, F.Barao, M.Nakagawa, L.Tavora, P.Vaz - eds., Springer-Verlag Berlin, p.159-164 (2001)
- [101] <http://www.fluka.org/>
- [102] A. Capella and J. Tran Thanh Van, Phys. Lett. 93B, 146 (1980)
- [103] K. Hänssgen and J. Ranft, *The Monte Carlo code NUCRIN to simulate inelastic hadron–nucleus interactions below 5 GeV*, Comp. Phys. Comm. 39, 53–70 (1986)
- [104] A. Ferrari and P.R. Sala, *A new model for hadronic interactions at intermediate energies for the FLUKA code*, Proc. of the MC93 International Conference on Monte Carlo Simulation in High Energy and

- Nuclear Physics, Tallahassee, Florida, 22–26 February 1993. Edited by P. Dragovitsch, S.L. Linn, M. Burbank, World Scientific, p 277–288, Singapore (1994).
- [105] A. Ferrari, J. Ranft, P.R. Sala and S. Roesler, *Cascade particles, nuclear evaporation and residual nuclei in high-energy hadron-nucleus interactions*, Z. Phys. C70, 413 (1996)
- [106] A. Ferrari, J. Ranft, P.R. Sala and S. Roesler, *The production of residual nuclei in peripheral high-energy nucleus-nucleus*, Z. Phys. C71, 75 (1996)
- [107] P.A. Aarnio, A. Fassò, A. Ferrari, H.-J. Möhring, J. Ranft, P.R. Sala, G.R. Stevenson and J.M. Zazula, *FLUKA : Hadronic Benchmarks and Applications*, Proc. of the MC93 International Conference on Monte Carlo Simulation in High Energy and Nuclear Physics, Tallahassee, Florida, 22–26 February 1993. (P. Dragovitsch, S.L. Linn, M. Burbank, Eds.), World Scientific, p 88, Singapore (1994).
- [108] A. Ferrari, T. Rancati and P.R. Sala, *FLUKA Applications in High-Energy Problems: From LHC to ICARUS and Atmospheric Showers*, Proc. of The Third Workshop on Simulating Accelerator Radiation Environments (SARE-3), KEK, Tsukuba, Japan, p.165 (1997).
- [109] C. Birattati, E. De Ponti, A. Esposito, A. Ferrari, M. Pelliccioni and M. Silari, *Measurements and characterization of high-energy neutron fields*, Nucl. Instr. Meth. A338, 534, (1994).
- [110] A. Ferrari, P.R. Sala, R. Guaraldi and F. Padoani, *An improved multiple scattering model for charged particle transport*, Nucl. Instr. Meth. B71, 412, (1992).
- [111] A. Morsch and B. Pastircak, *Radiation in ALICE Detectors and Electronics Racks*, ALICE Internal NOTE 28-2002 (2002)
- [112] *A Transition Radiation Detector for Electron Identification with the ALICE Central Detector*. Addendum to ALICE Proposal, CERN/LHCC 99-13, LHCC/P3-Addendum 2, 7 May 1999.

- [113] "Transition Radiation Detector" ALICE Technical Design Report, CERN/LHCC 2001-021 (2001).
- [114] M.N. Mazziotta, *A Monte Carlo code for full simulation of a transition radiation detector*, Comp. Phys. Comm. 132, 110 (2000).
- [115] A. Andronic et al., *Prototype tests for the ALICE TRD*, Presented at the IEEE Nuclear Science Symposium and Medical Imaging Conference, Lyon, France, 15–20 Oct. 2000, ALICE-PUB-2000-034 (2001).
- [116] O. Busch et al., Nucl. Instr. Meth. Phys. Res. A **525** (2004) 153.
- [117] A. Andronic et al., Nucl. Instr. Meth. Phys. Res. A **522** (2004) 40.
- [118] E. Cuccoli, A. Ferrari and G.C. Panini, *A group library from JEF 1.1 for flux calculations in the LHC machine detectors*, JEF-DOC-340 (91) (1991)
<http://www.slac.stanford.edu/esh/rp/docs/FLUKA/papers/~> bibliography.html>.
- [119] <http://www.nea.fr/html/databank/>
- [120] <http://www-rsicc.ornl.gov/rsic.html>
- [121] <http://www-nds.iaea.or.at/>
- [122] <http://t2.lanl.gov/codes/>
- [123] <http://www.nndc.bnl.gov/nndc/nudat/>
- [124] K.J.R. Rosman and P.D.P. Taylor, *Isotopic composition of the elements 1997*, J. Phys. Chem. Ref. Data 27, 1275 (1998).
- [125] G. Audi and A.H. Wapstra, *The 1995 update to the atomic mass evaluation*, Nucl. Phys. A595, 409 (1995)
<http://wwwndc.tokai.jaeri.go.jp/NuC/index.html>
- [126] <http://t2.lanl.gov/cgi-bin/nuclides/endind>
- [127] Academic Press, New York
- [128] <http://www.nndc.bnl.gov/nndc/ensdf/ensdfindex.html>
- [129] L.V. Groshev, L.I. Govor, A.M. Demidov and A.S. Rakhimov, *Spectra of γ rays and level schemes of Xe^{130} and Xe^{132} from the reaction (n,γ)* , Yad. Fiz. 13, 1129 (1971); Sov. J. Nucl. Phys. 13, 647 (1971).

- [130] W. Gelletly, W.R. Kane and D.R. MacKenzie, *Neutron-capture gamma rays from the 9.47-eV resonance in $^{129}\text{Xe}(n,\gamma)^{130}\text{Xe}$* , Phys. Rev. C9, 2363 (1974).
- [131] W. Gelletly, W.R. Kane and D.R. MacKenzie, *Neutron-capture gamma rays from the 14.1-eV resonance in $\text{Xe}^{131}(n,\gamma)\text{Xe}^{132}$* , Phys. Rev. C3, 1678 (1971).
- [132] B. Fogelberg and W. Mampe, *Determination of the neutron binding energy of the delayed neutron emitter ^{137}Xe* , Z. Phys. A281, 89 (1977).
- [133] S.G. Prussin, R.G. Lanier, G.L. Struble, L.G. Mann and S.M. Schoenung, *Gamma rays from thermal neutron capture in ^{136}Xe* , Phys. Rev. C3, 1001 (1977).
- [134] M.A. Lone, R.A. Leavitt and D.A. Harrison, *Prompt Gamma Rays from Thermal-Neutron Capture*, Atomic Data and Nuclear Data Tables 26, 511 (1981).
- [135] J.K. Tuli, *Thermal neutron capture gamma rays*, <http://www-nds.iaea.org/wallet/tnc/capgam.shtml>.
- [136] G.L. Molnár, Zs. Révay, T. Belgya and R.B. Firestone, *The new prompt gamma-ray catalogue for PGAA*, Appl. Rad. Isot. 53, 527 (2000).
- [137] S.A. Hamada, W.D. Hamilton and B. Moer, *Gamma-gamma directional correlation measurements in $^{130,132}\text{Xe}$ following neutron capture by natural xenon*, J. Phys. G14, 1237 (1988).
- [138] A. Fassò, A. Ferrari, P.R. Sala and G. Tsileidakis, *Implementation of Xenon capture gammas in FLUKA for TRD background calculations*, ALICE Internal NOTE 28-2001 (2001).
- [139] A. Morsch, *"ALIFE: A Geometry Editor and Parser for FLUKA"*, ALICE Internal NOTE 29-1998 (1998).
- [140] A. Morsch and S. Roesler, *Radiation studies for the ALICE environment using FLUKA and ALIFE*, CERN ALICE/PUB 98-19 (1998).

- [141] AliRoot <http://alisoft.cern.ch/offline/>,
Root <http://root.cern.ch/> .
- [142] GEANT 3.21 Package, CERN Program Library W5013.
- [143] N.van Eijndhoven et al., *The ALICE Event Generator Pool*, ALICE Internal NOTE 95-32 (1995).
- [144] N. Rohrig, *Plotting Neutron Fluence Spectra*, Health Physics Vol. 45, No. 3, (September), pp. 817-818 (1983).
- [145] G. Tsiledakis, A. Fassò, P. Foka, A. Morsch and A. Sandoval, *Background in the ALICE TRD due to neutron capture in Xe*, ALICE Internal NOTE 10-2003(2003).
- [146] S.A. Cetin and A. Romaniouk, *Induced radioactivity in the active gas system of ATLAS-ID-TRT*, ATL-INDET-2002-001 (2002).
- [147] *Radiological Health Handbook*, U.S. Department of Health Education and Welfare (1970).
- [148] *Caltech Radiation Safety Training and Safety Manual*, <http://www.cco.caltech.edu/~safety/trm.html> .
- [149] *CERN Radiation Safety manual*, (1996)
- [150] *ATLAS Inner Detector Technical Design Report*, CERN/LHCC/97-17 (1997)
- [151] I. Dawson and C. Buttar *The radiation environment in the ATLAS inner detector*, Nucl. Instr. Meth. A 453, 461-467 (2000)
- [152] The ALICE Collaboration, *Technical proposal for a large ion collider experiment at the CERN LHC*. CERN/LHCC/95-71 (1995).
- [153] G. Tsiledakis *et al.*, GSI Report 2004, in print.
- [154] *Time Projection Chamber ALICE Technical Design Report*, CERN/LHCC/2000-001 (2000).
- [155] *The ALICE TPC Front End Electronics*, <http://ep-ed-alice-tpc.web.cern.ch/ep-ed-alice-tpc/>.
- [156] R. Veenhof, *Choosing a gas mixture for the ALICE TPC*, ALICE Internal NOTE 29-2003(2003).

- [157] H.R. Schmidt, *The LHC Experiment ALICE-TPC Challenges at High Multiplicities*, ALICE Internal NOTE in preparation (2005).
- [158] C. Garabatos, *The ALICE TPC*, Nucl. Instr. Meth. A 535, 197-200 (2004).
- [159] J. Wiechula *et al* *High-precision measurement of the electron drift velocity in Ne-CO₂*, Nucl. Instr. Meth. A 548, 582-589 (2005).
- [160] R. Bouclier *et al.*, *Results of wire chamber ageing tests with CH₄* Nucl. Instr. Meth. Phys. Res. A **346** (1994) 114.

Curriculum Vitae

Personal Data

Name	Georgios Karolos
Surname	Tsiledakis
Place of Birth	Bologna (Italy)
Date of Birth	02 November 1972
Marital Status	single
Nationality	greek

Education

09 / 1982 - 06 / 1990	Lyceum (Secondary School), Serres, Greece Average grade 18.7 over 20 (excellent)
09 / 1990 - 11 / 2000	Aristotle University (graduate in Physics), Thessaloniki. Diploma thesis 'Living matter as a detector of weakly interacting particles', supervised by Prof. Zioutas Main subject Particle Physics Average grade 7.3 over 10 (very good)
08 / 2001 - 11 / 2005	Doctoral fellowship at the Gesellschaft für Schwerionenforschung and preparation of the dissertation

Publications

1. *Implementation of Xenon capture gammas in FLUKA for TRD background calculations* , ALICE Internal NOTE 28-2001 (2001)
2. *TRD gas regeneration by cryogenic distillation* , ALICE Internal NOTE 37-2002 (2002)

3. *Background in the ALICE TRD due to neutron capture in Xe*, ALICE Internal NOTE 10-2003 (2003)
4. *Pulse height measurements and electron attachment in drift chambers operated with Xe,CO₂ mixtures* Nucl. Instr. Meth. Phys. Res. A498 (2003)
5. *Drift velocity and gain in argon- and xenon-based mixtures*, Nucl. Instrum. Meth. A523 (2004) 302

Talks

1. *Measurements of electron attachment in Xe, CO₂ (15%) gas of ALICE TRD*, DPG Tagung, Tübingen, 2003
2. *Background in the ALICE TRD and in the TPC electronics based on FLUKA calculations*, DPG Tagung, Köln, 2004
3. *Event-by-Event Fluctuations of the Mean Transverse Momentum at SPS Energy*, DPG Tagung, Berlin, 2005
4. *Correlations/fluctuations from SPS*, overview talk, RHIC & AGS Annual Users' Meeting, BNL, USA, 20-24 June, 2005
5. *Scale dependence of Event-by-Event mean p_T fluctuations at top SPS energy*, RNM meeting, GSI, 4 July 2005
6. V-I Workshop on 'Physics of strongly interacting matter at high densities' Bad Liebenzell, 3-5 October 2005 (contents as previous)

Acknowledgements

I am sincerely indebted to my supervisor Prof. Dr. Braun-Munzinger for the opportunity to join his group and work at GSI. He patiently taught me how to think in science, the process to follow in order to do research and to express and understand complicated concepts by means of intuitive examples. I direct many thanks to Prof. Dr. Appelshäuser who has guided me in that complex field of fluctuations and watched over my progress with care and interest. I am also grateful to Prof. Dr. Stachel who has provided many valuable suggestions for improving the work. No word of thanks could ever express what I owe to Prof. Dr. Sandoval and to Dr. Foka who supervised a big part of my work here and for being always attentive to my problems and questions. Dr. Andronic, Dr. Garavatos and Dr. Miskowiec, saved the project during its darkest phase...their perceptive suggestions, comments and critiques did wonders for the study and were invaluable. Going far beyond the call of duty, Alberto Fassò commented in detail on the 'FLUKA' part of my thesis and gave me the confidence to attempt a more expansive study. All 'CERES' and 'ALICE' students and scientists of GSI, Heidelberg and CERN deserve a special mention, since they alerted me to themes demanding further attention and helped me to give a formal shape to my studies and fill the gaps of my always incomplete training.

Prof. Zioutas convinced me to abandon the adventurous life I had and invited me at CERN...I wish I could deserve his trust and I will do my best to live up to his high expectations.

To all my friends I apologize because I have not made a lengthy list of all of you, but you know I keep you in my thoughts.

Laetitia, thank you for being so patient and persistent. After so many sad washouts you had being the second priority, you showed me that 'Life must be understood backwards; but... it must be lived forward' with or without you in the near future. Last but not least, not to forget my family for their support during this demanding period.

Erklärung

Hiermit erkläre ich an Eides statt, daß ich die vorliegende Dissertation
selbständig verfaßt, keine anderen als die angegebenen Hilfsmittel
verwendet und noch keinen Promotionsversuch unternommen habe.

Darmstadt, den 28. Nov 2005,

gez. Georgios Karolos Tsiledakis.

Unterschrift

